Titre: Title:	Développement d'une pile solaire photosensibilisée à base d'oxyde de zinc (ZnO) dopé avec l'acide tungstique
Auteur: Author:	Padjagoto Sangmbaye
Date:	2022
Type:	Mémoire ou thèse / Dissertation or Thesis
Référence: Citation:	Sangmbaye, P. (2022). Développement d'une pile solaire photosensibilisée à base d'oxyde de zinc (ZnO) dopé avec l'acide tungstique [Ph.D. thesis, Polytechnique Montréal]. PolyPublie. https://publications.polymtl.ca/10703/

POLYTECHNIQUE MONTRÉAL

affiliée à l'Université de Montréal

Développement d'une pile solaire photosensibilisée à base d'oxyde de zinc (ZnO) dopé avec l'acide tungstique

PADJAGOTO SANGMBAYE

Département de génie chimique

Thèse présentée en vue de l'obtention du diplôme de *Philosophiae Doctor*

Génie métallurgique

Octobre 2022

POLYTECHNIQUE MONTRÉAL

affiliée à l'Université de Montréal

Cette thèse intitulée :

Développement d'une pile solaire photosensibilisée à base d'oxyde de zinc (ZnO) dopé avec l'acide tungstique

présentée par **Padjagoto SANGMBAYE**

en vue de l'obtention du diplôme de *Philosophiae Doctor*

a été dûment acceptée par le jury d'examen constitué de :

Rachid BOUKHILI, président

Oumarou SAVADOGO, membre et directeur de recherche

William Jésus PECH RODRIGUEZ, membre

Yacouba DIAWARA, membre externe

DÉDICACE

Oumarou Mamoudou qui m'a initié aux énergies photovoltaïques

REMERCIEMENTS

Mes profondes gratitudes au professeur Oumarou Savadogo pour la confiance qu'il a placé en moi en m'acceptant comme son étudiant. Expert chevronné dans le domaine des énergies renouvelables, le Professeur O. Savadogo m'a donné un sujet de thèse qui traduit mon rêve qui est celui de contribuer à améliorer le taux d'électrification par l'énergie solaire au Tchad, en Afrique et partout dans le monde.

Mes plus grands remerciements au Président du Jury Professeur Rachid BOUKHILI et aux membres du Jury Dr Yacouba DIAWARA, Professeur William Jesús Pech Rodríguez et Professeur Samuel PIERRE d'avoir accepté d'évaluer cette thèse.

Mes plus grandes reconnaissances au Professeur Tahereh Fanaei Sheikholeslami, pour ses connaissances théoriques et pratiques qui m'ont tant aidé dans le laboratoire et dans la révision.

Mes sincères remerciements à notre attaché de recherche Dr Kentaro Oichi pour son dévouement.

Mes remerciements vont aussi à l'endroit de l'institution Banque Islamique de Développement qui a financé cette étude dans une prestigieuse école qu'est Polytechnique de Montréal.

Merci à tous mes collègues du laboratoire LaNoMat pour leur contribution dans les discussions, présentations ou échanges scientifiques. Mes remerciements adressés particulièrement à Ulrich Landry Compaoré, Dieudonné Tshibanda Kabumana, Barham Thiam, Daniel Kalufya et Fabrice Kaboré pour leurs conseils et disponibilité qui ont permis de garder le cap.

Merci à mon épouse Hebletring Nodji et à mes enfants Modobé, Urielle, Charline, Junior et Djekoudja qui ont été une source de renouvellement de force durant cette thèse.

Merci aux amis, parents, collègues et à tous ceux que je n'ai pas cité ici mais qui ont contribué de loin ou de près à la réussite de mes études doctorales.

RÉSUMÉ

Cette thèse consiste à développer une cellule solaire photosensibilisée (DSSC) à base d'un nouveau matériau d'oxyde de zinc (ZnO) dopé à l'aide d'acide tungstique (H_2WO_4) que nous avons synthétisé par la méthode sol-gel. Les DSSC sont des cellules solaires photovoltaïques de dernières générations qui connaissent de nos jours un essor rapide de performance dans les recherches et développement. Le développement des DSSC à base d'oxyde de zinc présente des intérêts à cause de la disponibilité et des propriétés opto-électronique de ce matériau. L'oxyde de zinc peut être synthétisé à partir de plusieurs précurseurs (zinc, acétate de zinc dihydraté, ….) en empruntant plusieurs voie de fabrication (sol-gel, hydrothermal, …).

L'objectif de ce travail est de synthétiser un matériau susceptible de contribuer à l'amélioration de la performance des DSSC à base de ZnO. Si nous introduisons deux semi-conducteurs comme photo-anodes ayant tous les deux des niveaux de bandes de conduction en dessous du niveau de l'état excité du sensibilisateur (LUMO) dans une configuration d'une pile solaire photo sensibilisée, on augmenterait de deux fois la possibilité de transfert des électrons du sensibilisateur vers les semi-conducteurs. Ceci pourrait fortement contribuer à augmenter les performances du la pile par rapport à un seul semi-conducteur.

La méthode sol-gel a été utilisée pour la synthèse de l'oxyde et son dopage à l'acide tungstique. Les solutions à base d'oxyde de zinc ont été déposées sur un substrat en FTO par spin-coating ou doctor blade. Ces échantillons sont séchés et recuits pour éliminer les composants organiques, améliorer la cristallinité et la conductivité du matériau. L'oxyde de zinc et l'oxyde de zinc dopé obtenus ont été caractérisés par :

- la diffraction au rayon X (XRD) pour confirmer la cristallinité hexagonale de l'oxyde de zinc et le calcul des tailles des grains;
- la microscopie électronique à balayage (MEB) pour l'observation de la morphologie des grains ;
- La spectroscopie UV-visible pour les mesures de transmittance et d'absorbance afin déterminer différentes bandes gap des échantillons dopés allant de 3,24 à 3,57 eV.
- La spectroscopie photoélectronique à rayons X ou XPS ;

- la spectroscopie par la transformée de Fourier ont confirmé les liaisons chimiques telles que Zn-O, W-O dans les échantillons ;
- la méthode de courant de Foucault pour évaluer les résistances surfaciques;
- la spectroscopie dispersive d'électrons (EDS).

Les échantillons d'oxyde de zinc et d'oxyde de zinc déposé sur le FTO ont été utilisés comme anode dans la fabrication des DSSC. L'anode a été trempée dans une solution de 0,3 mM de colorant N719 pendant 30 minutes avant d'être retirée et séchée : c'est la photoanode qui donne une réponse spectrale dans le domaine de spectrale de l'UV-visible. La cathode a été élaborée en déposant une couche mince de la solution platisol sur le FTO. La solution déposée a été séchée et recuite à 450°C et on obtient la cathode en platine. Les deux électrodes ont été assemblées en insérant entre eux l'électrolyte en ion iodure et ion triiodure (I^-/I_3^-). Les mesures courant-tension ont permis d'évaluer d'autres performances électriques des DSSC : courbe puissance-tension, les résistances série et shunt pour les différentes DSSC fabriquées.

Pour les différentes cellules solaires DSSC élaborées et éclairées dans les conditions standards (STC), la tension en circuit ouvert est de 0,75 ±0,02 V alors qu'on a une augmentation significative de 24,6 % pour le courant de fonctionnement optimal (12,2 ±0,001 mA/cm^2) pour les DSSC dopé par rapport à celle non dopé (9,2±0,001 mA/cm^2). Cela engendre des rendements de conversion photovoltaïque de 5,52 % pour les DSSC non dopés et 7,1 % pour les DSSC dopés à 10^{-4} M de H_2WO_4. Par rapport à ZnO seul, ces améliorations sont attribuées à plusieurs raisons séparées ou concomitantes. La première qui serait probable est l'ajout de WO_3 à ZnO. Ceci favoriserait plus de transferts d'électrons du niveau d'énergie du LUMO du sensibilisateur aux bandes de conduction de WO_3 et de ZnO. La deuxième raison serait éventuellement due à une plus grande adsorption du colorant et à une diminution des centres de recombinaisons des électrons photoexcités. La troisième raison pourrait être due à un effet synergétique entre les deux raisons ci-dessus.

Par ailleurs, l'effet de l'acide tungstique (pour 10^{-4} M de dopant) a contribué à diminuer la taille des cristallites (de 27,42 nm jusqu'à une valeur minimale de 17,14 nm) ce qui correspond à une diminution des résistances surfaciques (de 2,29 Ω/sq à 1,45 Ω/sq) et séries (de 8,19 $\Omega.cm^2$ à 5,5 $\Omega.cm^2$) de la cellule DSSC dopée.

ABSTRACT

This thesis consists in developing a photosensitized solar cell (DSSC) based on a new material of zinc oxide (ZnO) doped with tungstic acid (H_2WO_4). DSSCs are the latest generation of photovoltaic solar cells that are experiencing a rapid increase in performance in research and development. The development of DSSCs based on zinc oxide is of interest because of the availability and opto-electronic properties of this material. It can be synthesized from several precursors (zinc, zinc acetate dihydrate, ...) using several fabrication routes (sol-gel, hydrothermal, ...).

The objective of this work is to synthesize a material that can contribute to the improvement of the performance of ZnO-based DSSCs. If we introduce two semiconductors as photoanodes both having conduction band levels below the excited state level of the dye (LUMO) in a photo-sensitized solar cell configuration, we would increase the possibility of electron transfer from the dye to the semiconductors by two factors. This could strongly contribute to increase the performance of the battery compared to a single semiconductor.

The sol-gel method was used for the synthesis of the oxide and its doping with tungstic acid. The zinc oxide solutions were deposited on an FTO substrate by spin-coating or doctor blade. These samples were dried and annealed to remove organic components, improve the crystallinity and conductivity of the material. The obtained zinc oxide and doped zinc oxide were characterized by:

- X-ray diffraction (XRD) to confirm the hexagonal crystallinity of zinc oxide and calculation of grain sizes;
- Scanning electron microscopy (SEM) for the observation of the grain morphology.
- UV-visible spectroscopy for transmittance and absorbance measurements to determine different gap bands of doped samples ranging from 3.24 to 3.57 eV.
- X-ray photoelectron spectroscopy (XPS);
- Fourier transform spectroscopy confirmed the chemical bonds such as Zn-O, W-O in the samples;
- Eddy current method to evaluate the sheet resistance;
- Electron dispersive spectroscopy (EDS) characterization.

Zinc oxide and zinc oxide samples deposited on the FTO were used as anode in the fabrication of DSSCs. The anode was soaked in a 0.3 mM solution of N719 dye for 30 minutes before being removed and dried: this is the photoanode that gives a spectral response in the UV-visible spectral range. The cathode was elaborated by depositing a thin layer of the platisol solution on the FTO. The deposited solution was dried and annealed at 450°C to obtain the platinum cathode. The two electrodes were assembled by inserting between them the iodide ion and triiodide ion electrolyte (I^-/I_3^-). The current-voltage measurements allowed to evaluate other electrical performances of the DSSCs: power-voltage curve, series and shunt resistances for the different DSSCs manufactured.

For the different DSSC solar cells developed and illuminated under standard conditions (STC), the open circuit voltage is 0.75 ±0.02 V while there is a significant increase of 24.6 % for the optimum operating current for the doped DSSCs (12.2 mA/cm^2) compared to the undoped one (9.2 mA/cm^2). This results in photovoltaic conversion efficiencies of 5.52 % for undoped DSSCs and 7.1% for DSSCs doped with 10^{-4} M H_2WO_4. These improvements can be attributed to several reasons. The first could attributed to the addition of the WO_3 to ZnO. This would easier more electron transferts from the LUMO band level of the photosensitizer to the WO_3 and ZnO conduction band levels. The second reason could be the possibly greater dye adsorption and a decrease in photoexcited electron recombination centers. The third reason could be the synergetic effect of these two above reasons.

Furthermore, the effect of tungstic acid (for 10^{-4} M dopant) contributed to decrease the crystallite size (from 27.42 nm down to a minimum value of 17.14 nm) which corresponds to a decrease in the sheets resistances (from 2.29 Ω/sq to 1.45 Ω/sq) and series resistances (from 8.19 Ω.cm^2 to 5.5 Ω.cm^2) resistances of the doped DSSC.

TABLE DES MATIÈRES

LISTE DES TABLEAUX

LISTE DES FIGURES

LISTE DES SIGLES ET ABRÉVIATIONS

a-Si : silicium amorphe

DSSC ou DSC : dye-sensitized solar cell

CBD : « chemical bath deposition ». Dépôt chimique de bain ou procédé à la solution contenant des précurseurs pour le dépôt des nanomatériaux sur un substrat.

CVD : « chemical vapour deposition ». Dépôt chimique en phase vapeur est une technique de dépôt sous vide de couches minces à partir des précurseurs gazeux. Le substrat est exposé aux précurseurs en phase gazeuse qui réagissent à sa surface pour générer le dépôt désiré.

DCM : "dip coating method". Technique de revêtement du substrat par immersion dans la solution du matériau de revêtement. Ensuite le substrat est retiré à vitesse constante de la solution pour avoir un dépôt de couche mince. La vitesse de retrait détermine l'épaisseur de revêtement requise.

DBT: « Doctor-blade technique ». Technique de revêtement des couches minces contrôlé à l'aide d'une lame/couteau.

DFT : density functional theoritical

EBPVD: Electron Beam PVD

EDM : « electrodeposited method ». L'électrodéposition est une technique électrolytique de dépôt des couches minces dans laquelle les ions métalliques présents dans l'électrolyte subissent un effet électrique pour aller se déposer sur le substrat.

FF : facteur de forme

FTIR : la spectroscopie par la transformée de Fourier Infra-rouge

FWHM: full width at half maximum désigne la largeur à mi-hauteur.

HTM : « hydrothermal method ». Technique de synthèse de nanocristaux à partir d'une solution aqueuse. Conditions d'opérations : hautes températures, fortes pressions de vapeur.

HPAs : hétéropolyacides

IR : Infra-rouge

Isc : courant de court-circuit est le courant qui traverse la cellule lorsque la tension aux bornes la cellule est nulle. Pour une cellule solaire, le courant de court-circuit résulte de la génération et de la collecte des porteurs de charges générés par les rayons lumineux. Pour une cellule solaire idéale (aucune pertes résistives) , le courant de court-circuit est identique au courant généré par la lumière.

Jsc : densité de courant de court-circuit est le rapport du courant de court-circuit par la surface à l'électrode.

MEB : microscope électronique à balayage

PEN: polyethylene naphthalate

PVD : « physical vapour deposition ». Dépôt physique par vapeur consiste à transformer le solide ou liquide de revêtement en vapeur et ensuite cette dernière est conduite et condenser pour dépôt sur le substrat.

PCE : power convertion effeciency or the ratio of incident light power to output electrical power.

PV : photovoltaïque

SGM : sol-gel method

sccm : standard centimètre cube par minute (ou système métrique centimètre cube par minute)

SP: screen-printing

S: Sputtering

SWCN : single wall carbon nanotubes

SCM : « spin-coating method ». Technique de déposition des couches minces à l'aide d'une machine tournante appelée "spinner" ou « spin coater ».

SGM : "sol-gel method". Solution – gélification.

StSt : stainless steel

STC: standard test conditions

TCF : transparent conducting films

TCO : transparent conducting oxide

UV : ultra-violet

Vco est la tension en circuit ouvert ou la tension maximale disponible aux bornes d'une cellule solaire et cela se produit à courant nul.

XRD ou DRX : désigne la diffraction par rayons X

XPS : la spectroscopie photo-électronique à rayons X

CHAPITRE 1 INTRODUCTION

Les activités industrielles, résidentielles ou d'approvisionnements de l'Homme ont atteint un niveau tel qu'elles perturbent significativement l'environnement et rendent nécessaire de reconsidérer nos ressources énergétiques, notamment en faisant apparaître la part des énergies renouvelables qui, par nature, nous permettent de mieux envisager un réel développement durable. Cette augmentation des besoins énergétiques de l'humanité s'accompagne de l'épuisement des sources d'énergies fossiles et causent sérieusement des impacts néfastes sur la santé de l'homme et sur l'environnement notamment par le changement climatique, la pollution de l'air par les gaz à effet de serres contribuant à un réchauffement de notre planète terre. Pour freiner ces phénomènes de changement et réchauffement climatique, de pollution de l'air par les gaz à effet de serre, engendrés par des sources d'énergie non propre et répondre à cette crise énergétique dans un souci de développement durable, des nouvelles technologies d'exploitation d'énergie solaire comme source d'énergie alternative ont connu un essor ces dernières années, des plans d'action sont encouragés par la plupart des gouvernements et des organismes internationaux pour promouvoir les énergies renouvelables. En guise d'illustration, la filière solaire photovoltaïque a connu une croissance de production dans le monde d'au moins 50 GW en 2015 et 2018 (Jäger-Waldau, 2019).

L'énergie solaire est abondante et est la principale source des énergies renouvelables mais qui reste sous exploitée par l'homme pour son bien-être. En effet, si on arrivait à capter une heure d'ensoleillement de 1000 W/m^2 incident sur la surface de la terre, cette énergie ($4{,}58\ 10^{20}$ J) suffirait à couvrir deux fois le besoin énergétique mondial en 2020. L'énergie solaire est exploitable via des capteurs solaires thermodynamiques à concentration (Fresnel, cylindro-parabolique, centrale à tour) ou des panneaux solaires pour la conversion en énergie électrique. Pour une même puissance électrique produite, les panneaux solaires photovoltaïques (PV) sont trois fois moins onéreux par rapport aux capteurs solaires thermodynamiques à concentration. Ces coûts sont liés à quelques atouts que présentent la technologie des panneaux solaires PV dont la facilité d'installation décentralisée en réseau autonome sur les sites d'exploitations, la facilité de maintenance et le fonctionnement de ses composantes qui sont fixes contrairement aux capteurs thermodynamiques qui sont mobiles. Cela permet de supprimer les pertes dans la gestion des composantes mobiles de la centrale et du transport d'énergie (qui est exigé des grandes lignes électriques).

La technologie solaire PV est une application dite verte qui peut apporter des solutions durables notamment sur la réduction des émissions de GES, sur la disponibilité et l'accessibilité de la ressource. Mettre en exergue les panneaux solaires dans cette illustration fait mention de l'effet photovoltaïque qui est la capacité que certains matériaux ont à convertir l'énergie contenue dans le rayonnement solaire en électricité.

Plusieurs technologies des cellules PV regroupées en 3 filières PV ont été développées depuis la découverte de l'effet photoélectrochimique par Becquerel en 1839 pour répondre aux besoins énergétiques en appoint, en autonomie ou comme centrale électrique. Ces différentes technologies de cellules solaires présentent des avantages mais aussi des inconvénients et des limites de performances.

La première filière solaire photovoltaïque à silicium qui est une technologie mature et qui domine le marché du solaire photovoltaïque avec plus de 90 % (Bhandari, Collier, Ellingson, & Apul, 2015; *Photovoltaics report*, 2021) des panneaux solaires à silicium en production dans le monde (Figure 1.1). Cette maturité peut être justifiée par le fait que ces cellules PV peuvent être produits comme des sous-produits des composants électroniques (diode, transistors, …) et que leur rendement maximal de conversion électrique au laboratoire est de 26,7 % (Green et al., 2021); ce qui est intéressant pour une utilisation quotidienne de l'électricité. Cependant, la génération des cellules à silicium pose des problèmes qui sont : procédés métallurgiques énergivores, peu respectueux de l'environnement avec des rejets des matières toxiques (monoxyde de carbone) durant leur fabrication. Sur le plan environnemental, pour une tonne de silicium produite, 5000 m^3 de CO sont émis (O. Savadogo, cours solaire PV, Polytechnique de Montréal, 2020).

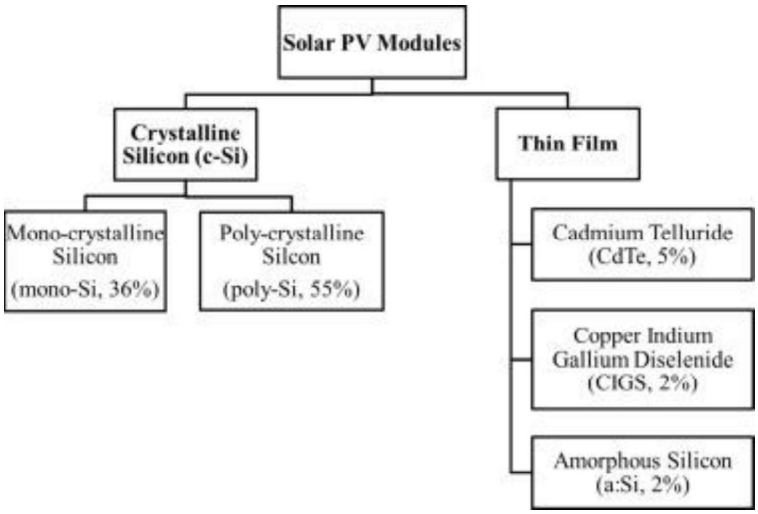

Figure 1.1 : Pourcentage des parts de marchés des technologies solaires PV (Bhandari et al., 2015)

La deuxième génération des cellules PV est celle des couches minces tels que le tellure de cadmium (CdTe), séléniure de cuivre indium gallium (CuInGa(Se)2 ou CIGS), silicium amorphe (a-Si). Les cellules solaires à base de Cd présentent l'inconvénient que le Cd a un impact de toxicité sur la santé humaine et une écotoxicité alors que les panneaux solaires CIGS sont onéreux à cause de la rareté de Ga qui est plus rare que l'or. Un autre frein technologique des filières des cellules PV ci-haut mentionnées est le temps récupération de l'énergie investie pour les différentes technologies pour une irradiation de 1700 kWh/m^2/an a été estimée entre 4,0 ans à 1,0 an (Bhandari et al., 2015; *Photovoltaics report*, 2021; Shah et al., 2004).

À la lumière des inconvénients écologiques et des limites de performances des cellules solaires PV ci-haut mentionnés, pourquoi ne pas développer des cellules solaires moins énergivores dans leur fabrication, plus respectueux de l'environnement et avec des meilleures performances comme une source d'énergie renouvelable ?

Pour répondre à cette question des chercheurs ont opté pour une troisième génération des cellules PV en effectuant des recherches sur des cellules PV organiques et les cellules semi-organiques telles que les cellules photosensibilisées à colorant constituées de composants renouvelables et écologiques. Les cellules photosensibilisées à colorant (en anglais « *dye-sensitized solar cell* » ou en abréviation *DSSC* ou encore *DSC*) sont des cellules solaires de troisième génération à couches minces (d'ordre nanométrique) élaborées à l'aide des colorants organiques ou synthétisés. On peut en effet citer quelques avantages de ces types de cellules qui sont:

- Faible coût de fabrication : possibilité des procédés de fabrication moins énergivore et aux basses températures tels que les DSSC à base de polymères;
- Flexibilités, facilement adaptable sur une géométrie. Réalisable sur un substrat rigide (verre par exemple) ou sur un substrat souple (polymère, métal);
- Matériaux avec différents bandes interdites;
- Cellules potentiellement semi-transparentes;
- Disponibilité des matériaux (colorant extrait des plantes naturelles, semi-conducteurs tel que l'oxyde de zinc abondant, électrode en carbone);
- Possibilité d'une forte diminution des matériaux (structure nanométrique) utilisés dans la fabrication;
- Fonctionnement aux faibles éclairements lumineux;
- Angles d'incidence des rayons lumineux peu influents;
- Accès aux cellules de grande surface.

Leur développement est une solution pour réduire la quantité d'énergie consommée lors de la fabrication des cellules photovoltaïques et protéger l'environnement. C'est sur cette ligne que nous inscrivons notre axe de recherche doctoral intitulé : « Développement des piles solaires photosensibilisées flexibles à base d'oxyde de zinc dopé ».

Les cellules photosensibilisées (DSSC) sont des cellules photo-électrochimiques fabriquées à base des couches minces des matériaux optiquement transparents et électriquement conducteurs (TCF ou *transparent conducting films*) sur les quels un sensibilisateur ou colorant est adsorbé pour obtenir une photoanode. On distingue les TCF inorganiques communément appelés couche d'oxyde conducteur (TCO ou *transparent conducting oxyde)* de celle organique tel que le nanotube de carbone, le graphène dans l'élaboration des DSSC. Les TCO sont des semi-conducteurs d'oxyde de titane tels que (TiO_2), d'étain (SnO_2), de zinc (ZnO), de tungstène (WO_3). Ce sont des semi-conducteurs à large bande interdite qui joue de rôle de transport des porteurs de charge photo-induites. Le choix d'une électrode à base de l'oxyde de zinc se justifie par l'abondance de zinc, le faible coût de fabrication de ZnO, la biocompatibilité de ZnO et la bonne mobilité des électrons de ZnO. Les DSSC sont respectueuses de l'environnement [2].

Toutefois, les DSSC présentent également quelques inconvénients :

- Rendement faible notamment les cellules à base de ZnO;
- Durée de vie plus courte par rapport à la cellule à Si;
- La plupart utilise l'électrolyte avec une température de stabilité maximale;
- La fatigue de ces cellules ne sont pas encore parfaitement non-maitrisée.

Le tableau 1.1 est le récapitulatif des cellules ci-haut cité avec leurs atouts et limites.

Tableau 1.1: Description de quelques technologies PV avec leur rendement maximal.

Cellule PV (Abréviation)	Description	Filière	Atouts majeurs	Limites majeures	Rendement (%) et référence
Silicium monocristallin (sc-Si)	Structure cristalline ordonnée, rigide, à bande directe. Apparence bleue.	Silicium	Ressource primaire abondant (silice), Technologie mature, bon rendement.	Fabrication énergivore, épaisseur : 200-350 µm, Rendement faible sous faibles éclairements, sensible à l'échauffement.	26,7±0,5 (K. Yoshikawa et al., 2017)
Silicium mutlicristallin (mc-Si)	Multitudes de petits cristaux à orientations variées rigide, bande directe. Apparence bleutée non uniforme.		Silice abondante, Bon rapport coût/rendement, production moins délicate que sc-Si, domine le marché.		19,8 (J. Zhao, Wang, Green, & Ferrazza, 1998)
Silicium amorphe(a-Si)	Structure désordonnée. Flexible, bande indirecte. Apparence gris foncé. Peu sensible à l'échauffement ≤60°C		Silice abondante, Fonctionnement aux faibles luminosités. Appliqué sur une grande surface	Faible rendement. Effet Wronski-Staebler.	10,3% (Lambertz, Finger, Schropp, Rau, & Smirnov, 2015)
Tandem (a-Si/sc-Si)	Jonction entre matériaux cristallins et amorphes		Rendement élevé.	Coût élevé.	12,3±0,3 (TEL Solar, Trubbach Labs, 2014)
GaAs	Matériau en couche mince flexible	Couche mince	Rendement élevé et peu sensible à la chaleur	Éléments rares. Coût élevé.	30,5 ± 1 (NREL, 1 jonction ,2018)
CIGS	Matériau en couche mince flexible			Éléments rares. Coût élevé.	23,35±0,5 (Solar Frontier, 2018)
CdTe	Matériau en couche mince flexible.		Moins sensible à chaleur que Si, fonctionne aux faibles luminosités, peu onéreux.	Toxicité de Cd. Rendement panneau commercial faible.	22,1 ± 0,5 (First Solar, 2018)
CZTS	Hétérojonction entre $Cu_2ZnSn(S,Se)_4$ et un semi-conducteur dopé		Matériaux courant et non toxique.	Rendement faible	11,0±0,2 (UNSW, 2017)
Multijonctions : AlGaInP/AlGaAs/ GaAs/GaInAs(3)	Jonctions de plusieurs (6 ici) semi-conducteurs à spectre d'absorption complémentaire		Très bon rendement	Coût élevé	47,1±2,6 (NREL, 2019)
Sensibilisée (DSSC/DSC) à base de ZnO	Composants mixtes organique (colorant) et inorganique (électrode), flexible.	Coût faible	Coût de fabrication faible, accès aux cellules de grandes surfaces, fonctionnement aux faibles éclairements.	Rendement faible.	7,5% (Vittal & Ho, 2017), (Gerrit Boschloo, Edvinsson, & Hagfeldt, 2006), (I.-D. Kim et al., 2007), (Chauhan, Shinde, Kumar, Gosavi, & Amalnerkar, 2016), (Y.-Z. Zheng et al., 2010)
DSSC à base de TiO_2					12,3-14% (Kakiage et al., 2015; Mathew et al., 2014; Yella et al., 2011)
Pérovskite				Fatigue non-maitrisée[1]	26,4±0,8 (Nanjing U., JET, 2021)
Organique (couche mince)	Composants polymère et/ou de composé organique moléculaire flexible		Coût de fabrication faible, fonctionnement aux faibles éclairements.	Fatigue non-maitrisée	18,2±0,2 (SJTU, NREL, 2020)

[1] Source: https://www.pv-magazine.fr/2020/11/25/une-cellule-solaire-perovskite-efficace-a-2517-grace-a-une-nouvelle-couche-photoactive/

Dans la revue de littérature de Kolodziejczak-Radzimska et al. (Kolodziejczak-Radzimska & Jesionowski, 2014) portants sur l'oxyde et ses additifs, il a été notifié l'effet des ions métalliques sur les propriétés physico-chimiques de l'oxyde de zinc. Les conclusions des travaux de Weinstock ont révélé que les hétéropolyacides et les additifs à base de W, O et H sont des excellents accepteurs d'électrons dans leurs bandes de conduction (Weinstock, 1998). L'hypothèse de ce travail se résume à doper l'oxyde de zinc par des additifs : acide tungstique (H_2WO_4), oxyde de tungstène (WO_3), hétéropolyacides (HPAs), afin d'améliorer ses propriétés électriques.

Les résultats attendus sont le développement des nouveaux matériaux obtenus à base de ZnO dopé à l'acide tungstique, à l'oxyde de tungstène, aux HPAs et le développement d'une nouvelle cellule DSSC à l'aide de ces nouveaux matériaux. Autrement dit à travers ce projet de recherche, nous voudrions contribuer à améliorer en rendement des piles solaires à couches minces à base de ZnO dopé. Cette thèse entre dans le cadre des recherches dans le domaine du photovoltaïque pour faire baisser le coût des piles solaires photovoltaïques par le développement d'une méthode fabrication des cellules solaires peu énergivore et plus écologique par rapport à la technologie silicium. La pertinence de ce projet s'inscrit dans le cadre du développement durable notamment la réduction des gaz à effet de serre, la protection de l'environnement par une production d'électricité sans émission de CO_2.
Ce document est reparti en 7 chapitres dont le premier chapitre commence par l'introduction.

Le chapitre 2 est l'article 1 qui aborde l'état de l'art sur l'oxyde de zinc dans sa méthodologie de fabrication, ses propriétés électriques, optiques, structurales et ses différents dopants comme photoanode en vue d'applications dans les cellules photovoltaïques sensibilisées à colorant (DSSC).

Le troisième chapitre fixe les objectifs de la thèse et décrit la méthodologie adoptée (techniques d'élaboration) pour traiter le sujet.

Le quatrième chapitre traite les techniques d'analyses physico-chimiques des composants de la cellule DSSC et la caractérisation courant-tension des cellules DSSC.

Le chapitre 5 est l'article 2 qui traite de l'élaboration des couches minces de ZnO et ZnO dopé à l'acide tungstique et leurs caractérisations comme photoanode.

Le chapitre 6 est l'article 3 consacré à la fabrication des DSSC à base de ZnO :H_2WO_4. Ces DSSC fabriquées ont été soumises aux mesures courant-tension et leurs performances (rendement, facteur de forme, résistance série, résistance parallèle, résistance caractéristique) ont été déterminées.

Une courte discussion a été menée sur l'ensemble de ces résultats au chapitre 7.

Enfin une conclusion générale de la thèse a été tirée avec des perspectives dans le dernier chapitre.

CHAPITRE 2 ARTICLE 1: STATUS ON DYE SENSITIZED SOLAR CELLS (DSSCS) DEVELOPMENT BASED ON ZINC OXIDE PHOTO-ANODE

Authors: Padjagoto Sangmbaye[1*], D. Tshibanda Kabumana[1], Oumarou Savadogo[1], Tahereh Fanaei Sheikholeslami[2]**

[1] Laboratory of New Materials for Energy and Electrochemistry, Polytechnique Montreal (QC), Canada.
[2] Department of Mechanical Engineering, Branch of Mechatronics, University of Sistan and Baluchestan, Zahedan, Iran
* Correspondence: *sangmbaye@gmail.com, **oumarou.savadogo@polymtl.ca; phone: +1 514 3404725*

Submitted to the Journal: Energies on August 3, 2022
(Review)

2.1 Abstract

A state of the art is made on the various materials of dye-sensitized solar cells (DSSC) based on metal oxides. A culmination was put on zinc oxide (ZnO), its properties (structural, electrical, optical, piezoelectric) and its dopants for use in electricity generating cells such as DSSC and nanogenerator. A dozen development methodologies (such as sol-gel, Hydrothermal, PVD, CVD, electrodeposition) and techniques for depositing thin layers in a DSSC cell (spin coating, doctor blade, dip-coating, pulsed laser deposition) from ZnO /doped ZnO have been reported. Depending on the technique's synthesis and doping elements, resistivity, charge carriers, band gap, morphology and size of crystallite in semiconductor (ZnO) are modified. Flexible and non-flexible substrates, complex of ruthenium or natural dyes, liquid or solid electrolytes constituting the DSSC have also been described. These technically assembled electrode, dye and electrolyte materials give DSSCs. Finally, a discussion was conducted on electrode materials: their performance, their limits and some development tracks are suggested.

Keywords: zinc oxide, band gap, electrodes, dye-sensitized solar cell

2.2 Introduction

DSSCs are solar cells that allow light to be converted into electricity using the concept of electrochemical photocell. In such a cell is an anode photo which can be semiconductor oxide particles shaped into a thin mesoporous layer sensitized using sensitizers such as the complex ruthenium dye. At the other electrode of the cell is a generally platinum counter electrode which bathes in an electrolyte containing ions such as the redox couple (I^-/I_3^-). When the cell is lit, chemical reactions in solutions and interfaces occur to produce a measurable electrical voltage at the terminals of the cell: this is the photoelectrochemical effect. After the discovery of the photoelectrochemical effect in 1839 by Becquerel (Williams, 1960) binary semiconductors including ZnO, ZnTe, ZnS, CdS, CdTe, Cu_2O immersed in electrolytes were tested as electrodes of solar cells in 1960 by R. Williams (Williams, 1960). Later in 1970, Tributsch and Calvin (Tributsch & Calvin, 1971) studied the phenomenon of photoexcitation in a cell based on ZnO with the sensitized anode with chlorophyll in contact with a platinum counter electrode. Tributsch and Calvin explained how a solar cell works sensitized by the fact that it is the sensitizer adsorbed on the ZnO which injects electrons into the conduction band of the semiconductor when the chlorophyll is excited with sufficient energy. Since then, advances in research and development have been made to develop new sensitized cells capable of supplying electricity to meet the ever-increasing energy need of ordinary people. Thus in 1980, by studying photosensitized cells based on CdS, TiO_2 or ZnO semiconductor with anode, Matsumura et al. .(Matsumura, Matsudaira, Tsubomura, Takata, & Yanagida, 1980) reach a record yield of 2.5% for the ZnO cell doped with aluminum / bengal pink as a dye and the redox (I^-/I_3^-) torque as an electrolyte. These researchers revealed the importance of the effect of doping ZnO by aluminum; this doping would have been the cause of an increase in the porosity of the interior of the semiconductor and the decrease in its electrical resistance, which would have contributed to the injection efficiency of the dye molecules. In 1991, O. Reagen and M. Gratzel (O'Regan & Grätzel, 1991) with an anode sensitized to the complex dye ruthenium (Ru) semiconductor, developed for the first time a DSSC cell with a record efficiency of 7.1- 7.9%, which is relatively usable as an energy source. This result had raised hopes that the DSSCs are now an alternative in the production of energy. However, there are some challenges to be met, apart from the efficiency of the cell to be increased among others: the stability of the dye and the electrolyte in the cell (in time and / or under heat), the phenomenon of corrosion

of materials, compatibility between the electrolyte and the electrodes. Liquid electrolyte poses problems including its volatilization, its influence on the distribution of the dye at the interface of the photoanode and a low stability of the cell. In response to these challenges, each component of a DSSC cell has attracted the attention of several research and development groups. Note that in 1993 the Swiss company Solaronix marketed materials to promote research, development, and the industry of sensitized solar panels. In 2002, the development of polymer gels in place of electrolytes led to DSSCs reaching a efficiency of 5.6% (P. Wang, Zakeeruddin, Exnar, & Gratzel, 2002). Until recently in 2014, Ahn et al. (Ahn, Kim, Chi, & Kim, 2014) broke this record with an 8.2% yield by developing a DSSC in the solid state. In 2006, thanks to the use of a 'high haze' TiO_2 anode on which the black dye dye and a platinum counter electrode in contact with the redox (I^-/I_3^-) torque are adsorbed, the efficiencies of DSSC quickly reached 11.1% (Chiba et al., 2006). Meanwhile in 2009, using a heteroleptic ruthenium sensitizer incorporating hexylthio-biothiophenic antennas rich in electrons, Chen et al. (C. Y. Chen et al., 2009) achieved a yield of 11.5%. In the same year 2009, the first commercializations of the DSSC were made by the company G-24 Power Limited. Shortly thereafter, several other DSSC marketing companies such as Dyesol, Solar print, Sony Corporation, H. Glass, Exeger Operations AB were created. In 2011, A. Yella et al. (Yella et al., 2011) formulated that redox torque shuttles (I^-/I_3^-) limit the performance of DSSCs. They implement DSSCs with a redox electrolyte based on cobalt (II/III) and with a dye (organic without metal) porphyrin reaching a yield of 12.3%. In 2014, other research by M. Gratzel's group on the use of porphyrin as dye molecules achieved 13% yield (Mathew et al., 2014). The following year, K. Kakiage et al (Kakiage et al., 2015) achieved 14% efficiency performance by developing solar cells with joint awareness of silyl anchor dyes (ADEKA-1) and carboxy anchorage (LEG 4). TiO_2-based DSSCs achieved a maximum effiency of 12.3-14% (Kakiage et al., 2015; Mathew et al., 2014; Yella et al., 2011). This figure increased to 15% thanks to the implementation of the perovskite pigment in a matrix of TiO_2 nanoporous (J. Burschka et al., 2013; Hu et al., 2014; Omar & Abdullah, 2014). The thermodynamic, kinetic and charge transport properties of TiO_2 and ZnO are comparable (K. Keis et al., 2002). Zinc oxide is considered the best alternative close to TiO_2 for DSSC cells since the start of research on TiO_2-based DSSCs ; this trend is attributable to the facts that TiO_2 and ZnO have the same electronic properties and the same prohibited band energies, respectively ~ 3.2 eV and ~ 3.3 eV, and ZnO has a much higher electron diffusivity than TiO_2

(Archana, Jose, Vijila, & Ramakrishna, 2009) and also has great electronic mobility (200 cm^2 V^{-1} s^{-1}) (Norton et al., 2004) which is favorable for efficient electron transport in the semiconductor and for the reduction of the recombination rate. In addition, the morphology and size of the ZnO crystals can be controlled in a synthesis (K. Keis et al., 2002) according to the conditions of preparations. However, ZnO-based DSSCs have an uncompetitive effiency which is less than or equal to 7.5% (Gerrit Boschloo et al., 2006; Chauhan et al., 2016; I.-D. Kim et al., 2007; Vittal & Ho, 2017; Y.-Z. Zheng et al., 2010) despite the advantages of the properties of this semiconductor. Zinc oxide is also non-toxic. In view of the above-mentioned assets and its abundance on earth, several researches intensify around ZnO including the morphology of the material which can improve the transfer of electrons in the mesoporous semiconductor, a decrease in the size of particles with high surfaces to increase the size, the amount of dye absorption, minimization of recombinations of photoexcited electrons, ... The objective of this review is to state the art on:

- The properties of ZnO: structural, optical (band gaps), electrical (resistivity) and piezoelectrical used in devices of generations of electricity.
- The operating principle of the DSSC cell.
- Some technologies for developing commonly used electrode materials
- The electrode materials used with their limits and challenges corresponding to DSSCs.
- Photo sensitizers used limits and challenges.
- Electrolyte used challenges and limits.
- Results and discussions on developed batteries.
- Conclusion and perspectives.

2.3 Materials and Methods

We have illustrated the literature review with some results we have obtained in our laboratory. The materials used are the following. The Factsage software was used to know the stability and synthesis range of ZnO. For the sol-gel method and thin film deposition, we had: the precursor zinc acetate dihydrate ($Zn(CH_3COO)2\ 2H_2O$, 98.0 to 101.0% Sigma Aldrich), the solvent which is an alcohol: ethanol 95.0%, methanol or isopropanol, catalyst (NaOH >97% Sigma Aldrich, HCl 15% or KOH) and stabilizer (monoethanolamine $HOCH_2CH_2NH_2$ 99.95% Fisher Chemical, diethanolamine, tetramethylammonium hydroxide or ethyldiaminetetraacetate). These chemicals

are used without further purification. The substrate used is a glass on which a layer of fluorine-doped tin dioxide FTO (SnO2 : F, glass) of the brand Sigma Aldrich TEC7 was applied. The characteristics (of a good substrate) of the FTO (for a DSSC cell) are:

- transparent to light with a transmittance of 80-82 % visible;
- low electrical resistance to facilitate electron flow; 7 Ω/m^2;
- This electrical resistance must be independent of temperature up to a temperature of 500°C, which is the operating temperature of the sol-gel method;
- Cut surface of the substrate: 2 cm x 2 cm for an active surface of deposit of 1 cm^2.

A KW-4A spin-coater (8500 rpm & 3.9″ max) and Automatic Doctor Blade MSK-AFA-III equipment are also available for the deposition of solutions on the FTO substrate. The solutions deposited at room temperature and under an atmosphere were dried in a Thelco Laboratory OVEN dryer. A VULCAN 3-550 programmable oven was used for annealing ZnO.

The JEOL JSM-7600F SEM was used to observe the surfaces of the ZnO and W doped ZnO samples.

2.4 ZnO and doped ZnO and its properties in electricity production devices

Zinc oxide is a binary compound belonging to group II and VI or binary II-VI semiconductor. Zinc oxide also known as "zinc white", "zinc monoxide" or "permanent white" with the formula ZnO is an inorganic component that looks like a powder of off-white to yellow and odorless color. This variation in white color depends on the impurities it contains or when it is heated at high temperature (a few hundred degrees Celsius) the zinc oxide turns yellow. This thermochromic effect that we checked during annealing between 400 °C and 500 °C in the laboratory is interpreted as the presence of the oxygen gaps that form during calcination. In natural form zinc oxide is presented as zincite containing magnesium and impurities. It is almost insoluble in pure water which allows in the case of synthesis where there is formation of water to separate it from the water. Zinc oxide is an amphoteric (acid and basic properties) but its area of stability is between pH = 5.8 to 14 (see diagram of Pourbaix Figure 2.1) and resists corrosion. The index Zn diagram (-2) indicates that its field of stability in an aqueous medium for almost neutral and basic pH (Figure 2.1). Its oxidation rate with the electrolyte is minimal which gives it stability and a long service life to the ZnO-based battery (Kay & Grätzel, 2002). Zinc oxide has a hexagonal wurtzite-type

crystallographic structure (Norton et al., 2004); this offers the possibility of flexibility of the material (Belaid et al., 2015). Its isoelectric point (zero load point) is at 9 pH. This justifies the choice of bases as sodium hydroxide (NaOH) or potassium hydroxide (KOH) as a catalyst in its synthesis.

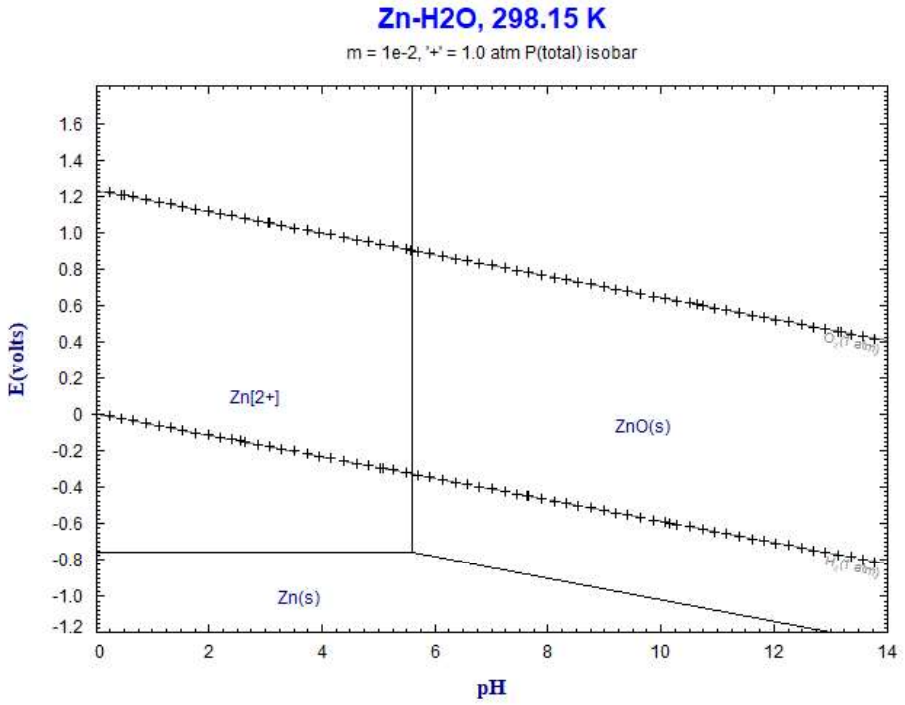

Figure 2.1: Pourbaix diagram of index (-2) of ZnO delimiting the stability zone of ZnO from pH=7 to 13.8 (simulation with data from Factasage 8.1)

Zinc oxide is obtained by purification of zincite or by synthesis from the precursors mentioned above. The abundance of the zinc precursor on the earth's crust is approximately 132 ppm (Center, Consulté le 28 Novembre 2021) making it the 24th most abundant element of the earth. Zinc ores are mined in more than 50 countries, the main ones being Australia, Canada, China, Peru and the United States (Center, Consulté le 28 Novembre 2021). In the future, we will make a brief history of ZnO, then we will discuss a state of art on its structural (crystalline), electrical, optical and piezzoelectric properties which are stressed in photovoltaic cells and piezzoelectric nanogenerators.

2.4.1 Brief history and applications of ZnO

500 years before Jesus Christ, zinc oxide was already used as a balm in traditional Indian medicine to treat open wounds and eye irritations (Craddock & Museum, 1998). The first factory factories were created in the 12th century in India before spreading to China, Europe and the world. Thus in 1743 the first European foundry in ZnO was installed in Bristol in the United Kingdom (Center, Consulté le 28 Novembre 2021). Between 1746 and 1749, Andreas Margaff installed a zinc smelter using a reduction of zinc oxide in the open air. In 1850, zinc white was manufactured throughout Europe and applied in the manufacture of oil paints to replace lead for economic and ecological reasons. Zinc oxide allows color shades to be done in the paint. In 1912, investigations of zinc oxide as a semiconductor were carried out after the first implementation of the transistors using semiconductors (Ellmer & Klein, 2008). A few years later, in 1920, the piezoelectric effect of ZnO was used in the first wireless radios as transducers in receivers. Then in 1935, the first diffractions of the electrons on the ZnO were observed confirming the crystallinity of the material. Three years later in 1938, the first Hall measurements dependent on the temperature of the ZnO were carried out confirming the intrinsic nature of type n of this material. In 1960, its piezolelectric properties led to the first electronic application (thin layer) in acoustic instruments. Eight years later, in 1968, zinc oxide was used in the manufacture of varistors.From the 1990s, research and development was increased in the synthesis of nanometric ZnO contributing to the development of Ipad chargers, laser devices. In 1995, emissions of UV laser from thin layers of ZnO were observed at room temperature. Zinc oxide is used in the rubber industry as an additive to resist corrosion. (Center, Consulté le 28 Novembre 2021) This is a key element in many industrial manufacturing processes such as paints, pharmaceuticals, plastics, batteries, electrical equipment, rubber, soap, textiles, flooring (Coleman & Jagadish, 2006). Indeed, zinc oxide has a high refraction index (2.01) (Sharma, Shukla, Sharma, & Kumar, 2020), high thermal conductivity, antibacterial properties and UV protection. It acts as an electrode, optical window or catalyst in batteries and electrical equipment. ZnO is recognized for its biocompatibility and low toxicity, which is why it is used in pharmaceutical and cosmetic products. The ZnO is inert in contact with the human body and does not present any danger in the event of a fire because its melting temperature is 1975 ° C (Sharma et al., 2020). The fields of application of zinc oxide nanoparticles are: electrodes of photovoltaic cells (Grätzel, 1999; Pradhan, Batabyal, & Pal, 2007; Y.-Z. Zheng et al., 2010), photocatalysis

(Chakrabarti & Dutta, 2004), electro catalysis (M. Singh et al., 2019), in varistors (J. Wu et al., 2002), photoluminescence (Studenikin, Golego, & Cocivera, 1998), batteries (Zou et al., 2014). According to data from Futures Market Inc, ZnO nanoparticles are distributed in the following fields: research and development (4%), electronics (1%), anti-bacteria products (5%), painting and coating (9%), ointment, cosmetics and sunscreen (80%), others (1%) (Markets & Inc., 2015).
Coleman et al. (Coleman & Jagadish, 2006) pointed out that we are entering an era where devices based on ZnO material will become more and more functional due to improvements in the growth technology of ZnO nanostructures, epitaxial layers, monocrystals and nanoparticles. The thin layers of ZnO based on nanomaterials are interesting in miniaturized technological devices such as detectors (presence, movement) in electronic security.

2.4.2 semi-conductor properties

2.4.2.1 Structural properties

The zinc atom has a tetrahedral coordination with 4 oxygen atoms and the electrons of zinc hybridize with the p electrons of oxygen. This tetrahedral coordination of Zn gives a polar symmetry along the hexagonal axis of ZnO, which polar symmetry is responsible for many properties of ZnO including piezolelectricity, spontaneous polarization, crystal growth, generation of faults, the possibility of substitution Zn^{2+} by a cation [28]. Zinc oxide is a material that can be synthesized at low temperature over a wide range of substrates (Coleman & Jagadish, 2006) such as glass, FTO, flexible polymer.

Structurally, the plan (0 0 0 1) is basal for wurzite zinc oxide and the best known faces are the polar faces at Zn termination (0 0 0 1) and at O termination (0 0 0 -1) (along axis c) and the non-polar faces (1 1 -2 0) along axis a) and (1 1 -1 0) both of which contain an equal number of atoms of Zn and O. Zinc oxide can crystallize in 3 forms: the hexagonal wurtzite structure, zinc cubic blende or the cubic structure of rock salt which forms under high pressure (10-15 GPa) (Özgür & Morkoç, 2018).Each zinc atom (Zn) or cation (Zn^{2+}) is surrounded by 4 oxygen atoms or 4 anions (O^{2-}) and vice versa. We have a coordination of 4 which corresponds to a covalent connection of type sp3. However, ZnO has a great iconicity due to a large difference in electronegativity make the Zn-O bond an ionic type of bond. Indeed, the electronegativity values of Zn and O are respectively 1.6 and 3.44.

The mixed nature of the bonds (covalent and ionic) in the ZnO crystal justifies these different possible configurations of ZnO according to the preparation conditions. Zinc oxide thus places itself on the border between an ion semiconductor and a covalent polar semiconductor. At room temperature ZnO crystallizes under a wurzite structure with a hexagonal mesh in the space group P63mc (Özgür & Morkoç, 2018) according to the notation of Hermann Mauguin.

P: designates the primitive mode with the network nodes at the top of the mesh;

ni: represents a rotation of $2\pi/n$ followed by a translation of i/n of the network vector parallel to the axis;

n = 6: represents the axes of rotation of angle $2\pi/6$ with n the order of rotation;

i = 3: the degree of translation is noted by an index;

m: the reflection or mirror plane.

Indeed, a group of space is defined from a combination of motif and punctual operations of symmetry such as reflection, rotation, and inversion to which are added translational operations. This structure is a stack of compact double layers of Zn and O oriented in the direction [0002] or along the c axis. The hexagonal wurtzite structure is that which is thermodynamically stable and technologically interesting (Özgür & Morkoç, 2018)

The mesh parameters are: a = b = 0.325 nm, c = 0.521 nm; $\alpha = \beta = 109.47$ °.(Özgür & Morkoç, 2018), (Norton et al., 2004)

2.4.2.2 Electrical properties

Several researchers have carried out measurements of the concentration of load carriers, the mobility and resistivity of zinc oxide but the values differ according to the synthesis technique and the operating conditions. According to Look (D.C.Look et al., 1998) at 300 K the concentration of donors in a ZnO massif synthesized by transport in the vapor phase is 6.10^{16} cm^{-3} with a mobility of 205 $cm^2.V^{-1}.s^{-1}$ (Table 2.1) while the concentration of acceptors is lower by approximately 2.10^{15} cm^{-3}. Nause and Nemeth (Nause & Nemeth, 2005) concluded in their work that the synthesis of ZnO by fusion of Zn and O leads to a type n material with a density of $5.045.10^{17}$ cm^{-3} and a mobility of 131 $cm^2.V^{-1}.S^{-1}$ to T = 296 K. The authors measured a decrease in load carrier density ($3.64.10^{16}$ cm^{-3}) and an increase in mobility (298 $cm^2.V^{-1}.s^{-1}$) of these load carriers at 78 K. Through

a laser deposition process (PLD), Kaidashev et al. (Kaidashev et al., 2003) deposited a layer of ZnO from 1 to 2 μm on plan-oriented sapphire substrates along axis c. The authors then carried out the measurements of the mobility values from 115 to 155 cm^2/V to 300K in a concentration range of the carriers 2 to 5.10^{16} cm^3. ZnO films produced by epitaxy of the molecular beams (MBE) assisted by the plasma were subjected to the measurements of the mobilities where a maximum value of 130 $cm^2.v^{-1}.s^{-1}$ was reached and a residual concentration of the carriers of $1.2.10^{17}$ cm^{-3} was reached (Kato, Sano, Miyamoto, & Yao, 2003). Layer of ZnO deposited on a sapphire c-plane substrate in contact with double buffer layers of ZnO / Mg (Miyamoto, Sano, Kato, & Yao, 2004). The deposit technique performed by Miyamoto et al. (Miyamoto et al., 2004) is by epitaxy of plasma assisted molecular beam. Analysis of these samples gave a maximum mobility value of 145 $cm^2.v^{-1}.s^{-1}$ and a concentration of 10^{17} cm^{-3} (Miyamoto et al., 2004). The growth parameters (such as temperature and speed of reagents) of the buffer layers significantly affect the structural properties of synthesized ZnO epitaxies. At low synthesis temperatures, Miyamoto et al noticed an improvement in the electrical properties of ZnO films justified by a decrease in the density of dislocations in the epitaxial structure.

Table 2.1: Summary of the synthesized ZnO samples with their n-type charge carrier concentration and electron mobility

Sample	**Fabrication technique**	**Carrier concentration (cm^{-3})**	**Electron mobility ($cm^2.V^{-1}.S^{-1}$)**	**Reference**
ZnO (solid)	Vapor phase transport	6.10^{16}	205	(D.C.Look et al., 1998)
ZnO (solid)	Fusion under pressure	$5,05.10^{17}$ (296 K) $3,64.10^{16}$ (78 K)	132 (296 K) 298 (78 K)	(Nause & Nemeth, 2005)
ZnO (solid)	Hydrothermal	8.10^{13}	200	(Maeda, Sato, Niikura, & Fukuda, 2005)
ZnO (thin film)	PLD* (sapphire substrate)	2.10^{16}	155	(Kaidashev et al., 2003)
ZnO (thin film)	MBE**(a-sapphire substrate)	$1,2.10^{17}$	130	(Kato et al., 2003)
ZnO in contact ZnO/MgO	MBE (sapphire substrate)	$1,2.10^{17}$	145	(Miyamoto et al., 2004)

*PLD: pulsed laser deposition. **MBE : molecular beam epitaxy.

Finally, it can be said that the concentration of load carriers in the ZnO is around 10^{16} cm^{-3} to 10^{17} cm^{-3} (Coleman & Jagadish, 2006; D.C.Look et al., 1998; Kato et al., 2003) while for doped ZnO of type n this concentration can reach 10^{20} electrons.cm^{-3} (Coleman & Jagadish, 2006). When doped with type p, the concentration of the carriers is of the maximum order of 10^{19} electrons.cm^{-3} (Look, Claflin, Alivov, & Park, 2004). The exciton energy is 60 meV to 300 K and the mobility of the electrons is around 200 $cm^2.V^{-1}.s^{-1}$ (Maeda et al., 2005) in the ZnO. Indeed, these electrical parameters (load carrier concentrations, mobility, and resistivity) are generally responsible for morphology, size, porosity, nanocrystal interconnections and dislocations in the structure of the ZnO synthesized sample. Doping is also a parameter for modifying electrical resistivity and which is often used in the search for a decrease in this value. Doping: zinc interstitials and oxygen gaps are at the origin of electron donors likely to reduce resistivity and therefore improve electrical performance.

2.4.2.3 Optical properties

According to Srikant and Clarke (Srikant & Clarke, 1998) the band prohibited at room temperature is 3.3 eV and that the other values 3.1, 3.2 eV are attributable to transitions of donor in the valence band. Tan et al. (S. T. Tan et al., 2005) claimed in their work to have prohibited bands of ZnO ranging from 3.15 to 4.06 eV depending on the synthesis temperature between 500 ° C and 200 ° C. According to the literature, the band gap of ZnO can vary according to ZnO synthesis such as temperature (Srikant & Clarke, 1998; S. T. Tan et al., 2005), pressure (Song, Aberle, & Xia, 2002), the presence of another element in the crystal lattice such as doping element or an element in a composite of ZnO. In each of the cases, the Burstein phenomenon justifies the change of the band gap by a modification on the Fermi level of the synthesized material.

The effect of temperature on the band gap of ZnO has been illustrated in the work of Tan et al (S. T. Tan et al., 2005). Tan el al deposited ZnO thin films on a SiO2 substrate by MOCVD synthesis, from dimethylzinc (DMZn) sources, nitrogen gas and oxygen. The synthesis were made at the temperatures between 200 and 500°C. The XRD results have been shown that there is an increase in crystal sizes from 5.57 nm to 10.11 nm in the (002) plane respectively for each deposition temperature. However, their optical analysis results give a decrease in the band gap from 4.06 eV to 3.13 eV. For a ZnO synthesis at 300°C with annealing at 450°C, the obtained band gap of ZnO

is 3.25 eV. For the latter authors, the band gap is inversely proportional to the square of the particle size (Kayanuma, 1988).

$$E_{(gap,nanocrystal)} = E_{(gap,bulk)} + \frac{\pi^2 h^2}{2R^2}\left(\frac{1}{m_e^*} + \frac{1}{m_h^*}\right) - 0.248E_{Ry}^*$$

With:

$E_{(gap,\ bulk)}$: band gap of ZnO ambient temperature; E_{Ry}*: bulk exciton binding energy; m_h*: hole effective masse; m_e*:electron effective masse , h: planck's constant ; R : radius of ZnO nanocrystals.

The effect of the synthesis pressure on the band gap of ZnO has been illustred by Song et al. (Song et al., 2002). Song et al. studied the properties of ZnO:Al synthesized by sputerring magnetron technique (100W rf power) at 250°C by varying the synthesis pressures 0.2 to 3.2 Pa. The optical analysis results show that the highest band gap is that of the ZnO:Al thin film deposited under 0.2 Pa (3.61 eV) pressure followed by that under 3.2 Pa (3.48 eV) and 1 Pa (3.35 eV). The authors attribute the band gaps of ZnO:Al thin films slightly higher than that of pure ZnO due to the Burstein-Moss phenomenon which is responsible for an increased concentration of free electrons brought by the doping element. Moreover, SEM analysis showed that the roughness and morphology of the thin films change according to the pressure of the argon gas. The latter authors used an optimal layer of synthesized ZnO:Al as a window layer and heterojunction partner in ZnO:Al/n-Si heterojunction solar cells reaching a conversion efficiency of 8.2%.

Considering the effect of the doping on the band gap of ZnO, Mahajan et al (Mahajan, Ahmed, Datt, Gupta, & Arya, 2022) have performed the doping of ZnO with WO3 by the sol-gel method. The obtained ZnO-WO3 nanocomposite was analyzed by UV-visible spectroscopy and their conclusion reveals an increase in the band gap at 3.7 eV compared to that of 3.3 eV of pure ZnO. The nanocomposite was used as an active layer in the fabrication of inverted organic solar cells (Mahajan et al., 2022). In another research, Sajjad et al (Sajjad, Sajjad, Iqbal, & Ryma, 2018) synthetized ZnO material by hydrothermal method from mixing of ZnO and WO_3 in absolute ethanol solvent. The resulting mixture was dried and calcined at 500°C. The authors noticed the presence of ZnO which inhibited the crystallization of WO_3 and caused agglomeration of WO_3 on the surface of nanoparticles (Sajjad et al., 2018). The XRD showed a decrease in the grain sizes of the crystallites from 24.06 nm to 17.22 nm as well as a decrease in the band gap of ZnO from 2.78

eV to 2.56 eV, when the percentage of ZnO increases from 1 to 4% in the doping of WO_3. The authors justify this band gap decrease due to the presence of the impurities corresponding to oxygen vacancies that are produced when W^{6+} ions (radius 0.074 nm) are replaced by Zn^{2+} ions (radius 0.065 nm) in the WO_3/ZnO composite. Therefore, the oxygen defects would have acted for band gap narrowing and at the same time, as color centers for visible light absorption (Sajjad et al., 2018).

For wavelengths between 200 nm and 360 nm (UV-visible domain) ZnO's transmittance is almost zero and therefore its absorbance is very high [49] while for wavelengths greater than 450 nm the transmittance of ZnO is approximately 80-90%. [50, 51] Electronic density calculation techniques (DFT for acronym density functional theoretical) used to calculate the electronic structure of the Doped ZnO and ZnO samples showed that the conduction band close to Fermi's energy was a combination of hybridized Zn sp states and Al states (Jantrasee, Moontragoon, & Pinitsoontorn, 2016). Jantrasee et al. (Jantrasee et al., 2016) combined this calculated band structure with the Boltzmann transport equation to determine the thermoelectric parameters of the samples. The measured and simulated conductivities are in concordances (Jie et al., 2004). Zinc oxide properties are summarised in table 2.2.

Table 2.2: Summary of the properties of ZnO and TiO_2

Properties	ZnO	TiO_2	Unit
Crystal structure at 300K	Wurtzite (Norton et al., 2004; Özgür & Morkoç, 2018)	Anatase	
Network parameter a=b	0.325 (Norton et al., 2004; Özgür & Morkoç, 2018)	0.378 (Burdett, Hughbanks, Miller, Richardson, & Smith, 1987)	nm
Network parameter c	0.521 (Norton et al., 2004; Özgür & Morkoç, 2018)	0.951 (Burdett et al., 1987)	nm
Density (kg/m^3)	5.6 (Sharma et al., 2020)	3.79 (Cromer & Herrington, 2002)	$g.cm^{-3}$
Binding energy in the exciton	60 meV		
Static dielectric constant	7.9-8.65 (Sharma et al., 2020)	31 (H. Yoshikawa & Adachi, 1997)	
Optical dielectric constant	3.7 (Sharma et al., 2020)	6.25 (H. Yoshikawa & Adachi, 1997)	
Band gap energy (E_g)	3.1-3.35 (Srikant & Clarke, 1998; S. T. Tan et al., 2005)	3.2 (Tang, Prasad, Sanjinès, Schmid, & Lévy, 1994; Zhang & Xu, 2020)	eV
Flat band potential	-0.5	-0.5	V vs SCE
Band structure	direct	indirect	
Conduction band orbitals	Zn (3d) and O (2p)		
Valence band orbitals	Zn (3d)		
Electron mobility	200	0.4-4	$cm^2V^{-1}s^{-1}$
Effective electron mass	0.24 - 0.3 m_0 (Kayanuma, 1988; S. T. Tan et al., 2005)	1.0 m_0 (Tang et al., 1994)	m_0=9.11 x 10^{-31}kg
Effective hole mass	2.31 m_0 (Kayanuma, 1988; S. T. Tan et al., 2005)	0.8me	
Refractive index	2,01 (Sharma et al., 2020)		
Melting point	1975 (Sharma et al., 2020)		°C
Point of charge (Pzc)	8-9	5.5-6.5	pH

Zinc oxide also has an anisotropy inherent in the crystal structure for the growth of nanofils (Khranovskyy, Lazorenko, Lashkarev, & Yakimova, 2012). According to S. Fay's work, the layers of ZnO have a high power diffusing light rays (Fay, 2003). This diffusing power extends the flow of light into the solar cell, which increases its absorption and therefore likely to provide a high photoelectric conversion efficiency (H. Yoshikawa & Adachi, 1997).

2.4.2.4 Piezoelectrical properties

Zinc oxide has piezoelectric properties widely used in signal processing, nanoelectromechanical, microelectromechanical systems, sensors. Piezoelectric property consists of subjecting an electrical

signal to a ZnO layer which will be converted into a mechanical wave and vice versa. Indeed, the space group P63mc not presenting a center of symmetry, the barycenters of the positive and negative charges of its elementary mesh cannot be superimposed. This induces an internal electrical dipole modulable by the application of an external mechanical stress: it is the direct piezzoelectric effect. The inverse piezoelectric effect is the interaction between this electric dipole and an external field. In 2008, Qin et al. (Qin, Wang, & Wang, 2008) developed ZnO-based piezoelectric nanogenerators. In their work they established a methodology to trap mechanical energy from bodily movements and light winds using the thin layers of ZnO nanofils deposited on the substrate (or fiber) in Kelvar 129. ZnO's nanofils were deposited hydrothermal. The authors used these samples to create a junction between the nanofils of ZnO covered with gold and the nanofils of ZnO. Under the effect of an external traction (wind or body movement), the vibrate junction generating a total current which is the sum of the currents in each nanofil and the potential is determined by a single nanofil. The authors justify these results by the fact that the nanofil interface of ZnO covered with gold and nanofil of ZnO behaves like a diode of Schottky polarized live (under mechanical effect) and generates an electric current.

A surface acoustic wave (SAW) transducer is one of the best-known applications of the ZnO layer as a piezolelectric material in signal processing. It is an electronic equipment playing the role of bandpass filter or bandpass filter. Emanetoglu et al. (Emanetoglu, Gorla, Liu, Liang, & Lu, 1999) have developed using epitaxial ZnO synthesized by MOCVD, an SAW transducer which receives an electric current at the inlet of the transducer interdigital (IDT) and converts it into a mechanical wave length of 10 to 16 μm propagating towards the output of the transducer. The terarous compound $Mg_xZn_{1-x}O$ and zinc oxide constitute a heterojunction $Mg_xZn_{1-x}O$/ZnO of the photoconductive and photoelectric type with UV radiation (Lu, Emanetoglu, & Chen, 2006) integrated into a UV photodetector by Emanetoglu et al .(Emanetoglu et al., 1999) The development of these piezoelectric technologies have a special place in the nanosystems to be self-supplied (Paradiso & Starner, 2005) , detection technologies, personal electronic equipment, signal processing. Zinc oxide (epitaxial layer, monocrystal) is also used as a GaN alternative in the field of ultraviolet blue optoelectronics (Look, 2001) and piezoelectric (Gardeniers, Rittersma, & Burger 1998) because of the similar properties of these two semiconductors. Indeed, the prohibited bands and the crystallographic structures are almost identical. In addition, given its good resistance

to radiation, zinc oxide is a serious candidate semiconductor to replace other semiconductors such as Si, GaAs, GaN in space applications (Look, Reynolds, Hemsky, Jones, & Sizelove, 1999).
Zinc oxide doped with aluminum or gallium are low resistivity semiconductors (10^{-4} to 10^{-5} Ω.cm) and very transparent (greater than 80%) (H. Liu, Avrutin, Izyumskaya, Özgür, & Morkoç, 2010; Minami, 2005) in the area of UV-visible. These properties make transparent thin layers and conductive of ZnO: Al and ZnO: Ga, potential candidates to substitute ITO (In_2O_3: Sn) in optoelectronic applications as electrodes (Minami, 2005). This solution track is all the more important as the indium contained in the ITO is rare and very expensive and the need for transparent electrodes for optoelectronic devices is increasing.

2.4.2.5 Doping and additives of zinc oxide

According to the applications and properties sought, zinc oxide can be affected by the presence of impurities or defects in its synthesis. Donor type impurities generally come from the H, Al, Ga, In atoms. Impurities of accepting types come from atoms such as N, P, As, Sb. One has defects in Zn's interstitial sites, Zn's gaps, O's and complex gaps in each of them.
Group I elements, in this case hydrogen is used as a donor to ZnO (Y.-S. Kang, Kim, & Lee, 2000) in order to improve semiconductor resistivity. Van De Walle justifies (Van de Walle, 2000) this donor state with thermodynamic equilibrium by a theory in which H^- always has a formation energy greater than H^o or H^+.
The elements of group II Mg and Cd form a solid solution with Zn offering a wide range of band prohibited from 2 eV to 8 eV (D.C.Look et al., 1998) Zinc oxide has the ability to grant its prohibited band by divalent substitution on one of its cationic sites. For example when doping ZnO by Cd^{2+} or Mg^{2+}, the band gap of ZnO increases to around 4.0 eV (Coleman & Jagadish, 2006). El Hamidi et al. (El Hamidi, El Mahboub, Meziane, El Hichou, & Almaggoussi, 2021) attributed optical changes simultaneous to the difference in electronegativity between Zn and Mg, and variation of grain size. Doping ZnO with metals such as Mn gives it a ferromagnetic property (J. Wu et al., 2017). Ternary compounds such as MgZnO and CdZnO formed using ZnO and elements Mg and Cd are used to form heterojunctions with ZnO in optical and electronic device (D.C.Look et al., 1998).

Elements of group III such as Al, Ga and In play the role of donor dopants of ZnO. According (K.-K. Kim et al., 2005) Al bring a concentration of load carriers greater than 10^{20} cm^3 in the doped matrix of ZnO. These latter authors have also demonstrated an improvement in the conductivity of ZnO doped to the elements of group III.

The Elements of group V such as N, P, As and Sb are used acceptors for doped ZnO as a p-type material (D.C.Look et al., 1998). These elements are likely to substitute the sites of O. The doping of ZnO by N attracts a lot of attention from researchers because of the ionic radius of N which is like that of O. However the materials of type produced are unstable and can change of properties under lighting (D.C.Look et al., 1998).

The elements of group VI can substitute the sites of O by obtaining compounds such as Zn-VI. Yoo et al. (Yoo et al., 2002) showed in their paper that S-doped ZnO has a lower resistivity than ZnO due to a higher carrier concentration.

Elements of group VII such as F, Cl, Br and I can substitute O as a ZnO donor. The doping of ZnO by F made it possible to obtain a reduction in the resistivity of the thin layer of the sample drawn up (Guilln-Santiago, de la L. Olvera, Maldonado, Asomoza, & Acosta, 2004).

Transition metal ions: Zinc oxide has been doped with several transition metal ions (Pearton et al., 2007) (Co, Mn, Sn, Fe, Sc, Ti, Cr, V, W, Neither) conferring ferromagnetic properties, electro-optical, electro-chromic, ferroelectric or catalytic (Georgieva, Armyanov, Valova, Poulios, & Sotiropoulos, 2007; Svensson & Granqvist, 1984; Haidong Zheng et al., 2011) to synthesized samples. Heteropolyacids (HPAs) or polyoxymetallates are also potential sources of doping in transition metal ion. The effect of $K_7HNb_6O_{19}$ polyoxomellates improving ZnO's electrical performance was shown by X. Sang et al (Sang, Li, Chen, & Wang, 2012) in a basic synthesis medium (pH = 8-14) by the hydrothermal route. In addition, J. Li et al. (J. Li et al., 2013) have proposed that heteroployacids improve the performance of sensitized photovoltaic solar cells but that they remain intact in the ZnO electrode in a quasi-neutral synthesis medium by solvothermal means. No study has yet been carried out in a basic environment for these additives in a matrix of ZnO. Heteropolyacids (HPAs) are compounds which have the general formula $H_nXM_iO_j$, Regarding the additives of ZnO, in 2014, Kolodziejczak-Radzimska et al. (Kolodziejczak-Radzimska & Jesionowski, 2014) summarized 3 categories: inorganic, organic and polymer additives. Inorganic additives such as metal ions, SiO_2, Al_2O_2, $LiCoO_2$. These additives have

properties that may change the size of nanoparticles, improve the degree of dispersion of ZnO nanoparticles and play on the photocatalytic effect of oxide. Organic additives such as carboxylic acid, silane are compatible with zinc oxide and bring characteristic groups to the surface of ZnO which modify its physicochemical properties. These additives improve the dispersion of ZnO in an organic matrix such as rubber mixtures contributing to greater stability of the material. Polymeric additives such as poly (ethylene glycol), polystyrene, poly (methyl methacrylate), poly (methacrylic acid), chitin are also likely to improve the electrical, thermal and optical properties of the ZnO / polymer composite.

Metal oxide nanocomposites are also used to improve the performance of DSSCs through efficient charge separation (Bibha Boro, Gogoi, Rajbongshi, & Ramchiary, 2018). As an illustration, the nanocomposites: Al_2O_3/TiO_2 (Palomares, Clifford, Haque, Lutz, & Durrant, 2002), MgO/TiO_2 (Taguchi et al., 2003) , ZnO/Al_2O_3 (Law, Greene, Johnson, Saykally, & Yang, 2005), TiO_2/ZnO (B. Boro, Rajbongshi, & Samdarshi, 2016), ZnO/SnO2 (Park et al., 2004). In their review, Boro et al. (Bibha Boro et al., 2018) summarized the performance of DSSC based on anode nanostructured TiO_2/ZnO nanocomposite: open circuit voltage, short circuit current, fill factor and efficiency lies in the range of 0.76–0.82 V, 3.24–16.70 mA/cm^2, 0.17–0.69% and 0.51–9% respectively. For examples composite anode:

- TiO_2 doped with different size ZnO nanorods with 5.8 % DSSC efficiency (Pang et al., 2007); the open circuit voltage, the short circuit current and the fill factor are 0.76V, 11.4 mA/cm2, 50% respectively (Pang et al., 2007)
- Coaxial TiO_2/ZnO nanotube arrays with 2.8 % DSSC efficiency (Xie, Li, Xu, & Zhang, 2011); the open circuit voltage, the short circuit current and the fill factor are 0.65 V, 7.28 mA/cm2, 60% respectively (Xie et al., 2011);
- ZnO/TiO_2 nanotube arrays with 3.75 % DSSC efficiency (R. Liu, Yang, Qiang, & Liu, 2012); the open circuit voltage, the short circuit current and the fill factor are 0.895 V, 5.96 mA/cm2, 70.4% respectively (R. Liu et al., 2012);
- ZnO-decorated TiO_2 nanotubes with 3.17 % DSSC efficiency (K. M. Lee, Lee, Yoo, & Shin, 2013);
- ZnO nanotube arrays coated with TiO_2 nanoparticles with 3.94 % DSSC efficiency (Giannouli, 2013);

- TiO_2-coated ZnO nanowires arrays with 5.65 % efficiency (C. Xu, Wu, Desai, & Gao, 2012);
- TiO_2/ZnO core-sheath nanofibers films with 5.17 % efficiency (Du et al., 2012);
- ZnO coated TiO_2 with 6.62 % DSSC efficiency (Chou, Chou, & Kang, 2012);
- TiO_2/ZnO nanodonuts with 9.00 % DSSC efficiency (F. Li, Jiao, Xie, & Li, 2015).

2.5 DSSC based on ZnO and doped ZnO

This part is devoted to a state of the art on some elaboration techniques of electrodes and their assemblies to form DSSC. However, let's start by describing the operating principle of DSSC.

2.5.1 Principles and technologies

In general, a DSSC consists of a transparent anode conducting a mesoporous film of inorganic semiconductor oxide sensitized by an organic dye or organometallic complex, a liquid electrolyte containing a redox mediator and a metal cathode (Figure 2.2 a). Inorganic semiconductor oxides must be transparent and porous to have a large contact surface with the dye adsorbed into a monolayer, and thus maximize the absorption of light. The pores of the semiconductor oxide nanoparticles adsorbed with dye form an interpenetrating heterojunction where the separation of photo-induced charges occurs at the interface between mesoporous oxide and the dye (Grätzel, 1999). Indeed, excite is always released from donor sites (color molecules) as a result of sufficient illumination. There follows a separation in the donor-acceptor junctions and diffusion to the electrodes. Semiconductor oxides with high surface / volume ratios are used in several applications. The fields of application of zinc oxide nanoparticles are: electrodes of photovoltaic cells (Grätzel, 1999; Pradhan et al., 2007; Y.-Z. Zheng et al., 2010), photocatalysis (Chakrabarti & Dutta, 2004), electro catalysis (M. Singh et al., 2019), in varistors (J. Wu et al., 2002), photoluminescence (Studenikin et al., 1998), batteries (Zou et al., 2014).

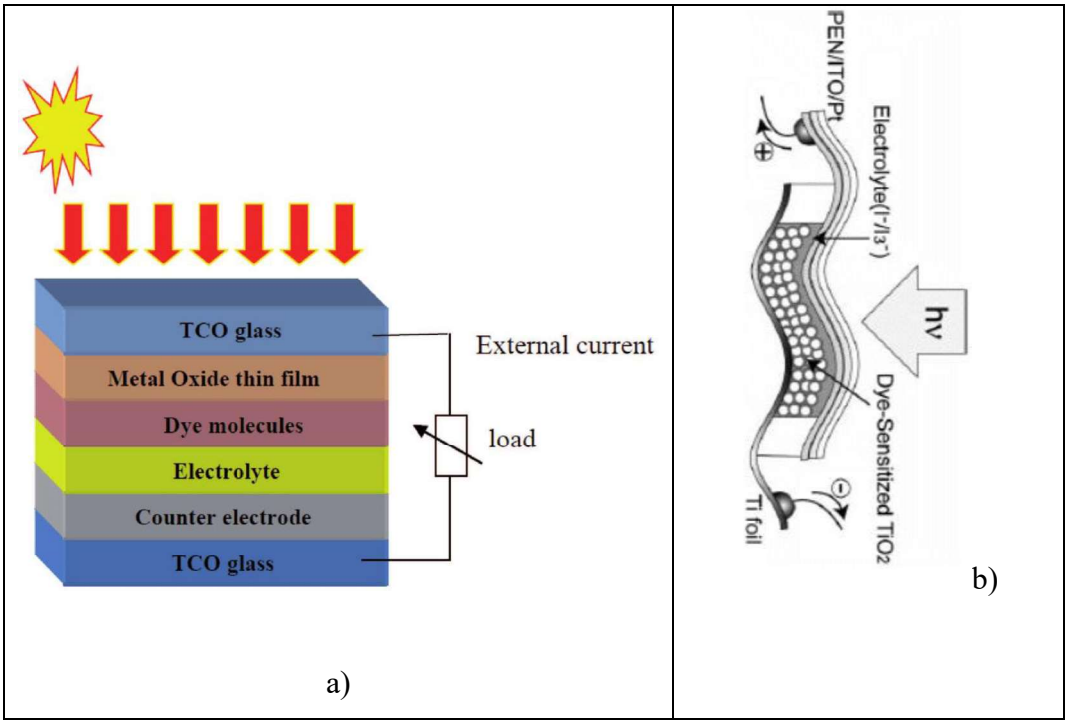

Figure 2.2 : a) Schematic device structure of a typical dye-sensitized solar cell (DSSC) (R. Agarwal, Vyas, Chundawat, Dharmendra, & Ameta, 2021). b) Configuration of a flexible dye-sensitized solar cell irradiated through Pt-counter electrode. (S. Ito et al., 2006)

In addition, semiconductor oxides must have a high mobility of loads in their volume to promote good efficiency in energy conversion to cells. They must also have a high recombination resistance of the electron to avoid efficiency losses. Also, to facilitate the injection of the dye electron to the semiconductor, the conduction band of the semiconductor must be located at a level of energy lower than that of the excited state of the dye. These materials should be easy to synthesize, stable and toxic to the environment and be carried out at low cost (Ajay Jena et al., 2012; Grätzel, 1999). The TiO_2 and the ZnO have a prohibited broadband (3 eV to 3.3 eV) which absorbs only wavelengths located in the ultraviolet region (UV) of the solar spectrum. For this reason, they are covered with a dye monolayer generally consisting of an inorganic ruthenium complex in order to increase its absorption in the UV-IR domain (Johansson, 2013; F. Wang, Liu, Pan, Xie, & Zou, 2007).

The Figure 2.2 b) is a configuration of a flexible TiO_2-based DSSC. The substrates are titanium foil at the anode and polyethylene naphthalate (PEN) cathode covered with an ITO layer. Apart

from the substrates which differ in flexibility, the active materials are identical for both rigid and flexible configurations of the DSSC. Glass coated with FTO or ITO are widely used substrates in rigid configurations.

Solar cells based on other conductive oxides (SnO_2, Nb_2O_5) have also been developed (Johansson, 2013; F. Wang et al., 2007). SnO_2 is also a broadband semiconductor, which can be used in this type of device. Indeed, it is a better electron acceptor than TiO_2 (BC lower by about 0.5 eV), an oxide more chemically stable and chemically photo (due to its widest band gap by ~ 3.7 eV), and its conductivity can be increased by doping. However, despite these advantages, the performance of SnO_2-based cells is to date much lower than that obtained with TiO_2, most of the work reporting effiencies in the range of 1.2 to 2.8% (Onwona-Agyeman et al., 2005), with however a team that recently described a performance (PCE) 6.02% (Xueyang Liu, Fang, Liu, & Lin, 2016);. Several reasons can be put forward to explain this behavior:

- A faster electron diffusion speed for tin oxide (125-250 $cm^2.V^{-1}.s^{-1}$ only for titanium oxide (0.1-1.06 $cm^2.V^{-1}.s^{-1}$) (Xueyang Liu et al., 2016);
- The effective mass of the electrons in SnO_2 is lower and allows the electrons trapped in intermediate states to recombine with the oxidized mediator;
- The "s" character of the SnO_2 conduction band makes injection less efficient from a type π * level of commonly used dyes, The conduction band is approximately 0.5 eV, lower than that of TiO_2, inducing much lower open circuit potentials. (Xueyang Liu et al., 2016).

A cell based on ZnO therefore demonstrates a reduced recombination of reactions than that based on TiO_2, because transport in TiO_2 nanoparticles is diffusive in nature and the electron must pass through a very large number of grain boundaries (Omar & Abdullah, 2014; Suzuki, Yamaguchi, Kumagai, & Yanagida, 2003). During photosensitization by a dye, zinc oxide puts Zn^{2+} type ions on the surface of the conduction band with vacant 4s orbitals (Borniol, 2006). The mechanism of transport of electrons in a DSSC is described on the basis of diffusion (de Jongh & Vanmaekelbergh, 1997; Omar & Abdullah, 2014) of the carriers of photo free loads generated. The gradient of an electric field is considered almost zero (Johansson, 2013). In these models, the electron diffusion takes place at the level of the conduction bands. (Johansson, 2013)

When a photon has sufficient energy, it allows the transition from sensitizer D to an excited state D *, which results in a transfer of an electron from the Higest Occupied Molecular Orbital (HOMO) the highest energy Orbital occupied by at least one electron, at the Lowest Unoccupied Molecular Orbiltal (LUMO) the lowest energy orbital not occupied by an electron. This is only possible when the incident photon has an energy greater than or equal to the energy difference between the HOMO and LUMO levels. This electron can then be injected into the conduction band (BC) of the semiconductor oxide. It is recognized that the LUMO must be above the bottom of the oxide BC to allow an efficient transfer of the dye electron to the oxide. The photoelectric conversion chain of these cells supplying an electrical circuit can be represented in Figure 2.3. The electron moves in the porous structure (H. C. Lin, Su, & Li, 2013; Omar & Abdullah, 2014; Savadogo, 1998; Villanueva-Cab, Oskam, & Anta, 2010) (from TiO_2, ZnO, SnO_2, Nb_2O_5, WO_3) before joining the TCO electrode (a transparent and conductive oxide on glass substrate) to finally be collected by the outside circuit. (Figure 2.3)

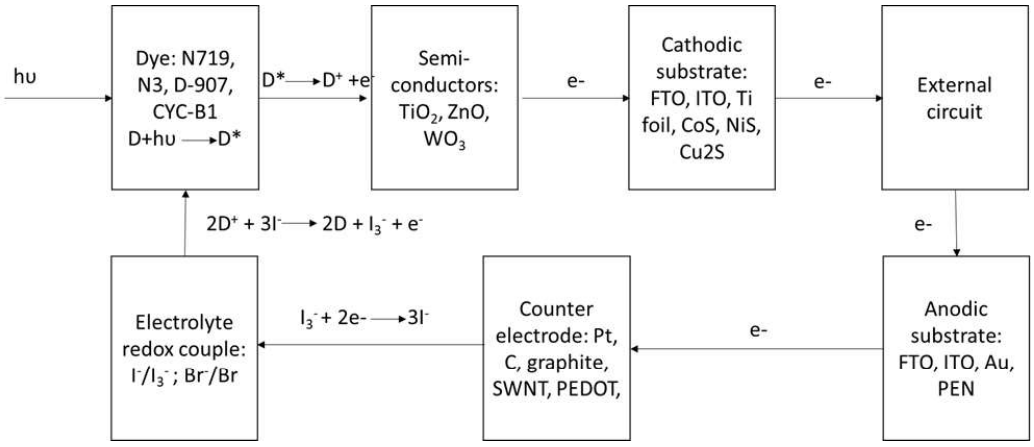

Figure 2.3 : The electron moves through the porous structure of semiconductor (TiO_2, ZnO, SnO_2, Nb_2O_5 or WO_3) before reaching the electrode substrate to finally be collected by the external circuit.

The transport of the electron in the semiconductor is governed by diffusion (Kay & Grätzel, 1996; Murakami & Grätzel, 2008)and trapping/deicing phenomena (Kay & Grätzel, 1996) at level of grain defects and seals. While the electron crosses to be routed to the outside circuit, the dye in an oxidized state D is reduced by the redox mediator and returns to state D. It is often accepted that

the redox potential of the mediator must be above the HOMO of the dye in order to allow a good injection of the hole in the dye in the electrolyte. . (Murakami & Grätzel, 2008) The electron returning by the counter-electrode (cathode) allows the reduction of the tri iodide anion in iodide anion. If we consider the overall balance, no chemical reaction takes place, this process of generating loads is therefore infinite. The entire redox cycle is summarized by the following equations:

$D \xrightarrow{h\gamma} D^*$ (1)

Excitement of dye (Photoexcitation)

$D^* \rightarrow D^+ + e^-$ (2)

Injection of the electron into the semiconductor (3) TiO_2, ZnO or WO_3 for example.

For this transfer to take place, first, the energy level of the excited state of the dye must be higher than the upper level of the conduction band of the semiconductor. The electron injection rate depends on parameters such as the separation length between the electron donor and the acceptor, the density of the acceptor, and the electronic coupling between the dye and the semiconductor (Haque et al., 2005). According to Haque et al. the time scale of the electron injection process is in the range of dozens of femtoseconds to hundreds of picoseconds (Haque et al., 2005).

$2D^+ + 3I^- \rightarrow 2D + I^-_3$ (4)

Dye reduction / oxidation of iodide ion (Regeneration of the oxidized dye) The regeneration of the oxidized dye is done in 5.10-7 seconds, which is faster than the colorant recombination of the electron (About 1 millisecond) (Haque et al., 2005). Therefore, rapid regeneration of the oxidized dye contributes to effective load separation.

$I^-_3 + 2e^- \rightarrow 3I^-$ (5)

Reduction of the triiodide ion to the cathode (Recombination of the electrolyte). The process of recombination of loads between the injected electrons and the oxidized dye is a harmful process for the cell. It must be slower than injecting electrons and transferring them from the ion to the oxidized dye to achieve effective load separation. The operating principle of the cell (DSSC) as governed by equations (1) (2) (4) and (5) can be illustrated in Figure 2.4.

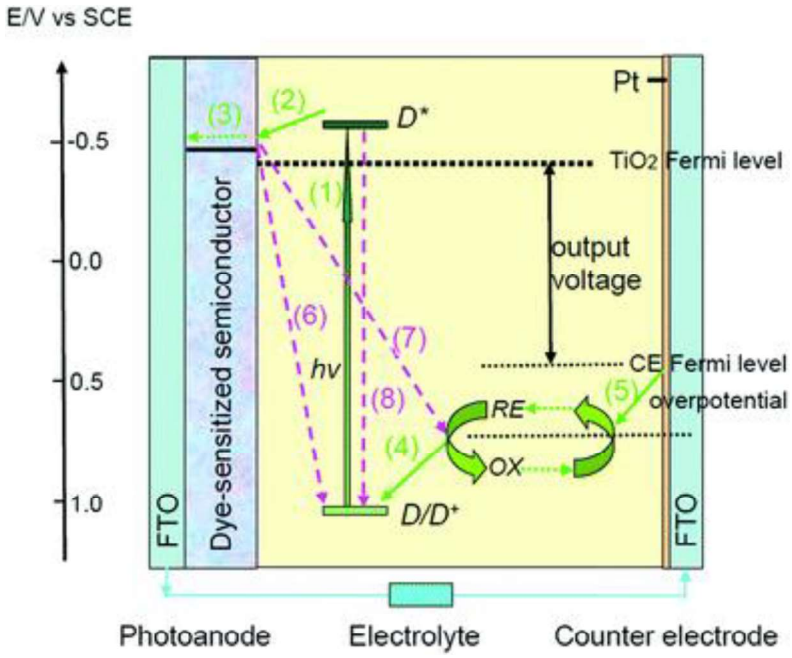

Figure 2.4 : Operating principle of dye sensitized solar cells (DSSCs) (J. Wu et al., 2017)

The numbered recombination phenomena (6), (7), (8) correspond respectively to the time of approximately 100 nanoseconds at 1 millisesecond, 1 millisecond and 20 nanosecondes (G. Boschloo & Hagfeldt, 2009; Haque et al., 2005). (6) is the recombination of electrons with the dye; (7) the recombination of the electrons with the redox electrolyte. However, it should be noted that reaction 7 is not possible between an electron and an electrolyte. (8) is a phenomenon of relaxation of the electron which returns to its fundamental level. These recombination phenomena represent the shunt resistance in a DSSC are to be minimized because they reduce the energy performance of the photovoltaic cell. However, given their slower reaction time (speed), their impacts are negligible compared to the process of injecting electrons into a functional solar cell.

Apart from the substrates which differ in their flexibility, the active materials are identical regardless of the DSSC in rigid or flexible configuration. Glass covered with a layer of FTO or ITO are substrates widely used in rigid configurations.

In the following paragraphs, a state of the art was made on the methodology for manufacturing the ZnO or ZnO semiconductors doped as anode material, electrolytes, dyes, cathode materials and some rigid and flexible substrates for DSSCs based on ZnO.

2.5.2 Fabrication of ZnO electrode

One of the most promising applications in ZnO anode is the use of zinc oxide as a semiconductor in photovoltaic solar cells because of its many properties already listed above. It is often used as an alternative in DSSCs because of its prohibited band similar to that of TiO_2, its greater mobility of electrons (200 $cm^2.V^{-1}.s^{-1}$ against 1 $cm^2.V^{-1}.\ s^{-1}$ respectively) its abundance, accessibility at a lower cost, its monocrystalline structure facilitating a direct electrical conduction path.

Marschall (Marschall, 2014) has drawn up (Figure 2.5) the photocatalytic semiconductors of type n and p with their prohibited bands and the energy levels of the conduction and valence bands compared to the normal hydrogen electrode (ENH). For example, semiconductors such as TiO_2, ZnO and WO_3 have valence band levels, which juxtaposed with that of SnO_2, are likely to facilitate the movement of the electrons from these semiconductors to SnO_2.

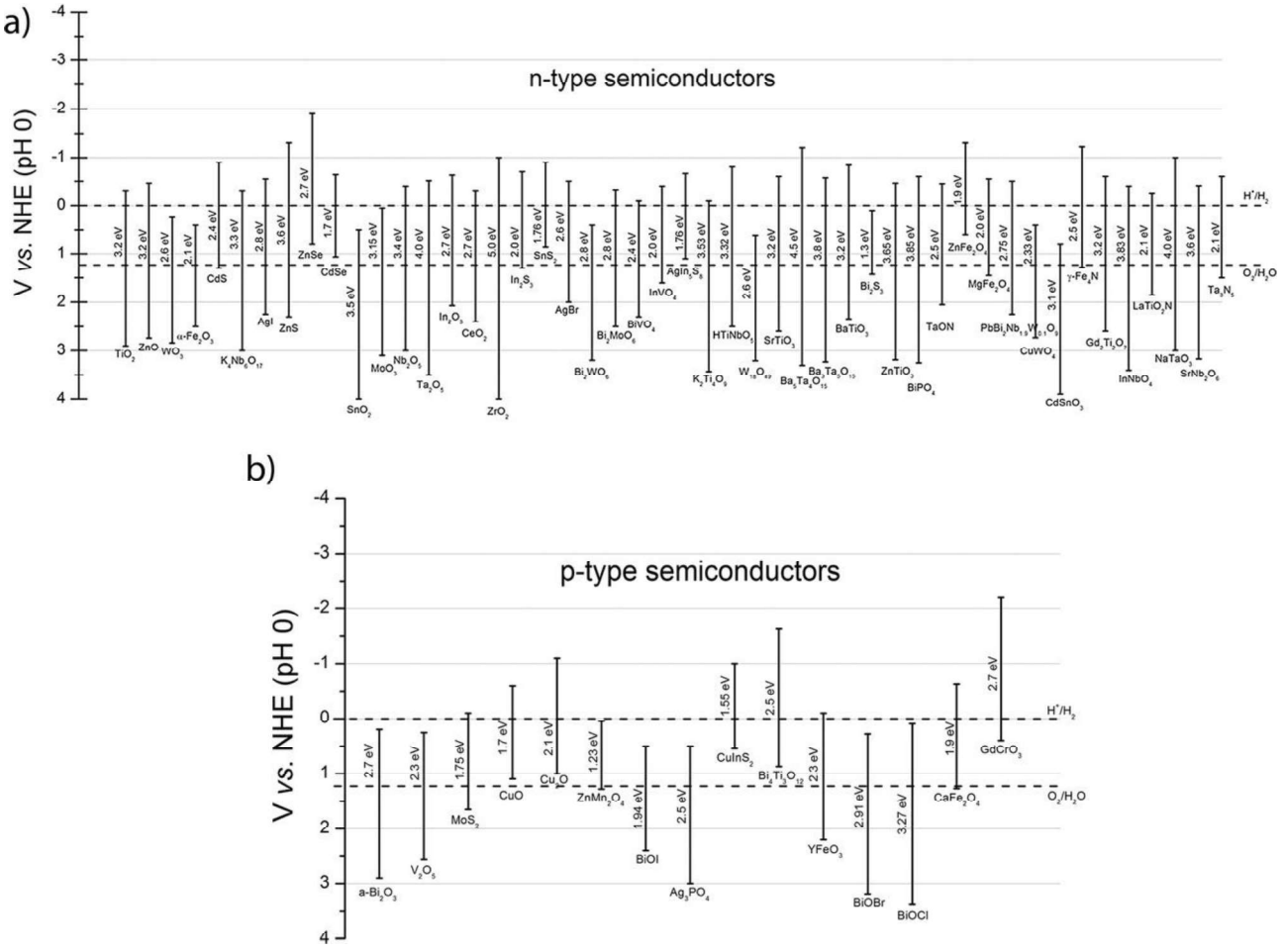

Figure 2.5 : Positions of valence levels, conduction levels, band gaps of n-type (a) and p-type (b) semiconductors used by composite photo-catalyst heterojunctions. (Marschall, 2014)

Several researchers synthesized the ZnO using various preparation methods leading to various morphologies such as nanoparticles, nanotubes, nanowires, nanorods. These different synthesized nanostructures aim to improve the collection and transport of electrons in the mesoporous structure of the semiconductor in the DSSC cell (Cheng, Chiu, Lee, Tsai, & Hsieh, 2008; Omar & Abdullah, 2014). ZnO nanowires and nanorods provide a one-way and fast conduction path inside the thin layer of semiconductor (Cheng et al., 2008; Omar & Abdullah, 2014). Table 2.8 lists the nanostructures used as photoanode and counter electrode in the development of DSSCs with their conversion efficiency. Some synthesis methods and techniques for depositing thin layers in electrodes for photovoltaic applications of DSSCs are reported.

2.5.2.1 Sol - gel method

The sol-gel or “sol-gel method” (SGM) or Solution - gelling method, is a process for developing materials allowing the synthesis of glasses, ceramics and organo-mineral hybrid compounds, from precursors in solution. It allows thin layers made of stack of nanoparticles of metal oxides to be produced. This process is carried out under so-called soft chemistry conditions, at temperatures significantly lower than those of conventional synthetic pathways. These conditions also offer the possibility of associating organic and mineral species to form new families of hybrid organo-mineral compounds, having new properties. This process can be used in different areas such as encapsulation and the development of hyper-porous materials, but it is in the making of thin film deposits that it finds its main application. The principle of the sol-gel process is based on the use of a succession of hydrolysis-condensation reactions, at moderate temperature, close to the ambient, to prepare networks of oxides, which can in turn be treated thermally. It is a process of conversion to metal alkoxide solution, such as silicon, zirconium, aluminum, titanium, zinc, etc. alcoholides. The soluble metallic species can also contain organic constituents which can be adjusted according to the applications. There are two sol-gel synthesis pathways which are: Inorganic or colloidal pathway: obtained from metal salts (chlorides, nitrates, oxychlorides) in aqueous solution. This path is inexpensive but difficult to control, which is why it is still very little used. However, this is the preferred route to obtain ceramic materials. Metalloorganic or polymeric use: obtained from metal alkoxides in organic solutions. This route is relatively expensive but allows fairly easy control of the particle size. In both cases, the reaction is initiated by hydrolysis

(addition of water for the alcohol route and change of pH to form hydroxides for the inorganic route) allowing the formation of M-OH groups then intervenes the condensation allowing the formation of M-O-M bonds. The second channel promotes polymerization which takes place in two stages: hydrolysis and condensation. The hydrolysis and condensation of metal alkoxides is equivalent to a nucleophilic substitution of the alcoholic ligands by hydroxylated species XOH.

$M(OR)z + x\ XOH \rightarrow [M(OR)z\text{-}x, (OX)x] + x\ ROH$ (5)

The hydrolysis reaction (case X = H and x = z = 1) can be written in this case as a result:

$M\text{-}OR + H_2O \rightarrow M\text{-}OH + R\text{-}OH$ (6)

Its purpose is to generate reactive M-OH functions, this is the conversion of alcohol functions into hydroxy functions. The solution thus obtained is called soil. The condensation reaction is that where X = M and x = z = 1. It consists of the conversion of the hydroxy functions (or more rarely an alcoholic) in M-O-M species. This corresponds to the formation of the mineral macromolecular network which can then be done via polycondensation reactions (oxo bridge formation by insulation reactions) with elimination of water or alcohol:

$M\text{-}OH + YO\text{-}M \rightarrow M\text{-}O\text{-}M + Y\text{-}OH$ with (Y = H or Y = R) (7)

It is an oxolation. The bond between atoms is ensured by an oxo bridge (-O-)

The soil - gel process has the following advantages: Possibility of making thin layers of mineral oxides at low temperature on heat-sensitive supports,Possibility of making organo-mineral hybrid materials (true nanocomposites in which mineral and organic species are mixed on a molecular scale) in the form of thin or monolithic layers with specific properties,Deposit of thin layers on both sides of the support in a single operation,Multi-component deposits in a single transaction. It also has limits: Cost of high alcohol precursors, Delicate control of the process and time of long processes. The most used reagents in a sol-gel synthesis are:

- a precursor zinc acetate dihydrate ($Zn(CH_3COO)_2\ 2H_2O$)) (Alias & Mohamad, 2014) ,
- a solvent (alcohol): ethanol, methanol or isopropanol) (Alias & Mohamad, 2014)
- a catalyst: NaOH or KOH) (Alias & Mohamad, 2014)

- a monoethanolamine stabilizer ($HOCH_2CH_2NH_2$) diethanolamine, tetramethylammonium hydroxide or ethyldiaminetetraacetate)) (Alias & Mohamad, 2014)

For the ZnO synthesis, the reactions (5), (6) and (7) can be expressed as:

- $Zn(CH_3COO)_2\ 2H_2O+H_2O \rightarrow$ HO-Zn-(CH_3COO) + $2H_2O$+ CH_3COOH (hydrolysis) (8)
- HO-Zn-(CH_3COO) + $H_2O \rightarrow Zn(OH)_2$ + CH_3COOH (alcohol condensation) (9)
- $Zn(OH)_2 \rightarrow ZnO+H_2O$ (gelation) (10)

The sol-gel method is often associated with a deposition technique such as spin coating, doctor blade, dip coating to make a thin layer deposit (Figure 2.6).

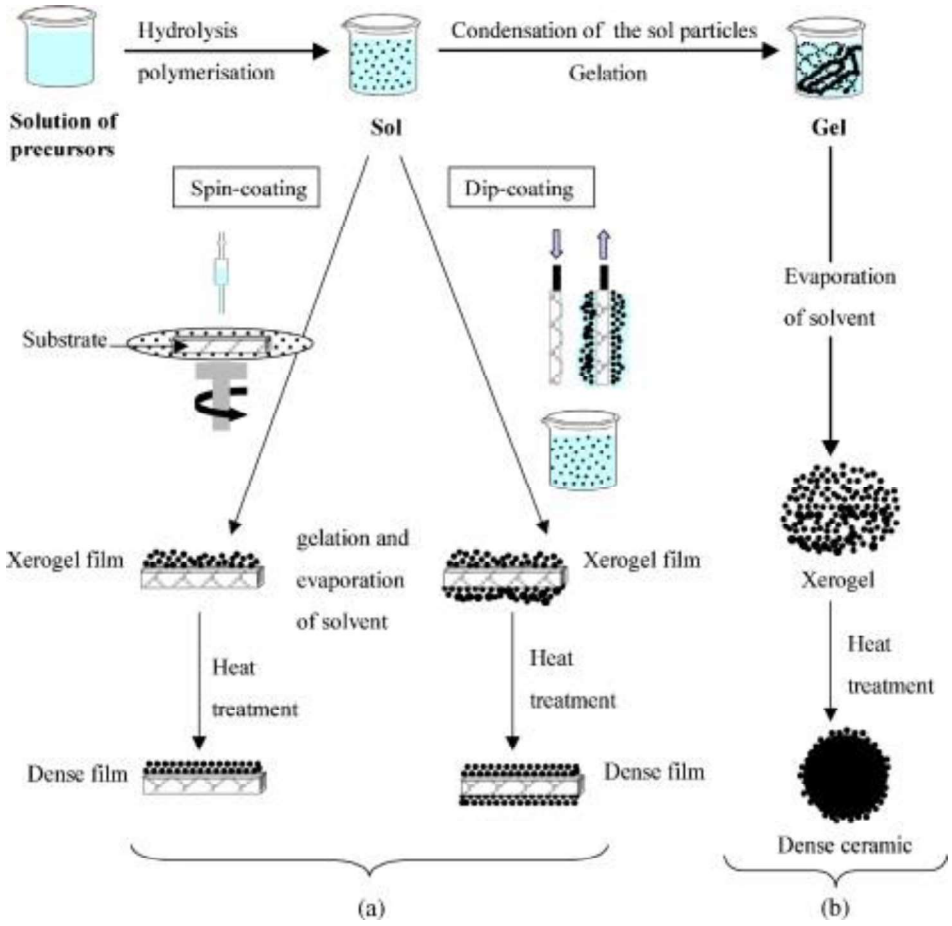

Figure 2.6 : Representation of sol-gel synthesis from a colloidal sol leading to a thin layer (a) or a gel transformed into a dense ceramic (b) . (Znaidi, 2010)

2.5.2.2 Spin coating or Spin-Coating Method (SCM)

It is a technique for deposition of thin layers using a rotating machine called spinner or spin coater. Checking the thickness of the film deposited depends on the parameters of the spinner (angular speed, acceleration, time) and nanomaterial (quantity, concentration, viscosity) (Yilbas, Al-Sharafi, & Ali, 2019).A homogeneous liquid solution, viscous (viscosity required) prepared from a precursor, a solvent and stabilizer is deposited at a fixed speed for a given time. We developed a solution using 4.4 g of the zinc acetate precursor, 100 ml of ethanol solution as solvent, 1.2216 g monoethanolamine (MEA) as a stabilizer. We deposited at a speed of 3000 rpm for 20 s, then dry at 150 ° C for 10 minutes. The repetition of a deposit increases the thickness layer of the film to a desired value. The sample was subjected to heat treatment at 450 ° C. The SEM results (Figure 2.7) of this synthesis show nano grains of ZnO similar to Foo(Foo, Hashim, Muhammad, & Voon, 2014) results.

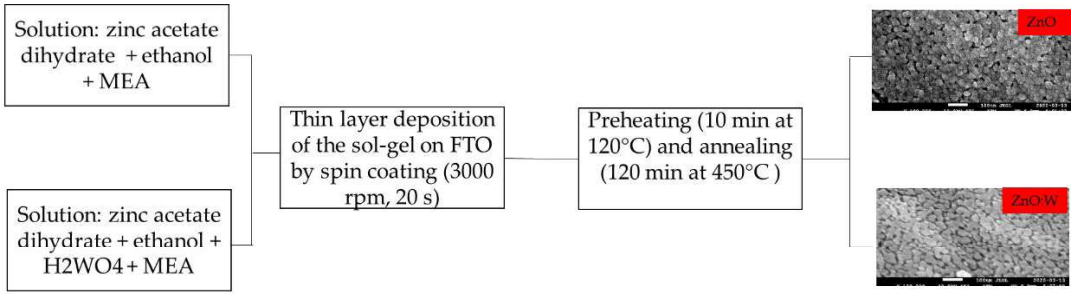

Figure 2.7 : Schematic diagram for the synthesis of pure and W doped ZnO thin films using spin coating method.

The results of the SEM analysis (Figure 2.7) reveal the following: spherical nanoparticles grains for the thin layers of ZnO. When, zinc oxide is doped with tungsten W, the grains are deformed into fractal shape. These fractal shapes have a higher ratio surface/volume than the spherical nanograins. These results corroborate those obtained by G. Vijayaprasath et al (Vijayaprasath, Murugan, Ravi, Mahalingam, & Hayakawa, 2014) who have developed by the sol-gel centrifugation method thin layers of ZnO pure and doped with transition metals (Neither, Mn, Co). Dopant concentrations are 0.03% in moles.

2.5.2.3 Doctor Blade or Doctor - Blade Technic (DBT)

Technique is a thin layer coating technique controlled using a blade. The Doctor Blade deposit technique consists of 3 parts: an adequate substrate for the deposition (step 1), a semiconductor paste (ZnO, TiO_2 mixed in a liquid) deposited by moving blade at a fixed height defining the thickness of the thin film (step 2) and the evaporation of the liquid ata fixed temperature (step 3). Liquid is alcohol that can be combined with two types of polymeric additives to increase viscosity. These are for example ethyl cellulose (EC) and polyethylene glycol (PEG) which act as a binder. These additives, due to their viscosity properties, promote porosity and act on the size of the pores (S. Ito et al., 2006; Seigo Ito et al., 2007; Tsoukleris et al., 2005). The dough is then spread using the squeegee on the FTO. The thickness of the semiconductor layer (ZnO, TiO_2) is obtained as a function of the position of the height of the squeegee above the substrate.

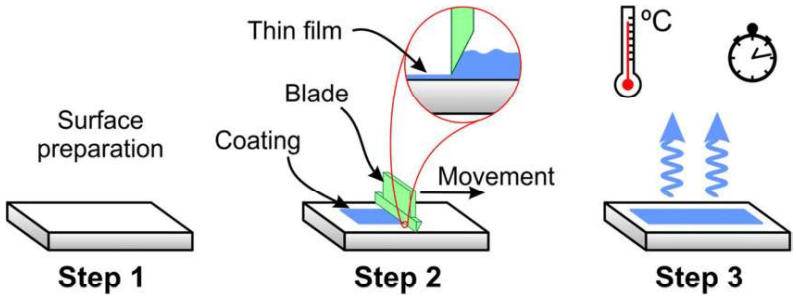

Figure 2.8: The mechanism of the doctor blade method (Frederichi, Scaliante, & Bergamasco, 2021)

S. Ito et al. (S. Ito et al., 2006) have speculated that to establish a good chemical bond between the particles of the semiconductor (TiO_2) and SnO_2 particles: F of the substrate, hydroxides (-OH) must be on the surface and create a strong chemical bond between the different particles (Tsoukleris et al., 2005) ; which could be illustrated by the reaction:

$$M_1\text{-OH} + \text{HO-}M_2 \rightarrow M_1\text{-O-}M_2 \qquad (8)$$

With M1 which represents a metal atom on the surface; M_2 another metal atom or a tin atom on the substrate. The water added at the start makes it easier for the hydroxide to cover the surface. (Seigo Ito et al., 2007). The acetic acid added and adsorbed to the surface makes it possible to avoid an aggregate of particles in the layer to be deposited (Seigo Ito et al., 2007). Indeed, acetic acid can change the zeta potential from negative to positive, which results in the repulsion of particles from

each other. The mechanisms favoring the connection between the ZnO nanoparticles and the substrate are the surface charge effect and the binding effect(Seigo Ito et al., 2007). Comparing the viscosity values of some alcohols at 20°C to that of water, butanol ($2.9*10^{-3}$ Pa.s according to BASF Petronas data) is more viscous than water (10^{-3} Pa.s), ethanol ($1.21*0^{-3}$ Pa.s) and methanol ($0.59*10^{-3}$ Pa.s). Butanol is a good choice because it has a good viscosity.

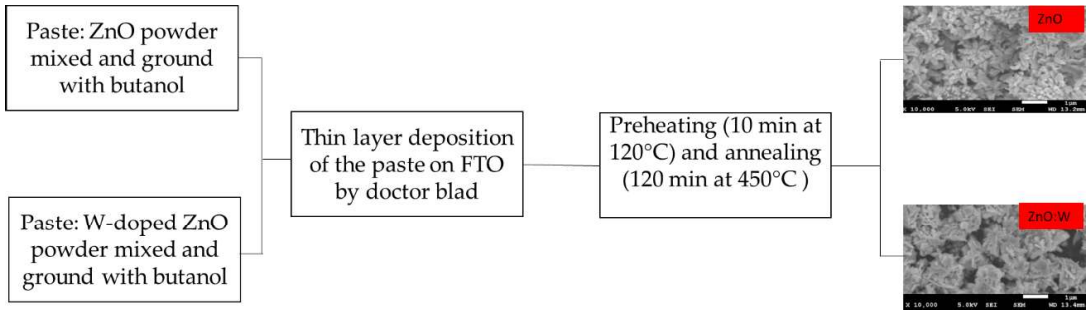

Figure 2.9 : Schematic diagram for the synthesis of pure ZnO (nanorod)and W doped ZnO (ZnO-W: clustered nanorods) thin films using doctor blade method

ZnO nanotige morphology is almost in agreement with that obtained by Bahadur et al. 2007, Morkoc and Ozgurb 2009, Moezzi et al. 2012. Note that the temperature of this synthesis (50°C) is smaller than that used by these authors. The SEM observation of ZnO modified with tungstic acid gives clustered nanorods (Figure 2.9).

Biswas et Chaterjee (Biswas & Chatterjee, 2020) studied the effect of surface modification via sol-gel spin coating of ZnO nanoparticles on the performance of WO_3 photoanode based dye sensitized solar cells (Table2.3). The authors first deposited by doctor blade a layer of WO_3 by mixing WO_3 powder with terpineol and ethyl cellulose. Then ZnO was deposited by sol-gel spin coating on WO_3 from the zinc acetate dihydrate precursor (98% Merk). A DSSC was fabricated using the WO_3 material as anode, the dye N3, the redox couple I^-/I_3^- and a platinum counter electrode. The DSSC was reported to have low performance: an efficiency of 0.44% and a form factor of 0.39. The authors justify this low performance by a high recombination rate of photoexcited electrons and a low dye adsorption due to a high acidity of the WO_3 surface. To improve the performance of this solar cell, the authors incorporated a thin layer of ZnO on the WO_3 surface creating an energy barrier and limiting the recombination of photoexcited electrons. The obtained performances are an efficiency of 1.21% and a form factor of 0.62.

In 2020, Das et al. (Das, Wary, & Nair, 2020) synthesized ZnO and doped ZnO (nanoflakes particles) as the anode of the DSSCs they fabricated. The results of their publications show that ZnO-based DSSCs doped with 1% copper have a higher electrical conversion efficiency of 0.89% compared to the ZnO-based DSSC which has an efficiency of 0.25%. Their UV-visible spectroscopy analysis shows that the 1% copper-doped ZnO thin film exhibits better absorption between 350 -650 nm compared to the pure ZnO layer. Copper (at 1 wt% ZnO) altered the spectral response of visible light on ZnO and the accessibility of the defect states by delaying the recombination process to achieve better photocatalytic performance.

These results corroborate the work of Zhuang et al . (Zhuang et al., 2019) performed in 2018 on copper-modified ZnO anode-based DSSCs. For the latter authors the modification of ZnO with copper (at 1.5 wt%) significantly improved the electron transport and delayed the charge recombination on the ZnO-dye interfaces; this would justify an 84% improvement in the short circuit current density and a 1.6th-factor increase in the solar radiation to electricity conversion efficiency. According to the authors, the maximum PCE of 7.27% was achieved on Cu1.5-ZnO photoelectrode films that consisted of cross-linked multileveled porous nanoflowers, which offered a more porous structure for dye loading and electrolyte diffusion. The presence of copper in the ZnO matrix decreased the crystallite size of the modified samples compared to the undoped nanoparticles according to their X-ray diffraction results. However, if the presence of copper is excessive in the ZnO matrix, it would reduce the active sites and slow down the diffusion process of charge carriers.

Table 2.3: Performance of DSSC based on WO_3 and modified ZnO

Subs-trate	Catalyst on CE	Electrolyte solvent	Anode	Dye	Jsc ($mA.cm^{-2}$)	Voc (mV)	FF (%)	η (%)	Tech-nic	Reference
ITO	Pt	(I^-/I_3^-)	WO_3	N3	2.65	0.42	39	0.44	DBT/SCM	(Biswas & Chatterjee, 2020)
ITO	Pt	(I^-/I_3^-)	WO_3-ZnO	N3	3.58	0.55	62	1.21	DBT/SGM	(Biswas & Chatterjee, 2020)
FTO	Pt	(I^-/I_3^-)	ZnO: Cu	N719	0.81	0.47	63	0.89	DBT	(Das et al., 2020)
FTO	Pt	(I^-/I_3^-)	ZnO: Cu	N719	17.61	0.68	59.8	7.27	HTM/ DBT	(Zhuang et al., 2019)
FTO	Pt	(I^-/I_3^-)	ZnO: Cu	N3	1.8	1.08	68.6		DBT	(Aneesiya & Louis, 2020)

2.5.2.4 Dip - coating

Withdrawal soaking or "dip coating method" (DCM) , is a technique for coating the substrate by immersion in the solution of the coating material. The substrate is then removed at constant speed from the solution to have a thin layer deposit. The withdrawal speed determines the required coating thickness. The objective in a "dip-coating" or soaking-withdrawal deposit is to make a relatively uniform thin layer deposit without discontinuity of the particles. The average thickness obtained is controlled by the concentration of the solution (ZnO/ZnO doped), its viscosity and the speed of withdrawal of the substrate of the solution. The soaking-withdrawal technique can be summarized in two basic steps:

1) soaking of the substrate for a period in the solution containing the precursor. This soaking step avoids the formation of wake during the draw generated by the moving liquid;

2) removal of the substrate at slow and constant speed by adjusting the potentiometer of a stepping motor.

Boumazai et al (Boumaiza, Boudine, & Sebais, 2021) synthesized pure ZnO and lead (Pb: 5% et 10%) doped ZnO by sol-gel method combined with dip coating technique at a speed of 10 mm/h. The deposited sol-gel was dried at 350°C and annealed at 500°C. The XRD analysis do not reveal Pb peaks but show a decrease in peak intensity and crystallite size in the presence of Pb dopant. The optical results show an increase of the band gap with the increase of the dopant quantity from 3.19 eV to 3.30 eV.

Guo and Aegerter (P. Guo & Aegerter, 1999) , adopted the speed of 0.5 cm / min in the synthesis of nobium oxide (Nb_2O_5) nanocrystalline from the precursor $NbCl_5$ dissolved in ethanol at a concentration of 0.32 mol Nb/L . (P. Guo & Aegerter, 1999) The deposit was made on an ITO glass substrate and the sample (Nb_2O_5) synthesized, heat treated and immersed in a Ru II dye solution (0.3 mmol/l) constitutes an elaborate DSSC photoanode. The results obtained with a closed cell under radiation of 100 W/cm^2 are: Isc = 1.7 mA/cm^2; Vco = 0.57 V; FF = 0.55; η = 5% (P. Guo & Aegerter, 1999). During the ascent, the gelling begins in seconds because the solvent is alcohol and a deposit of a uniform thin layer. The withdrawal soaking process can be repeated to obtain the desired layer. The prepared ZnO or TiO_2 paste must be viscous enough to adhere to the substrate when the latter is removed. The solvents used to make ZnO paste are alcohol associated with ethyl cellulose (EC) and polyethylene glycol (PEG) to increase viscosity.

2.5.2.5 Chemical Vapor Deposition (CVD)

Chemical vapor deposition is a technique for vacuum deposition of thin layers from gaseous precursors which undergo thermal decomposition and/or a chemical reaction in its gaseous phase. A substrate is exposed to decomposed molecules (from precursors) which react to its surface to deposit in a thin layer of sought-after materials in solid phase. The reaction by-products are evacuated by a gas flow which continuously crosses the reaction chamber.

In 2005, J.B. Baxter and E.S. Aydil (Baxter & Aydil, 2005) synthesized ZnO nanowire for DSSC using the MOCVD technique. The precursors are: the powder of hydrated zinc acetylacetonate [$Zn(C_5H_7O_2)_2$ x H_2O or $Zn(AcAc)_2$] and oxygen and substrate is FTO. Zn's powder $Zn(AcAc)_2$ was heated to 75 ° C and its vapor was brought into the MOCVD chamber by an Ar carrier gas and oxygen was introduced by another entry into the same chamber (Baxter & Aydil, 2005). The gases have a flow rate of 20 sccm and the total pressure maintained in the enclosure is 2.5 Torr (Baxter

& Aydil, 2005). Nanofils with a diameter ~ 100 nm develop spontaneously on a thin layer of ZnO polycrystalline (~ 20 nm) which is deposited on the substrate. This results in an increase in smooth nanofils which reach several microns (Baxter & Aydil, 2005). The prepared FTO-ZnO electrode was immersed in an ethanol solution of 0.2 mM N719 (Solaronix) for 30 minutes. The counter-electrode was obtained by depositing 200 Å of platinum deposited by e-beam evaporation on FTO. The separator is made of polypropylene 20 µm thick. The cathode electrolyte is composed of 0.5 M of 0.05 I_2 and 0.5 M 4-terbutylpyridine iodide in acetonitrile. The electrodes are pressed together using clips. (Baxter & Aydil, 2005) Using a halogen tungsten lamp, the DSSC cell was subjected to irradiation of 100 W/cm^2 and the following performances are obtained: Open circuit voltage: Vco = 0.74V; Short-circuit current density: Isc = 1.62 mA/cm^2; Form factor: FF = 55%; Electrical efficiency: η = 0.5% [98]. Using the Xe 1000W lamp and a monochromator, the authors plotted the IPCE efficiency curve which reached a maximum value of more than 6% at 525 nm close to the maximum absorbance of the dye. Likewise, the light collection efficiency (LHE) or the absorption curve (measured using the spectrometer) of the adsorbed dye follows the same form as that of IPCE and reaches a maximum value of 9%. This low efficiency in collecting incident sunlight justifies the low performance of the DSSC stack, unlike those with compacted nanoparticles of 10 to 15 µm which generally absorb more than 80% of incident solar rays (Baxter & Aydil, 2005). By dividing the IPCE by absorption, we see that the injection and load collection product is around 70% (Baxter & Aydil, 2005). This value corresponds to a high internal quantum efficiency and therefore confirms the lowest current density of solar cells based on nanofils. The slope on the current-voltage curve which corresponds to the shunt resistance (Rsh) is weak, therefore the phenomenon of recombination of photoexcited electrons is high in nanofils and triiodide ions of the electrolyte. This also justifies the low filling factor value. The 0.5% DSSC yield is low compared to previous methods.

In 2008, H. Chen et al (H. Chen, Du Pasquier, Saraf, Zhong, & Lu, 2008) also developed DSSCs based on ZnO nanotips and ZnO doped with gallium (GZO) by making a chemical vapor deposition. The precursors are diethylzinc (ZnEt2) and oxygen for the synthesis of ZnO and triethylgallium (TEGa) has been used as a source of gallium doping (H. Chen et al., 2008). In the presence of metallo-organic precursors, the CVD process is called Metalorganic Chemical Vapor deposition (MOCVD). The ZnO-based electrode was immersed in an ethanol solution of the 0.3

mM N719 sensitizer. The cathode is a platinum sheet fixed to a glass slide. The separator (Celgard) is made of 25 μm microporous polyenin soaked in electrolyte composed of 0.5 M LiI, 0.005 mM I2 and 0.2 M tert-butyl pyridine in a methoxypropionitrile electrolyte (H. Chen et al., 2008). The yield of the DSSC developed is 0.77% under standard measurement conditions (STC) and is close to the results obtained by Baxter and Aydil above cited.

In 2009, Ahmad Umar (Umar, 2009) made the deposit of ZnO nano-piges (ZnO nanocombs) on an FTO substrate for the manufacture of DSSCs. By placing 1.5 g of metallic zinc powder (99.999% purity) in an oven, it increased the temperature of the oven until zinc evaporated. The FTO substrate located near the zinc powder is raised to a temperature of 570 ° C. Ahmad Umar continuously sends oxygen and nitrogen to the enclosure where the substrate and zinc are located. Finally, the metallic zinc oxidizes by forming zinc oxide deposited in a thin layer on the FTO. The process lasts 1 hour. (Umar, 2009). Visimberga et al (Visimberga, Faulkner, Boese, & O'Dwyer, 2012) have schematized and adopted CVD method for the synthesis of ZnO nanorods layers (Figure 2.10 (a)) and SEM images were presented in (b) , (c) and (d).

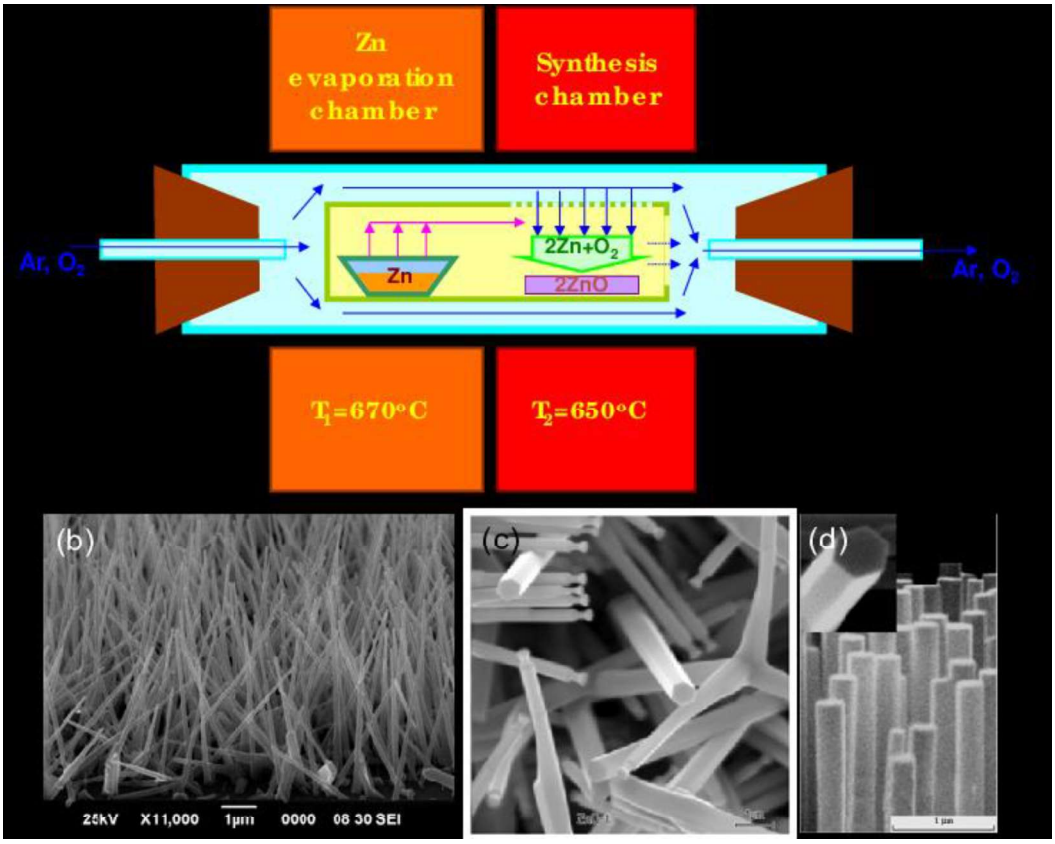

Figure 2.10: (a) Schematic of the CVD system for growing ZnO nanorods layers. (b) SEM image of a layer of ZnO nanorods grown directly on silicon. (c) SEM image of nanorods with disk-shaped heads and (d) hexagonal single-crystal nanorods with flat (0001) endfacets from which optical measurements were taken. (Visimberga et al., 2012)

The electrode produced was immersed in a 0.3 mM solution of N719 (Solaronix) for adsorption of N719 by ZnO. The counter-electrode is a thin layer of platinum (~ 60 nm) deposited by electron beam on ITO [100] An electrolyte was manufactured using 0.5 M LiI, 0.005 mM I2 and 0.2 M tert-butyl pyridine in acetonitrile). This electrolyte was introduced into the cell by one of the two small holes drilled in the counter electrode and the holes were closed using a seal glass (\"sealing sheet and microscope objective glass\") (Umar, 2009). The DSSC under a light intensity of 100 mW / cm2 (AM = 1.5) has the following electrical performance: a light conversion efficiency into electricity of 0.68%, a filling factor of 34%, a short circuit current density of 3.14 mA / cm2 and an open circuit voltage of 0.671 V (Umar, 2009) The author justifies this poor electrical performance by a high recombination rate of the carriers of photoexcited loads with the electrolyte

at the interface (Baxter & Aydil, 2005). The close contact between ZnO and the electrolyte is also reported as a source favoring the recombinations of carriers of photoexcited loads (Baxter & Aydil, 2005). The performance of this DSSC is also close to that of Baxter et al. and H. Chen et al. who also borrowed the CVD. Table 2.4 summarizes the above mentioned DSSCs whose anode was fabricated by CVD.

Table 2.4: Summary table of DSSC by CVD at the anode

Substrate	Anode	dye	Separator	Electro lyte	Cathode	FF (%)	η (%)	Preparation	Ref.
FTO-glass	ZnO nanowire. Precursors : $Zn(AcAc)_2$, O_2	N719	20 µm poly-propylene	(I^-/I_3^-)	Pt	38	0,5	MOCVD/Electron beam	(Baxter & Aydil, 2005)
Glass	ZnO nanotips Precursors: ZnEt2, O_2, TEGa	N719	Celgard	(I^-/I_3^-)	Pt	-	0,77	MOCVD	(H. Chen et al., 2008)
FTO-glass/ITO	ZnO nanocombs Precursors: Zn and O_2	N719	*sealing sheet*	(I^-/I_3^-)	Pt	34	0,68	CVD/Electron beam	(Umar, 2009)

2.5.2.6 Plasma-Enhanced Chemical Vapor Deposition (PECVD) or Chemical Deposit Phase Steam assisted by Plasma (PECVD)

Is a variant of the CVD process. During this process, the molecules of a precursor are fragmented into target materials and deposited in thin layers on the substrate. The main operating characteristics of a PECVD device are: 13.56 MHz RF radio frequency plasma or 2.45 GHz 2.45 microwave. (Ramos et al., 2014; Stuckelberger, Biron, Wyrsch, Haug, & Ballif, 2017; Vega-Poot et al., 2014)The amount of energy supplied per unit mass to the precursor. This energy is responsible for the fragmentation of the precursor molecules. Substrate temperature: 150 ° C to 250 ° C; Work pressure; Possibility of deposit in large areas (> 10 m^2).

The precursor used by A.G. Vega-Poot et al. is zinc diethyl (ZnEt2) (Vega-Poot et al., 2014). The temperature of the FTO substrate is set at 150 ° C during the deposition process. The source of

Plasma is a microwave at 2.45 GHz. The gases used for plasma are a mixture of O_2 (90%) and H_2 (10%). The plasma source is fixed at a power of 600 W and the pressure varying from $5x10^{-3}$ torr to 10^{-2} torr. (Vega-Poot et al., 2014) The glass-FTO-ZnO sample was subjected to heat treatment and then immersed in a 0.5 mM solution of the dye N719 (Solaronix) for 1 hour (Vega-Poot et al., 2014). After that, the sample was removed, washed with ethanol and dried under a stream of nitrogen according to A.G. Vega-Poot et al. This gives the photoanode used for the manufacture of DSSCs. The counter electrode was manufactured by Doctor Blade platinum deposit (Platisol solution, Solaronix) on FTO (TEC 8, Pilkington Glass) and annealed at 400 ° C for 10 minutes. Against electrode and photoanode were sealed using a Surlyn polymer (60 µm, Solaronix). An electrolytic solution was prepared by the addition of 0.6 M 1,2-dimethyl-3-propylimidazole iodine (DMPII), 0.1 M LiI, 0.5 M 4-tert-butyl-pyridine (TBP), 0.05 M I2 and 0.1 M guanidium thiocyanate mixture dGuSetonitrile. This solution was inserted into holes in the Surlyn polymer ensuring a bridge between photoanode and counter electrode (Vega-Poot et al., 2014). The electrical performance measurements give yields of 0.4% to 2.4%, open circuit voltages of 0.62 V to 0.71 V, and short circuit currents of 1.4 mA/cm^2 to 6.5 mA/cm^2. These performance ranges are proportional to the thickness (1.5 µm to 10 µm) and to the surface of the electrodes involved for DSSCs. (Vega-Poot et al., 2014)

2.5.2.7 Physical Vapour Deposition (PVD)

Physical vapor deposition consists in transforming a source material (solid, liquid or concentrated gas) of vapor coating; the latter is driven and then condensed for deposit on a substrate. The principle is illustrated in Figure 2.11.

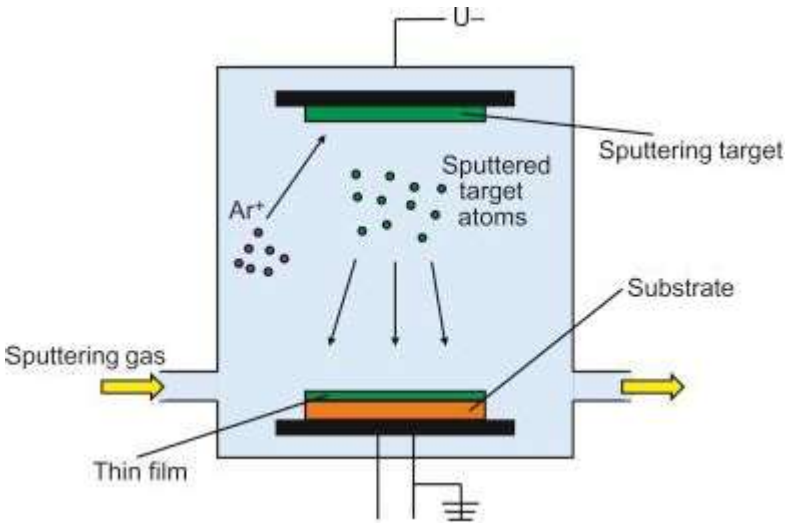

Figure 2.11: Principle of the PVD process (Faraji, Kim, & Kash, 2018)

It is the seat of basic physical phenomena, namely: thermal evaporation, sublimation or dispersion of molecules of the source material. The steam generation technique can determine PVD technology. A distinction is made between vacuum evaporation (vacuum heating and evaporation ~ 10^{-3} Pa) electron beam evaporation (Electron Beam PVD or EBPVD) cathodic spraying (sputtering) pulsed laser removal (PLD where the atoms are torn from the target under vacuum and under the effect of intense pulsed laser radiation for a deposit) ion beam spraying, ion implantation (Ion Plating or Ion Assisted Deposition- IAD) electric arc process. Ion implantation consists of bombarding the substrate of ions (of the target material) continuously or periodically. This technique is often accompanied by terms which indicate the source of the material of deposit or the technique of bombardment: Sputtering Ion Plating, Arc Ion Plating. The magnetron process is an evolution of conventional cathode spray which uses a magnetic field around the target at the cathode thus increasing the ionization rate of the target gases at a lower pressure. This also increases the speed and deposition efficiency of spraying compared to traditional sputtering. The medium that can be passive (such as vacuum or an inert atmosphere) or active like a plasma or reactive gases. An active medium is the seat of chemical reactions between atoms or molecules of source materials and reactive gases. For a deposit of metal oxides, reactive gases are introduced which can be combined with the vapors of metals. For a ZnO deposit, for example, oxygen is introduced as a reaction medium with the zinc metal gas. The substrate is the necessary support to make the deposit of the desired thin layer. It is carefully chemically cleaned and/or stripped (ionic pickling) to

remove surface contamination before starting the deposit. Chemical cleaning is in an acetone bath followed by an ethanol bath to remove fat, dust or any contamination. Ion stripping consists of bombarding the substrate with neutral gas ions like argon to make the substrate clean.

In 2005, L. Wang and X. Zhang (L. Wang et al., 2005) synthesized and deposited ZnO nanofils by evaporating Zn powders at 750 ° C for 90 minutes in a tube enclosure . The source materials used are 1 g of zinc powder (~ 74 µm) in diameter and a purity of 99.99%) vaporized to 750 ° C and oxygen which react to give the ZnO. The substrate is a thin layer of ZnO. XRD analyzes have proven the hexagonal crystal structure of ZnO nanofils synthesized with a preferential orientation in the direction of the c axis. (L. Wang et al., 2005)

In 2007, F. Wan et al synthesized ZnO tapes (layers) by oxidation of ZnS in the air (F. Wang et al., 2007) according to the following reaction:

$$ZnS + 3/2O_2 \rightarrow ZnO + SO_2 \qquad (9)$$

This reaction takes place at 700 ° C (F. Wang et al., 2007). The physical vapor deposition enclosure is a horizontal tubular electric furnace in quartz (35 mm in diameter, 120 cm in length). ZnO ribbons have been synthesized from powders of ZnS and CdS (in molecular ratio less than or equal to 0.05%) who have undergone physical evaporation to settle on substrates in a silicon wafer covered with a thin layer of gold (~ 10 nm). These are ZnS ribbons. The oven temperature is raised to 1100 ° C for 1 hour before heating stop. By natural cooling, the authors obtain a deposit of the white ribbons of porous ZnO of width 2-7 µm and of average length of 100 µm on the silicon wafers. (F. Wang et al., 2007)

By evoking a high surface /volume ratio of the porous ZnO samples, the authors immersed the ZnO ribbons in an ethanolic solution of the dye N3(RuL2 (NCS)2) for 10h. After removal and drying of these samples, they were subjected to the responses. (F. Wang et al., 2007)

The phototension spectrum has a wide band between 300-425 nm and two other additional bands around 400 nm and 515 nm. By comparing the phototension spectra of ZnO and ZnO/N3, the authors conclude that the ribbons sensitized by the dye extend their photo-response over almost the entire visible domain. This foresees that ZnO/N3 is a good candidate for the DSSC. (F. Wang et al., 2007)

ZnO fibers doped with Sb (L. E. I. Guo & Kerr, 2011) were produced by PVD from zinc powders and Sb_2O_3. The ZnO: Sb was deposited on the FTO and the assembly immersed in a solution of dye N3 for the photoanode. The cathode is made of platinum and the electrolyte is a solution of the redox I^-/I^-_3 pair. The electrodes assembled in DSSC provide an electrical efficiency of 2.64% (Table 2.5). (L. E. I. Guo & Kerr, 2011)

From the target zinc acetate dihydrate dissolved in ethanol in the presence of diethanolamine G. J. Fodjouong et al. . (Fodjouong, Feng, Sangare, & Huang, 2013) deposited a thin layer of ZnO on an FTO substrate by thermal evaporation (245 ° C or 350 ° C for 6 hours). Then, the synthesized sample was immersed in 0.05 mM of N719. The cathode is made of platinum and the electrolyte is a solution of the redox I^- / I^-_3 pair. The electrodes assembled in DSSC provide an electrical efficiency of 1.56% . (Fodjouong et al., 2013) (Table 2.5).

Table 2.5: materials and performance of two DSSC by PVD at the anode

Anode	**Substrate**	**Technic**	**Dye**	**Separator**	**Electrode**	**Cathode**	**η(%)**	**Reference**
ZnO: Sb fiber (targets: Zn powders and Sb_2O_3)	FTO	Thermal evaporation	N3	-	I^-/I_3^-	Pt	2.64	(L. E. I. Guo & Kerr, 2011)
ZnO. Target: zinc acetate dihydrate dissolved in ethanol in the presence of diethanolamine	FTO	Thermal evaporation (245°C or 350°C for 6 hours	N719 0.05 mM	Surlyn 1702 60 μm	I^-/I_3^-	Pt (60 nm)	1.56	. (Fodjouong et al., 2013)

In DSSCs made using ZnO nanotiges aligned vertically as photoelectrode, incident photons can propagate along and between nanofils without being absorbed by dye molecules and therefore hinder the collection of light (Ko et al., 2011).

2.5.2.8 Hydrothermal Method (HTM)

It is a technique for synthesizing nanocrystals from an aqueous solution. The operating conditions are higher (temperatures, high vapor pressures) than those of sol-gel. K.L. Foo et al. (Foo et al., 2014) synthesized ZnO nanorods (NRs) deposited on ZnO seed layer. The synthesis was carried out from the zinc nitrate precursor hexahydrate (208.2 mg) and hexamethyleneetramine HMT (98.12 g) in deionized water. The ratio of the two reagents is 1: 1 in a total volume of 40 ml. The ZnO seed layer substrate was immersed in the solution at 93 ° C for 6 hours. The synthesized sample is annealed at 500 ° C for 2 hours which gives ZnO NRs. Through these syntheses, these authors highlighted the influence of different solvents (methanol, ethanol, isopropanol and 2-metoxyethanol) in the synthesis of ZnO NRs. The conclusions of their work reveal that the ZnO NRs synthesized using 2-methoxyethanol have the smallest grain size (39.18 nm), the smallest crystallite and the largest band gap (3.21 eV). (Foo et al., 2014)

2.5.2.9 Solvothermal growth

J. Li et al. (J. Li et al., 2013) have synthesized ZnO nanoparticles by solvothermally. Using 0.33 g of zinc acetate dihydrate, dissolved in 10 ml of ethanol in a stainless steel autoclave heated in a forced air oven at 120 °C for 24 hours and then cooled to room temperature; a white precipitate (ZnO) was obtained, separate, washed with distilled water and ethanol, then dried at 60 ° C for 8 h. (J. Li et al., 2013). The authors mix these ZnO nanoparticles with heteropolyacids at 10^{-4} M (compared to zinc oxide) and a certain proportion of binders (terpineol, ethylcellulose in ethanol) to drop a thin layer by squeegee (Doctor Blade) on the FTO. The sample obtained is heat treated at 450 ° C and constitutes the anode. The electrode is then immersed in a N719 solution to give a photoanode. Using a platinum counter electrode, and an electrolyte solution (DHS-E36), they assemble photoanode in contact with the electrolyte (DHS-E36) and against electrode to form a DSSC cell. The heteropolyacids used are $HxM_{12}WO_{40}$ (M = P, x = 3 and if M = Si). The overall efficiency of converting solar energy into electricity reached 2.7% in the presence of $H_3P_{12}WO_{40}$, an improvement of 49.2% compared to efficiency without $H_3P_{12}WO_{40}$ (J. Li et al., 2013).. A cell operating mechanism has been suggested considering the presence of intact heteropolyacids in the conduction of electrons. (J. Li et al., 2013).

2.5.2.10 Electrodeposited Method (EDM)

Electrodeposition is an electrolytic technique for depositing thin layers in which the metal ions present in the electrolyte undergo an electrical effect to settle on the substrate (Figure 2.12). The deposition control parameters are: the composition of the electrolyte; the type of polarization (continuous or pulsed); the agitation and the speed of circulation of the electrolyte.

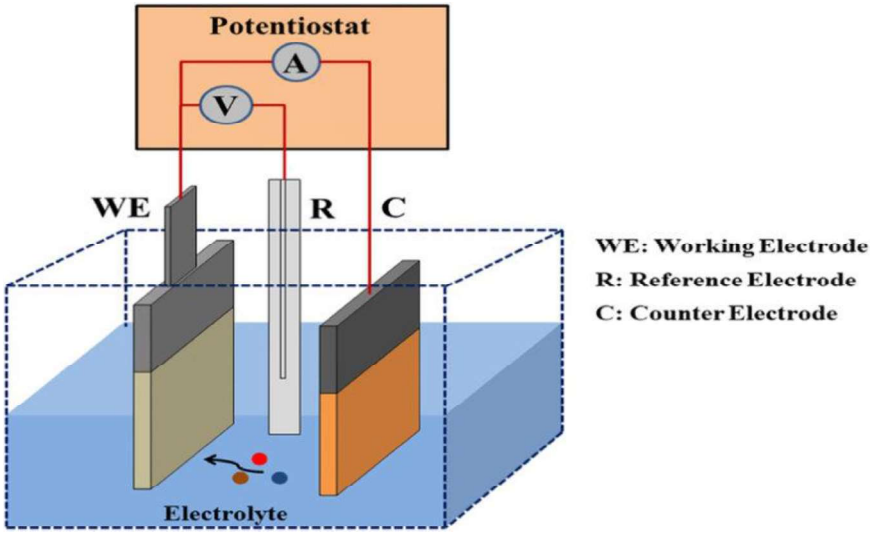

Figure 2.12: schematic st-up of the electrochemical deposition adopted (Ikhioya, Akpu, & Nkele, 2021)

The materials and performances of two DSSCs produced from ZnO by electrodeposition are presented in table 2.6 below. The DSSCs developed by J. Qiu et al. (Qiu, Guo, & Wang, 2011) reach a yield of 3.12% while those developed by S. Karuppuchamy (Karuppuchamy, 2002)

Table 2.6: Materials and performance of two ZnO-based DSSCs developed by electrodeposition

Anode	Substrate	Dye	Separator	Electrolyte	Cathode	η (%)	Réference
ZnO nanorod-nanosheet :	ITO	N719	Thick spacer 50µm	I^-/I_3^-	Pt/FTO	3.12	(Qiu et al., 2011)
ZnO-TiO_2	ITO	N3	Thick spacer 50µm	I^-/I_3^-	Pt/foil	0.13	(Karuppuchamy, 2002)

2.5.2.11 Pulsed Laser Deposition

Pulse laser ablation is a thin layer deposition technique based on the interaction between the target material being sought to be deposited and a high energy pulse laser beam. The apparatus consists of a laser irradiation source system, a pumping system which allows vacuuming in the vacuum chamber, a target door, a heating substrate door, lenses, mirrors and control instruments.

2.5.3 Dye

A dye is responsible for absorbing photons in a DSSC cell. It is present as a monolayer on the entire surface of the semi-driver and constitutes the key element of the Grätzel cell, because it must fulfill three major criteria:

- Its absorption spectrum must be as wide as possible and be in the visible. In Graetzel's report the ideal dye should absorb all of the wavelengths of light below the 920 nm threshold (Grätzel, 1999).
- It must be able to easily transfer its excited electrons to the conduction band of the semiconductor oxide, that is, the molecular orbitals involved must have good recovery. Graetzel estimated that the injection of electrons into the solid must be done with a quantum efficiency.
- It must be able to ensure hundreds of millions of cycles of oxidationreduction without degrading; which eliminates the main organic dyes. (Colodrero et al., 2009; Sauvage et al., 2010)

To remedy the problem of degradation of dyes, research and developments have made it possible to find additives capable of:

- Maintaining the stability of the dye in light such as 1-ethyl-3 methylimidazolium tetrocyanoborate (EMIB (CN) 4);
- Improve the conversion efficiency from light to electrons. Diselenium copper (Cu (In, Ga) Se_2) in a dye offers this possibility.

The dye must also bear fixing groups such as carboxylate or phosphonate to firmly encumber on semiconductor oxide (Grätzel, 1999). There are thousands of dyes studied and offered for DSSCs,

however there are two families, namely natural dyes and synthesized dyes. The synthesized dyes are: Metallic complexes (ruthenium); Organic dyes without metal (porphyrin); Dyes based on perovskite; Bite dyes; Quantum dots dyes.

Natural dyes are the first to be used in DSSCs in the 1970s (Tributsch & Calvin, 1971). They are extracted from plants (leaves, flowers, fruits, roots, petals) in the form of anthocyanins, flavonoids, carotenoids and chlorophyll pigments. Carotenoids are isoprenoids or organic pigments with a C40 hydrocarbon skeleton. Carotenoids are responsible for the colors red, yellow and orange from the many fruits and flowers. According to Shalini et al (Shalini et al., 2016), the synthesis of natural sensitizers begins with the picking of flowers or plant fruits followed by the extraction of dyes with suitable solvents such as water, alcohol.

Flavonoids are organic pigments found in vascular plants. Having a basic structure formed of two aromatic cycles connected by three carbons C6-C3-C6, the flavone consists of 2 aromatic cycles linked together by a cycle Y. According to Shalini, HOMO to LUMO load transfer transitions require little energy in the case of flavonoid and a wide absorption band in the visible region. (Shalini et al., 2016)

Anthocyanins are also natural pigments responsible for the colors of the scarlet with blue in the visible spectrum. Their basic structure consists of C6-C3-C6. They are sensitive, unstable and degradable dyes depending on the light intensity and a change in pH. Anthocyanins are soluble in water and alcohol. They are extracted from the numerous fruits, flowers and leaves such as aronia, eggplant, cranberry, cherry, blackberry, blueberry, orange, apple (skin), grape (red).

Chlorophyll is a natural green pigment in plants with two bands of red and blue absorption in the visible spectrum (400 nm-700 nm). During photosynthesis chlorophyll intercepts light energy to produce chemical energy (gluicides) and oxygen. The basic chemical structure of chlorophyll contains cycles of carbon, nitrogen, hydrogen, Mg2 atoms as. The presence of Mg ensures the color green. Natural dyes are interesting because of their low cost of implementation since they are extracted directly from plants and their abundance in nature. Using an anode zinc oxide electrode, DSSCs with natural dyes have been developed. This is the case for dyes extracted from nuts, rhubarbes and pomegranates by boiling these plants in water for a few hours until solid extracts are obtained. (El-Agez, Tayyan, Al-Kahlout, Taya, & l-Latif, 2012). The solid extracts were then dried at 70 ° C overnight and the product obtained was dissolved in ethylene glycol to obtain the desired

dyes. These dyes were used to develop DSSCs with a low conversion efficiency of 0.014% for dyes from nuts and rhubarb and 0.0043% for dyes from pomegranate (El-Agez et al., 2012).

Taya et al. (Taya, 2013) extracted dyes from five plants (anethum graveolens, parsley, arugula, spinach oleacea) to develop DSSCs with anode ZnO and TiO_2. Their best conversion yields are for the dye extracted from spinach associated with a redox torque electrolyte (I^-/I^-_3) forming a DSSC: In the case of the electrode based on ZnO the conversion yield is very low 0.008% (Taya, 2013). For the anodic electrode in TiO_2, Taya et al. observe an increase in yield at 0.29% (Taya, 2013). However, the trend is that the latter DSSCs have a higher conversion performance than those based on zinc oxide (Richhariya, Kumar, Tekasakul, & Gupta, 2017).

Direct extraction of dyes from plants (fruits, vegetables, flowers, roots) often involves grinding, drying, lyophilization or soaking steps in a suitable solvent. Other chemical and physical extraction techniques are also used. Chemical extraction passes through a combination of solvents for example for the extraction of anthocyanins, the solvent commonly stressed is a combination between water, alcohol (ethanol and methanol), acetone and a range of acids (such as hydrochloric, citric, tartaric, acetic, propionic acid (Barnes, Nguyen, Shen, & Schug, 2009; Metivier, Francis, & Clydesdale, 1980). This combination gives acidified solvents such as acidified methanol which is recognized as a more effective solvent compared to acetone or methanol alone (Barnes et al., 2009). A mixture of methanol, water and trifluoroacetic acid in a volume ratio of 70:30: 1 performed by Barnes et al. (Barnes et al., 2009) in 2009, was found to be the best solvent for the extraction of blueberry anthocyanins (blackberries). The addition of weak organic acids or strong acids at low concentrations in these acidified solvents such as trifluoroacetic acid (0.5-3.0%) or hydrochloric acid (<1.0%) prevents the acidified solvent does not destroy the extraction anthocyanin pigments (Amogne, Ayele, & Tsigie, 2020; Barnes et al., 2009; Metivier et al., 1980). The choice of these solutions was justified by the fact that anthocyanins are polar molecules and that high polarity solvents such as water or those with low polarity cannot effectively extract anthocyanins. Physical extraction techniques are ultrasound-assisted extraction, microwave assisted extraction, supercritical fluid extraction and high-pressure extraction. After extraction, the products obtained are subjected to purification to recover the dye at high purity. Natural dyes have certain drawbacks including instability under the effect of heat and a lower yield of conversion of light rays into electrons by compared to synthesized dyes. Although research and development is still articulated

on plants in order to exploit natural dyes, synthesized dyes offer better performance and are best used in DSSCs. Richhariya et al. (Richhariya et al., 2017) suggest a mixture of natural and synthesized dyes to achieve better performance. This suggestion is based on the improvement of absorption of light rays by the NIR solar spectrum allowing more solar radiation to enter the dye and therefore to increase the flux of electrons which arrives in the semiconductor, it should be noted that some authors (Fu, Zhao, Yang, & Wu, 2014; Silva et al., 2019) have extracted bacteria from natural dyes for DSSC applications, but the yields of conversion of light energy into electrical energy obtained are very low (less than 1).According to Vankar (Vankar, 2000) natural dyes do not combine directly with the material they are supposed to color and require a bite to attach to the material and prevent the dye from degrading to light. The teeth used are:

- Metallic salts of aluminum, chromium, iron, copper and tin;
- Tannins;
- Sulphon oils which have better metal fixation than natural oils due to the presence of sulfonated groups. This group forms with the dye a metal complex to give a solidity and a higher dye. (Vankar, 2000)

The dyes synthesized below are used:

- Halogenated perovskites of chemical structure CH3N3PbX3 (X = Cl, Br or I) were used as sensitizers for the first time in 2009 in DSSCs providing a conversion yield of 3, 8%. Very quickly, developments of the DSSC with this sensitizer experienced a remarkable boom in light conversion performance into electrical energy: 15% (J. Burschka et al., 2013; Hu et al., 2014; Omar & Abdullah, 2014) in 2013, 19.42% (Yang et al., 2016) in 2016 and 29.52% for the perovskite-silicon tandem. Tandem has a wide range of wavelength absorption. Perovskite DSSCs have the advantage of low-cost production and the possibilities for improving yield. However, their drawbacks lie in aging and structural instability at the module level.
- Metal complexes, such as ruthenium or osmium, are excellent candidates. They have a wide absorption band in visible light, as well as a very good ability to inject electrons into semiconductor oxide. The conversion rate of an incident photon into an electron, at a given wavelength, is very high in visible radiation. Ruthenium (Ru) complexes provide the best yields for Grätzel cells, between 11% and 12%. (Sauvage et al., 2010).

These complex ruthenium dyes have advantages:

- An octahedron geometry which tolerates the extension of specific ligands in a controlled manner;
- Photophysical properties, photochemical and electrochemical are tunable;Stable and accessible oxidation states from I to IV;
- Good stability in many solvents. Ru-based dyes are distinguished by their functional groups and their areas of absorption of solar radiation.

The complex ruthenium dyes frequently used are: Di-tetrabutylammonium bis (isothiocyanato) bis (2,2'-bipyridyl-4,4'-dicarboxylato) ruthenium (II) (N719), Cis-Bis (isothiocyanato) bis (2,2'-bipyridyl-4,4'-dicarbox. The N3 dye has in its structure two bipyridine ligands and two other isothiocyanoto absorbent ligands in the UV-visible domain until 800 nm. The absorption of light by the dye is attributed to the transfer of charge from the transition metal to the ligand and to the molecular orbitals HOMO and LUMO (Shalini et al., 2016). The N719 dye is a modification of N3 by substitution of hydrogen by the TBA group. Their result indicates that for an N719 dye dissolved in 0.27 mM of ethanol, the absorption of the dye reaches 250-800 nm. The dye N749 absorbs up to 860 nm of light radiation (Shalini et al., 2016).

The dye N719, made from ruthenium, is most often used in DSSC cells. These ruthenium complexes are used because they mainly absorb in the visible light spectrum. It takes about 0.1 grams of Ru per m² of cell. (Colodrero et al., 2009; Sauvage et al., 2010) Previous studies have shown that the dye N719, if it is very well suited to TiO_2, however, it is not suitable for the use of ZnO. Indeed, there appears an accumulation of dye in the pores of ZnO which results in its dissolution into Zn^{2+} ions and which makes ineffective the phenomenon of absorption of photons and transfer of electrons. (Karin Keis, Lindgren, Lindquist, & Hagfeldt, 2000) A suggested solution for optimizing the awareness process in the DSSCs would be to raise awareness with basic solutions or with dyes which do not have acid protons in their structure but which will nevertheless attach to the particles of ZnO so that an effective injection takes place. (Karin Keis et al., 2000) The record characteristics of sensitizers N719 and N3 are given by the manufacturer Sigma Aldrich (table 2.7). These dyes were used in a solar cell based on TiO_2 and the electrolyte I^-/I^-_3.

Table 2.7: Performance of sensitizers N719 and N3 in a DSSC based on TiO_2 (Source: Sigma Aldrich)

Dye	Voc (V)	Jsc (mA/cm^2)	FF (%)	η (%)
N719	0,84	17,73	74	11,2
N3	0,726	15,8	71	8,2

In 2011, Yella et al (Yella et al., 2011) have developed a metal-free organic sensitizer called porphorin to achieve a high conversion efficiency of 12.3%. The electrolyte used in this DSSC is cobalt-based. These metal-free dyes have several advantages compared to those based on metals, namely: a very high molar extinction coefficient, absence of the cutter of the expensive and toxic Ru, ease of synthesis, stability at high temperature. Organic dyes without metal generally have a molecular structure D-π-A (Donor-Link-Acceptor). Donors are electron-rich groups such as phenylamine, aminocoumarin, indoline, (difluenyl) triphenylamine, triarylamines and carbazoles. (Shalini et al., 2016). Some groups π used in literature (Shalini et al., 2016) thiophenes, polyenes, benzethiadiazoles and some acceptors are cyanoacrylic acid, rhodamines, pyridines. Organic dyes without usual metal are porphyrin, coumarin, indoline and derivatives Zn-porphyrin.

Quantum dots dyes (QDs) are one of the last generations of developing and research dyes for DSSCs. In a QDSSC cell, the DSSC dye is replaced by inorganic nanoparticles called QDs (quantum dots). QDs are either adsorbed from a colloidal solution or they are produced in situ. Cadmium chalcogenide QDs (CdX, X = S, Se or Te) show increased absorption of photons by CdX due to its prohibited band greater than 1.3 eV.

2.5.4 Substrate

In most of the work carried out on DSSCs, the semiconductor is placed on a glass on the surface of which a thin layer of a conductive and transparent metal oxide is previously deposited (TCO, Thin Conductive Oxide). In the area of DSSC, it is usually a layer of fluorine-doped tin oxide (SnO_2: F, FTO); tin-doped indium oxide (In_2O_3: Sn, ITO) is also used (Ngamsinlapasathian, Sreethawong, & Yoshikawa, 2008) but not in the case of large-scale development of DSSCs, because global indium production is low (less than 600 t / year) due to its rarity in the earth's crust.

This TCO glass must be both very transparent in order to allow lighter to enter the cell and very conductive to be able to transport the electric current during the operation of the cell. The TCO22-7, a substrate 2.2 mm thick and having a surface resistance of 7Ω/sq, is much more used, so you must find a compromise on the thickness of the conductive oxide layer, because the thicker it is, the better it will be a good driver, but the less transparent it is. Flexible substrates are also used in the manufacture of DSSC cells, they are very practical and above all well suited for transport. In particular, flexible DSSCs using thin and light conductive plastic substrates for their photoelectrodes are inexpensive and suitable for the production of rollers. Most conventional processes involve high temperature sintering (450-500°C) for the annealing of ZnO nanoparticles, to obtain a good connection between the particles; this high temperature cannot be used in the case of plastic substrates. Therefore, it was necessary, in the case of plastic substrates, to develop a new manufacturing process achievable below 150 °C, with post-treatment, if necessary, to improve the binding between ZnO particles. Several methods have been proposed to overcome this problem; we will cite as examples: the method of dissolution and precipitation (Ueno, Utsunomiya, & Fujihara, 2013), pyrolysis below 120 °C (Utsunomiya, Ueno, & Fujihara, 2013) and hydrothermal growth at low temperature of a layer of germ derived from a sol-gel, etc. (W. K. Tan et al., 2013). Some work on the manufacture of DSSC based on ZnO with plastic substrates has been listed (Choudhury, Kishi, & Soga, 2016; Jiang et al., 2008; Yin, Liu, Wang, & Liu, 2010); M.S.H. Choudhury et al. (Choudhury et al., 2016) broke the conversion efficiency record by 0.9% (table 2.6) obtained by C. Y. Jiang et al (Jiang et al., 2008) adding 10% of TiO_2 to the ZnO matrix and obtain a conversion efficiency of 1.75%.

A study involving a deposit process by electrophoresis (EPD) followed by the compression of the film as post-treatment was carried out (H.-W. Chen et al., 2011). This compression method is simple and fast enough to prepare a ZnO photoelectrode for a flexible plastic-based DSSC cell. H.W. Chen et al. (H.-W. Chen et al., 2011) achieved a conversion efficiency of 4.04% by immersing the ZnO electrode deposited on an ITO-PEN substrate in 0.5 mM D149 for 3 hours at 50 ° C to develop the photoanode. The cathode was developed using platinum deposited on an ITO-Pt substrate in contact with a typical electrolyte (I^-/I^-_3) and a joint 25 µm Surlyn Solaronix.

2.5.5 Cathode

The role of the cathode or counter electrode in a DSSC cell is to recover the electron which has been injected by the dye and to regenerate the reduced shape of the redox pair from the closing oxidized form, thus the electrical circuit of the cell. The criterion for choosing an electrode is based on: A high rate of reduction of the mediating electrolyte causing the regeneration of the sensitizer; The lowest possible resistance to neglecting the game losses. There are several types of cathodes for DSSC cells which can be classified into 4 groups: metals, metal oxides, carbon electrodes and polymers.

2.5.5.1 Cathodes types for DSSC based on ZnO

Platinum is mainly used as a counter electrode (platinum film on a conductive glass substrate) because this metal offers very low overvoltage (almost zero) and therefore catalytic conditions favorable to the reduction of I^-_3 in I^- present in the electrolyte. The cathode is made from a platinum precursor, usually a platinum salt, this is the case, for example, of H_2PtCl_6, heat treated on a glass substrate. This technique minimizes the amount of platinum used (approximately 5 nmol/cm^2), since platinum is very expensive and remains less abundant in nature. (Murakami & Grätzel, 2008; O'Regan & Grätzel, 1991)

Other metals have the advantage of low resistance but are corrosive in the mediating electrolyte. To overcome this corrosion phenomenon, some researchers cover metals from anti-corrosive materials such as carbon, tin oxide, platinum, nickel. This is how stainless steel (SUS 304) covered with platinum was used by Ma et al. in the manufacture of DSSC with a yield of 5.24%. Although platinum is recognized for its stability in the face of corrosion in the electrolyte (triiodide /iodide), E. Olsen et al. have revealed in their work an instability of platinum when it is in contact with the electrolyte containing the torque (triiodide / iodide) and therefore its catalytic activity decreases as a function of the time of exposure to the electrolyte due to the formation of the PtI_4 compound (Olsen, Hagen, & Eric Lindquist, 2000).

Esgin et al. (Esgin, Caglar, & Caglar, 2022) published in 2022, a DSSC based on copper-doped ZnO at the anode associated with a platinum cathode. The performance of this cell solar is low with an electrical conversion efficiency reaching 2.03% and a form factor of 55.9%. (table 2.8)

Research has progressed in the direction of gradually replacing platinum in the composition of the cathode, in order to reduce the cost of manufacturing DSSC cells and also to optimize their long-term stability. Thus cathodes without platinum have been developed; this is particularly the case for carbon compounds which are tested a lot, although carbon has a low catalytic activity vis-à-vis; its analogs with a specific high surface (carbon nanotubes, etc. have catalytic activities that may exceed those of platinum. Carbon black, carbon nanotubes and graphene, are a good alternative to platinum, because they have a good catalytic activity with regard to the reduction of ions, and in addition they are resistant to heat and corrosion. (Anwar, George, & Hill, 2013; Murakami et al., 2006; Roy-Mayhew, Bozym, Punckt, & Aksay, 2010; Satapathi et al., 2014; Suzuki et al., 2003; Trancik, Barton, & Hone, 2008). It is also noted that carbon costs less than platinum and that it is generally insoluble in several solvents. Graphite is used for its high electronic conductivity which allows a good transfer of charge to the electrolyte. Carbon black can also be used for its large porosity, which increases the catalytic effect of the electrode. (Kay & Grätzel, 1996). Carbon nanotube cathodes, in graphite and carbon black have improved the yields of DSSC cells (Murakami et al., 2006; Satapathi et al., 2014; Suzuki et al., 2003) A carbon nanotube is made up of one or more coiled graphene sheets, following a nanometric radius of curvature, so as to form a cylindrical structure. There are two types of carbon nanotubes (Dürkop, Getty, Cobas, & Fuhrer, 2004):

- Mono-leaf carbon nanotubes also called mono-wall or mono-layer (Single-Wall Carbon Nanotubes - SWNT) consisting of a graphene sheet wrapped on itself and which can be closed at both ends by half a molecule of fullerene. Suzuki et al. (Suzuki et al., 2003) have developed a DSSC based on SWNT on the counter electrode and TiO_2 on the anode deposited by doctor blade. The dye used is N719 and the electrolyte is the torque (I^-/I^-_3) in 3-Methoxyacetonitrile. The DSSCs produced achieve a yield of 4.5% which is comparable to using the FTO as against electrode under the same preparation conditions (Suzuki et al., 2003).
- Multi-leaf carbon nanotubes also called multi-wall or multi-layered (Multi-Wall Carbon Nanotubes - MWNT) consisting of several graphene sheets wrapped around each other.

Carbon nanotubes are used in DSSC cells to improve their efficiency, by conferring good electrical conductivity on nanocomposed metal oxides. They can be added in electrolytes, counter-electrodes and even in the active layer of nanocomposite semiconductor oxides such as TiO_2. (Uk Lee, Seok Choi, & Hong, 2010) Other materials can also be used as counter-electrodes; this is particularly the case for conductive polymers, or certain metallic sulfides. (Murakami & Grätzel, 2008; M. Wang et al., 2009) The conductive polymers (polyaniline, polypyrrole, poly (3 - 4ethyleneioxythiophene)) known by the acronym PEDOT, have also demonstrated good catalytic activities. (Julian Burschka et al., 2012; K.-M. Lee et al., 2010; Z. Li et al., 2009; Saito, Kubo, Kitamura, Wada, & Yanagida, 2004; Jihuai Wu et al., 2008; Xia, Chen, & Yanagida, 2011) These materials have good intrinsic electronic conductivity and have in addition good optical, mechanical and electronic properties (load transfer). These conductive polymers can be easily deposited as a thin film on a substrate with a uniform thickness, making it good electrodes for DSSC cells. (Saranya, Rameez, & Subramania, 2015)

Metallic sulphide cathodes have also been developed, these include metallic sulfides below - after: CoS, NiS, Cu_2S and PbS. (J.-Y. Lin & Liao, 2011; Shuai et al., 2014; Sun et al., 2011) An earlier study has shown that CoS is more stable in the long term than PbS and Cu_2S used as a cathode in DSSC cells (LAHMANI, DUPAS, & HOUDY, 2009) Another study (LAHMANI, BRÉCHIGNAC, & HOUDY, 2012) revealed that cobalt sulfide (CoS) would have more catalytic activity than platinum for the reduction of triiodide ions. Thin CoS movies on conductive plastic (Polyethylene Naphthalate / ITO or PEN / ITO) were used as a counter-electrode in a DSSC cell with a yield of 6.5% under a standard illumination with a power of 100 W/cm^2 with an AM1.5G filter (M. Wang et al., 2009)

Table 2.8: DSSC performance with different materials under irradiation 100 mW/cm^2

Substrate	Catalyst on CE	Electrolyte solvent	Anode	Dye	Jsc (mA.cm^{-2})	Voc (mV)	FF (%)	η (%)	Method Technic	Reference
FTO	Pt	(I^-/I_3^-)	ZnO:Cu	N719	0.69	596	55.9	2.03	HMT	(Esgin et al., 2022)
FTO	Pt	(I^-/I_3^-)	ZnO	N719	8.23	542	46.7	2.7	HTM[a], DBT[b]	(J. Li et al., 2013)
PET/ITO (flexible)	Pt	(I^-/I_3^-)	ZnO	N719	(chart)	(chart)		0,9	HTM[a], *EBPVD*[c]	(Jiang et al., 2008)
ITO/FTO	Pt	(I^-/I_3^-)	ZnO	CYC-B1	16.09	565	59	4.85	DBT, S[d]	(C.-P. Lee et al., 2014)
ITO/FTO	Pt	(I^-/I_3^-)	ZnO	N3	10.7	549	45	2.5	DBT, S	(C.-P. Lee et al., 2014)
FTO	Graphite and Carbon black	acetonitrile	TiO_2	Complexe RU (II)	11.34	826	71	6.67	DBT	(Kay & Grätzel, 1996)
FTO	Pt	Acetonitrile + valeronitrile	TiO_2	N719	16.25	779	73	9.24	DBT	(Seigo Ito et al., 2007)
FTO-glass	Pt	Acetonitrile + valeronitrile	TiO_2	N3	17.73	846	75	11.18	Dip coating	(Nazeeruddin et al., 2005)
ITO-PEN and Ti foil	Pt	Acetonitrile + valeronitrile	TiO_2	N719	13.6	780	68	7.2	SP[e], EDM[f]	(S. Ito et al., 2006)
Glass	SWCN	3-Methoxyacetonitrile	TiO_2	N719	9.7	750	62	4.5	DBT	(Suzuki et al., 2003)
ITO/SiOx/StSt	Pt	(I^-/I_3^-)	TiO_2	Complexe RU (II)	11,2	610	61	4,4	DBT	(M. G. Kang, Park, Ryu, Chang, & Kim, 2006)
ITO/StSt					9,1	610		3,6		
StSt					6,35	610		2,1		
Glass	Ag	PEDOT	TiO_2	Complexe RU (II)	5,69	781	0,72	3,19	Photoelectrochemisrty	(Manseki et al., 2011)
	FTO				5,30	460	0,63	1,54		
	Carbon				4,90	456	0,52	1,17		

HTM[a]: «hydrothermal method». Nanocrystal synthesis technique from an aqueous solution. Operating conditions: high temperatures, high vapor pressures.
CE: counter electrode
DBT[b]: «Technical Doctor-blade». Small layer coating technique controlled using a blade /knife.
EBPVD[c]: Electron Beam PVD
SP[e]: screen-printing
S[c]: Sputtering
SWCN: single wall carbon nanotubes
PEN: Polyethylene Naphthalate
EDM: «electrodeposited method». Electrodeposition is an electrolytic technique for depositing thin layers in which the metal ions present in the electrolyte undergo an electrical effect to settle on the substrate.

SCM: «spin-coating method». Thin layer deposition technique using a rotating machine called «spinner» or «spin coater».
CBD: «chemical bath deposition». Chemical bath deposit or solution containing precursors for the deposition of nanomaterials on a substrate.
SGM: «sol-gel method». Solution - gelation.
CVD: «chemical vapor deposition». Chemical vapor deposition is a technique for vacuum deposition of thin layers from gaseous precursors. The substrate is exposed to precursors in the gas phase which react to its surface to generate the desired deposit.
PVD: «physical vapor deposition». Physical vapor deposition consists of transforming the solid or liquid of coating into vapor and then the latter is driven and condensed for deposit on the substrate.
StSt: stainless steel S.

Ito et al. concluded from their work that the effectiveness of flexible DSSCs on polymer films is lower than that of DSSCs on high temperature annealed FTOs. Indeed, a low temperature heat treatment is a cause of loss of energy from the conversion of light rays into the DSSC cell (Nakade et al., 2002). S. Nakada et al (Nakade et al., 2002) found:

- A poorer interconnection between the annealed particles at 150 °C compared to those annealed at 450 °C in their observation at MEB.
- Through peaks of analysis at XRD showed better crystallization at 450 °C than at low temperatures.
- A lower short-circuit current density in an annealed sample at 150 °C than at 450 °C.
- The electron diffusion length of all films annealed at 150 °C was much shorter than that of films annealed at 450 °C.

Stainless steel substrates (StSt, stainless steel) offer the possibility of annealing at higher temperatures than those in plastic; which results in the evaporation of water, disposal of organic residues, improving interparticle interconnection and improving the grip of the semiconductor on the substrate. Kang et al (M. G. Kang et al., 2006) made thin layer deposits of TiO_2 on a stainless steel substrate (according to the TiO_2/StSt, TiO_2/ITO/StSt and TiO_2/ITO/SiOx/StSt stacks) stacks. For the flexible electrode of TiO_2/ITO/SiOx/St St associated with a counter electrode in Pt, the yield of the elaborate DSSC is 4.2% while for the substrate in FTO the DSSC developed under the same conditions gives a conversion efficiency of 4.8%. This performance of the stainless steel working electrode is also attributed to the reflexivity of the light rays of steel towards the cell and to the presence of the SiOx layer which would facilitate the diffusion of these rays in the dye particles. Without the SiOx layer, the yield of DSSC drops by 17% and 50% respectively for the working electrodes of TiO_2/ITO/St/St and TiO_2 /StStSt. Jun et al (Jun, Kim, & Kang, 2007) also carried out in their studies on the performance of DSSCs based on stainless steel substrates are

almost equivalent in terms of yield compared to that with FTO substrate manufactured under the same conditions. One of the strategies to contain the liquid electrolyte in the DSC and improve them performance of the solar cell is to replace the liquid mediator with a solid hole driver such as PEDOT. Manseki et al (Manseki et al., 2011) have studied PSSCs based on PEDOT associated with counter-electrodes (Ag, C and FTO) and a nanocrystalline TiO_2 anode deposited on the FTO. For impedance, they found that the internal resistance of money is more than that of carbon. They also note that the TiO_2/dye/PEDOT charge transfer process varies considerably depending on the electrode material at the cathode. Indeed, IPCE analyzes based on light radiation show that the silver dough interface is the most efficient in load transfer and that the carbon dough interface is the least efficient. The FTO interface has an intermediate charge transfer efficiency between the FTO and the money. This justifies the conversion yields of the DSSC obtained from the counter silver electrodes, FTO and carbon which are 3.19% respectively, 1.4% and 1.17% using PEDOT as a hole conductor and TiO_2 / FTO at the anode. The DSSC based on the driver PEDOT / Au at the cathode and TiO_2 at the anode have low yields and less than 1% (Senadeera et al., 2005).
The promising substrates are Ti, stainless steel, the W, and the Zn (S. Ito et al., 2006).

2.5.6 Electrolyte

Electrolyte plays an essential role in the operation of the DSSC cell, since it ensures the regeneration of the dye. It must meet a number of conditions for cells to be stable. Thus it must not be toxic, it must have a low vapor pressure, a boiling point above 70 °C, be low reactive, stable and inexpensive. Aqueous systems meet these criteria, but water generally causes dye desorption and can react with the usual mediators. The most commonly used and effective mediator is the triiodide/iodide pair. The reasons for this wide use are:

- S. Pelet et al. (Pelet, Moser, & Grätzel, 2000) have shown that the adsorption of cations on the surface of TiO_2 allows the oxidation of via a rapid mechanism.
- Ruthenium dyes adsorbed on TiO_2 are regenerated with an efficiency close to 100% in the presence of the redox torque. (Clifford, Palomares, Nazeeruddin, Grätzel, & Durrant, 2007)
- A high diffusion coefficient due to particles of the redox torque which are small sizes (Su'ait, Rahman, & Ahmad, 2015);

- Does not undergo decomposition in the operating conditions of the solar cell, therefore stable (Su'ait et al., 2015);
- A low light absorbance compared to that of the dye (Su'ait et al., 2015).

The first generations of redox pair electrolytes (I^-/I^-_3) are volatile electrolytes produced using organic additives. The most used are iodolytes consisting of a solvent (3-methylpropionitrite, acetonitrile, propionitrile), additives (ionic liquid, alkylbenzimidazole, thiocyanate, lithium salt, derived from pyridine) with a concentration (30 mM, 50 mM, 100 mM, 150 mM torque. (**(www.solaronix.com)**). The additives consist of cations and anions likely to improve the conductivity of the electrolyte and the solar cell. The electrolyte is synthesized using a high boiling solvent to ensure its stability in the cell operating under a high temperature. The volatility of the electrolyte is a factor of instability leading to a expansion of the liquid and a plausible rupture of the tightness of the DSSC. Damage to the DSSC can be seen, a production disruption or a drop in production. To remedy this volatility problem, a tetracyanoborate additive is added during the synthesis of the electrolyte. This additive is stable in light and heat due to light radiation. We finally get non-volatile electrolytes. Mosalytes are an example of electrolytes with negligible vapor pressure and are therefore compatible with high temperatures. **(www.solaronix.com)**

Other redox couples have been tested, such as (Br^{3-}/Br). However, these systems have not proven to be as effective. At low temperatures the electrolyte tends to freeze, which results in damage to the cell and interruption of electricity production. At high temperatures, the electrolyte containing volatile organic compounds tends to expand, which results in the rupture of the seal of the cell. In order to alleviate the problems of using a liquid electrolyte, solid or quasi-solid electrolytes based on polymers have been developed. The simple gelling of the electrolyte with PEG achieved an 8.21% yield (Chalkias et al., 2021) in 2021. Ionic liquids were also used due to their stability, such as the mixture of 1-propyl-3-methyl-imidazolium iodide and 1-ethyl-3-methylimidazolium tetracyanoborate, yields reaching 7.8% have thus been reported, as well as carriers of solid holes like CuI or even spiro - MeOTAD. (Krüger, Plass, Grätzel, & Matthieu, 2002) The latter system achieved 5.1% efficiency under AM1.5 illumination at 126 mW/cm^2. However, the performance of cells containing these solid or quasi-solid electrolytes never exceeds that observed with liquid electrolytes due to the lower penetration into the pores and / or the slower diffusion of the mediator

in these more viscous systems. (Krüger et al., 2002) In 2014, Ahn et al. have developed a PEBII polyionic electrolyte (SnO_2 hollow sphere TiO_2 nanosheet organized TiO_2) from 0.2 $.10^{-3}$ S.cm-1 Indeed, it is essential that the material responsible for transporting the loads between the dye and the cathode completely coats the electron-carrying material so as to allow the regeneration of the entire dye and at all times. However, penetrating a solid within a network of nanoscale pores is far from trivial. Much work is being done on the use of dry or gelled polymer electrolytes to replace liquid electrolytes. (Su'ait et al., 2015) The use of a gelled electrolyte makes it possible to maintain ion conductivities equivalent to those of liquid electrolytes, but the problem of the volatility of solvents remains intact, moreover, most often, the gels obtained are not stable and an exudation of the solvent is observed. Recent studies show the potential of polyoxyethylene skeleton polymer electrolytes (POE) incorporating DSSCs (Chang et al., 2014; Dong et al., 2013), although ion conductivities are still low. In addition to the chosen polymer, the cation has a significant influence on the efficiency of the solar cell. (Chang et al., 2014)

2.5.7 Seal materials

These are materials used when assembling anode and cathode to ensure containment of the liquid electrolyte. The electrolyte should be carefully sealed to avoid leakage due to its volatility. Some attached materials are cited in tables 2.7 and 2.8: Dupont Surlyn 25µm Solaronix, 20 µm poly-propylene, Celgard, sealing sheet. The development of solids instead of electrolyte liquids is a way to do without the materials to be sealed. These materials to be sealed are polymers. Dupont Surlyn 25µm of Solaronix is a transparent, thermoplastic or hotfusible polymer material of 25µm which melts at 100 °C. The sealing process which consists in melting this joint on the two electrodes (by rolling) at a pressure and a controlled temperature (100 °C). It is recommended that its area be slightly larger (approximately 1 to 2 mm additional to the active perimeter) than that of the active surface to adhere to the substrate and contain the electrolyte.

2.6 Advantages and disadvantages of ZnO versus TiO_2 in DSSCs

According to studies conducted by Tiwana et al. (Tiwana, Docampo, Johnston, Snaith, & Herz, 2011), 2011, the photoexcited electron injection process is slow (lasts hundreds of picoseconds) in ZnO-based DSSCs compared to that of TiO_2-based DSSc which lasts a few picoseconds. This

slowness limits the overall photocurrent. The authors attribute this to the local environment of the dye-nanoparticle interface, which is governed by the dye-binding modes and the densities of states available for the injection of photoexcited electrons. Furthermore, the absorbance curves obtained from TiO_2, ZnO and SnO_2 adsorbed with dye Z907 shows a better light absorption performance for TiO_2-based DSSCs compared to ZnO and SnO_2. (Tiwana et al., 2011)

2.7 Estimating the manufacturing cost of TiO_2 based DSSC

According to Solaronix Ltd data (Figure 2.13), the cost of large-scale manufacturing of DSSCs is shared as follows: materials (69%), personnel (12%) and fixed costs (19%). This cost of materials is detailed as follows: TiO_2 (14%), dye and electrolyte (32%), TCO glass (17%), sealing and contacts (37%).

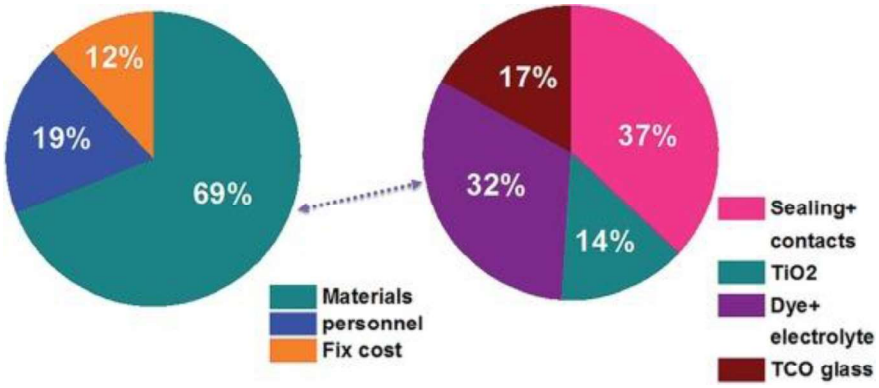

Figure 2.13 : Estimation of overall projected cost of DSSCs manufacturing on a large scale (left) and contribution of individual materials cost (right). This data was obtained from Solaronix Ltd

In 2009 Kalowekamo and Baker (Kalowekamo & Baker, 2009) performed work to estimate the cost of manufacturing DSSCs based on TiO_2, the ruthenium complex dye, a platinum counter electrode, the redox couple (I^-/I_3^-), sealing Surlyn. The conclusions of their estimates lead to a levelized electricity cost of 0.07 $/kWh for a 15% efficiency of DSSCs operating between 15-20 years while this same levelized electricity cost would be between 0.49 $/kWh and 0.85 $/kWh for a 5% efficiency of DSSCs operating for 5 years.

Based on Sigma Aldrich data (October 2022) for the same amount (50 g) of ZnO and TiO_2 nanopowder, zinc oxide[2] is cheaper ($100) than titanium oxide[3] ($158). This means that by replacing ZnO with TiO_2 under the same processing conditions, ZnO-based DSSCs would be cheaper than TiO_2-based ones.

2.8 Discussions

Resistivity, band gap and topography of ZnO and doped ZnO depend with the synthesis conditions. However, ZnO and doped ZnO crystal structure is always hexagonal wurtzite under ambient conditions. The band gap results of Sajjad et al (Sajjad et al., 2018) (for doped WO3) do not follow those of Kayanuma (Kayanuma, 1988) , Tan et al (S. T. Tan et al., 2005) , which state that the band gap of the semiconductor (ZnO) decreases as a function of the square of the crystal size radius. In the most of case, the band gap of the semiconductor (ZnO) decreases as a function of the square of the crystal size radius. It would be interesting to verify if these results of Sajjad can be extended to other syntheses and analysis of doped ZnO.

The DSSCs based on perovskite and TiO_2 have conversion yields close to those of cells in silicon while cells based on ZnO have yields lower than the first two categories of DSSC. Doping certainly improves the light conversion yields in electricity but they have not yet made it possible to obtain the expected results for the DSSC based on ZnO. The performance limits of DSSCs based on ZnO-N719 or complex ruthenium dye are:

- A low efficiency of electron injection in the ZnO conduction band (Katoh, Furube, Yoshihara, et al., 2004);
- A low dielectric constant which promotes the recombination of injected electrons (Guillén, Peter, & Anta, 2011);
- The N719 acid group reacts with Zn^{2+} ions for a complex (Dai et al., 2019; Katoh, Furube, Yoshihara, et al., 2004) ;

---

[2] https://www.sigmaaldrich.com/CA/en/product/aldrich/677450

[3] https://www.sigmaaldrich.com/CA/en/product/aldrich/637254

- A lower open circuit voltage than that of the TiO_2-based DSSCs. Voc depends on the Fermi level of the dye semiconductor interface and the redox potential of the electrolyte;
- The phenomenon of recombination of photoexcited electrons is high in nanofiles and triiodide ions of the electrolyte (Baxter & Aydil, 2005).
- Corrosion observed under the electron microscope S. Ghosh et al (Ghosh, Sartape, & Chakraborty, 2020).

According to their report, when an electrode based on ZnO is immersed in an ethanolic solution of sensitizer, adsorption and corrosion occur simultaneously. And so it would be wise to find a balance between the right amount of adsorbed dye and little possible corrosion. (Ghosh et al., 2020). An optimization compromise between the immersion time of the electrode and the concentration of the dye solution. Thin layers of synthesized nanofy ZnO were immersed in an ethanolic solution of sensitizer N719 at variable concentrations of 0.1 mM to 3 mM with varying durations of 2 minutes to 24 hours. S. Ghosh et al. have shown that when these nanofils were immersed in a sensitizer solution of 0.1 mM for 2 minutes, no significant corrosion was observed while corrosion was more significant when the concentration of the sensitizer was increased for the same duration. Also for a low concentration of sensitizer, corrosion is all the more important as the duration of immersion is longer. In short, corrosion on the surface of the electrode increases if the concentration of the sensitizer increases and / or the duration of immersion of the electrode increases. Excess non-adsorbed dye on the surface of the electrode does not effectively contribute to the photocurrent [33, 34]. Ghosh et al. explain in their report that corrosion is due to the anchor groups (-COOH) present in the dye molecules N719. By passing the thin layer of ZnO through a thin layer of ZnS as protection against corrosion, the authors have developed a DSSC with varying immersion times in the dye. For immersion times greater than 10 minutes, the results reveal low electrical conversion yields and low short circuit currents.

To meet these performances which are relatively weak for commercial exploitation, it would be necessary:

- Adding appropriate barriers against any degradation of the solar cell such that additives are suggested in the composition of dyes and mediators to ensure stability and improve the performance of the solar cell.

- Optimize adsorption and reduce (or eliminate) corrosion of ZnO by the dye (Ghosh et al., 2020; K. Keis et al., 2002) Improve the injection efficiency of electrons and reduce recombination phenomena.
- Study the effect of other routes previously used in the literature to improve these properties, in particular by treatment with ammonia (NH3) (X. Liu et al., 2007) the method of dissolution and precipitation (Ueno et al., 2013) pyrolysis below 120 °C (Utsunomiya et al., 2013) for plastic polymer substrates, and hydrothermal growth at low temperature of a layer of germ derived from a sol-gel, etc. A solvent and a technique allowing a synthesis of the smaller nanoparticles in grain sizes, increase the width of the forbidden band of the semiconductor.
- Metals are exposed to corrosion and polymer substrates require synthesis conditions at low temperatures. The covering of metals using anti-corrosive materials is a track for the use of flexible DSSCs.

Polymeric substrates have the advantage of being flexible but their performance in DSSCs is lower.

2.9 Conclusion

This literature review highlights the influence of ZnO doping on its band gap, resistivity, and topography. The semiconductor band gap increases with the presence of dopant while its resistivity decreases. The crystallite size, porosity and morphology are also modified in the presence of additives in the ZnO.

The materials generally used in the manufacture of ZnO-based DSSCs reaching maximum efficiency (4 to 7.5%) are:

- Platinum, metal more used at the cathode because it has a high catalytic activity.
- The FTO, substrate (has a lower resistivity compared to ITO) compatible with the oxide semiconductor and the dye
- Additives or dopants of ZnO (to improve the performance of the anode)
- The N719 dye, more used for ZnO-based DSSCs, TiO_2, Nb_2O_5 and WO_3, because its HOMO and LUMO meet the requirements of energy levels to develop photovoltaic cells.

- The liquid mediator (I^-/I^-_3) is the most used with a higher yield in front of solid mediators.
- The Surlyn type separator

A review of the literature was also done on a few:

- Dopants, ZnO additives and their influences on the properties of ZnO and ZnO-based DSSCs.
- Oxide layers as a coating of ZnO which also have an influence on the solar cell.
- Electrode synthesis techniques for the manufacture of DSSCs based on doped ZnO.
- Performance limits and corrosion phenomenon were discussed for these types of DSSC. Solutions proposals have been suggested to improve the efficiency of DSSCs. The current densities of DSSCs based on ZnO are comparable to those of TiO_2, but lower filling factors, lower open circuit voltages and lower electrical conversion efficiency.

CHAPITRE 3 ASPECTS MÉTHODOLOGIQUES

Ce chapitre fixe les objectifs de la thèse et décrit les techniques d'élaboration des couches minces des échantillons d'oxyde de zinc (ZnO) et d'oxyde de zinc dopé, des matériaux d'électrodes assemblables en cellules solaires. La technique de synthèse par la voie sol-gel a été adoptée pour la synthèse de l'oxyde de zinc et de son dopage avec l'acide tungstique associée à des techniques de dépôts sur un substrat FTO. Les techniques de dépôts utilisés pour les électrodes sont : le doctor-blade et le spin-coating. Les électrodes ont été assemblées à l'aide de colorant N719 et de médiateur (couple redox I^-/I_3^-) soigneusement choisi.

3.1 Objectifs de la thèse

L'objectif principal est d'étudier l'effet de l'acide tungstique et des HPAs sur le ZnO comme matériau dopé et le comportement de la photo anode à base de ZnO dopé dans une cellule solaire photo sensibilisée.

Les objectifs spécifiques sont :

1) Élaborer le semi-conducteur intrinsèque ZnO et le semi-conducteur extrinsèque ZnO dopé par la méthode sol-gel;

2) Caractériser les semi-conducteurs fabriqués par la diffraction par rayons X, le microscope électronique à balayage, la spectroscopie UV-visible, la spectroscopie photoélectronique à rayons X, la spectroscopie par la transformée de Fourier;

3) Mettre en œuvre les matériaux d'électrodes de la cellule DSSC en vue de les assembler;

4) Mesurer les performances de la cellule solaire à base de ZnO dopé.

Les deux premiers objectifs spécifiques ont été atteints et décrits dans l'article traitant les propriétés de ZnO :H_2WO_4 au chapitre 5. Les deux derniers objectifs ont été atteints et matérialisés dans l'article présentant des DSSC-ZnO-H_2WO_4 chapitre 6.

3.2 Méthodologie d'élaboration des semi-conducteurs ZnO et ZnO dopé

Plusieurs méthodes de synthèse de ZnO et de ZnO dopé existent et ont été abordées dans l'article intitulé revue de la littérature sur ZnO (cf. chapitre 2), ses méthodologies de fabrications, ses

propriétés et applications dans les cellules solaires photovoltaïques. Dans le cadre de cette thèse, pour synthétiser le ZnO ou effectuer son dopage, la méthode sol-gel a été adoptée à cause de ses avantages technologiques. La méthode sol-gel a des avantages suivants : le contrôle de la composition du semi-conducteur synthétisé, la faible température d'opération (proche de la température ambiante), la possibilité de revêtement de grande surface du substrat avec le semi-conducteur, une bonne pureté du produit obtenu, une bonne homogénéité de la solution des précurseurs, un faible coût des équipements. En effet, Znaidi (Znaidi, 2010) a évoqué les paramètres clés jouant un rôle dans l'évolution de la texture des films d'oxyde de zinc. Il s'agit :

1. La nature du précurseur et sa concentration;
2. Le type de solvant et l'acidité du milieu de synthèse;
3. Le type d'espèces additives et leurs concentrations;
4. Le temps de vieillissement du mélange initial;
5. La technique d'enduction du substrat à une vitesse donnée;
6. La nature du substrat;
7. La température de séchage (traitement pré-chauffage) et le recuit (traitement post-chauffage).

Sol-gel ou solution-gélification est un procédé chimique en milieu liquide de dépôt des couches minces (Kamaruddin et al., 2010). La méthode sol- gel requiert 4 étapes fondamentales qui sont: l'hydrolyse (mélange d'un précurseur avec son solvant), la condensation, la gélification et le séchage. La Figure 3.1 est une illustration de ses paramètres à travers 3 différentes étapes :

1. La préparation du précurseur (dissolution);
2. Le dépôt de la solution obtenue (sol) par une technique de dépôt choisi (spin-coating, dip-coating) ou la condensation (gélification) et évaporation;
3. Le traitement thermique ou film xérogel.

On appelle xérogel le gel séché à pression ambiante et l'aérogel le gel séché dans les conditions supercritiques.

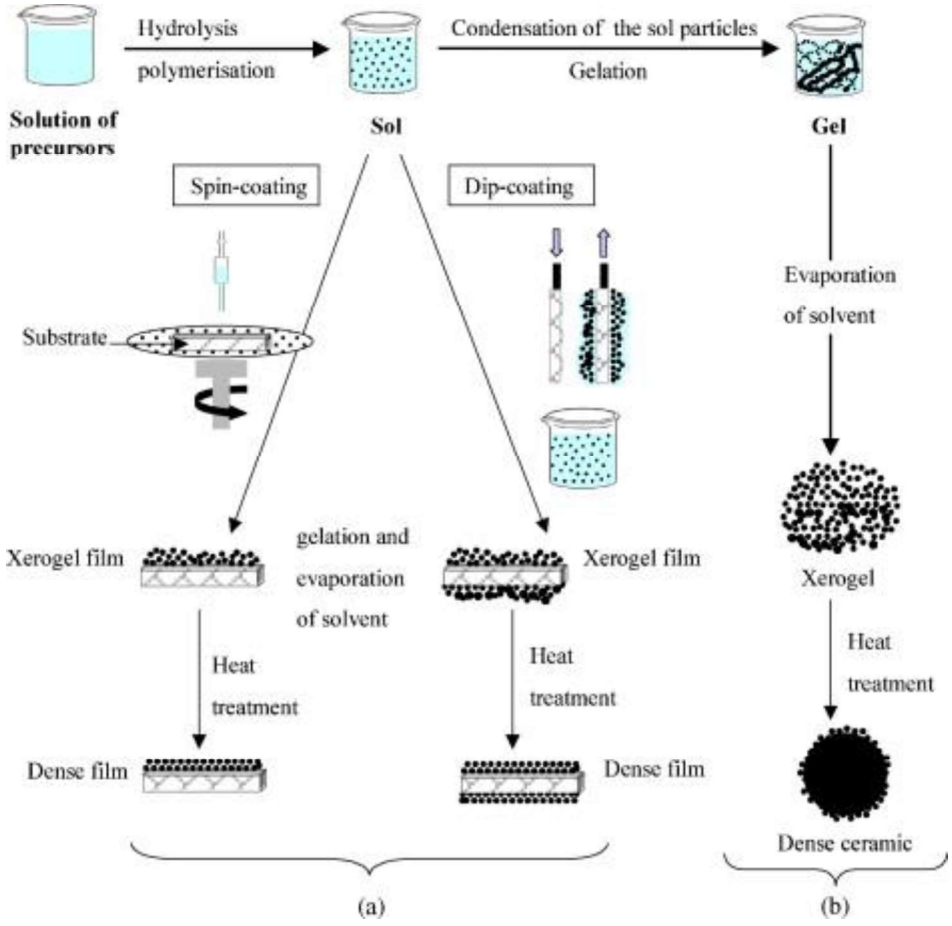

Figure 3.1: Représentation de la synthèse sol-gel à partir d'un sol colloïdal menant à une couche mince (a) ou un gel transformé en céramique dense (b). (Znaidi, 2010)

En général les mécanismes réactionnels de synthèse dans une méthode sol-gel peuvent se résumer par les réactions suivantes :

M-OR + H_2O ⟶ M-OH + ROH (Hydrolyse)

M-OR + HO-M ⟶ M-O-M + R-OH (Condensation de l'alcool)

M-OH + HO-M ⟶ M-O-M + H_2O (Condensation de l'eau ; gélification)

Au cours de l'hydrolyse, les groupes alcoolates (-OR) sont replacés via l'attaque nucléophile de l'atome d'oxygène d'une molécule d'eau, ce qui entraine la libération de l'alcool et la formation d'hydroxyle de métal (sol).

Au cours de la condensation, une réaction entre les deux espèces métalliques hydroxyle/alcoxy conduit à des liaisons M-O-M avec libération de H_2O/R-OH. Ce processus de condensation se

poursuit et aboutit finalement à un gel, un réseau inorganique rigide et poreux, recouvert entièrement de phase liquide. Cette transformation est appelée transition sol-gel.

Le séchage consiste à éliminer la phase liquide du réseau gel. Si la phase liquide est éliminée dans les conditions ambiantes, le produit obtenu est du xérogel. Mais si la phase liquide est éliminée sous condition hypercritique sans détruire le réseau, le produit obtenu est un aérogel.

En utilisant le précurseur acétate de zinc dihydraté pour la synthèse de l'oxyde de zinc, les mécanismes réactionnels pour la formation de l'oxyde de zinc sont :

$$Zn(CH_3COO)_2\ 2H_2O+H_2O \rightarrow\ HO\text{-}Zn\text{-}(CH_3COO) + 2H_2O+ CH_3COOH \text{ (hydrolyse)}$$

$$HO\text{-}Zn\text{-}(CH_3COO) + H_2O \rightarrow Zn(OH)_2 + CH_3COOH \text{ (condensation de l'alcool)}$$

$$Zn(OH)_2 \rightarrow ZnO+H_2O \text{ (gélification)}$$

La méthodologie adoptée peut être décrite par la synthèse de ZnO/ZnO dopés par la méthode sol-gel combinés aux techniques de dépôts des couches minces sur un substrat. À travers cette méthode nous avons synthétisé ZnO et ZnO dopé de deux manières en s'inspirant de la méthode décrite par :

- Foo et al. (Foo et al., 2014), nous avons effectué les synthèses des échantillons à partir du précurseur acétate de zinc dihydraté (tel que décrits dans l'article 1 sur les propriétés de ZnO dopé). La technique de dépôt sur le FTO de la solution gélifiée est le spin coating (tel que décrit dans les articles 1,2 et 3) avec une vitesse de 3000 rpm.
- Hasnidawani et al. (Hasnidawani et al., 2016), nous avons effectué la synthèse des poudres de ZnO et de ZnO dopés à partir du précurseur acétate de zinc dihydraté (tel que décrit dans l'article 2 sur les DSSC). Les poudres ont été transformées en pâte par mélange avec de l'éthanol et liants (ethyl cellulose, terpineol) (Seigo Ito et al., 2007; J. Li et al., 2013). La pâte a été déposée par la technique doctor blade (article 2 et review) sur le FTO.

3.3 Techniques de dépôts des couches minces

Les produits synthétisés ont été déposé sur un substrat appelé FTO ou oxyde d'étain dopé au fluor. Le FTO a été choisi comme substrat à cause de ses bonnes propriétés thermoélectriques (température de sublimation 1500°C et 7 Ω/cm^2 comme *sheet resistance*) favorables aux opérations de synthèse sol-gel. À l'aide du logiciel Factsage, nous avons simulé et présenté dans l'article le

comportement stable de l'oxyde d'étain lorsqu'il est chauffé de la température ambiante à 1000 K. Les techniques de dépôts expérimentées sont : le spin-coating, le doctor blade et le dip-coating.

3.3.1 Le spin-coating

C'est une technique simple et relativement peu couteuse largement sollicitée pour réaliser les couches dans l'industrie mico-électronique, ou dans les laboratoires. Son principe est basé sur l'utilisation d'une force centripète pour répartir uniformément une solution appliquée sur un substrat. Le spin-coating peut-être décrit en 4 étapes (Figure 3.2):

i. Le dépôt de la solution sur le substrat FTO qui est fixé au préalable à l'aide d'un aspirateur;
ii. La mise en mouvement par une accélération (*spin on*) du système substrat-solution jusqu'à atteindre une vitesse de consigne de sorte que la solution appliquée s'étale uniformément sur le substrat.
iii. L'ensemble (substrat-solution) tourne durant un temps fixé permettant un revêtement et un amincissement de la couche mince déposée (*spin off*).
iv. Le solvant est évaporé de la couche mince par séchage. Cette évaporation entraine un amincissement supplémentaire de la couche mince déposée.

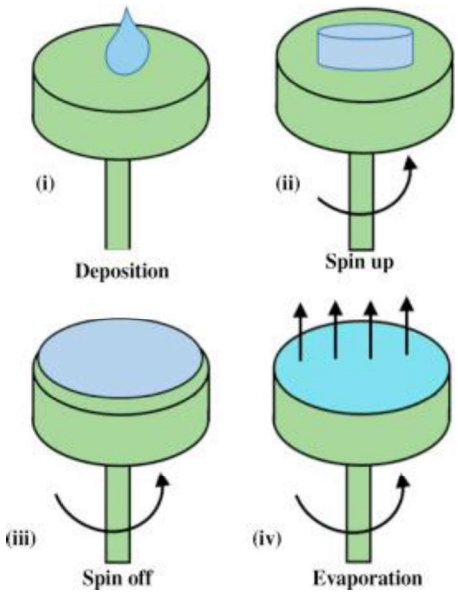

Figure 3.2: Les étapes de dépôt par spin coating (Yilbas et al., 2019)

Pour obtenir plusieurs couches minces superposées, on répète les 4 étapes.

L'épaisseur de la couche mince déposée est contrôlée par :

- la vitesse de rotation de l'ensemble. Pour obtenir une couche mince uniforme, une gamme de vitesse élevée entre 1000-8000 rpm (A. Kumar & Nanda, 2019) est recommandée ;
- l'accélération de l'appareil spinner ou spin-coater ;
- le temps de rotation ;
- la volatilité du solvant lors de l'opération ;
- la viscosité de la solution ;
- la masse molaire des composants dans la solution ;
- L'environnement (air, humidité, température, pression) qui pourrait interagir sur le système fluide-substrat en mouvement.

Plusieurs modèles mathématiques[4] ont été mis au point pour décrire l'épaisseur d'une couche déposée par spin-coating en fonction des paramètres de contrôle d'épaisseur mais en général, cette épaisseur est inversement proportionnelle à la vitesse angulaire du système substrat-fluide, au temps d'opération et à la densité du fluide. Aussi, nous pouvons dire que le fluide est soumis aux forces : centripète (rotation), visqueuse, capillaire (fluide-air), d'évaporation et à la relation fondamentale de la dynamique. En négligeant les effets d'évaporation pour un fluide visqueux sur un disque infini, Emslie, Bonner et Peck ont établi le modèle le suivant :

$$\frac{\partial e}{\partial t} + \frac{\rho \omega^2 r}{\eta} e^2 \frac{\partial e}{\partial r} = \frac{-2\rho\omega^2 e^3}{3\eta} \qquad (3.1)$$

t : temps de l'opération ; ω : vitesse angulaire ; r :distance à partir du centre rotation ; ρ : densité ; η : viscosité ; e : épaisseur de la couche du fluide ; $\frac{\partial e}{\partial t}$: variation de l'épaisseur dans le temps; $\frac{\partial e}{\partial r}$: variation de l'épaisseur dans l'espace.

[4]Sources : DOI: 10.1063/1.1723300; DOI: 10.1039/b408857n

Si initialement la couche déposée est uniforme, la solution à l'équation d'Emslie, Bonner et Peck est :

$$e = \frac{e_0}{\left(1 + \frac{4\rho\omega^2 e_0^2 t}{3\eta}\right)^{\frac{1}{2}}} \qquad (3.2)$$

e_o : représente l'épaisseur uniforme de la couche à l'instant initial t=0 (au départ du processus).

Cette dernière expression montre que l'épaisseur déposée est inversement proportionnelle à la vitesse de rotation angulaire, au temps de rotation et à la densité de la solution. En revanche, l'épaisseur déposée est proportionnelle à la viscosité.

3.3.2 Doctor Blade

Le principe repose sur une lame (*blade*) en mouvement au-dessus d'un substrat qui étale une pâte visqueuse de façon horizontale et uniforme (Figure 3.3 (a)). L'équipement est constitué de 3 parties principales:

- Un dispositif lame raclette réglable;
- Un moteur à courant pour la mise en mouvement rectiligne uniforme de la raclette;
- Un support pour fixer le substrat.

Le dispositif lame raclette est constitué de :

- Un micromètre manuel ou digital pour régler l'écart entre la raclette et le substrat.
- Un port d'injection du fluide à déposer pour une opération automatique. Pour un équipement doctor blade semi-automatique ou manuel, l'injection du fluide à déposer s'effectue manuellement;
- Une fente où est fixée la raclette;

L'épaisseur de la couche déposée est fixée par l'écart entre le substrat et le bord de la lame. La lame est dotée d'un dispositif de réglage de hauteur et d'injection de la pâte visqueuse (Figure 3.3 (b)). La lame est mise en mouvement rectiligne uniforme par rapport au substrat à l'aide d'un moteur à courant continu

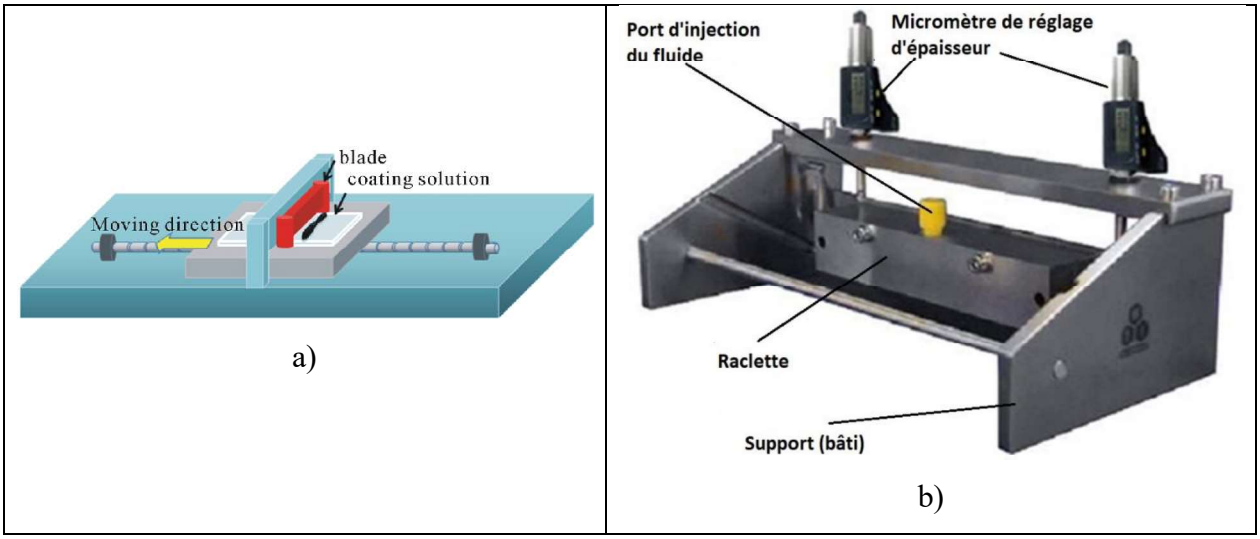

Figure 3.3: a) Mode d'opération de la technique doctor blade (K.-R. Chen et al., 2013), b) Lame avec son dispositif de réglage de hauteur et d'injection de la pâte visqueuse (Corporation & group, 1994-2022).

La procédure de mise en œuvre du dépôt passe par 4 étapes décrites par la Figure 3.4:

- Le choix et la préparation (lavage, rinçage et séchage) du substrat qui est une surface conductive (tel que le FTO);
- La délimitation de la surface active de ses bordures par des rubans,
- Le dépôt de la pâte sur la surface active,
- L'étalement horizontal de la pâte en couche mince.

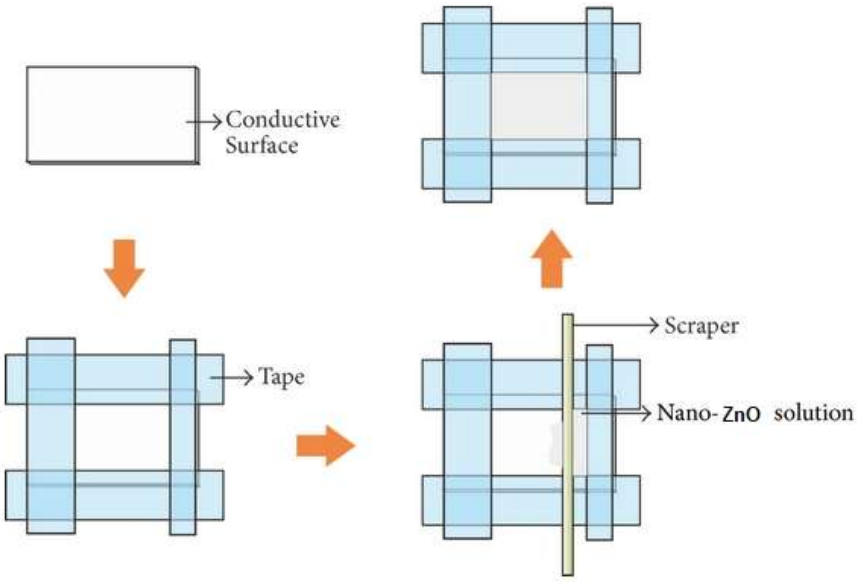

Figure 3.4 : Étapes de dépôt de semi-conducteur (ZnO/ZnO dopé) sur le substrat conducteur (FTO) (inspiré de Chen (C.-C. Chen & Ting, 2013))

Cette technique est adaptée pour des couches d'épaisseur supérieure ou égale à 1 micromètre et donc présente une précision des épaisseurs des couches minces d'ordre micromètre.

3.4 Méthodologie d'élaboration des électrodes et assemblage de la DSSC

La méthodologie adoptée peut être décrite par la synthèse de ZnO/ZnO dopés, les techniques de dépôts des couches minces sur un substrat, la technique d'assemblage des cellules DSSC et les techniques de caractérisations. Les échantillons de ZnO/ZnO :H_2WO_4 obtenus après recuits ont été immergés dans une solution de colorant N719. L'analyse de ces échantillons à la spectroscopie UV-visible a permis de prouver leur possibilité d'exploitation comme photoanode dans une DSSC. L'assemblage manuel de la photoanode avec une contre électrode en platine et un électrolyte iodolyte (I^-/I_3^-) en une cellule DSSC a été décrit par l'article abordant les DSSC à base de ZnO dopé au H_2WO_4.

Après avoir élaboré les matériaux et les cellules solaires DSSC, nous avons procédé à l'analyse de ces matériaux par des caractérisations pour étudier leurs propriétés structurales, chimiques, optiques et électriques. Chaque technique présente ses avantages et inconvénients c'est pourquoi nous en avons choisi plusieurs pour mieux élucider les propriétés de nos matériaux élaborés.

Nous consacrons le chapitre suivant aux techniques de caractérisations utilisées dans cette thèse.

CHAPITRE 4 TECHNIQUES DE CARACTÉRISATIONS

Les échantillons obtenus ont été recuits à 450°C et soumis à des analyses physico-chimiques appelées caractérisations. Les principales techniques de caractérisations des matériaux utilisées dans ces travaux sont: la diffraction des rayons X (XRD), la microscopie électronique à balayage (ou MEB), la spectroscopie à dispersion d'énergie (EDS), la spectroscopie UV-visible, la spectroscopie photoélectronique à rayons X ou XPS, la spectroscopie par la transformée de Fourier, la conductimétrie, la profilométrie. Ensuite, les performances des cellules DSSC ont été présentées grâce aux mesures courant-tension effectuée dans les conditions standard de test (STC). Ce chapitre vise à établir une corrélation entre les expérimentations, les résultats obtenus dans les articles et les techniques de caractérisations adoptées. Pour chaque technique de caractérisation, les lois fondamentales qui sont à la base de l'analyse et le principe de fonctionnement de l'appareil sont abordés.

4.1 La spectroscopie UV-visible

La spectrophotométrie UV-visible étudie l'interaction entre la matière et le photon dans le domaine de longueur d'onde :

- 400-750 nm dans le visible ;
- 100-400 nm dans l'ultra-violet (UV).

La Figure 4.1 est une illustration du spectre électromagnétique détaillé en longueur d'onde, d'énergie et d'interactions possibles pour :

- ultra-violet dans les domaines lointains(UV lointain) et proches (UV proche) ;
- le visible ;
- l'infrarouge dans les domaines moyen (IR proche) et lointain (IR lointain).

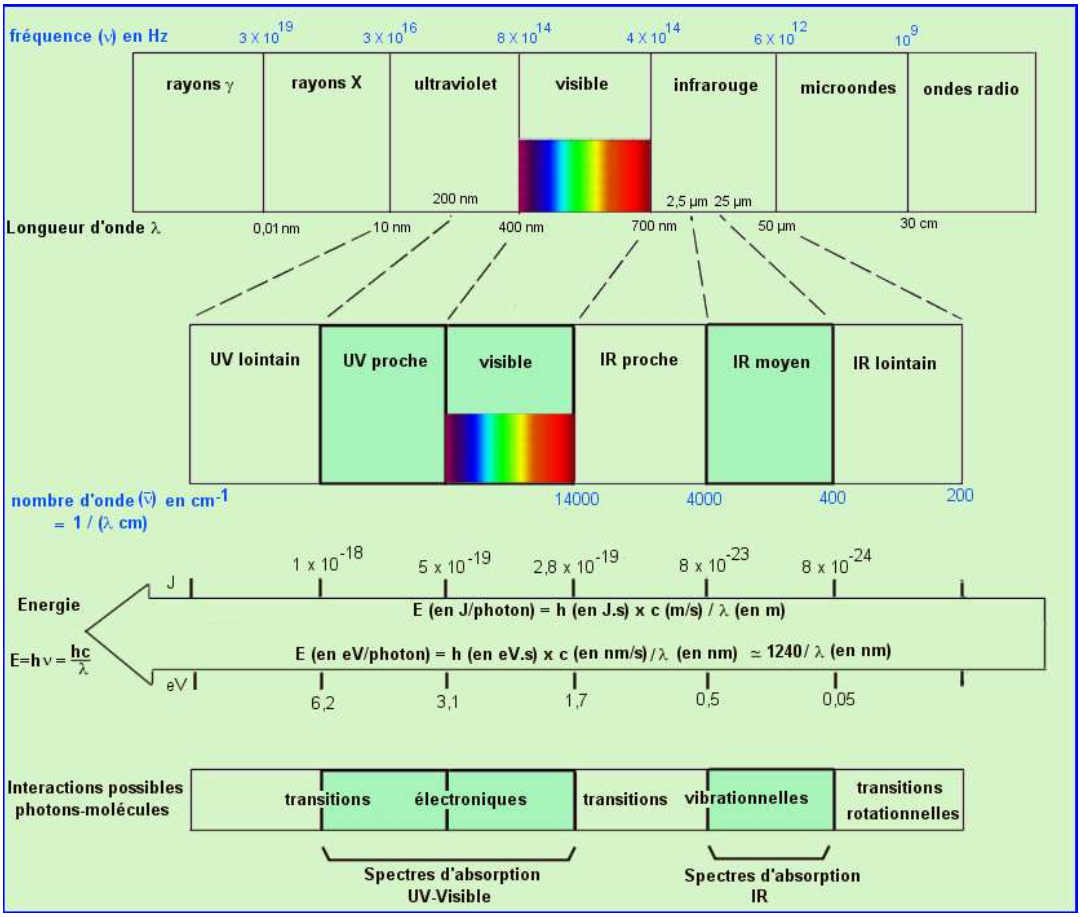

Figure 4.1: Spectre électromagnétique intégrant UV-visible[5].

L'objectif visé à travers cette méthode est d'analyser les propriétés optiques des échantillons, à savoir :

- La mesure de la transmittance, réflectance et absorbance ;
- Calcul de la bande interdite des semi-conducteurs.

C'est une technique d'analyse qualitative et quantitative, non-destructive, rapide et fiable utilisée pour caractériser des couches minces semi-conductrices.

[5] http://jean-jacques.auclair.pagesperso-orange.fr/ftirUV/spectre_electro.htm, consulté le 5 Novembre 2021

Considérons un atome caractérisé par 2 niveaux énergétiques quantifiées E_1 et E_2 ($E_1<E_2$) illustré dans la Figure 4.2 (a). L'absorption d'une radiation de longueur λ dans le domaine de l'UV-visible par une molécule s'accompagne d'excitations des électrons de la bande de valence (Figure 4.2 (b)). Dans un semi-conducteur, si l'énergie absorbée est supérieure ou égale à l'énergie de la bande interdite, il y aura injection des électrons de bande de valence vers la bande de conduction selon la théorie de Bohr :

$$\Delta E = h\nu = \frac{h \cdot c}{\lambda} = h\bar{\nu} \qquad (4.1)$$

h : constante de Planck ($6{,}63\ 10^{-34}$ J.s) ;

υ : fréquence de radiation en hertz (Hz) ;

λ : longueur d'onde de la radiation monochromatique en nm ;

$\bar{\nu}$: nombre d'onde.

Selon la loi de Bohr, l'énergie électromagnétique est d'autant plus grande que sa longueur d'onde est faible. L'énergie minimale du photon capable de provoquer cette transition est le seuil d'absorption optique. Ce seuil d'absorption de l'énergie correspond à l'énergie de la bande interdite Eg qu'il faudrait vaincre pour que les électrons quittent de la bande de valence vers la bande de conduction.

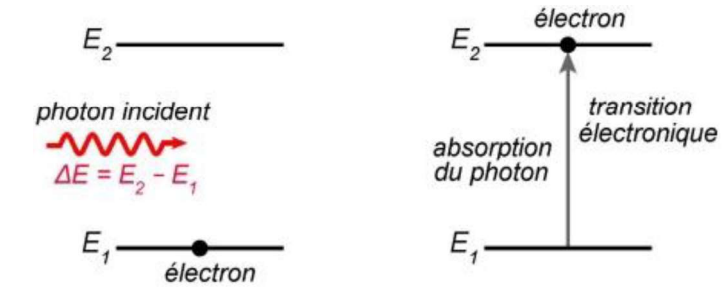

Figure 4.2: Transition (b) électronique d'un électron par suite d'absorption (a) de photon entre deux niveaux d'énergie.[6]

La description de l'absorption des photons dans un semi-conducteur est un phénomène quantique qui implique la structure de bande de ce semi-conducteur. L'oxyde de zinc est un matériau à bande directe (Norton et al., 2004). Pour une structure à bande directe (Figure 4.3 (a)), la transition optique d'un électron de valence occupant l'état 1 vers l'état 2 de la bande de conduction requiert la conservation de l'énergie et du vecteur d'onde :

$$E_1 + h\nu = E_2 \qquad (4.2)$$

$$k_1 + 2\pi/\lambda = k_2 \qquad (4.3)$$

Le vecteur d'onde du photon est petit devant celui des électrons ; donc $k_1 \approx k_2$ et la transition optique est verticale ou directe.

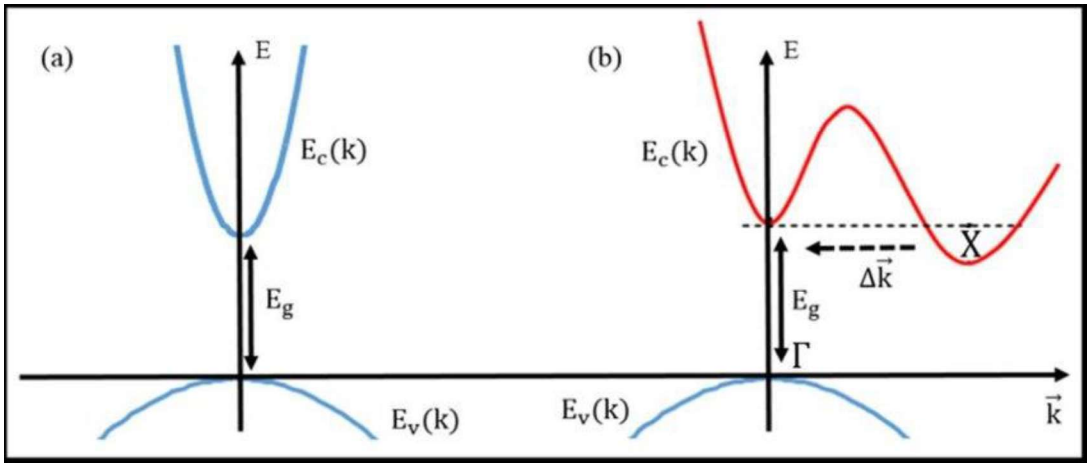

Figure 4.3: (a) Structure de bande directe où la transition de l'électron est directe de la bande valence vers la bande de conduction. (b) structure de bande indirecte où la recombinaison (et la transition) d'un électron en X (courbe rouge) et d'un trou (courbe en bleu) doit nécessairement se faire par l'intermédiaire d'un phonon afin de conserver le moment cristallin du réseau. (Mehdi, 2019)

[6] https://www.maxicours.com/se/cours/emission-et-absorption-quantiques/, consulté le 5 Novembre 2021

Près du seuil d'absorption, la loi de variation du coefficient d'absorption avec l'énergie des photons est de la forme :

$$\alpha h\nu = B\left(h\nu - E_g\right)^{1/2} \qquad (4.4)$$

α : coefficient d'absorption ;

h : constante de Planck ;

υ : fréquence de rayonnement incident ;

B : constante proportionnel

Cette relation est généralisée sous la loi de Tauc :

$$\alpha h\nu = B\left(h\nu - E_g\right)^{n} \qquad (4.5)$$

n : l'indice dépendant du type de transition de l'échantillon. n prend les valeurs ½ pour une transition directe, 2 pour une transition indirecte.

Les données détectées par les détecteurs, traitées et enregistrées en spectroscopie UV-Visible sont les phénomènes d'absorption, de transmittance ou de réflectance dans l'échantillon semi-conducteur.

Transmittance, réflectance et absorbance

Les échantillons mesurés sont transparents : FTO déposé sur verre (verre-FTO ou substrat), la couche mince de ZnO déposé sur le substrat (verre-FTO-ZnO), la couche mince de ZnO dopé déposé sur le substrat, la couche mince de H_2WO_4 déposé sur le substrat. Ces différents échantillons sont soumis aux rayons lumineux dans le domaine UV-visible (cf. Figure 4.4) correspondant au spectre solaire.

Les mesures de réflectance et de transmittance ont été effectuées à l'aide du spectrophotomètre Lambda 1050. L'absorbance, la transmittance et la réflectance sont calculées par la formule (4.6):

$$1=T+A+R \text{ ou } A=1-(T+R) \qquad (4.6)$$

où A désigne l'absorbance ; R : réflectance ; T : transmittance.

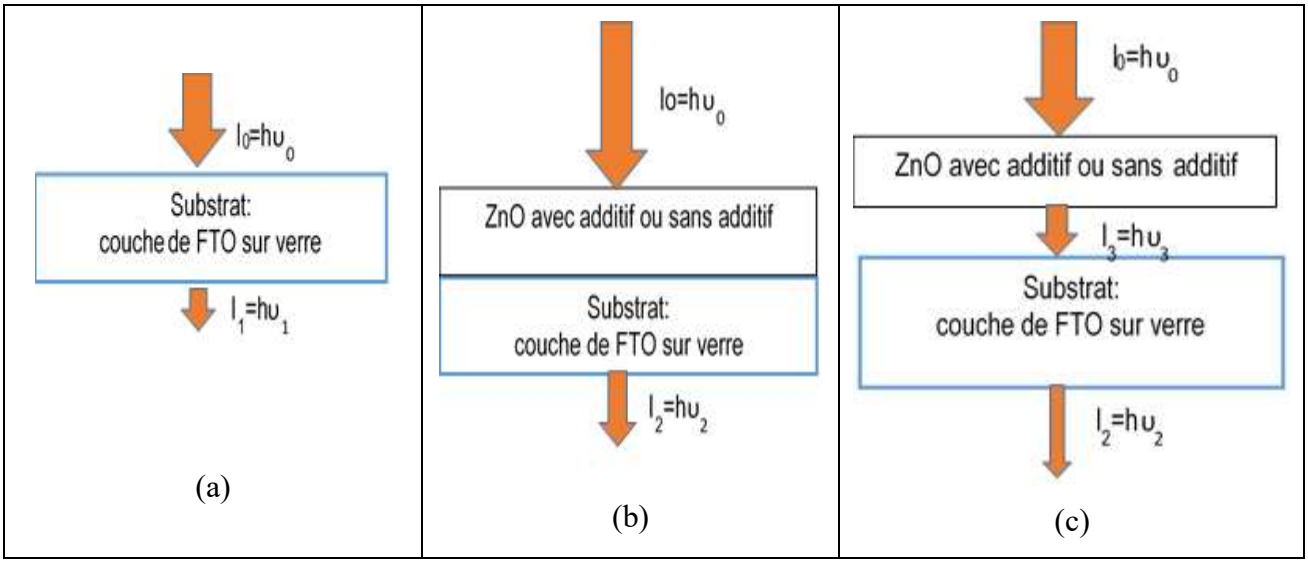

Figure 4.4: Illustration des intensités des faisceaux lumineux incidents et transmis dans le substrat (a) et les échantillons (b), (c).

La transmittance du substrat est :

$$T_{Subtrat} = \frac{I_1}{I_0} \qquad (4.7)$$

I_0 : lumière monochromatique incidente;

I_1 : intensité lumineuse transmise par le substrat.

La transmittance de l'échantillon est :

$$T_{échantillon} = \frac{I_2}{I_0} \qquad (4.8)$$

En considérant que la couche de ZnO transmet un faisceau I_3 qui arrive sur le substrat, l'expression de la transmittance devient :

$$T_{échantillon} = \frac{I_2}{I_3} \bullet \frac{I_3}{I_0} \qquad (4.9)$$

La transmittance du substrat est égale à :

$$T_{Subtrat} = \frac{I_2}{I_3} = \frac{I_1}{I_0} \qquad (4.10)$$

La transmittance de la couche mince de ZnO/ZnO+additif est :

$$T_{ZnO} = \frac{I_3}{I_0} \qquad (4.11)$$

Finalement :

$$T_{ZnO} = \frac{T_{échantillon}}{T_{substrat}} \qquad (4.12)$$

L'absorbance de ZnO est obtenue en appliquant le logarithme à base 10.

$$A_{ZnO} = -\log(T_{ZnO}) \qquad (4.13)$$

$$A_{ZnO} = A_{échantillon} - A_{substrat} \qquad (4.14)$$

Ces résultats TznO et AznO différencient clairement l'intensité transmise par le dépôt ZnO et celle transmise par l'échantillon préparé FTO-ZnO. Pour obtenir la transmittance propre au dépôt de ZnO ou ZnO dopé, il faut diviser la transmittance de l'échantillon par celle du substrat. De même pour obtenir l'absorbance propre au dépôt ZnO ou ZnO dopé, il faut faire la différence entre l'absorbance de l'échantillon préparé et l'absorbance du substrat.

Le spectrophotomètre est constitué d'une source de lumière, un monochromateur, un porte-échantillon et d'un détecteur.

La source de lumière est émise par une combinaison de deux types lampes dont une lampe à :

- deutérium ou hydrogène émettant des rayonnements lumineux entre 100 nm et 360 nm;
- tungstène dans une atmosphère halogène (lampe à iode) émettant des rayonnements entre 350 nm et 800nm.

La lumière émise de la source arrive sur le monochromateur qui sélectionne la longueur d'onde requise à sa sortie.

Un monochromateur est constitué :

- d'une fente d'entrée pour un fin faisceau polychromatique provenant des lampes (source de lumière) ;

- d'un prisme ou système dispersif de type réseau capable de séparer les rayonnements de différentes longueurs d'onde en un faisceau monochromatique ;
- d'une fente de sortie dotée d'une motorisation qui assure sa mobilité pour sélectionner le faisceau monochromatique. La motorisation de la fente de sortie se justifie par le fait que le faisceau monochromatique issu du prisme est réfracté et donc dévié par rapport à son angle d'incidence.

Pour un spectrophotomètre mono-faisceau, l'onde monochromatique arrive directement sur l'échantillon et se décompose en transmittance, réflectance et absorbance.

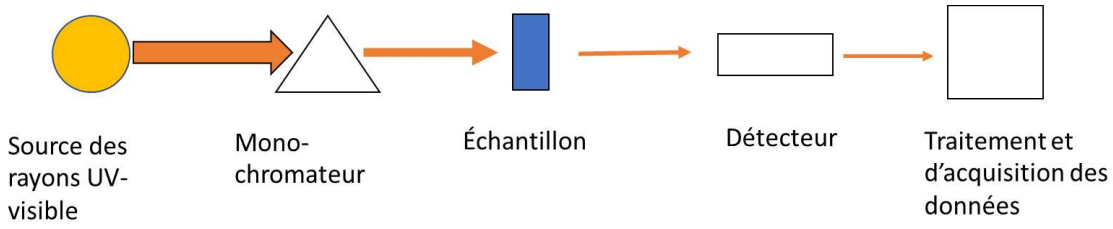

Figure 4.5: Schéma spectrophotomètre de mono-faisceau

Dans notre cas de mesure, le faisceau lumineux de longueur d'onde sélectionné provenant d'un monochromateur est divisé en deux faisceaux identiques par un diviseur de faisceau. L'un arrive sur l'échantillon et l'autre sur une référence. L'absorbance, la transmittance ou la réflectance de l'échantillon sont mesurées par comparaison à celle de la référence à l'aide d'un photodétecteur de type InGaS (cf. démonstration formule A_{ZnO} et T_{ZnO} ci-dessus). D'autres technologies utilisent des photomultiplicateurs (PMT), photodétecteurs type PbS.

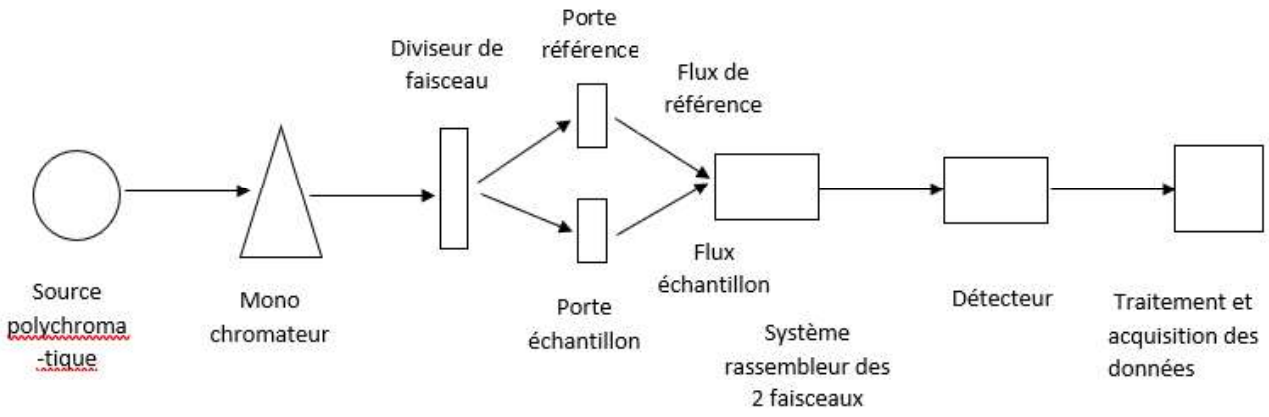

Figure 4.6: Schéma de principe du spectrophotomètre bifaisceau

Le détecteur fonctionne par effet photoélectrique. Les rayons lumineux qui arrivent sur le détecteur génère des paires électrons-trous qui sont détectées et converties sous forme de tension ou de courant. Le signal détecté est amplifié, traité et affiché.

Le spectrophotomètre utilisé est un PerkinElmer LAMBDA 1050 UV/Vis/NIR. C'est un spectrophotomètre bi-faisceaux destiné à analyser des couches ou revêtements de matériau, des matériaux en verre, des semiconducteurs et des matériaux en recherches, développement et industrie. PerkinElmer LAMBDA 1050 UV/Vis/NIR est piloté par un logiciel PerkinElmer. Ce logiciel permet d'effectuer le domaine d'opération, les choix des sources de lumières et l'acquisition de l'absorbance, la réflectance ou la transmittance.

Pour effectuer les mesures, le spectrophotomètre est démarré 15 minutes à l'avance pour stabiliser la source de la lumière. Ensuite, le logiciel PerkinElmer est ouvert sur l'ordinateur et on fait l'autozéro en ne plaçant aucun échantillon au niveau du porte échantillon et du porte référence ou en plaçant un même substrat (FTO) dans les deux porte essais. L'autozéro permet d'équilibrer les deux flux incidents qui arrivent sur la porte référence et la porte échantillon par comparaison des deux flux sortants de ces portes essais. Le rapport des deux flux sortants devrait donner l'unité ou ajuster à l'unité ou encore consigné comme flux de référence dans l'acquisition et le traitement des données. L'appareil de mesure est doté d'une sphère d'intégration ayant l'avantage de comparer la différence entre le flux de l'échantillon et le flux de référence. Une fois terminé cet équilibrage de flux lumineux, on insère l'échantillon dans le porte échantillon et commence les mesures des transmittances, absorbances et réflectance. Étant donné que les mesures ont été effectuées à température ambiante, la limite spectrale a été fixée à 200 nm afin d'éviter tout dérèglement causé par l'absorption d'oxygène. La limite supérieure de mesure est fixée à 1100 nm. Toutefois les domaines d'absorptions correspondant à la bande interdite de ZnO et des échantillons étudiés sont situés à l'intérieur de 300 nm à 750 nm.

Le choix porté sur cet équipement se justifie par ces caractéristiques (domaine de longueurs d'onde) et ses hautes performances qui répondent aux exigences que nous voudrions mesurer (Tableau 4.1).

Tableau 4.1: Récapitulatif des composantes dans un spectrophotomètre

Rayonnement	λ(nm)	Sources lumineuses	Transition électronique	E=hυ (eV)	Détecteurs
UV	100-400	Lampe à hydrogène ou à deutérium	Eg	6,2 à 3,1 eV	Photodétecteur PMT* InGaAs PbS
Visible	400-800	Lampe à incandescence tugnstène ou halogène tugnstène	Eg	3,1 à 1,55 eV	
Infra-rouge	800-10^6	Lampe à incandescence aux oxydes de zirconium et de terres rares	Transition vibrationnelles et rotationnelles	1,55 à 1,24 10^{-3} eV	

*PMT : photomultiplicateur

Les résultats sont présentés dans l'article 2 : **Structural and Optical Properties of Tungstic Acid-Doped Zinc Oxide for Semitransparent Dye Sensitized Solar Cell Applications.**

4.2 La diffraction des rayons X (XRD)

La diffraction des rayon X (ou simplement XRD acronyme anglais) vise à déterminer les phases cristallines d'un échantillon et la taille des cristallites. C'est une technique non-destructive d'investigation par diffraction des rayons X utilisée dès lors que l'échantillon est considéré comme cristallin. La technique se fonde sur les interactions de la structure cristalline d'un échantillon avec des rayons X.

Un cristal est un empilement d'atomes ou de molécules ordonnés, périodiques organisés en motif dans une maille élémentaire. La technique XRD est sollicitée aussi bien en industrie tout comme dans le domaine de recherche lorsqu'on a besoin de vérifier si le produit obtenu a une forme cristallographique désirée.

La découverte par des rayons X a été faite en 1895 par le physicien Allemand Röntgen. L'émission d'un rayon X est provoqué par un électron source (incident) qui arrive sur un autre électron dans

un atome (d'un métal) et l'éjecte de cet atome. À la suite de cette éjection, il y a une émission de rayon X.

L'analyse XRD se fait à l'aide d'un diffractomètre de rayons-X. Un diffractomètre de rayons-X est constitué de 4 grandes parties : un tube à rayons X, un porte-échantillon, un détecteur de rayons X et un goniomètre. Les diffractomètres utilisés dans cette étude sont de marque Bruker D8 ADVANCE et Philipps X'perts constitués d'une chambre où est insérée un porte- échantillon. Le porte-échantillon est doté d'un support aspirant qui fixe l'échantillon sur le support. Le goniomètre est un appareil ou capteur servant à mesurer les angles.

Pour produire les rayons X, on chauffe électriquement un filament (le plus souvent en tungstène) qui émet des électrons qui sont accélérés sous haute tension (20-50 kV). Ces électrons vont frapper un métal (Mo, Cu, Co, Cr) à l'anode pour éjecter des électrons de la couche K de ce métal qui est refroidi à l'aide d'un liquide de refroidissement comme de l'eau. L'émission des électrons de la couche K produit des rayons X (K_α, K_β). Les rayons K_β sont filtrés à l'aide d'une feuille de métal de numéro atomique Z-1 par rapport au numéro atomique du métal à l'anode. La feuille de nickel a été utilisée pour filtrer le K_β du cuivre qui sont canalisés à travers une fenêtre de béryllium de 300 µm pour arriver sur l'échantillon. Pour le diffractomètre Bruker D8 ADVANCE, la source de rayon X est un dispositif constitué d'un filament de tungstène à la cathode et cuivre à l'anode. Le filament en W émet des rayons qui viennent sur le métal cuivre à l'anode. Le cuivre émet des raies de Kα de de valeur pondérée de 1,5418 angström qui frappent les échantillons à base de ZnO, les agents additifs et le FTO. La tension imposée est 40 kV et le courant est de 40 mA.

Un détecteur placé au-dessus de l'échantillon dans le diffractomètre détecte l'intensité lumineuse diffractée en fonction de l'angle de diffraction. Le détecteur est dans l'équipement est un détecteur rapide 1 D LynxEye. Le détecteur LynxEye est un détecteur unidimensionnel dispersif en énergie. Il filtre la fluorescence, le rayonnement K-bêta et élimine les pertes d'intensités.

Les données enregistrées sont sur un intervalle angulaire allant de 20 à 80° avec un pas de 0,02 °. L'appareil est utilisé en configuration Bragg-Brentano.

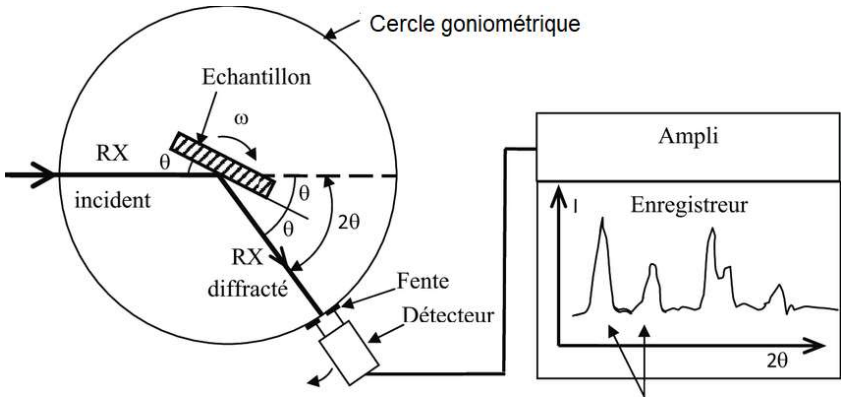

Figure 4.7: Configuration Bragg-Brentano (BROURI, 2011)

C'est le montage le plus courant pour des échantillons en plaquette solide ou dans une coupelle remplie de poudre avec un niveau plan. Deux types de configuration possibles : la configuration dite « θ-θ » («thêta-thêta ») et celle dite « θ-2θ » («thêta-deux-thêta »). Dans la configuration dite « θ-θ » («thêta-thêta ») l'échantillon est fixe et horizontal alors que le tube et le détecteur de rayon X se déplacent symétriquement à l'aide de 2 moteurs pour régler les angles d'incidences et de diffraction**.** L'angle entre l'horizontal et le faisceau incident est égal à l'angle entre l'horizontal et le détecteur; 2 θ est la déviation du faisceau.

Cette configuration est très peu utilisée au détriment de la configuration («thêta-deux-thêta » à cause de la masse importante du tube à rayons X. Et donc dans cette dernière configuration l'échantillon et le détecteur qui se déplacent à l'aide de 2 moteurs pour régler les angles d'incidences et de diffraction.

Lorsqu'un rayon X pénètre un matériau, plusieurs phénomènes peuvent se produire à savoir : l'absorption de ces rayons, la transmission des rayons X, la fluorescence ou émission des électrons secondaires lors de l'excitation du matériau par les rayons X, la diffusion avec possibilité de changement de direction ou d'énergie des rayons incidents. S'il n'y a pas de changement d'énergie, il s'agit d'une diffusion élastique ou diffusion Rayleigh. Dans le cas contraire, il s'agit d'une diffusion inélastique aussi appelée diffusion Compton. La diffusion de ces rayons dans les plans du réseau cristallins créent des interférences. On a alternativement des interférences constructives ou destructives.

Pour des interférences constructives, on observe des pics de diffraction pour lesquels Bragg a établi une relation entre la longueur d'onde (λ), l'angle d'incidence (θ_{hkl}), la distance interéticulaire (d_{hkl}) et l'ordre de diffraction (n) :

$$2d_{hkl}\sin\theta_{hkl} = n\lambda \qquad (4.15)$$

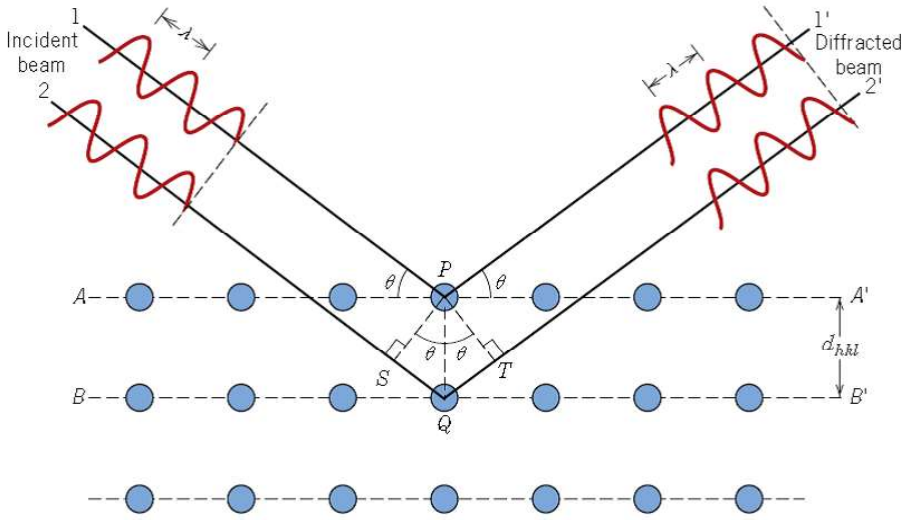

Figure 4.8: Faisceaux diffractés dans un plan [7]

(h,k,l) indice de Miller; n est un entier obtenu par balayage angulaire (2θ = 20°- 80° pour les échantillons à base de ZnO).

Les distances interatomiques entre les plans dans un réseau cristallin ou distances interréticulaires dépendent de la nature du matériau. On détermine la distance interréticulaire étant donné que pour un pic de diffraction les autres paramètres (λ, θ_{hkl}, n) sont connus. La distance interréticulaire (d) et les paramètres de maille dans un système hexagonal est donnée par la relation :

$$\frac{1}{d^2} = \frac{4}{3}\left(\frac{h^2 + hk + k^2}{a^2}\right) + \frac{l^2}{c^2} \qquad (4.16)$$

Avec a=b=0,325 nm; c=0,521 nm;

[7] DOI : 10.13140/RG.2.2.28647.70561; 2019 consulté 11 mars 2021

La relation entre l'angle Φ entre le plan (h_1, k_1, l_1) ayant une distance interréticulaire d_1, et le plan (h_2, k_2, l_2) ayant une distance interréticulaire d_2 est déterminée par l'expression :

$$\cos\Phi = \frac{h_1h_2 + k_1k_2 + \frac{1}{2}(h_1k_2 + h_2k_1) + \frac{3a^2}{4c^2}l_1l_2}{\sqrt{\left(h_1^2 + k_1^2 + h_1k_1 + \frac{3a^2}{4c^2}l_1^2\right)\left(h_2^2 + k_2^2 + h_2k_2 + \frac{3a^2}{4c^2}l_2^2\right)}} \qquad (4.17)$$

L'intensité des interférences diffusées dans une maille d'un cristal est donnée par le facteur de structure :

$$F(\theta) = \sum_i f_i e^{2\pi i(hxi+kyi+lzi)} \qquad (4.18)$$

(x,y,z) position d'un atome dans la maille. (h,k,l) indice de Miller; f_i : facteur de diffusion (diffraction) ou de forme atomique d'un atome dans une maille.

Les spectres obtenus après analyse sont indexés au spectre de l'échantillon pur référence JCPDS pour identifier les phases. Pour les cas des échantillons à base de ZnO/ZnO dopé et l'additif (acide tungstique) les résultats sont présentés dans l'article 1. Ces résultats montrent que le ZnO synthétisé une structure cristallographique hexagonal de type wurtzite (a=0.325nm, c=0.521nm) et de groupe d'espace P63mc.

La taille des cristaux est déterminée si la larguer à mi-hauteur est déterminée. La largeur a mi-hauteur ou en anglais *full width at half maximum* (FWHM) est comme « la différence entre les deux valeurs extrêmes de la variable indépendante pour lesquelles la variable dépendante est égale à la moitié de sa valeur maximale » (source : Federal Standard 1037C).

La taille du cristal (désigné par τ) est déterminée par mesure de l'élargissement du pic maximum XRD et en utilisant la formule de Scherrer :

$$\tau = \frac{180}{\pi}\frac{k\lambda}{\cos\theta\sqrt{FWHM^2 + s^2}} \qquad (4.19)$$

Avec : π=3,142; λ=1,5406 angstron: longueur d'onde de radiation de $CuK_{\alpha,}$ k=0,89 est la constante de Scherrer; s est la largeur instrumental (correspond à 0 pour Bruker Advanced X-ray solutions

D8 instrument); Θ=36°/2 angle correspondant au plan (101) ; FWHM=0,28° : est la pleine largeur au demi-plan (101).

La taille moyenne des cristallites s'exprime en nanomètre.

$$\tau = \frac{180}{\pi}\frac{k\lambda}{\cos\theta \times FWHM} = \frac{180 \times 0,89 \times 1,5406}{3,142 \times \cos(18° \times 3,142/180) \times 0,28} = 29,8 \text{ nm} \qquad (4.20)$$

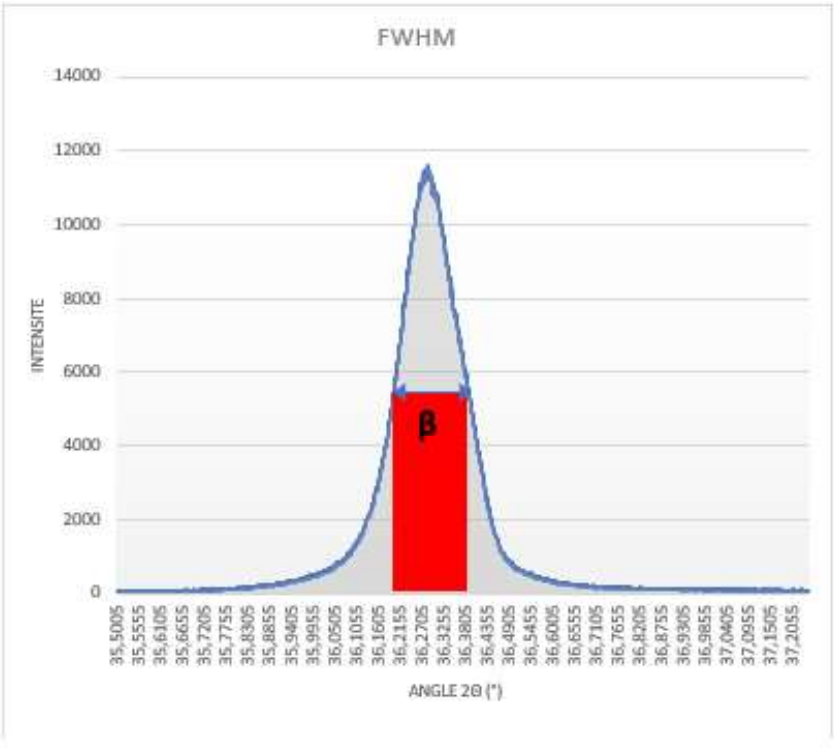

Figure 4.9: FWHM ou pleine largeur au demi-plan (101) poudre de ZnO

L'aire sous un pic est proportionnelle au nombre d'atomes détectés correspondant au plan de ce pic et à la densité du nuage électronique de l'atome. Cette analyse ouvre la possibilité d'une analyse quantitative de l'échantillon analysé.

L'appareil Bruker D8 Advance est équipé d'un logiciel EVA pour le traitement des données et une base de données JCPDS des spectres de références.

Les échantillons de ZnO et ZnO :H_2WO_4 synthétisés ont été analysés à l'aide du diffractomètre Philipps X'perts avec une anode en cuivre avec un détecteur linéaire de type X'Celerator couplé à monochromateur arrière à cristal graphite. Les pics de diffraction pour le ZnO sont présentés dans

les articles (2 et 3) et ces pics montrent bien une structure cristallographique hexagonale de type wurtzite (a=0.325nm, c=0.521nm) et de groupe d'espace P63mc.

4.3 La microscopie électronique à balayage (ou MEB)

Le MEB est un outil d'observation des surfaces des échantillons afin de les analyser (topographie et composition chimique). Le MEB est une technique d'investigation de la surface d'échantillons massifs avec pour principales caractéristiques :

- Une grande résolution spatiale objet de l'ordre de 1 nm;
- Des possibilités d'agrandissements continus, de x 10 à x 10^5 et plus;
- Une grande profondeur (d'ordre μm) de champ;
- Peu ou pas de préparation d'échantillon avant son insertion dans le prote-échantillon mais l'échantillon est placé sous vide et soumis à un bombardement électronique. Pour un échantillon de faible conductivité (ou isolant) son revêtement par un métal est nécessaire pour une analyse au MEB. Les métaux utilisés pour la métallisation de l'échantillon de faible conductivité sont : or, l'argent, le cuivre, aluminium, le platine, le carbone,…(BRISSET, 15 Janvier 2009); pour nos échantillons semi-conductrices, une petite couche de cuivre a été utilisée aux abords des couches minces déposées.
- La possibilité d'analyse chimique élémentaire.

Son fonctionnement peut se décrire à partir d'une source primaire d'électrons qui émet des faisceaux d'électrons. Les faisceaux d'électrons primaires sont émis d'un canon à électrons type : tungstène, FEG (*Field Emission Gun*), LaB6, W-ZrO (schottky) ou tungstène tunnel (BRISSET, 15 Janvier 2009). On chauffe électriquement un filament (par exemple en tungstène) qui émet des électrons qui sont accélérés sous haute tension (0,5-40 kV). Le faisceau d'électrons émis est mis en forme à l'aide des lentilles condensatrices et objectives et des diaphragmes avant d'arriver sur l'échantillon (voir Figure 4.10). Grâce aux bobines de balayage, les faisceaux d'électrons primaires balaient la surface de l'échantillon analysé. Les électrons rétrodiffusés et secondaires émis de l'échantillon sont détectés par des détecteurs, observés à l'aide de l'écran, analysés et interprétés par l'opérateur. L'écran a une taille et un facteur de grossissement de la zone de l'échantillon balayée par la sonde d'électrons primaires.

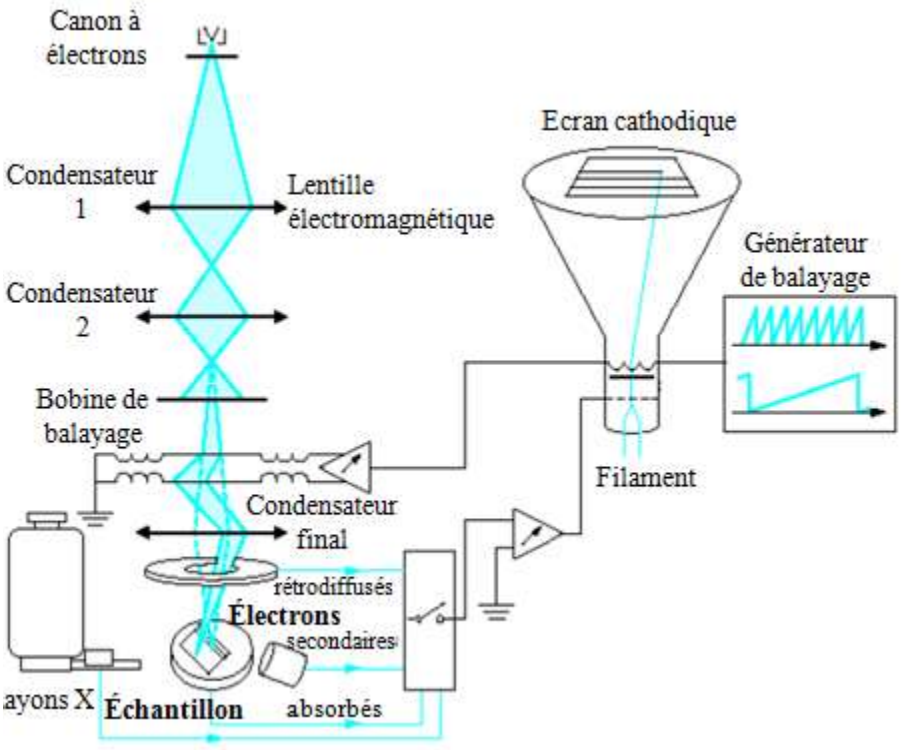

Figure 4.10: Schéma de microscope électronique à balayage (Jeaidi, 2017)

Les électrons secondaires sont des électrons issus des atomes ou des molécules de l'échantillon analysé (cible) par suite d'une interaction électrons primaires avec matière constituant la cible. En effet, l'interaction entre électrons incidents avec les électrons faiblement liés à la couche de valence ou de conduction des atomes cibles provoque une émission des électrons dits secondaires. L'observation en mode électrons secondaires donne les informations topographiques: morphologie. Selon les synthèses effectuées, nous avons obtenu des nano grains de ZnO et des nanotiges avec des dimensions variées observées selon les grossissements.

Les électrons rétrodiffusés sont des électrons incidents qui ressortent de l'échantillon avec une énergie inférieure aux électrons primaires. En effet lorsque les électrons incidents traversant les nuages électroniques des atomes du cible sans entrer en collisions avec aucune particule, ils subissent une déviation sous l'effet des charges électroniques. L'observation effectuée en mode électron rétrodiffusé a permis de visualiser les particules de l'acide tungstique dans une matrice de l'oxyde de zinc. Les contrastes chimiques ont été observés en fonction des numéros atomiques pour ce mode d'opération. La brillance est d'autant plus importante que le numéro atomique de l'élément chimique est important.

Le MEB de marque JEOL JSM-7600F (Field Emission Scanning Electron Microscope) a été utilisé pour observer les surfaces les échantillons à base de ZnO afin d'interpréter leur topographie et leur composition chimique. C'est un MEB à type d'électrons primaires FEG. La tension d'accélération des électrons a été fixée 10 kV et les grossissements des échantillons ont été de 35 000 fois et 220 000 fois des graines de particules.

Principe de formation de l'image

Les électrons primaires e_p de la sonde de diamètre d_{sonde} arrivent sur l'échantillon ayant une limite de résolution d_{objet} (Figure 4.10). L'interaction électrons-matière (ou électrons-échantillon) produit des électrons retrodiffusés et des électrons secondaires sous forme de signal i_s. Pour que ce signal i_s soit entièrement détecté par les détecteurs, le diamètre de la sonde d_{sonde} ne doit pas dépasser la limite de résolution de l'échantillon $d_{objet.}$

$$d_{sonde} \leq d_{objet} \qquad (4.21)$$

Le signal détecté est amplifié par un facteur de grossissement G=L/l et observable en image sur l'écran (Figure 4.10). Donc on a la relation :

$$d_{image} = d_{objet} \times G \qquad (4.22)$$

Pour un grossissement de 100 000 et une limite de résolution spatiale de 0,2 mm de l'image, le diamètre de la sonde ne doit pas dépasser 2 nm.

$$d_{sonde} \leq \frac{0,2mm}{100000} = 2nm \qquad (4.23)$$

En balayant l'étendu de l'échantillon à l'aide de la sonde, on obtient l'image de l'échantillon en mode électrons rétrodiffusés ou en mode électrons secondaires selon le choix du type de détecteur dans l'analyse. Les images des particules observées dans cette thèse sont à l'échelle d'ordre nanométrique (20-60 nm).

Les résultats des images des échantillons sont présentés dans les 3 articles aux chapitres (1,2 et 3) dans les deux modes d'observation : topographique et contraste chimique. Les limites de cette technique sont les risques d'artéfacts qui sont souvent source d'erreur d'interprétation.

4.4 La spectroscopie à dispersion d'énergie (EDS)

La spectroscopie à dispersion d'énergie (EDS) est une technique d'imagerie d'analyse chimique de surface. L'EDS fournit la composition élémentaire de la surface numérisée et ressort une cartographie de la distribution latérale d'éléments. L'appareil EDS utilisé est de marque OXFORD Instruments couplé au MEB JEOL JSM-7600F ayant un même type d'électrons primaires comme faisceau incident. La préparation de l'échantillon a été faite par dépôt des nanoparticules de ZnO sur le porte échantillon. Étant donné que l'oxyde de zinc est un semi-conducteur, une couche de carbone a été utilisée comme substrat sur le porte échantillon. En général, la même préparation de l'échantillon est utilisée aussi bien pour l'analyse au microscope électronique à balayage que dans l'EDS.

Son fonctionnement est basé sur les faisceaux d'électrons primaires incidents sur l'échantillon qui entrent en collision avec les atomes de cet échantillon. Des rayons X caractéristiques des éléments chimiques sont émis de cette collision. Le détecteur EDS capte ces rayons issus de l'échantillon, les traitent et donne les éléments de surface qui ont eu collision avec les électrons primaires. En Effet, connaissant le rayon X émis par la source primaire et le rayon X détecté par le détecteur, le rayon X absorbé par l'électron est déterminé par la conservation de l'énergie. Ce dernier rayon X est caractéristique de l'atome inspecté dans l'échantillon. Les résultats EDS sont présentés dans l'article 3 (chapitre 6).

4.5 La spectroscopie photoélectronique à rayons X

La spectroscopie photoélectronique à rayons X ou XPS (X-ray Photoelectron Spectroscopy) anciennement dénommée ESCA (Electrical Spectroscopy for Chemical Analysis) est une technique qualitative et quantitative. Le XPS est une technique d'investigation de l'état de surface d'un matériau dans le but de déterminer sa composition chimique, le pourcentage des éléments chimiques sur la surface analysée, le niveau de Fermi d'un semi-conducteur, son degré d'oxydation. Le XPS est une technique qui repose sur la collecte des électrons de cœur (Figure 4.11) qui sont éjectés des atomes de l'échantillon analysé lorsqu'ils sont irradiés par un rayon X. Ces électrons éjectés sont détectés et analysés pour déterminer l'état des éléments et la composition de l'échantillon. Autrement dit cette technique s'appuie sur l'effet photoélectrique.

C’est une technique non destructive donc utilisée dans l’analyse d’une large gamme de composés organiques, inorganiques, fragiles ou non fragiles. On cite à titre d’exemple la mesure des surfaces des échantillons en verres, oxydes, métaux, biomatériaux, fibres, céramiques, carbones, nanomatériaux, plastiques, polymères, poudres. Plusieurs industries ont recours à cette technique dont les fabricants des cellules solaires photovoltaïques, des automobiles. Le spectromètre à photoélectron X a été développé par le professeur Kai Siegbahn et son équipe dans les années 1950, cependant c’est à partir de 1970 que les appareils de mesure XPS ont été mis sur le marché.

Contrairement à la spectroscopie UV-visible où les électrons émis sont des électrons de valence, la spectroscopie photoélectronique XPS émet les électrons de cœur des atomes à la surface de l’échantillon lorsque l’énergie d’un rayon X incident est suffisamment grande pour éjecter un électron de cœur des atomes à la surface de l’échantillon. Étant donné que l’hydrogène et l’hélium n’ont que des électrons de valence, ils ne sont pas observables par mesures XPS cependant les éléments détectables dans une analyse XPS vont du lithium au l’uranium car ces atomes ont des électrons de cœur.

Les rayons X incidents ont une énergie $E=h\upsilon$ de 0 à 1000 eV et peuvent atteindre une profondeur d’analyse de 10 nm dans un échantillon solide. Les rayons X utilisés dans un spectromètre XPS sont issus de l’aluminium (Al) ou du magnésium (Mg). Les rayons X issus de l’aluminium sont les rayons Al $K\alpha$=1486.6 eV. Le diamètre du spot est de 30-400 µm. L’émission d’un rayon X est provoqué par un électron source incident qui arrive sur un autre électron d’un atome d’aluminium. L’électron incident éjecte un électron autour du noyau de l’atome Al. À la suite de cette éjection, il y a une émission de rayon X. L’interaction rayon X-atome de surface de l’échantillon provoque le départ des électrons des atomes de surface avec une énergie cinétique Ec. L’accès à la densité d’états électroniques occupée peut être schématisé par la Figure 4.11.

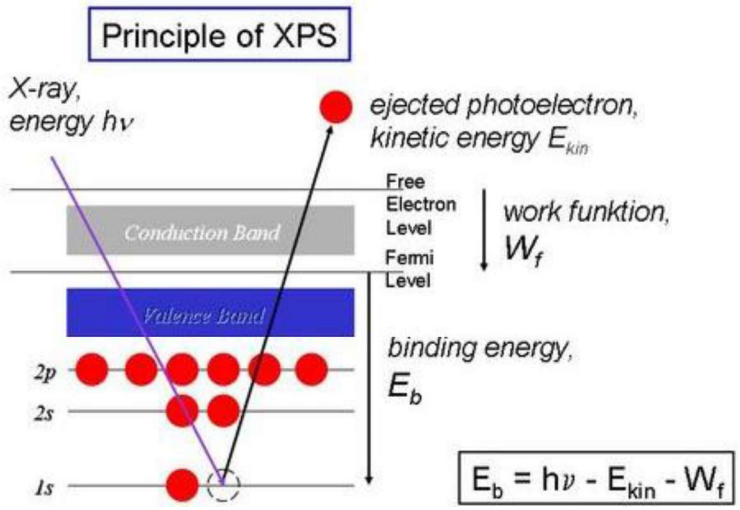

Figure 4.11: Principe de XPS[8]. Bilan énergétique -Conservation de la matière

En effet la conservation de l'énergie se traduit par l'énergie incident qui est repartie en une énergie de liaison et en énergie cinétique de l'électron photo-émis. L'énergie de liaison est l'énergie nécessaire pour rompre la liaison électron-atome et donc l'ioniser.

Le spectre en énergie cinétique présente des pics. On peut déterminer l'énergie correspondant à chaque pic par la relation d'Einstein déduite de la relation de la conservation de l'énergie :

$$E_L = h\nu - E_c \qquad (4.24)$$

Avec :

- hυ : énergie du photon incident ;
- E_L : énergie de liaison de l'électron avec le noyau ;
- Ec : énergie cinétique dans le vide de l'électron éjecté.

L'énergie de liaison de l'électron dans l'atome correspond à la somme de l'énergie de liaison relative au niveau de Fermi et le travail de sortie de cet électron (Figure 4.11):

$$E_L = E_L^F + W_f \qquad (4.25)$$

[8] : https://www.ifw-dresden.de/ifw-institutes/ikm/micronano-structures/methods/xps

L'équation de conservation de l'énergie devient selon le niveau de Fermi (niveau de plus haute énergie ayant de électrons à O°K) :

$$h\nu = E_L^F + W_f + E_C \qquad (4.26)$$

E_L^F : énergie de liaison relative (l'électron) au niveau de Fermi;

W_f : constante de la fonction de travail de l'échantillon.

- W : énergie nécessaire à l'électron pour franchir la frontière matériau/vide (ou travail de sortie)
- h : constante de Planck ;
- υ : fréquence de l'onde incidente.

Chaque énergie cinétique est caractéristique d'une liaison de cet électron éjecté avec son atome ou sa molécule. Le détecteur XPS mesure cette énergie et l'analyse par la conservation de la matière pour en déduire l'élément chimique sur la surface de l'échantillon. Le nombre des électrons détectés dans chaque pic étant proportionnel à la quantité d'éléments chimiques dans le volume d'échantillonnage XPS, on en déduit les pourcentages atomiques.
La composition chimique de la surface de l'échantillon analysé est obtenue par comparaison avec des spectres connus récapitulés dans le Handbook XPS.

L'appareil de mesure dans cette étude est le spectromètre XPS Thermo Scientific capable de détecter tous les éléments du tableau périodique sauf l'hydrogène. Sa précision est de 0.05 % pour la plupart des éléments détectés. Le spectromètre XPS est constitué de 3 chambres isolées (automatiquement ou manuellement) les unes des autres :

- Une chambre de préparation dans laquelle on ajuste une pression sur l'échantillon. La pression doit est être supérieure ou égale à 10^{-7} Bar. Tout matériau compatible avec un environnement ultra-vide peut être analysé au XPS.
- Une chambre d'introduction des échantillons ;
- Une chambre d'analyse. (Figure 4.12)

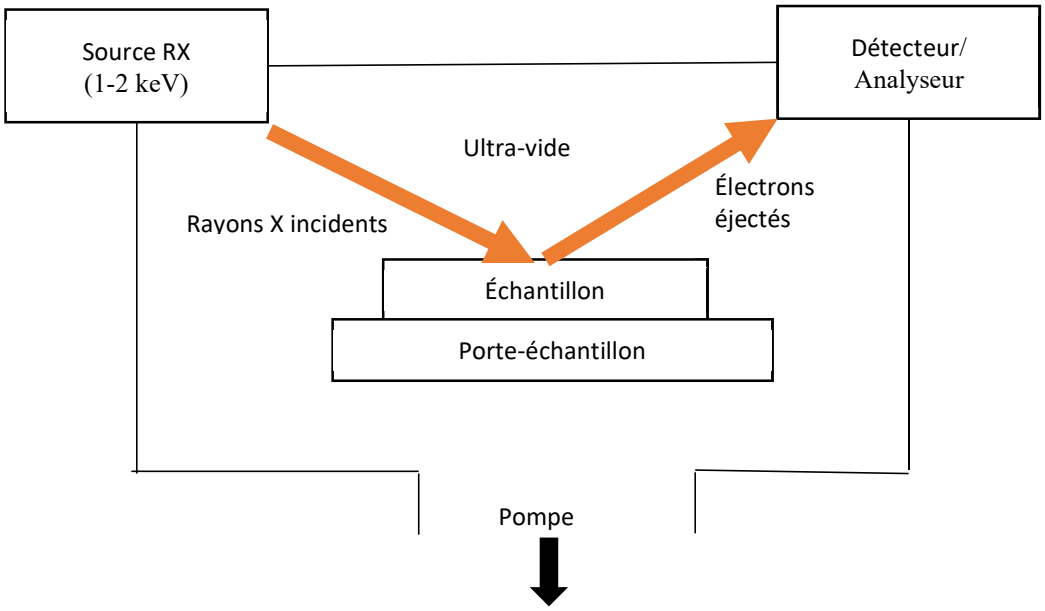

Figure 4.12: Spectromètre XPS et son principe de fonctionnement de mesure

Les résultats XPS sont présentés dans l'article sur ZnO :H_2WO_4. L'identification des spectres XPS a été faite par comparaison des pics de références XPS dans les bases des données Handbook (Moulder, Stickle, Sobol, & Bomben, 1995) ou en lignes. Chaque pic du spectre représente le nombre des électrons émis associé à une énergie de liaison spécifique. Cette énergie de liaison est caractéristique d'un atome et/ou de son état d'oxydation. L'intensité de chaque pic est proportionnelle au nombre d'atome investigué ayant émis des électrons. Autrement dit, les intensités des pics XPS sont proportionnelles au pourcentage atomique de la surface investiguée. Dans notre cas, nous pouvons remarquer que les pics XPS de grande intensité sont les pics Zn , O alors que le pic de liaison du dopage W est très faible.

Certains pics d'un spectre XPS se chevauchent alors qu'ils peuvent provenir des atomes différents. Pour séparer les pics, nous avons utilisé le logiciel Origin pro pour le traitement de déconvolution de ces pics. Dans ces spectres XPS, Il existe aussi des pics qui ne sont pas liés à l'énergie cinétique d'ionisation des électrons tels que des pics des électrons Auger. Les électrons Auger sont des électrons secondaires issus des atomes en surface lors de l'investigation XPS. L'énergie de ces électrons Auger est connue dans la littérature pour le cas ZnO. Les différents types d'électrons Auger se distinguent par la notation de 3 lettres :

- La 1ère lettre désigne la couche de l'électron ionisé;

- La 2ème lettre indique la couche de l'électron qui vient combler le trou;
- La 3ème lettre désigne l'électron émis (Auger).

Il convient de noter aussi la présence des faibles pics parasites qui ont été identifiés et éliminés. Les résultats XPS des échantillons de ZnO pur et ZnO dopé sont au chapitre 5 article 2 (**Structural and Optical Properties of Tungstic Acid-Doped Zinc Oxide for Semitransparent Dye Sensitized Solar Cell Applications).**

4.6 La spectroscopie infrarouge par la transformée de Fourier

La spectroscopie IR étudie l'interaction entre la matière et le rayonnement infra-rouge. Le domaine de l'infrarouge s'étend de 750 nm à 10^{-3} m. C'est une technique de mesure des spectres d'absorption, d'émission ou de transmittance d'un échantillon solide, liquide ou gazeux. C'est une technique d'analyse spectrale qui met en œuvre des transitions entre les niveaux vibrationnels d'une molécule dans le but d'identifié cette molécule. La spectroscopie IR vise à déterminer les liaisons des molécules d'un échantillon à l'aide des spectres des bandes d'absorption en fonction des nombres d'onde correspondants. Ce qui revient à identifier dans le spectre obtenu par transformée de Fourier les groupes caractéristiques des différentes liaisons chimiques des molécules de l'échantillon. Un spectre IR est utilisé pour déterminer un ou plusieurs groupes caractéristiques ou fonctionnels à l'aide des tables de corrélation ou d'un logiciel prédéfinissant ces groupes chimiques. À chaque bande d'absorption spécifiques au nombre d'onde précis sont associés des groupes fonctionnels tels qu'alcool, aldéhyde, cétone, acide carboxylique, ester, amine, amide, groupe alkyle, une liaison métal-oxygène.

L'absorption d'un rayonnement infrarouge a lieu lorsque la longueur d'onde du faisceau incident est de l'ordre de grandeur de l'énergie de vibration des liaisons des molécules de l'échantillon. L'absorption d'énergie provoque une transition entre les niveaux vibrationnels. Une transition entre niveaux vibrationnels s'accompagne d'un changement de niveau rotationnel ; c'est pourquoi on parle souvent de transition rotatio-vibration pour une bande d'absorption. Les liaisons vont vibrer à des fréquences différentes générant des pics spécifiques caractéristiques de la nature des liaisons chimiques dans l'échantillon.

Pour une molécule diatomique (comme le ZnO), on distingue 3 types de vibrations : une vibration d'élongation liée à l'étirement d'une liaison entre deux atomes, une vibration rotationnelle liée à la variation de l'angle de deux liaisons et la vibration rotatio-élongation.

Le niveau d'énergie d'un atome ayant absorbé un rayonnement infrarouge peut être décomposé en 3 parties :

$$E = E_{el} + E_v + E_r \qquad (4.27)$$

- E_{el} : énergie électronique.
- E_v : énergie électronique, associée aux mouvements de vibrations des atomes autour de leur position d'équilibre.
- E_r : énergie vibrationnelle, associée au mouvement de rotation de la molécule autour d'un axe passant par le centre d'inertie.

Le Tableau 4.2 recapitule quelques types de transitions électroniques en fonction du type de radiations incidents. La connaissance du type de transition permet de déterminer soit les propriétés physiques (bande interdite par exemple pour les niveaux électroniques excités) ou chimiques (liaisons chimiques, groupes fonctionnels des molécules) de l'échantillon.

Tableau 4.2: Classification des spectroscopies

Lon-gueur d'onde	**Nombre d'onde**	**Type de rayonne-ment**	**Transition obtenue**	**Information déduite**	**Caracté risation**
10^{-3} m à $2{,}5.10^{-5}$ m	400 à 10 cm^{-1}	Infra-rouge lointain	Transition rotationnelle	Groupe fonctionnel	Spectros copie IR (FTIR)
25 µm à 2,5 µm	400 à 4000 cm^{-1}	Infra-rouge moyen	Transition vibrationnelle et rotationnelle	Groupe fonctionnel, liaison chimique	
2,5 µm à 0,75 µm	14000 à 4000 cm^{-1}	Infra-rouge proche	Vibration des harmoniques	Groupe fonctionnel	
750 nm à 400 nm		Visible	Transition des électrons de valence	Bande interdite des semi-conducteur	Spectros copie UV-Visible
400 nm à 100 nm		Ultraviolet			
≤ 50 nm		Rayon X	Transition électronique des électrons au cœur de l'atome	Structure cristalline, composition chimique	Diffracti on par rayon X (DRX)

Pour un spectromètre à un faisceau, une source lumineuse envoie une radiation électromagnétique sur un monochromateur qui sélectionne un rayonnement à une longueur d'onde précise dans le

domaine de l'IR. Le rayonnement sera dirigé vers l'échantillon et à sa sortie de l'échantillon le signal est détecté et traité pour en obtenir un spectre IR de l'échantillon.

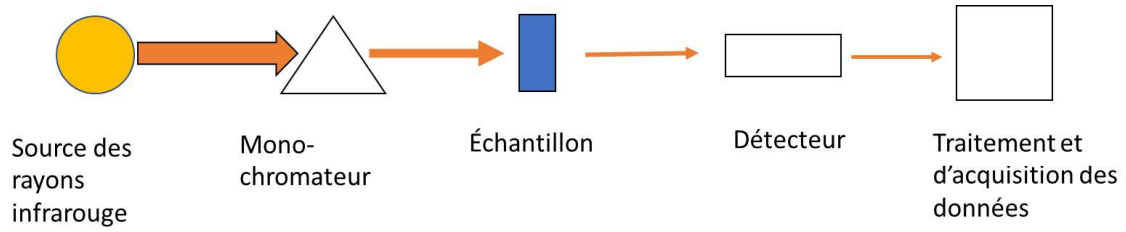

Figure 4.13: Schéma de principe d'un spectromètre IR à transmission à simple faisceau.

Pour un rayonnement électromagnétique de longueur d'onde λ traversant un échantillon, la transmittance T exprimée en pourcentage est le rapport I/Io:

$$T = \frac{I}{Io}$$

Avec

Io : intensité de la lumière incidente;

I : intensité de la lumière sortante;

L'absorbance A est donnée par la relation :

$$A = -\log(T) = \log\left(\frac{Io}{I}\right)$$

Les mesures effectuées sont celles d'absorbance en fonction des nombres d'onde.

On définit le nombre d'onde en cm^{-1} par l'inverse de la longueur d'onde :

$$\sigma = \frac{1}{\lambda} = \frac{\nu}{c} \qquad (4.28)$$

La dualité onde corpuscule d'un rayonnement électromagnétique se traduit par :

$$E = h\nu = \frac{hc}{\lambda}$$

Les liaisons chimiques se comportent comme un ressort et chaque liaison a une fréquence d'oscillation propre à elle. Deux modélisations décrivent les différentes vibrations : la modélisation classique et la modélisation quantique.

Vibration d'une molécule diatomique A-B : modèle classique

La force de rappel F qui déplace une masse m de x élongation est:

$F = -kx$ (4.29)

k étant la constante de rappel caractéristique du ressort.

Équation du mouvement de vibration d'élongation (x) est :

$$m\frac{d^2x}{dt^2} + kx = 0 \text{ ou } \ddot{x} + \frac{k}{m}x = 0 \qquad (4.30)$$

La solution à cette équation de vibration est une harmonique :

$$x = x_0 \cos(\omega t + \varphi) \qquad (4.31)$$

Avec $\omega = 2\pi\upsilon = \sqrt{\frac{k}{m}}$ est la pulsation ou fréquence angulaire ; υ : fréquence

Soit une molécule diatomique A-B constituée d'atomes A et B de masse m_A et m_B respectivement. En considérant que A et B constituent une liaison oscillante avec une constante de raideur k autour de leur position d'équilibre avec une fréquence υ_0.

En considérant que le système A-B est un oscillateur harmonique, la fréquence de vibration est :

$$\nu_0 = \frac{1}{2\pi}\sqrt{\frac{k}{\mu}} \qquad (4.32)$$

avec μ masse réduite de la molécule $\mu = \frac{m_A m_B}{m_A + m_B}$

Pour un rayonnement électromagnétique de fréquence υ incident sur la liaison A-B, il y a absorption et vibrations si la fréquence du rayonnement incident est égale à la fréquence propre de la liaison :

$$\nu = \nu_O \qquad (4.33)$$

Si cette condition est remplie, on est à la résonnance.

L'énergie potentielle :

$$F = -\frac{\partial E_P}{\partial x} \Rightarrow E_P = \frac{1}{2}kx^2 = \frac{1}{2}kx_0 \cos^2 \omega t \qquad (4.34)$$

En réalité, la forme du potentiel n'est pas parabolique mais suit la loi de Morse :

$$E_P(x) = k\left(1 - e^{\beta x^2}\right) \qquad (4.35)$$

Au voisinage de 0 ou pour des vibrations de faibles amplitudes, la courbe de l'énergie potentielle est assimilée à la parabole de l'oscillateur harmonique.

$$E_P = \frac{1}{2}kx^2 \qquad (4.36)$$

Vibration d'une molécule diatomique A-B : modèle quantique

L'équation de Schrodinger pour une onde électromagnétique φ vibrant selon la direction x est :

$$-\frac{\hbar^2}{2\mu}\frac{d^2}{dx^2}\psi(x) + \frac{1}{2}kx^2\psi(x) = E\psi(x) \qquad (4.37)$$

La solution qui est une énergie vibrationnelle est :

$$E_V = h\nu_0\left(\nu + \frac{1}{2}\right) \qquad (4.38)$$

Avec υ=0,1, 2,… appelé nombre quantique vibrationnel est un entier positif ; υ_0 fréquence de vibration propre définie dans le modèle classique.

Pour des niveaux de vibrations équidistants, l'énergie de vibration est aussi ici un oscillateur harmonique. Cependant les liaisons chimiques n'étant pas des ressorts parfaits, on a des pas des oscillateurs harmoniques. En tenant compte de l'anharmonicité, les niveaux de vibration sont de plus en plus rapprochés selon la loi de Morse.

On distingue deux modes de vibrations dans une liaison chimique :

- Des vibrations d'élongations (ou de valence) longitudinales ou mouvement dans l'axe de la molécule ;
- Des vibrations de déformation angulaires ou vibration perpendiculaire à l'axe de la liaison.

Les transitions roto-vibrationnelles correspondent à des raies avec des intensités proportionnelles aux transitions impliquées. Les séries de raies constituent le spectre infrarouge de l'échantillon. Pour une liaison chimique forte, le nombre d'onde correspondant est élevé.

Appareil

Le spectromètre IR utilisé dans cette étude est un spectromètre FTIR 65 Perkin Elmer type ATR (« Attenuated Total Reflectance ») connecté à un ordinateur (acquisition des données, calcul des TF et affichage).

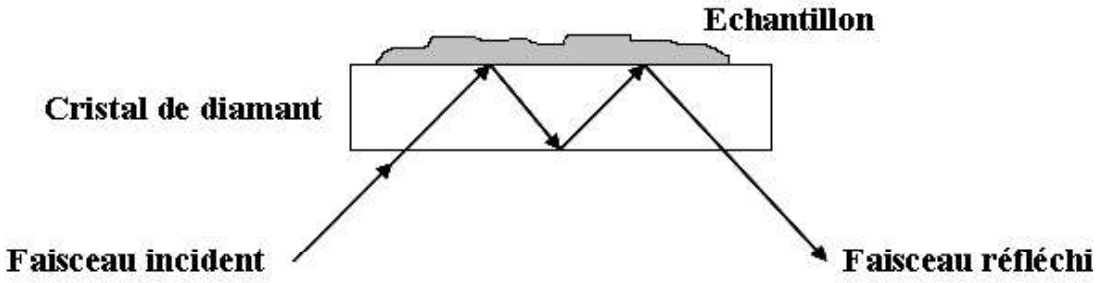

Figure 4.14: Schéma de principe d'un spectromètre IR ATR (Benabdallh, 2008)

L'échantillon est déposé sur une surface réfléchissante et les analyses des faisceaux sortant de l'échantillon s'effectuent par réflexion (Figure 4.14). On place l'échantillon à analyser au contact d'un cristal à fort indice de réfraction dans l'infrarouge tel que le germanium.

Bien que l'infra-rouge soit découvert par F.W Herschel en 1800, la spectroscopie FTIR a connu un essor pour les recherches au milieu du XX^{ème} siècle. La FTIR repose sur le concept d'espace de Fourier, les mesures des spectres sont effectuées dans l'infrarouge et l'infrarouge lointain de 100 cm^{-1} à 10 000 cm^{-1}. L'appareil de mesure repose sur l'interféromètre de (Albert Abraham) Michelson qui effectue les mesures des transitions vibrationnelles, rotationnelles ou roto-vibrationnels dans les molécules constituants un échantillon. La FTIR est avantageuse par rapport à l'IR pour des mesures plus rapides, non-destructives avec une excellente résolution et un bon rapport signal sur bruit grâce au développement des ordinateurs qui effectuent les calculs rapides des transformées de Fourier. L'interféromètre de Michelson est constitué de :

- Une source lumineuse monochromatique émettant un rayonnement lumineux de longueur d'onde λ donnée dans le domaine de l'infrarouge ;
- Un miroir fixe qui réfléchit la lumière vers la lame ;

- Un miroir mobile dont le déplacement est contrôlé par pas ;
- Une lame diviseuse des faisceaux qui divise le rayonnement incident en un rayonnement vers le miroir fixe, un second rayonnement vers le miroir mobile et le troisième vers l'échantillon. Le rayonnement vers l'échantillon est une combinaison des deux premiers rayonnements orientés vers les miroirs ;
- Un détecteur du signal provenant de l'échantillon
- Un système de traitement de signal (transformation du signal en données discrètes dans le temps puis dans le domaine fréquentiel, calculs des transformées de Fourier des signaux) qui génère l'interférogramme.

L'acquisition des données est fondée sur l'enregistrement des fréquences des vibrations en fonction des longueurs d'ondes absorbées par l'échantillon selon les modèles vibratoires ci-haut décrits. Après la mise en marche de l'appareil, un signal de référence a été acquis avant l'insertion de l'échantillon pour les mesures. Le signal de référence, appelé interferogramme est soumis à une transformation de Fourier qui fournit le spectre de référence pré-enregistré. Ensuite, on a inséré l'échantillon dans le spectromètre sur le porte-échantillon et on a lancé la mesure en répétant la procédure de mesure précédente (acquisition d'un signal soumis à la transformée de Fourier). Le spectre FTIR recherché est obtenu par division du dernier spectre par le spectre de référence.

La résolution de l'appareil est 4 cm^{-1} pour les mesures. Le choix du domaine de mesure est 4000 cm^{-1} - 450 cm^{-1} dans le domaine IR moyen. Les spectres de transmittance ou d'absorbance sont enregistrés en fonction de longueurs d'onde.

Le spectre obtenu est la transmittance en fonction du nombre d'onde ou l'absorbance en fonction du nombre d'onde. Pour une forte absorbance (100% est le maximum ou absorption totale) du rayonnement électromagnétique, on a une faible transmittance. Pour une faible absorbance (0% d'absorption ou transmittance totale) du rayonnement électromagnétique, on a une forte transmittance.

Les spectres d'absorptions traduisent les états de vibrations des liaisons des molécules de l'échantillon et sont tracés dans l'article 3 au chapitre 6. Les bandes d'absorptions sont plus ou moins intense, fine ou large. Les mesures effectuées ont permis de mettre en exergue les liaisons :

- Zn-O dans la couche mince de ZnO. Pic observé à 425 cm^{-1} à 560 cm^{-1} ;

- W-O et O-H dans l'échantillon d'acide tungstique. Pic observé respectivement à de 550-950 cm^{-1}, à 1641 cm^{-1} et à 3494 cm^{-1} ;

Zn-O, W-O et O-H dans l'échantillon de ZnO dopé avec l'acide tungstique.

La spectroscopie FTIR mesurée par A. Dhanalakshmi et al. (Dhanalakshmi, Natarajan, Ramadas, Palanimurugan, & Thanikaikarasan, 2016b) montre des vibrations au nombre d'onde 450 cm^{-1} , 848 cm^{-1} et 900 cm^{-1}. (Tableau 4.3) Pour ces chercheurs, le dopage de ZnO par le Mn n'a pas eu d'influence sur la vibration de la liaison pour un nombre faible de 450 cm^{-1}. Ce nombre coïncide avec les pics que nous avons obtenu pour ZnO entre 425 cm^{-1} à 560 cm^{-1}

Tableau 4.3: FTIR vibration frequencies for different modes of ZnO pure and Mn-doped ZnO (Dhanalakshmi et al., 2016b)

Undoped ZnO (cm^{-1})	Mn-doped ZnO (cm^{-1})	Vibration mode
450	450	Zn-O
-	677	Mn-O
848	-	Zn-O
900	-	Zn-O
1036	1036	C-O stretching vibration
2360	2360	CO_2 molecule
3451	3451	O-H

4.7 Résistivité et résistance surfacique des couches minces semi-conducteur

La mesure de la résistivité peut être effectuée à l'aide de la méthode de 4 pointes qui mesure la résistivité surfacique ou à l'aide d'un moniteur de conductimètre.

4.7.1 Résistivité par la méthode de 4 pointes

Le principe de mesure par 4 pointes schématisé sur la figure 4.15 peut se décrire comme suit : :

- Placer les 4 pointes équidistantes loin des bords de la couche à caractériser. Les pointes doivent être alignées.
- Le courant est envoyé par un générateur de courant entre les pointes 1 et 4, tandis que la tension est mesurée entre les pointes 2 et 3.

- Le rapport de la tension mesurée sur l'intensité qui traverse l'échantillon donne la résistance du tronçon entre les pointes 2 et 3

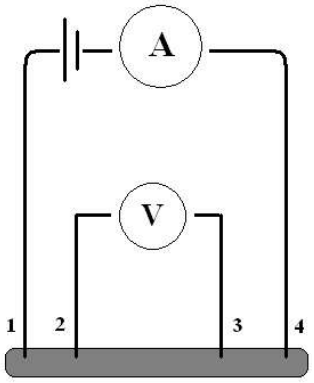

Figure 4.15 : Principe de la technique de mesure par 4 pointes [9]

Une revue de la littérature a été faite sur les propriétés électriques notamment sur la mobilité des porteurs des charges, la concentration des porteurs de charges, le type (n ou p) du matériau et la conductivité des échantillons ZnO.

La mobilité des porteurs de charges μ ($cm^2.V^{-1}.s^{-1}$) est la capacité de diffusion des porteurs des charges dans un réseau cristallin. Elle est étroitement liée à la conductivité et aux nombres des impuretés dans un semi-conducteur. La conductivité σ exprimée $(\Omega.cm)^{-1}$ est une caractéristique du matériau à laisser les porteurs de charges (ou courant) à circuler dans le matériau. Elle est l'inverse de la résistivité (Ω.cm). Loi d'Ohm dans un matériau est:

$$\vec{j} = \sigma\vec{E} \text{ soit } \vec{E} = \rho\vec{J} \qquad (4.39)$$

avec $\sigma = \frac{1}{\rho}$

Pour un champ électrique appliqué E ($V.cm^{-1}$) à un matériau, la mesure de la vitesse v ($cm.s^{-1}$) des porteurs charges permet de calculer la mobilité recherchée de ces porteurs de charges.

$$\vec{v} = \mu\vec{E} \qquad (4.40)$$

[9] http://en.wikipedia.org/wiki/File:Four-point.png

Par définition, le vecteur densité de courant total est proportionnel à la vitesse des porteurs de charges :

$$\vec{j} = q\left(p\vec{v}_h - n\vec{v}_n\right) \qquad (4.41)$$

Pour les électrons, le vecteur densité de courant est: $\vec{j} = qn\vec{v}_n$ (4.42)

Pour les trous, le vecteur densité de courant est : $\vec{j} = qn\vec{v}_h$ (4.43)

Donc, en combinant les équations de densité de courant, la conductivité le long des abscisses devient :

$$\sigma = q\left(p\frac{\vec{v}_h}{\vec{E}} - n\frac{\vec{v}_n}{\vec{E}}\right) = q\left(p\frac{v_{hx}}{E_x} + n\frac{v_{nx}}{E_x}\right) = q\left(p\mu_p + n\mu_n\right) \qquad (4.44)$$

On pose l'expression des mobilités des trous et des électrons:

$$\mu_p = \frac{v_{hx}}{E_x};\ \mu_n = \frac{v_{nx}}{E_x} \qquad (4.45)$$

Pour un matériau de type N comme le ZnO:

$$\mu_n > \mu_p\ ; n > p \text{ et } n\mu_n \gg p\mu_p \qquad (4.46)$$

Donc la conductivité devient :

$$\sigma = \frac{1}{\rho} \approx qn\mu_n \qquad (4.47)$$

Pour ces oxydes métalliques transparents et semi-conducteurs déposés sous formes de couches minces, on définit la résistance de surfacique (ou *sheet resistance* en anglais) exprimée en Ω/sq comme la résistance d'une couche mince uniforme dans un élément de plan carré. Considérons un conducteur tridimensionnel régulier de longueur l, de largeur w, d'épaisseur x_j tel que décrit par la figure 4.16. Pour un courant traversant ce matériau, la résistance exprimée en ohm (Ω) est régie par la relation :

$$R = \rho\frac{l}{A} = \frac{\rho l}{x_j w} \qquad (4.48)$$

Où :

- ρ est la résistivité s'exprime en Ω.cm,
- A est la section transversale et s'exprime cm^2. Elle peut être obtenue par le produit de la largeur w (cm) et de l'épaisseur x_j (cm);
- l est la longueur et s'exprime en cm.
- R : résistance en Ω.

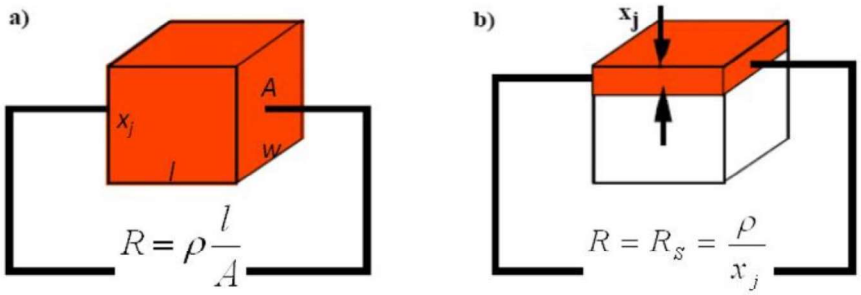

Figure 4.16: a) Résistance (résistivité); b) résistance surfacique (*sheet resistance*)

Si l=w (carré), alors la résistivité est égale à la résistance surfacique : $R=R_s$

R_s (Ω/sq) est appelée « *sheet resistance* » et mesure la résistance d'une couche mince uniforme dans un élément de plan carré. Cette résistance est utilisée pour caractériser les matériaux élaborés par dopage de semi-conducteurs, impression de pate résistive ou revêtement de verre.

Pour un semi-conducteur extrinsèque, on définit la résistivité moyenne $\bar{\rho}$ (ou conductivité moyenne $\bar{\sigma}$):

$$\bar{\rho} = \frac{1}{\bar{\sigma}} \qquad (4.49)$$

La résistance surfacique (*sheet resistance*) pour le semi-conducteur est alors :

$$R_s = \frac{\bar{\rho}}{x_j} = \frac{1}{\bar{\sigma} x_j} = \frac{1}{\int_0^{x_j} \sigma(x)dx} \qquad (4.50)$$

$$\text{Avec : } \bar{\sigma} = \frac{1}{x_j}\int_0^{x_j} \sigma(x)dx \qquad (4.51)$$

4.7.2 Mesure de la résistivité surfacique (sheet resistance)

La mesure de la résistivité surfacique a été faite à l'aide du moniteur de conductance Delcom Instruments. La technologie Delcom Instruments est basée sur un assemblage de deux inductances dans un noyau de ferrite (Figure 4.17 b). Un courant oscillant issu de la source de courant RF (Figure 4.17 a) circule dans les bobines d'inductances générant un champ magnétique oscillant entre les deux inductances en regard (Figure 4.17 b et c). Lorsqu'un échantillon conducteur est introduit entre les deux inductances dans le champ magnétique oscillant, un flux d'électron circulaire appelé courant de Foucault est induit dans la couche conductrice de l'échantillon (Figure 4.17 d). La difficulté à maintenir ce courant de Foucault est mesurée en résistance surfacique du matériau étudié.

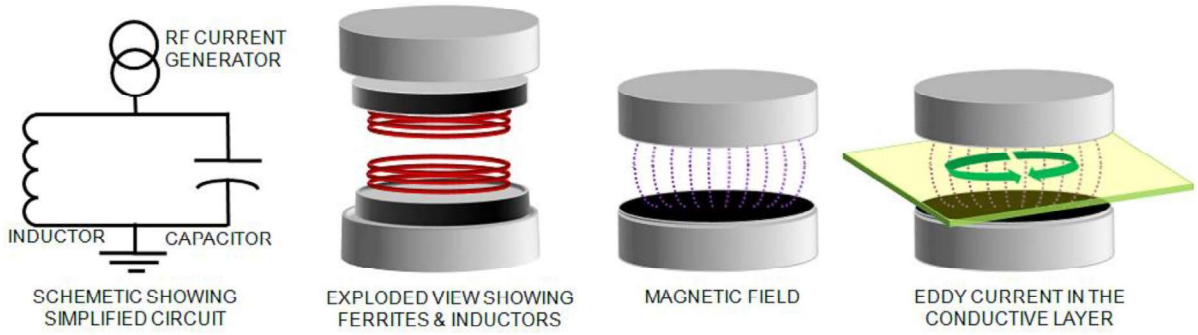

a) b) c) d)

Figure 4.17: Schéma de principe de Delcom Instruments [10]: a) électrique, b) deux inductances dans un noyau de ferrite, c) génération de champ magnétique, d) présence d'un échantillon soumis à un champ magnétique

Contrairement aux mesures effectuées par les sondes à 4 pointes, Delcom Instruments offre l'avantage des mesures sans contact, non destructives, instantanées, peu onéreuses.

Les résistances surfaciques ont été présentées dans l'article 2 (chapitre 5) et article 3 (chapitre 6).

[10] source: http://www.delcominst.com/technology.html; consulté le 4/11/2021

4.8 Le profilomètre DektakXT Bruker

L'épaisseur et l'uniformité des couches minces peuvent être mesurées à l'aide du profilomètre DektakXT Bruker. La rugosité des couches est évaluée en comparant l'épaisseur des couches à différents endroits (Figure 4.18). L'épaisseur d'une couche est évaluée en faisant la différence entre la hauteur de la couche et celle du substrat.

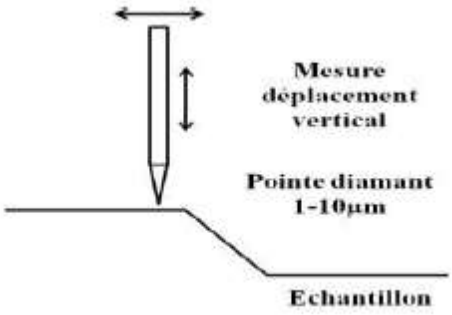

Figure 4.18 : Principe de mesure d'épaisseur à l'aide d'un profilomètre

C'est une technique de mesure rapide, sans contact, non-destructive qui fonctionne par le déplacement d'un stylet en pointe de diamant et d'une caméra optique entre le substrat et différents points sur la couche mince pour effectuer la mesure sur une épaisseur 3D. Cet appareil est utilisé pour les mesures des couches des semi-conducteurs, en microélectronique, en médecine ou en science des matériaux. L'appareil a une résolution permettant d'effectuer des mesures des hauteurs de pas inférieures à 10 nm. Les profils des échantillons obtenus présentent toutes des rugosités.

4.9 Caractéristique courant-tension des DSSC

Deux types d'électrodes sont à identifier dans les DSSC élaborées

- Une électrode ZnO-dye ou photoanode;
- Une seconde métal-électrolyte ou platine-couple redox (I^-/I_3^-):

Lorsqu'on plonge l'électrode ZnO déposée sur le substrat FTO dans une solution de dye (N719), le colorant pénètre dans le réseau du semi-conducteur et peut atteindre le substrat. L'électrode nanoporeuse atteint l'équilibre dans l'obscurité si les 3 phases (FTO-ZnO-Dye) ayant des fonctions de travail différentes s'équilibrent à une valeur unique du niveau de Fermi.

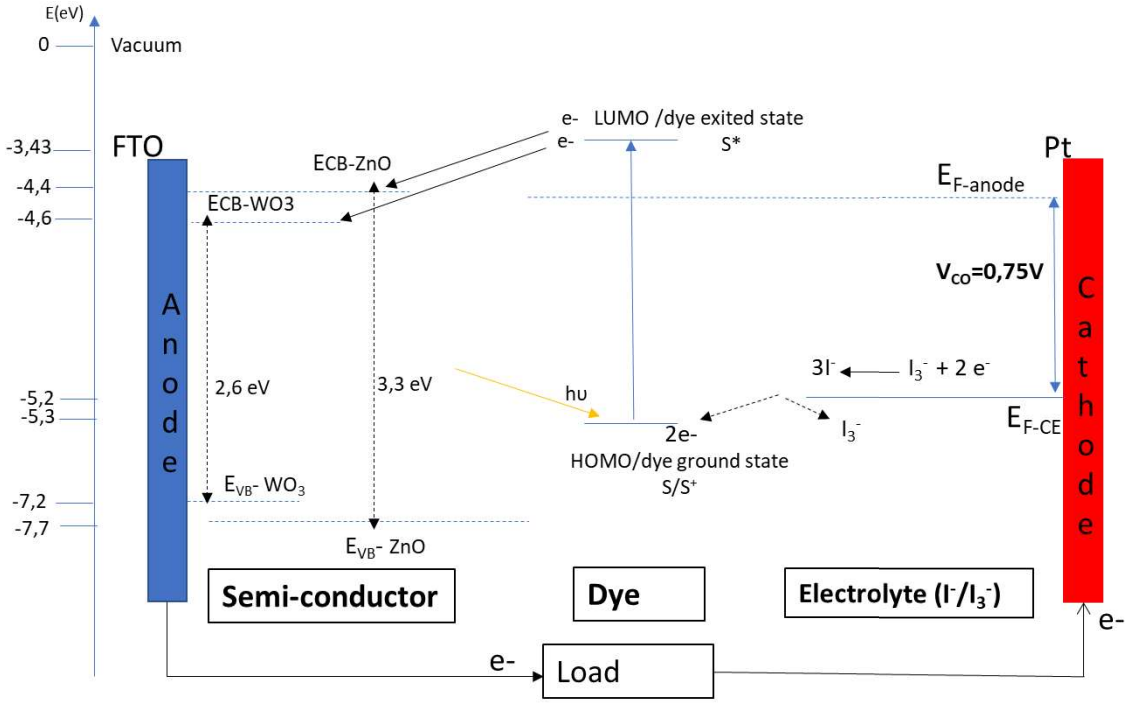

Figure 4.19 : Schéma de fonctionnement d'une DSSC à base de ZnO-WO_3 avec leurs niveaux d'énergies

La mise en contact d'un semi-conducteur, d'un oxyde transparent conducteur (FTO) ou d'un métal (platine) plongé dans une solution provoque un état d'équilibre électrochimique qui s'établit par l'égalité du niveau de Fermi de l'électrode plongée dans une solution et celui du couple redox contenant cette solution. La tension d'équilibre aux bornes de la pile est la différence de potentiel entre les deux électrodes :

$$V_{DSSC}^{eq} = V_{cathode}^{eq} - V_{anode}^{eq} \qquad (4.52)$$

Les valeurs énergétiques des niveaux d'énergie de conduction, de valence ou de Fermi des différents matériaux et couples redox sont données dans la littérature. À l'aide de ces valeurs, on peut tracer le diagramme énergétique de la cellule et calculer la valeur de de la tension de court-circuit.

Les électrodes de référence à savoir standard (ou normale) d'hydrogène (ESH ou ENH) et SCE (électrode au calomel saturé) sont utilisées en électrochimie alors que les valeurs énergétiques en des niveaux d'énergies (valence, Fermi et conduction) par rapport au vide en physique des solides.

La relation entre électrode standard (ou normale) d'hydrogène (ESH ou ENH) et l'échelle du vide est :

$$E_{F,redox}(eV) = -4,5eV - qE_{redox} \text{ pour ENH} \quad (4.53)$$

$$E_{F,redox}(eV) = -4,74eV - qE_{redox} \text{ pour SCE} \quad (4.54)$$

Avec : $E_{F,redox}$ énergie de Fermi d'un coupe redox s'exprime en eV;

E_{redox} potentiel du couple redox s'exprime en (V)

Les niveaux d'énergie influençant les propriétés électriques dans un semi-conducteur sont :

- le niveau de valence occupé par des électrons de valence;
- le niveau de Fermi;
- le niveau de conduction;

Le travail de sortie Φ est l'énergie correspond à l'énergie entre le niveau de Fermi et le vide alors que l'affinité χ entre la bande de conduction et la sortie.

Un couple redox est caractérisé par son potentiel standard E^0_{redox} qui correspond à son état d'énergie.

$$V_{CO} = \frac{1}{q}\left(E_F - E(I^- / I_3^-)\right) \quad (4.55) \quad \text{(Trémillon, 1993)}$$

Interface anode/sensibilisateur vs Pt/électrolyte (I^-/I_3^-)

Anode - Tension due au couple redox sensibilisateur

Tension standard (table du couple redox N719)

Tension d'équilibre : on applique la loi de Nernst

$$V_{D+/D}^{eq} = V_{D+/D}^0 + \frac{RT}{nF} ln \frac{[a_{ox}]}{[a_{red}]} \quad (4.56)$$

$$V_{D+/D}^0 = \frac{1}{q}(V_{LUMO} - V_{HOMO}) \quad (4.57)$$

$$V_{D+/D}^0 = (-3,43V - (-5,34V)) \quad (4.58)$$

$$V_{D+/D}^0 = 1,91V \quad (4.59)$$

D, D^+ : étant adsorbé et séché, leur activité est assimilée à celle d'un solide donc égale à 1;

$$a_{ox} = \gamma[D^+] = a_{red} = \gamma[D] = 1 \qquad (4.60)$$

Donc,

$$V_{D+/D}^{eq} = V_{D+/D}^{0} = 1{,}91V \qquad (4.61)$$

A la contre électrode, on a la réaction de réduction suivante :

$$I_3^- + 2e^- \longrightarrow 3I^-$$

On peut donc écrire le potentiel selon la loi de Nernst :

$$V_{I-/I3-} = V_{I-/I3-}^{0} + \frac{RT}{nF} ln \frac{[I_3^-]}{[I^-]^3} \qquad (4.62)$$

Pour 2 électrons mis en jeu, n=2 et l'équation devient :

$$V_{I-/I3-} = V_{I-/I3-}^{0} + \frac{RT}{2F} ln \frac{[I_3^-]}{[I^-]^3} \qquad (4.63)$$

La tension d'équilibre aux bornes de la pile est la différence de potentiel entre les deux électrodes :

$$V_{DSSC}^{eq} = V_{cathode}^{eq} - V_{anode}^{eq} \qquad (4.64)$$

$$V_{DSSC}^{eq} = V_{I-/I3-}^{0} + \frac{RT}{2F} ln \frac{[I_3^-]}{[I^-]^3} - V_{D+/D}^{0} \qquad (4.65)$$

L'interface anode/sensibilisateur est traversée par une densité de courant anodique i_a. L'interface Pt/électrolyte (I^-/I_3^-) est traversée par une densité de courant cathodique i_c.

La densité de courant i(A/cm^2) et la surtension η dans une cellule électrochimique peuvent être décrites selon la relation de Butler-Volmer :

$$\boxed{i = i_o \left[\exp(\frac{\alpha n F \eta_a}{RT}) - \exp(-\frac{\beta n F \eta_c}{RT}) \right]} \qquad (4.66)$$

i_o est la densité de courant d'échange. Si i_o est élevé alors le catalyseur est performant.

α : coefficient de transfert de charge à l'anode ; β : coefficient de transfert de charge à la cathode.

On a toujours : **α+β=1**

En utilisant l'approximation de Tafel, on a:

- à la cathode, on néglige la surtension anodique et l'expression de Butler-Volmer devient :

$$i_{total} = i_a + i_c = i_c = i = -i_o \left[\exp(-\frac{\beta n F \eta_c}{RT}) \right]$$

Surtension: $\eta_c = -\frac{RT}{\beta nF}\ln(-\frac{i}{i_o})$ (4.67)

- à l'anode, on néglige la surtension cathodique et l'expression de Butler-Volmer devient :

$$\eta_a = \frac{2{,}303.R\cdot T}{\alpha\cdot n\cdot F}\log(\frac{i}{i_o}) = \left[\frac{2{,}303R\cdot T}{\alpha\cdot n\cdot F}\log i - \frac{2{,}303R\cdot T}{\alpha\cdot n\cdot F}\log i_o\right] \quad (4.68)$$

La tension réelle de la cellule la tension d'équilibre diminuée de la surtension anodique, de la surtension cathodique et des pertes joules.

$$V_{DSSC}^{reelle} = V_{DSSC}^{eq} - \eta_a - |\eta_c| - i\sum R_j \quad (4.69)$$

Avec
$i\sum R_j$: chute de tension ohmique;
$\sum R_j$: résistance interne de la cellule DSSC;
η_a : surtension anodique;
η_c : surtension cathodique.

La Figure 4.20 est un schéma de base expérimental du potentiostat pour une tension contrôlée et un courant mesuré pour une cellule électrochimique. La variable est la différence de potentiel du potentiostat imposée aux bornes des électrodes de travail et la contre-électrode et on mesure le courant traversant la cellule électrochimique (Figure 4.20). Un générateur génère des tensions contrôlées avec une rampe et un pas de tension. Du point de vue électrochimique, le potentiostat injecte un flux d'électrons nécessaire (courant et potentiel étant fonctionnellement lié, ce flux est unique à chaque pas) pour entretenir les processus électrochimiques actifs à des vitesses compatibles avec le potentiel.

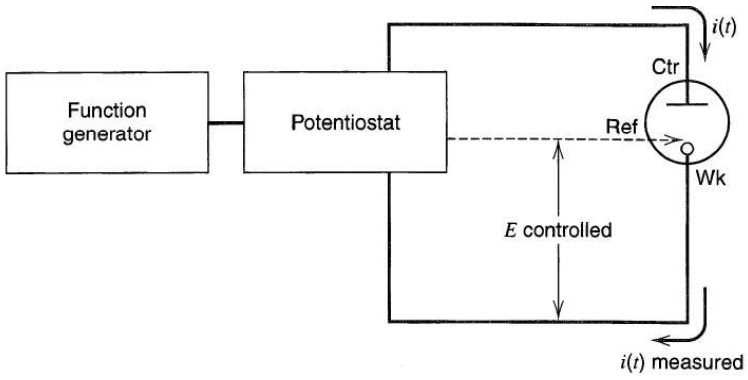

Figure 4.20: Schéma de base expérimental du potentiostat à tension contrôlée pour une cellule électrochimique (Bard & Faulkner, 2001)

La mesure courant-tension dans l'obscurité peut être simplifiée par le schéma de la Figure 4.21. En appliquant la source de tension continue aux bornes de la cellule DSSC, on mesure à l'aide d'un voltmètre et d'un ampèremètre, le courant en fonction de la variation de la tension. On obtient finalement la caractéristique courant-tension est une courbe similaire à une jonction p-n. (voir article DSSC).

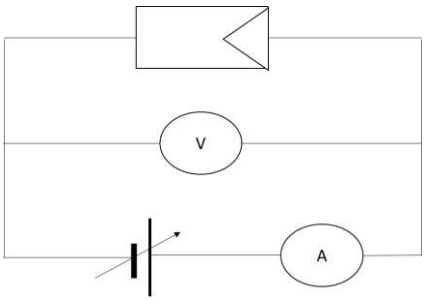

Figure 4.21: Schéma simplifié de mesure courant-tension d'une cellule solaire dans l'obscurité.

Les résultats obtenus ont permis de mettre en évidence que les cellules solaires fabriquées se comportent comme une diode dans l'obscurité.

La mesure courant-tension avec éclairement peut être assimilée au schéma simplifié de la Figure 4.22 avec une source de tension variable appliquée aux bornes de la cellule PV. À l'aide d'un voltmètre et d'un ampèremètre, on mesure le courant en fonction de la variation de la tension.

La caractéristique courant-tension est une courbe courant-tension type générateur de puissance. C'est la caractéristique d'une cellule solaire photovoltaïque.

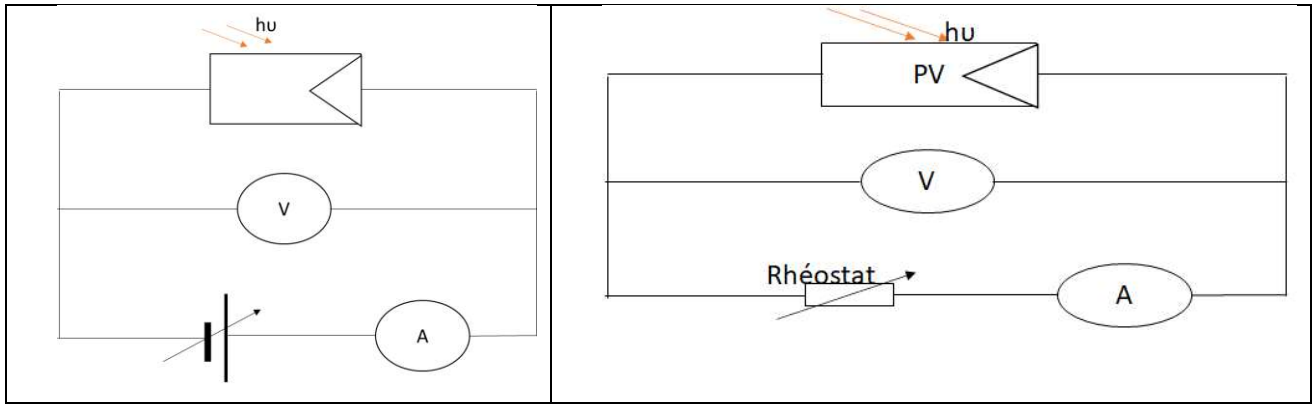

Figure 4.22 : Schéma simplifié de mesure courant-tension avec éclairement

Les mesures courant-tension ont été effectuées et présentées dans le chapitre 6 article 3.

4.10 Erreurs de caractérisation

L'erreur absolue δX ou écart de mesure est la différence entre la valeur expérimentale à la valeur exacte.

$$\delta X = X - X_e$$

X: valeur expérimentale ou approximative de la grandeur.

X_e: valeur exacte de la même grandeur.

Pour les mesures courant tension, l'erreur de mesure pour la tension est de 100 mV et celle du courant est 10 µA.

Le pourcentage d'erreur ou erreur relative (± %) est le quotient de l'erreur absolue et de la valeur exacte : $(\delta X / X_e) \times 100$.

4.11 Conclusion

Dans ce chapitre nous avons décrit la méthodologie de synthèse de ZnO et ZnO dopé à l'acide tungstique. En nous inspirant des auteurs qui ont déjà emprunté cette méthode, nous avons effectué les synthèses avec succès en y ajoutant l'additif H_2WO_4 qui s'est totalement dissout dans la matrice de ZnO en milieu basique. Les analyses :

- XRD ont permis de déterminer la structure cristalline hexagonale et la taille moyenne des cristaux (cf. chapitre 5 article 2);
- MEB ont donné les reliefs et morphologies des nanoparticules en grains, . Ces morphologies sont clairement modifiées en polyèdres lors du dopage de ZnO par H_2WO_4; (cf. chapitre 5 article 2);
- EDS pour déterminer les pourcentages atomiques dans les échantillons (cf. chapitre 6 article 3)
- UV-visible ont donné les bandes interdites des différents échantillons allant de 3,25 eV à 3,75 eV. Notons une augmentation de la bande interdite avec une augmentation en concentration de dopant; (cf. chapitre 5 article 2);
- La spectroscopie FTIR a donné des bandes de vibrations entre 425 cm^{-1} à 560 cm^{-1} correspondant aux liaisons Zn-O; (cf. chapitre 6 article 3)

- La spectroscopie XPS a confirmé les liaisons Zn-O pour les échantillons et les liaisons Zn-O, W-O pour les échantillons ZnO dopé H_2WO_4. (cf. chapitre 5 article 2)
- De résistivité au moniteur de conductance ont permis de déterminer les sheets resistance des semi-conducteurs. (cf. chapitre 5 article 2);
- D'épaisseur des échantillons à l'aide de DektakXT. (cf. chapitre 5 article 2 et chapitre 6 article 3);
- Performances des cellules par des mesures courant-tension.

Nous avons également diminué la température de synthèse de ZnO à 50 °C pour le cas de synthèse inspiré de Hasnidawani et al.(Hasnidawani et al., 2016).

CHAPITRE 5 ARTICLE 2 : STRUCTURAL AND OPTICAL PROPERTIES OF TUNGSTIC ACID-DOPED ZINC OXIDE FOR SEMITRANSPARENT DYE SENSITIZED SOLAR CELL APPLICATIONS

Padjagoto Sangmbaye[1], Oumarou Savadogo[1]*, Tahereh Fanaei Sheikholeslami[2], Kentaro Oishi[1]

[1]Laboratory of New Materials for Energy and Electrochemistry, Polytechnique Montreal (QC), Canada.

[2]Department of Mechanical Engineering, Branch of Mechatronics, University of Sistan and Baluchestan, Zahedan, Iran.

*sangmbaye@gmail.com, *oumarou.savadogo@polymtl.ca; phone: +1 514 3404725*

Submitted to Journal: Solar Energy Materials and Solar Cells on July 25, 2022

5.1 Abstract

The effect of tungstic acid doping on the structural and optical properties of ZnO material synthesized using sol-gel method is studied for the first time. The concentration of 0.00005 to 0.00015M of tungstic acid (H_2WO_4) was respectively added to the initial solution as a doping agent of ZnO. The synthesis was done in a basic medium at pH of 9.5 to 10 in the presence of alcohol and monoethanolamine. This sol-gel mixture was used to deposit ZnO thin films by spin coating on the FTO/glass substrate. X ray diffraction (XRD) methods results showed that ZnO deposited with and without taungstic acid has the same hexagonal crystal structure. Scanning Electron Microscopy (SEM) micrographs showed a significant effect of the tungstic acid on the morphology of ZnO seeds. The high porosity of the ZnO films and their chemical composition due to tungstic acid addition are also shown. UV-visible spectroscopy measurements indicated one band gap energy value for samples deposited without tungstic acid and two band gap energy values for samples deposited with tungstic acid. It was found that Eg of ZnO is indeed 3.26 eV at 300°K and increases with the amount of dopant up to 3.88 eV for a value of 1.5×10^{-4} M of H_2WO_4. XPS semi-quantitative analysis was performed to determine the chemical composition of the ZnO samples. It was concluded that WO_3 was incorporated in the films of ZnO doped with tungstic acid which may form ZnO-WO_3.

Keywords - zinc oxide, tungstic acid, sol-gel method, transparent dye solar sensitized solar cell

5.2 Introduction

Zinc oxide (ZnO) which is a high band gap transparent semiconductor is an interesting material to be used shows promising for fabrication of semitransparent dye-synthetized solar cells (DSSC). A semitransparent DSSC structure use ultraviolet (UV) light for producing the electricity but allowing visible light to pass through the building facades and windows.

Semiconducting metal oxide thin films are widely used in optoelectronic applications, particularly in solar cell devices. Zinc oxide is an inorganic compound with the formula ZnO which corresponds to the group II-VI binary semiconductor compound according. Some of the other semiconductors in this groups are Cadmium Sulfide (CdS), Cadmium Selenide (CdSe) and Cadmium Telluride (CdTe) which are widely used for the fabrication of thin film solar cells (Williams, 1960). Among the important characteristics, ZnO is a non-toxic, photoconductive and piezoelectric material which has a wide band gap energy (around 3.3 eV) (S. Agarwal, Jangir, Rathore, Kumar, & Awasthi, 2019) at room temperature, and an exciton bond of 60 meV (Jie et al., 2004; Laurent, Yu, Tusseau-Nenez, & Leprince-Wang, 2008; Sengupta, Sahoo, Bardhan, & Mukherjee, 2011; Thomas, 1960; Vyas, 2020). Zinc oxide is already used as a transparent window for several types of solar PV cells (Alias & Mohamad, 2014; Ellmer & Klein, 2008; Fodjouong et al., 2013; Matsubara et al., 2003; Vittal & Ho, 2017). Also, due to its hexagonal crystallographic wurtzite type structure (a=0.325nm, c=0.521nm) (Özgür & Morkoç, 2018)) (Norton et al., 2004), ZnO can be deposited as a flexible thin film that made it interested for fabrication of flexible devices such as solar cells and sensors (Belaid et al., 2015; Xiang et al., 2006).

Among of the electrical and optical properties, ZnO is inherently a n-type material with a good electron mobility (200 cm^2 V^{-1} s^{-1})) (Norton et al., 2004); which facilitates high electrical conductivity of the material. According to the literatures (Matsubara et al., 2003; Segets, Gradl, Taylor, Vassilev, & Peukert, 2009), the light transmission coefficient of ZnO is 91% in the visible spectrum, between 400 nm and 1100 nm. For the wavelengths between 200 and 360 nm (UV-visible range) the transmittance of ZnO is almost zero and therefore its absorbance is very high. The mechanical properties of ZnO ~~modified~~ are also interesting which a good stability (Fan,

Zhang, Wu, Yu, & Russell, 2020; Wei et al., 2019) and a long lifetime are reported for the fabricated ZnO-based solar cells (Kay & Grätzel, 2002).

In addition to the above mentioned properties of ZnO, this material is among of the inexpensive and very abundant materials on the earth (Pan, Risley, Martindale, & Heagy, 2018; Y. Wang et al., 2018; H. Zheng, Tachibana, & Kalantar-Zadeh, 2010). ZnO thin film can be synthesized by various methods such as hydrothermal (J. Qu et al., 2014), chemical bath deposition (C.-P. Lee et al., 2014), sputtering (magnetron) (Pham et al., 2015) and sol-gel method gel (Foo et al., 2014; Hasnidawani et al., 2016; Saleem, 2012). Regard it, the morphology of ZnO is also controllable according to the preparation methods and conditions, such as temperature and pressure (Arya et al., 2021; T. Guo et al., 2019; Sivakumar, Victor, Nayak, & Dhas, 2019).

In order to use a material in solar cell applications, its electrical properties should be improved using suitable doping elements that can be carried out in the synthesis process. As the doping additives, polyoxymetalates are excellent electron acceptors in their conduction bands. (Weinstock, 1998). Previous works had shown the improvement of the properties of solar cells based on CdS, CdTe, CdSe and In_2Sb_3 which had been prepared by chemical and electrochemical deposition with different heteropolyacids such as phosphotungstic acid, silicotungstic acid and phophomolybdic acid as the dopants (Savadogo, 1998). It had been resulted that there is dissociation of the tungsten-based heteropolyacid additives into different products including tungsten oxide in the doped material, in the case where silicotungstic acid is used. But until now from our previous results, the effect of heteropolyacid modifications of semiconductor on their properties is not well known.

It has been shown that heteropolyacids improve the performance of sensitized solar cells but remain intact in the ZnO (J. Li et al., 2013). The pH of the synthesis medium would be near neutral as it is a mixture of zinc acetate (0.33g) in ethanol solvent in the presence of a very small amount of polyoxymetalate (10 mL, 10^{-4} M) (J. Li et al., 2013). Moreover, the effect of polyoxometellates in improving the electrical performance of ZnO has been shown (Sang et al., 2012). The role played by phosphotungstic acid in improving the properties of ZnO has been also shown in a solvothermal synthesis from zinc acetate dehydrate (Q. Y. Li et al., 2008). The presence of PW_{12} observed in ZnO matrix has contributed to the enhancement of the photoluminescence and absorbance of phosphotungstic acid modified ZnO (Q. Y. Li et al., 2008)**.** The pH of the synthesis

medium has been kept nearly neutral by mixing a 0.5-1 g of zinc acetate dihydrate in 10-20 mL of ethanol, in the presence of 4 x 10^{-4} M of $H_3PW_{12}O_{40}$ (J. Li et al., 2013). In the process of doping ZnO, the W^{6+} ion with an ionic radius close to the radius of Zn^{2+} and is prone to substitute Zn^{2+} (Ngom et al., 2009).

As an additive, tungsten has a highly variable oxidation state (-4, -2, -1, 0, 1, 2, 3, 4, 5, 6) and tungstic acids (sources of the dopant) are distinguished according to their water content. Tungstic acids or WO_3 hydrates of the general formula WO_3-nH_2O are closely bound to the tungsten oxides (WO_x) and generally produce WO_3 hydrates in solution, which are annealed and cooled to give the desired crystalline phase of WO_x (Haidong Zheng et al., 2011) where x is a positive value expressing the oxygen content in the molecule since tungsten has a variable oxidation state. The most studied hydrates of WO_3 are : WO_4 . $2H_2O$ (the dihydrate), WO_4 .H_2O (the monohydrate), WO_4 . $0.5H_2$ O (the hemihydrate) and WO4 . 0.33H2 O. Zheng and Thanh-Khue stated in their reports that the hydrates of WO_3 can be dehydrated and finally transformed into WO_3 by calcination (J. Y. Zheng et al., 2015).

Tungsten oxide has electro-optical, electro-chromic, ferroelectric and catalytic properties (Georgieva et al., 2007; Svensson & Granqvist, 1984; Haidong Zheng et al., 2011). WO_3 is an n-type wide bandgap semiconductor that can act as an anode and/or help improve the performance of photovoltaic solar cells (Georgieva et al., 2007; Hara et al., 2011; H. Zheng et al., 2010). WO_3 can be considered in a simplified model as a modification of the ABO_3 perovskite lattice in which the A site remains unoccupied and the W atoms occupy the B site (Gillet, Aguir, Lemire, Gillet, & Schierbaum, 2004; Haidong Zheng et al., 2011). The perovskite electronic structure of WO_3 reveals that the band gap of WO_3 corresponds to the difference between the energy levels of the valence band formed by the O_2 p orbitals and the conduction orbitals W5d (Gillet et al., 2004).

The above literature reviews show that the species responsible for the improvement of the properties of semiconductors modified with the same heteropolyacid are different from one work to another. Moreover, in the case of ZnO, the effects of tungstic acid as a dopant for this material does not exist in the literature. Specially, it is interesting to study the optical and structural properties of the tungstic acid modified ZnO and determining the issues that are responsible for the modification. Our final objective will be the development of semi-transparent electrodes for applications in photosensitized cells. Based on our previous studies on the effect of hetero

polyacids on the physical-chemical, optoelectronic and PV solar cells properties of various semiconductors, this work will add significant knowledge for the understanding of the properties and behavior of these nanocomposites materials.

5.3 Methodology

In this work, the effect of tungstic acid monohydrate (H_2WO_4) as the additive in the precursor solution for synthesizing of W-doped ZnO material is studied. Sol-gel method as an efficient and less expensive method is considered for preparing ZnO material and depositing it as thin film on FTO/glass substrate for further application in DSSC solar cells. Investigations include the role of the additive on structural, optical, and electronic properties of ZnO material, through various characterization methods including XRD, SEM, UV-Visible spectroscopy and XPS. The chemicals products and equipment used are summarized in the following paragraph, then synthesis method and characterization techniques were presented.

5.3.1 Materials

To prepare the solution for synthesis, zinc acetate dihydrate $Zn(CH_3\ COO)_2\ 2H_2\ O$ with the purity of 98.0 to 101.0%, was purchased from Sigma Aldrich as the precursor. For the solvent, alcohol ethanol 95.0%, methanol or isopropanol were used. The catalyst consisted of NaOH >97% (Sigma Aldrich), HCl 15% or KOH. Finally as the stabilizer, monoethanolamine $HOCH_2CH_2NH_2$ 99.95% (Fisher Chemical), diethanolamine and tetramethylammonium hydroxide or ethyldiaminetetraacetate were used. These chemicals are used without further purification. As the substrate, a glass board with a layer of fluorine-doped tin dioxide FTO (SnO_2/glass) on its top was purchased from Sigma Aldrich TEC7. FTO was considered as the substrate (for a DSSC cell) because it is a good transparent to the light with transmittance of 80-82% Visible, and also, it has low electrical resistance of about 7 Ω/m^2 which facilitate electron flowing to the material. In addition, its electrical resistance is not changed in the temperature up to 500°C (according to Sigma Aldrich), which is the process temperature of the sol-gel method.

Before synthesis, the FTO coated glass was cut into the 2 cm x 2 cm samples where the area of the deposition was considered to be about 1 cm^2. Deposition of ZnO layer from prepared sol-gel was done using a KW-4A spin-coater (8500 rpm & 3.9″ max) at the room temperature and atmospheric

pressure. The samples were dried in a Thelco Laboratory OVEN dryer and annealed in a VULCAN 3-550 programmable oven.

5.3.2 Synthesis of samples

5.3.2.1 Synthesis of ZnO thin film

The synthesis of ZnO seed layer using sol-gel method was started by preparing a solution of 4.4g zinc acetate in 100 mL ethanol and stirring using a magnetic stirrer at 60°C for 15 minutes until a white solution was produced. After that, 1.2216 g of monoethanolamine (MEA) solution was drop by drop added to the solution which was kept at 60°C, under magnetic stirring for 2 hours, until a clear solution was reached. This solution was left for 24 hours at room temperature then its pH was measured which was about 7.5.

To prepare the substrate, the FTO/glass plates were cleaned in ultrasonic bath of acetone followed by ethanol, rinsed with deionized water and dried under a jet of ozone gas. Also, to keep reaching the conductive substrate, the two edges of FTO were covered with a Teflon tape. For producing a uniform deposition of the solution on the substrate, the prepared solution was spin coated on FTO at 3000 rpm for 20s. Then the sample was dried at 150°C for 10 minutes**.** The deposition-was repeated about 3 times to increase the thickness of the film to about 150 nm. The sample was annealed at 450°C for 2 hours using VULCAN 3-550 programmable oven, followed by cooling to 25°C, with the cooling rate of 10°C/min from. Finally, the sample was annealed in average temperature of 470° to improve the connections between the ZnO and the FTO substrate, and also, to rearrange the ZnO material into a hexagonal crystal structure. The final annealing also leads to produce a porosity of nanoparticles.

5.3.2.2 Synthesis of Doped-ZnO with H_2WO_4

The procedures of the synthesis of ZnO, which is doped with tungstic acid, is similar to that described above, except that the acid tungstic of different respective concentrations is added to the emulsion solution when the white solution is prepared. Tungstic acid was added with three different concentrations: 0.5×10^{-4} M, 10^{-4} M,1.5×10^{-4} M. Then a solution of 1.2216 g of monethanolamine (MEA) was added to this mixture under magnetic stirring at 60°C. The procedure be justified to reach a pH of 9.5 to 10 for the solution as a neutral to basic medium is

appreciated for successfully synthesis of ZnO (Alias & Mohamad, 2014). To ensure the complete dissolution of the tungstic acid, it was necessary to add drop by drop an additional amount of a solution of monoethanolamine until the pH of the solution was between 9.5 and 10. The mixture was kept under magnetic stirring at 60°C for 2 hours where the color of the solution get yellow. The yellow color is attributed to the presence of tungstic acid. The prepared solution was kept for 24 hours at room temperature. Finally, the sol-gel solution was used for depositing the thin film of doped-ZnO on the prepared FTO/glass substrate as the previous deposition was done. Like the deposition step in section 3.1, the spin coating was repeated three times where the final thickness of the thin films was increased to 300 nm. A summary of the synthesis procedures are given in Figure 5.1.

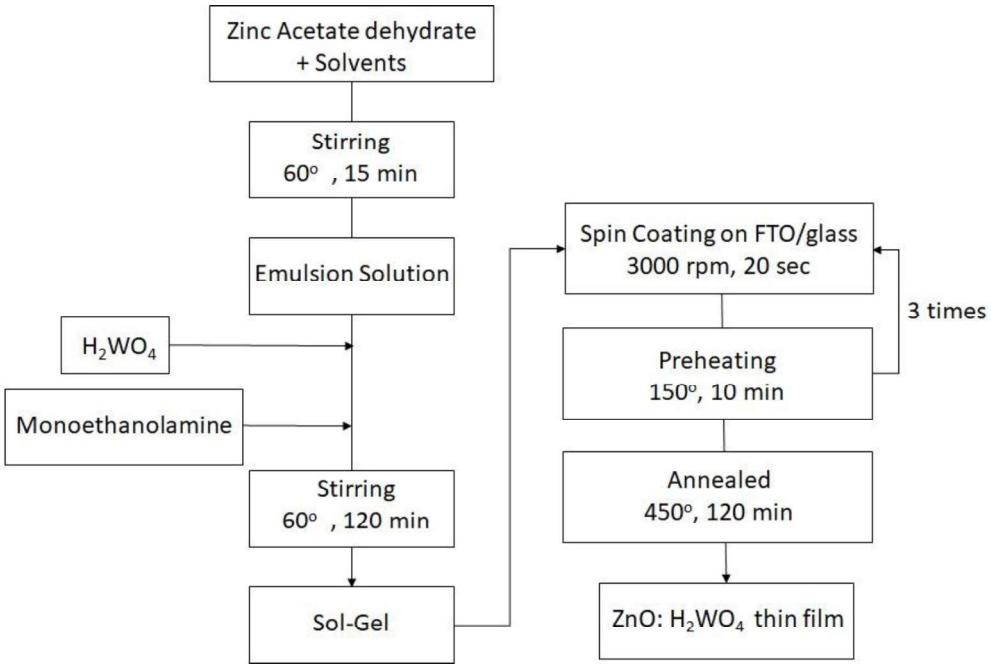

Figure 5.1 : A summary of the synthesis method for preparation of W-doped ZnO thin film and doping processes.

The synthesized ZnO thin film which made it suitable for DSSC solar cell application should have a large surface area to allow a high chemisorption of the electrolyte molecules. It is expected that the solid structure be cracks and defects free to facilitate fast and efficient interfacial load transfer. In addition, a porous structure is favored to hold a large amount of the electrolyte and ensure the interaction between the sensitizer molecules and those of the dye. This interaction is the

regeneration of the sensitizer. The oxidized sensitizer is regenerated by taking electrons from the triiodide ions in solution. Furthermore, to avoid accumulation of the charge carriers when the DSSC is subjected to a light irradiation, continuity of the bonds should be maintained between the particles of the semiconductor which allows the movement of the produced charge carriers.

To be suitable for solar cell application, the optical and electrical properties of ZnO is expected to be improved through the employed doping procedure. Dissolving tungstic acid ($WO_3.H_2O$) in synthesis solution would have mainly produced WO_3 with excess oxygen. (J. Y. Zheng et al., 2014). When calcining WO_3 hydrate in the presence of oxygen, WO_3 product obtained will contain an excess of oxygen due to the oxidation of WO_3 tungsten. Under vacuum (in the absence of oxygen), calcination at 450°C of WO_3 hydrate produces WO_3 with an oxygen deficit WO_{3-x}. ($x<0.0001$). Oxygen excess or deficit are defects that affect the optical and electrical properties of WO_3.

In further sections, the properties of the synthesized ZnO will be inspected using standard characterization methods and the observed behaviors will be discussed.

5.3.3 Characterization methods

5.3.3.1 X-ray Diffraction (XRD)

The XRD analysis allowed to identify the crystalline structure of the semiconductor. The diffractometer used in this work was a Buker D8 ADVANCE brand consisting of an X-ray source, a chamber where the ZnO samples are inserted in a slide, and the adhesion is ensured by the vacuum grease. The X-ray source was a tungsten filament at the cathode and copper at the anode. The device emits Kα lines of Cu with a weighted value of 1.5418 angstrom that strike the ZnO-based sample. The imposed voltage was 40 kV and the current was 40 mA. The detector above the sample in the diffractometer detects the diffracted light intensity as a function of the diffraction angle. The incident light arrives on two successive planes (of atoms) which is diffracted. If there is a constructive interference, based on Bragg's law, the following relation will be applied (Le Pevelen, 2010):

$$2d_{hkl}\sin\theta_{hkl} = n\lambda \qquad (70)$$

Where (h,k,l) is Miller index, d is the distance between atomic planes or inter-reticular distance, n is the diffraction order, λ is wavelength, and θ is the angle of incidence.

The inter-reticular distance in a hexagonal system is given by the relation:

$$\frac{1}{d^2} = \frac{4}{3}\left(\frac{h^2 + hk + k^2}{a^2}\right) + \frac{l^2}{c^2} \qquad (71)$$

With a=b=0.325 nm and c=0.521 nm.

5.3.3.2 The Scanning Electron Microscope (SEM)

To interpret the morphology and chemical composition of the ZnO thin films, A JEOL JSM-7600F SEM equipment was used which is a primary electron field emission SEM. The acceleration voltage was set at 10 kV. Also, the magnifications of the samples were 35,000 times and 220,000 times of the particle seeds.

5.3.3.3 UV-visible spectroscope

UV-visible spectroscopy was used to measure the light transmittance or absorbance as a function of wavelength to determine the absorbance property and band gap energy of the undoped and W-doped ZnO. The spectrometer used was a LAMBDA 1050 UV vis/NIR with PerkinElmer processing software in analytical mode. Using a monochromatic deuterium light source, wavelengths from 250 nm to 1200 nm are emitted onto and through the sample. Measurements was made with an error of 5 nm using two different detectors, the center mount and the sphere. The measurement system produce an error of ± 2% in the transmission spectra.

For electromagnetic radiation of wavelength λ passing through a transparent medium, the transmittance T expressed as a percentage is the ratio I/I_o (Picollo, Aceto, & Vitorino, 2019):

$$T = \frac{I}{Io} = e^{-\alpha d} \qquad (72)$$

Where I_o and I are the intensity of the incident and outgoing light, respectively. A is the absorption coefficient and d is thin film thickness or optical path length.

The absorbance A is given by the relation:

$$A = -\log(T) = \log\left(\frac{Io}{I}\right) = \alpha d \qquad (73)$$

The curve of the variation of the absorbance according to log (I_0 /I) makes it possible to deduce the coefficient of absorption alpha if the thickness of the sample is known.

According to Tauc's equation, the absorption coefficient is related to the width of the band gap of the material by the following relation:

$$\alpha h\upsilon = B\left(h\upsilon - E_g\right)^{\frac{1}{2}} \qquad (74)$$

Where B is a constant, E_g is the optical gap in eV, and hυ is energy of the photons.

5.3.3.4 XPS measurement

Some surface points of the electrode samples were subjected to XPS analysis to determine the presence of WO_3 and the chemical composition of the inspected surfaces. The measuring instrument in this study was Thermo Scientific capable of detecting all elements of the periodic table except hydrogen. The accuracy was 0.05% for most of the elements detected. The X-rays used in these measurements were Al with Kα=1486.6 eV. The diameter of the spot for XPS analysis was 400 µm.

5.4 Results and discussion

5.4.1 X-ray diffraction (XRD)

The ZnO sample deposited on the FTO was also subjected to XRD. The XRD spectrum of ZnO deposited on FTO (Figure 5.2) is a superposition of the detected ZnO and FTO spectra. The spectrum obtained after analysis is compared to the reference spectrum of pure ZnO (red peak above the XRD spectrum). The comparison of this superimposed spectrum of the sample prepared with tungstic acid to that of the reference spectrum of ZnO without tungstic acid highlights the contribution of tungstic acid on its chemical composition.

- ZnO reference pattern 01-071-6424 JCPDS identifies ZnO synthesized by the peaks: (100), (002), (101) , (102), (110), (103), (200), (112), (201), (004) around 31.77°, 34.44°, 36.26°, 47.55°, 56.6°, 62.88°, 66.38°, 67.96°, 69.10°, 72.61°, respectively (the 2*Theta diffraction angles). A hexagonal wurtzite structure is identified for the samples with a preferential orientation along the (101) direction. These results confirm that the method used led to a synthesis of ZnO with hexagonal crystallographic structure of wurtzite type (a=0.325nm, c=0.521nm) and space group P63mc.

- SnO_2 reference spectrum (JCPDS: Pattern: 00-041-1445 Quality: Star*) identifies peaks: (110), (101), (200), (111), (210), (211), (220), (002), (310), (221), (112), (301) respectively around the diffraction angles (2*Theta). A tetragonal structure is identified for the fluorine-doped tin oxide layer.

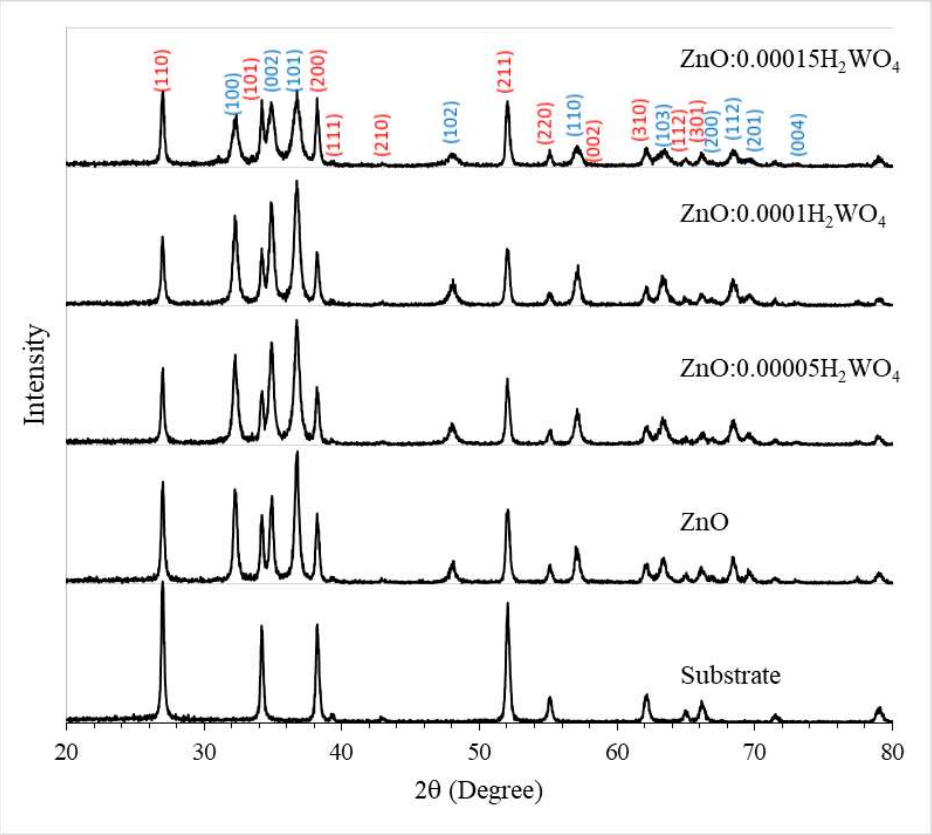

Figure 5.2 : all the diffraction peaks of the XRD spectrum of the prepared ZnO electrode on the FTO substrate: superposition of the 2 spectra. In blue: indexation of ZnO and in red indexation of SnO_2:F (FTO).

Note that there is no additional diffractogam for the tungsten oxide phases due to the presence of the tungsten additive. Calculations performed on the XRD data showed that W had almost no influence on the orientation of the diffraction planes. The wurzite structure is therefore the growth structure of the elaborated nanoparticles. These diffraction results corroborate those obtained by doping ZnO with P (D. Zhao, Li, Sathasivam, & Carmalt, 2020).

The two thin films: ZnO and FTO have perfectly diffracted X-rays according to the Bragg's law for the electrodes prepared with ZnO.

Crystal size: The crystal size (denoted by τ) is determined by measuring the broadening of the maximum XRD peak and using the Scherrer formula:

$$\tau = \frac{180}{\pi} \frac{k\lambda}{\cos\theta\sqrt{FWHM^2 + s^2}} \qquad (75)$$

With : π=3.142; λ=1.5406: radiation wavelength of CuKα, k=0.89 is the Scherrer constant; s is the instrumental width (corresponds to 0 for Bruker Advanced X-ray solutions D8 instrument); Θ angle corresponding to the plane; FWHM: is the full width at the half plane.

The positions of the diffraction peaks (101), the values of the total width at half maximum (FWHM) and the sizes of the crystallites of the samples calculated are shown in the table 5.1 below and plotted in Figure 5.3.

The effect of tungstic acid is to decrease the crystallite size to a minimum value of 17.14 nm for 10^{-4} M dopant. The average crystallite size is obtained by averaging the crystallite sizes in all the diffracted planes. The resistivity of the samples was measured using the conductance monitor Delcom Instruments. Similarly, there is also a decrease in resistivity to a minimum value of 1.45 Ω/sq.

Table 5.1: XRD data and crystallites size and sheet resistance of samples

% H_2WO_4 in ZnO	(101) FWHM	Peak Position 2θ(Degree)	Crystallite size τ (nm)	Mean crystallite size (nm)	Sheet resist (Ω/sq)
0	0.339	36.26	27.42	26.88±1	2.29±0.05
0.00005	0.44	36.74	21.11	22.09±0.8	1.81±0.03
0.0001	0.543	36.76	17.14	16.08±0.9	1.45±0.02
0.00015	0.448	36.75	20.4	20.9±0.7	1.95±0.03

The evolution of FWHM or crystallite size decreases with the content of the H_2WO_4 additive and can be attributed to an interaction between the ions from the additive in solution in a matrix of ZnO crystals. As mentioned in the introduction, tungsten ions are likely to replace zinc ions in the same hexagonal crystal structure giving the samples a doping. Figure 5.3 shows the effect of the tungstic acid additive which decreases the size of the ZnO crystallites. And the doping size of ZnO with tungstic acid is minimal for a doping of 10^{-4} % of the dopant

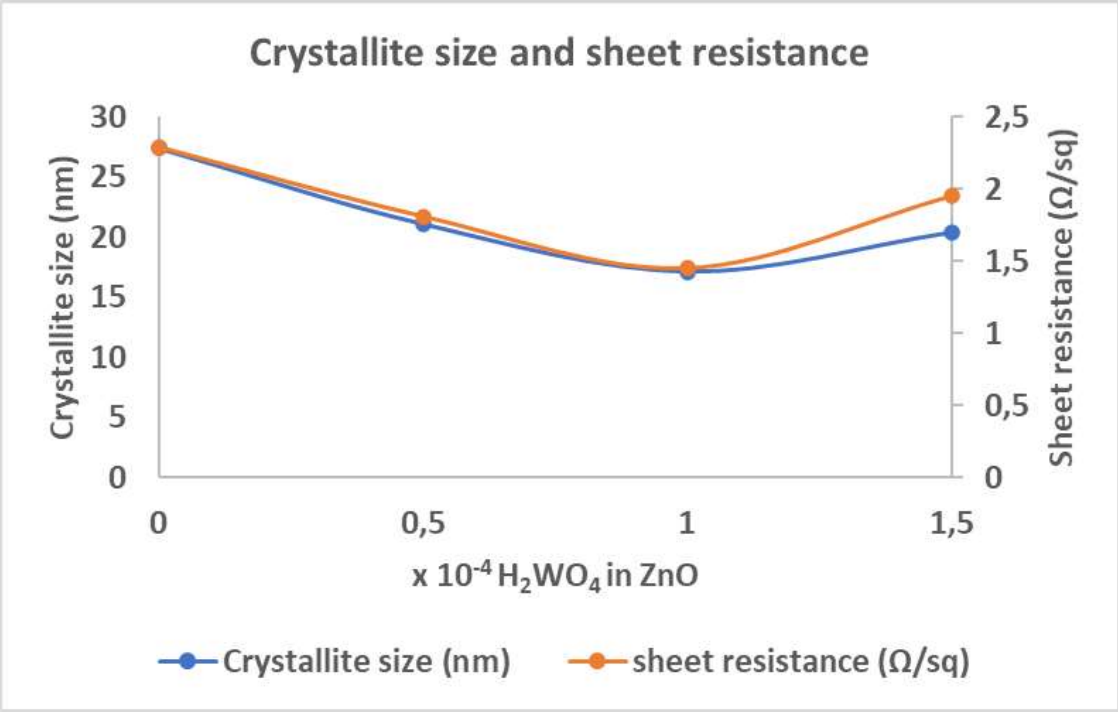

Figure 5.3: Variation of the crystallites size and sheet resistance with the concentration of the dopant.

5.4.2 Scanning electronic microcopy (SEM)

The SEM image of the synthesized ZnO samples is presented in Figure 5.4. The topographic view in Figure 5.4 (a) shows the nanometer size ZnO seeds in the form of spheres, with a variable diameter between 20 to 30 nm. The notion of surface-volume of nanoparticles seems fundamental in this study of modified ZnO material. Indeed, for samples with spherical nanoparticles (Figure 5.4 (a)), the surface volume ratio is low and thus the absorption capacity of dyes and light rays is low.

On the other hand, for modified ZnO samples where the spherical shape is deformed in the form of a polyhedron (Figure 5.4 (b) and (c)) and fractals (Figure 5.4 (d)), the surface-to-volume ratio is high and therefore a better absorption of dyes and light rays could be predicted for DSSCs.

The SEM results shows that by increasing the quantity of the acid in the sol-gel, the grain size of ZnO is slightly increased from an average of 25 nm to 50 nm which indicates that the material is more crystallize when it is doped by tungsten acid.

The SEM results show that by increasing the quantity of the acid in the electrolyte of the sol-gel

process the grain size of ZnO is slightly increased from an average of 25 nm to 50 nm which indicates that the material is more crystallize when it is doped by tungsten acid.

For ZnO doped with H_2WO_4, a change in the thin film morphology is observed which is proportional to the amount of doped tungstic acid. Figure 5.4 (b) show the morphology of ZnO which is prepared by adding 0.00005M H_2WO_4 to the initial solution. A modification of the relief of ZnO seed layer into polyhedral seeds is seen in this figure. Also, in some part of the image (Figure 5.4 (c)), the presence of tungsten in the ZnO matrix can be observed by a more voluminous and sub-bright phase. In Figure 5.4 (d), the morphology of the ZnO thin film is presented where the quantity of the acid is increased to 0.00015M, the image show that the porosity of the layer is increased by increasing the quantity of the dopant element to 0.00015M. This porosity is an asset for the adsorption of dyes and light rays.

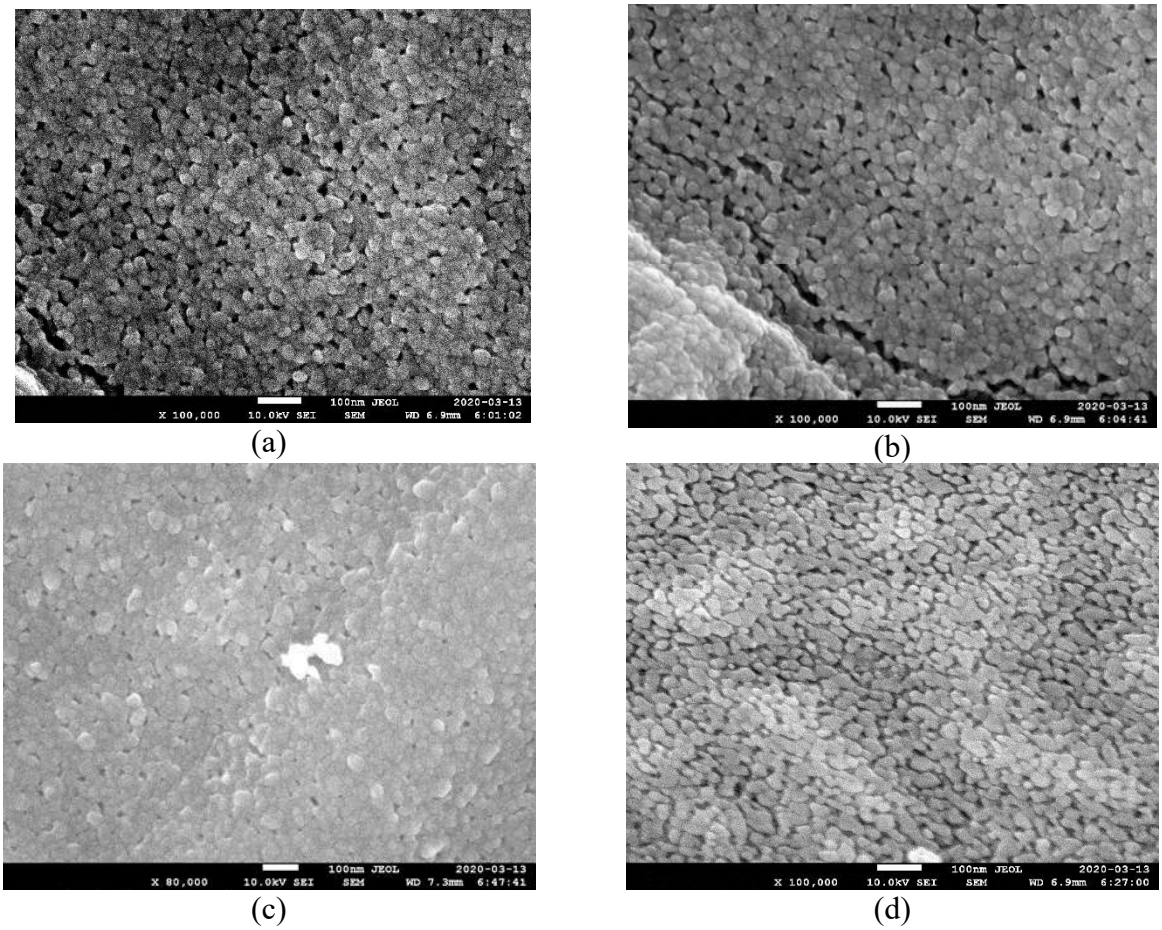

Figure 5.4 : Morphology of ZnO thin film deposited using sol-gel method: a) Seed layer, b) Doped with 0.00005%H_2WO_4, c) Doped with 0.0001%H_2WO_4, and d) Doped with 0.00015%H_2WO_4.

5.4.3 UV/visible spectroscopy

UV-visible transmittance curve of ZnO and ZnO doped versus wavelength is shown in the Figure 5 (a). It is seen that electronic absorption peaks for all the samples are occurred between 250 nm to 380 nm. Also, By adding H_2WO_4 to the synthesis solution, the transmittance peaks are decreased between 375 nm and 750 nm. Through the absorption peaks, calculation of the band gap is possible using equation (5). But a more precise values for the bandgap energy can be determined from tauc plot which was obtained from equation (4). This plot directly shows the absorption peaks versus absorbed energy in electron-volt at the point where the tangent meets the x-axis. The slopes of the curve $(\alpha h\upsilon)^2$ as a function of $h\upsilon$ are shown in Figure 5 (b).

The optical criteria for the semiconductor to be photosensitized is that the ZnO must have a wide band gap. WO_3 monoclinic has a band gap of 2.62 eV while WO_3 amorphous with the most distorted structure has a band gap of 3.25 eV. Furthermore, J. C. Chou et al. demonstrated that the WO_3 based semiconductor can have a variable band gap ranging from 2.66 eV to 3.24 eV depending on the proportions of excess or deficit oxygen in the semiconductor (D. Zhao et al., 2020). The experimental parameter in this sputtering synthesis is the variation of the deposition pressure of the target material WO_3. The modifications of ZnO by a source H_2WO_4 widen the gap band in the new sample with an observation of 2 linear parts on the curves of modified ZnO (Figure 5 (b) in grey and yellow). This can be identified as two semiconductors in one sample: ZnO and another tungsten-based semiconductor, WO_3 from tungstic acid.

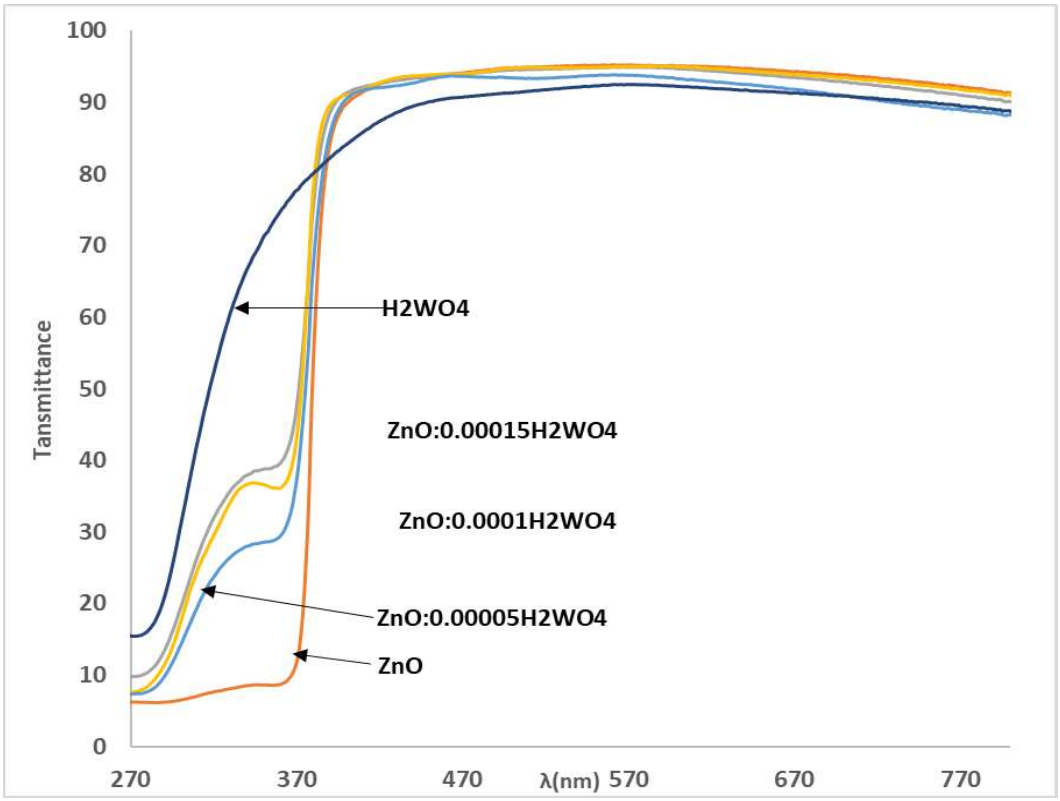

(a)

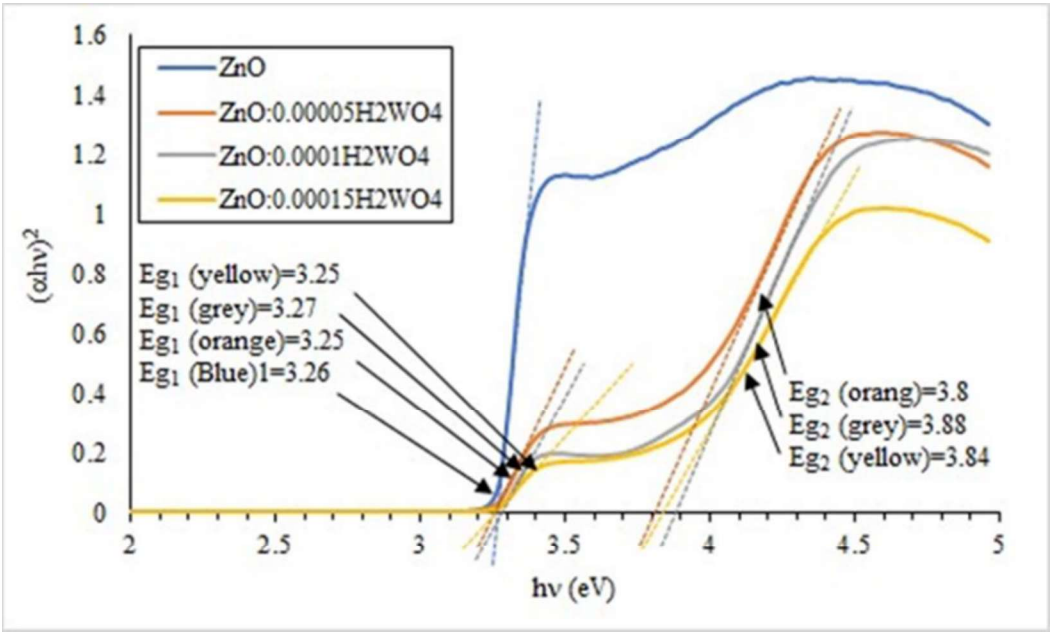

(b)

Figure 5.5 : UV-Visible spectroscopy of ZnO doped by various quantity of H_2WO_4, a) UV-visible Transmittance curve and b) Tauc plot for bandgap estimation

Plotting the slopes (in black) of the different parts of the $(\alpha * h\upsilon)^2$ curves of the samples gives the following summary gap band values (Table 5.2).

Table 5.2: Effect of the grain size of the particles on the low region band gap and high region band gap respectively of the samples

Sample	Grain Size (nm)	Eg_1 (eV)	Eg_2 (eV)
ZnO	25	3.27±0.030	-
ZnO:0.00005H_2WO_4	30	3.26±0.026	3.80±0.02
ZnO:0.0001H_2WO_4	45	3.25±0.023	3.88±0.01
ZnO:0.00015H_2WO_4	50	3.24±0.025	3.84±0.01

Tungstic acid doped ZnO nanoparticles are direct transition type semiconductor. The band gap for intrinsic ZnO nanoparticles was 3.27 eV while the bands gap (Eg1) between 3.26 and 3.24 are attributed to ZnO in tungstic acid doped ZnO. The band gaps (Eg_2) for tungstic acid doped ZnO was increased from 3.8 to 3.88 eV probably because the donors atoms provide additional carriers that causes the shifting of Fermi level towards conduction. Therefore, band gap becomes larger.

From these analyses we deduce that the sample consists of the semiconductors ZnO and probably a mixt nanocomposite ZnO-WO_3. The relative variation of the band gap of the the nanocomposite ZnO-WO_3 material must be related to the concentration of the doping agent as shown in Figure 5.5 and Table 5.2. These ZnO and tungsten-doped ZnO-based samples are potential candidates as DSSC electrodes. Sensitization of these newly synthesized materials was done by immersion in a 0.3 mM N719 dye solution for 30 minutes. We obtain a purples and semi-transparent electrodes. Spectral responses with broad absorption bands in almost the entire UV-visible range are obtained for the dye-immersed ZnO and doped ZnO curves (Figure 5.5) while the absorption band of the non-immersed electrode stops at around 385 nm (Figure 5.5). These results prove that the fabricated electrode samples are likely to be good candidates for DSSC. These results corroborate those obtained by F. Wang et al. [52] in their studies on the spectral behavior of ZnO and ZnO immersed in N3 dye.

These curves help to identify the effect of the doping on the absorption spectral response of the ZnO based sample with the dye. N719 and in the widest possible range of solar rays. The significant increase of the band gap after doping (3.25 vs 3.8 eV) is favorable for a better

absorption of the solar rays of the dye when doped samples are used. With an absorption of sufficient energy ($E=h\upsilon$), the electrons will be released from the Highest Occupied Molecular Orbital (HOMO) to the lowest energy Lowest Unoccupied Molecular Orbital (LUMO).

These electrons are then injected into the conduction band (CB) of the semiconductor oxide and are transported to the anode terminal to be discharged into the circuit. The photocurrent depend on the interaction between semiconductor-dye and the absorption of solar rays bye the dye (C.-Y. Chen, Wu, Wu, Chen, & Ho, 2006). In Figure 5.6, dye N719 is responsible for this very high absorption. In fact, the absorption of light by the dye is attributed to the transfer of charge from the transition metal to the ligand and to the molecular orbitals HOMO and LUMO (Shalini et al., 2016). The metal-to-ligand charge transfer peak position is around 530 nm. The slight blue shift when increasing the doping concentration is due to the electron coupling between the excited dye and the surface of the material. The oxide semiconductor plays more the role in the transport of charge carriers and as adsorption material for the dye. By increasing the doping level from 0.0001 to 0.00015, it is seen that the absorption peak between 450 and 600 nm is decreased, but between 300 to 400 nm, there is an increasing in the absorption peak when the concentration of the doping is augmented.

Finally, it is resulted that the absorption peaks are shifted towards the lower wavelengths, when ZnO is doped with tungsten, by adding H_2WO_4 to the solution. The latter indicates that the material is more suitable for fabrication of the ultraviolet solar cell detector device.

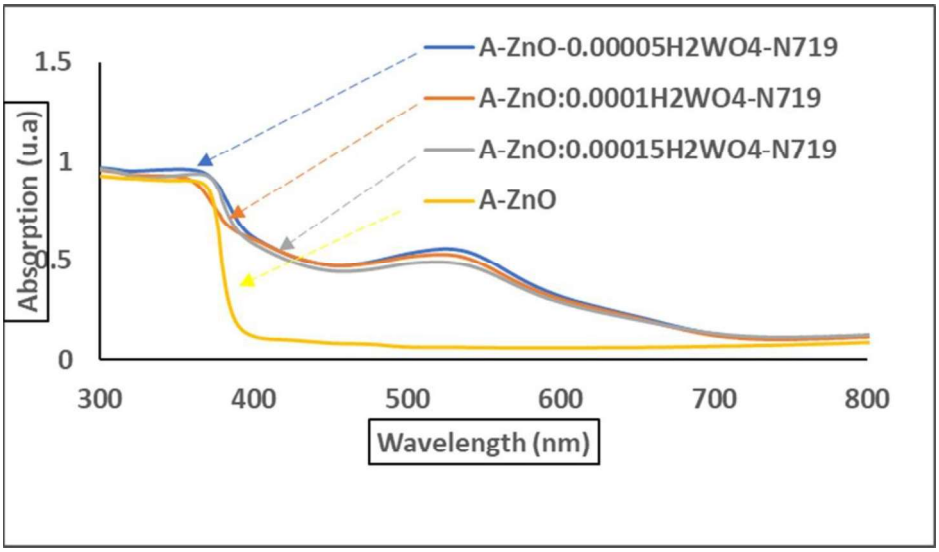

Figure 5.6 : Electronic absorption spectra of ZnO based electrodes immersed in the N719 sensitizer. In Yellow: absorption of ZnO; in Blue, pink and grey spectra of samples (ZnO, ZnO : 0.5 x 10^{-4} H_2WO_4, ZnO: 10^{-4} H_2WO_4 and ZnO :1.5.10^{-5} ZnO) immersed in N719.

5.4.4 X-ray photoelectron spectroscopy (XPS)

XPS analysis was used to determine the oxidation state of the chemical species present as well as their chemical composition. The XPS survey spectra at energy range of 1400 to 0 eV shows nanoparticle morphology for samples with and without tungstic acid (Figure 5.7). W is only detected with the samples doped with tungstic acid. The deconvolution peaks of zinc,, oxygen and tungsten detected in the sample are shown in Figures 5.8 a), b) and c) respectively.

The two Auger peaks of Zn L2MM and Zn L3MM are centered at 475 and 499 ±0.54eV, respectively. For all the ZnO and tungstic acid -doped ZnO samples, the analysis shows two main peaks attributed to the Zn^{2+} doublet peaks type, related to the Zn–O bonding where the peaks at 1022±0.035% eV and 1045 eV (figure 5.8 a)) correspond to Zn $2p_{3/2}$ and Zn $2p_{1/2}$, respectively. It has been verified experimentally that the binding energy of Zn is the same for doped and undoped ZnO.For all W-doped ZnO samples, the W4f submitted for analysis reveals an assigned W^{6+} doublet with a binding energy centered around 36.0 ±0.32 eV (figure 5.8 (b)).

Figures 5. 8 (c) shows the fitting curves of the oxygen 1s peak by Gaussian functions around a binding energy of 531 ±0.53% eV which is characteristic of O^{2-} (D. Zhao et al., 2020). This binding energy attests the presence of WO_3 (Ji et al., 2017) material in the doped ZnO sample. XPS analysis

identified Zn, O, and W in the doped ZnO samples. The binding energies of Zn prove that they are oxides: ZnO, WO_3.

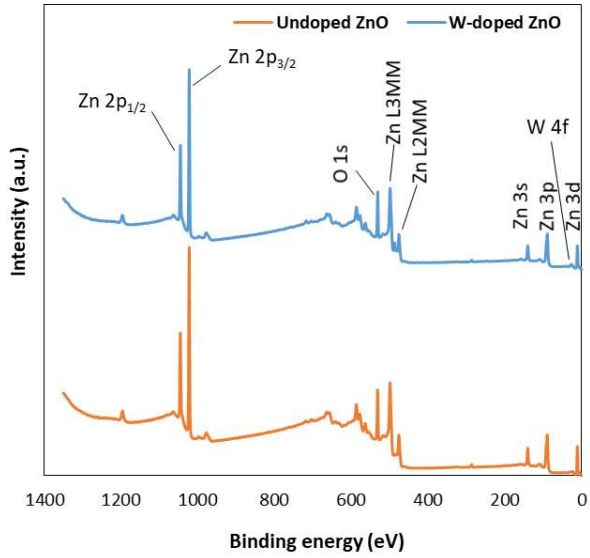

Figure 5.7 : X-ray photoelectron overview spectra of ZnO films prepared without tungstic acid (red curve) and with tungstic acid (blue curve)

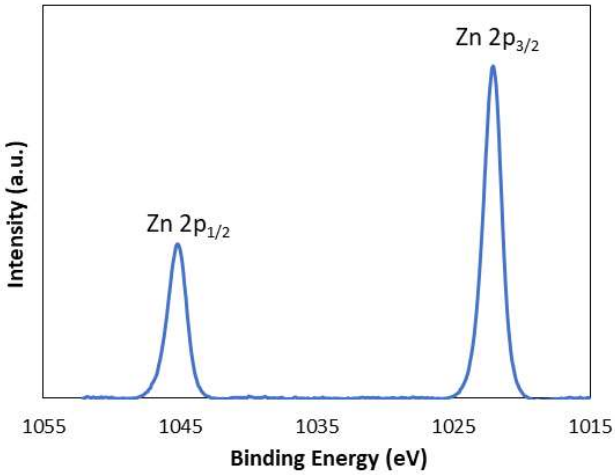

Figure 5.8 (a)

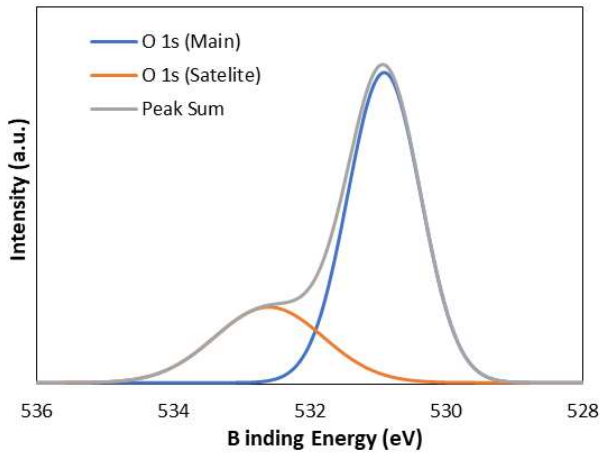

Figure 5.8 (b)

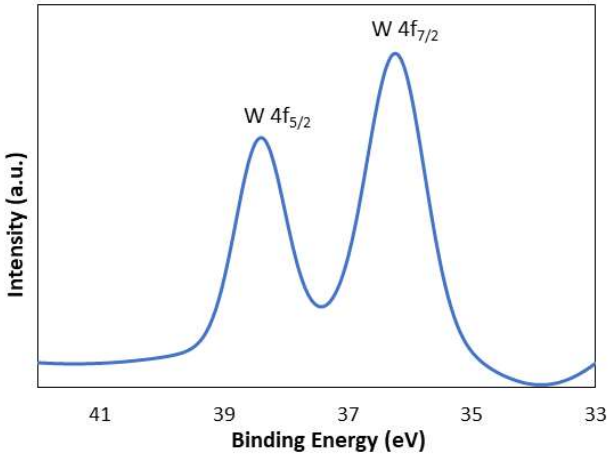

(c)

Figure 5.8 : a) XPS spectrum of detected Zn 2p, on the surface of all the doped and undoped samples, b) XPS spectrum of detected O1s, on the surface of all the doped and undoped samples, and c) XPS spectrum of detected W on the surface of tungstic acid-doped sample

5.5 Conclusion

The Sol-gel method was used to fabricate ZnO with and without tungstic acid. In the presence of tungstic acid a total dissociation of H_2WO_4 in the ZnO matrix was observed. The obtained products were subjected to XRD analyses for identification of XRD structural compositions. The XRD analyses allowed to determine the phases of the samples: ZnO with hexagonal structure. A decrease in the size of the crystallites was determined when zinc oxide was doped with tungstic acid. This decrease in crystallite size results in an increase in the band gap of the W-doped ZnO.

This is a first route of modification of ZnO by tungstic acid in total dissolution and this leads to the elaboration of semi-transparent electrodes for DSSC application.

SEM observations of the relief and morphologies reveal for tungstic acid-doped ZnO: polyhedral and fractal morphologies susceptible to high dye adsorption and high light absorption. SEM observations of the relief and morphologies show: the effect of the modification on the seed layer particles of ZnO, the tungsten base wungsten, high porosity based on fractal morphology which allows high dye adsorption and high light absorption. The XPS spectra of the sample prepared with tungstic acid shows the presence of WO_3 in the sample. This may conduct to the formation of new composite ZnO-WO_3.

The UV-Visible spectra shows a variation of the band gap ZnO with the concentration of tungstic acid. The band gap value (3.25 eV) obtained without H_2WO_4 is attributed to that of ZnO. The value of the band gap increases from 3.5 eV to 3.88 eV for various concentrations of tungstic acids. The results show that without band gap of ZnO is indeed 3.26 eV at 300°K and increases to 3.75 eV when the concentration of the H_2WO_4. is 0.5×10^{-4} M and up to 3.88 eV for a dopant concentration of $1.5.10^{-4}$ M. The variation of the band-gap with concentration of H_2WO_4 might be attributed to the band gap of the new nanocomposite ZnO-WO_3 which relative ratio between ZnO and WO_3 may probe the band gap to large values toward entire UV- visible spectrum when the concentration of the doping agent increases. By immersion of these ZnO and tungstic acid-doped ZnO electrodes in 0.3 mM ethanolic solution of N719, the spectral responses are almost in the entire UV-visible range. This makes these samples good candidates for DSSC.

CHAPITRE 6 ARTICLE 3 : PERFORMANCES OF DYE SENSITIZED SOLAR CELLS (DSSCS) BASED ON ZINC OXIDE (ZnO) PHOTO-ANODE DOPED WITH TUNGSTIC ACID PREPARED BY SOL-GEL METHOD

Padjagoto Sangmbaye, Oumarou Savadogo
Laboratory of New Materials for Energy and Electrochemistry, Polytechnique Montreal (QC), Canada.
*sangmbaye@gmail.com, **oumarou.savadogo@polymtl.ca; phone: +1 514 3404725

Submitted to the Journal Discover Energy on August 2, 2022

6.1 Abstract

The elaboration and characterization of dye (photo)sensitized solar cells (DSSC) based on ZnO un-doped and ZnO doped with tungstic acid (H_2WO_4) samples as photo anodes are shown. The tungstic acid was added at 10^{-4} M during the synthesis processes to modify/dope the zinc oxide. Zinc acetate dehydrate is used as the precursor, the sol-gel synthesis route was used to produce solution-gels of ZnO and ZnO: H_2WO_4 which are respectively deposited by spin-coating in thin films on Florine-doped Tin Oxide (FTO) coated glass. The cathodes were fabricated using doctor blade deposited platinum thin film pastes. XRD analysis of ZnO powders and ZnO seed layer (deposited by spin-coating) allowed to determine the hexagonal crystal structure of the synthesized ZnO grains. The SEM observation showed the effect of the tungstic acid doping on the morphology of ZnO seeds. It was clearly shown that this morphology is modified by the addition of tungstic acid doping. The current-voltage (I-V) performance of DSSCs fabricated with ZnO and ZnO:H_2WO_4 were measured. Moreover, an improvement of the DSSCs with H_2WO_4 additive was obtained.

Keywords -- sol-gel method, zinc oxide, acid tungstic, dye (photo)-sensitized solar cell (DSSC).

6.2 Introduction

(Photo)sensitized solar cells (DSSC) are more and more developed during the recent years because

they are promising as an alternative power supply (Babar et al., 2020; Kokkonen et al., 2021). They are considered as part of the third generation of photovoltaic cells technology. They have various advantages which include: (i) low manufacturing cost, low fabrication energy consumption, thin film cell (monolayer) requiring very small material. Their operation at low intensity and diffuse lights levels, their conversion efficiency not very sensitive to the angle of incidence of light rays and their flexibility (glass or plastic substrate) make them serious candidates as a source of autonomous power or energy backup on portable objects or any electrical receiver outdoors or indoors to capture the illumination of light bulbs. As examples of applications we can indicate their integration on the windows of buildings, laptops, bags, clothing, etc.

Photosensitized cells are photo-electrochemical cells made of titanium oxide (TiO_2), tin (SnO_2), zinc (ZnO), tungsten (WO_3) semiconductors on which a sensitizer is adsorbed (Babar et al., 2020; Kokkonen et al., 2021) (Figure 6.1). TiO_2-based DSSCs achieved a maximum efficiency of 12.3-14% (Kakiage et al., 2015; Mathew et al., 2014; Yella et al., 2011). The DSSC efficiency depends on the one hand on the ability of the dye to inject electrons (under the effect of solar rays) into the HOMO layers (highest occupied molecular orbital) of the semiconductors and on the other hand on the ability of the semiconductors to accept these electrons.

Solar cells based on ZnO semiconductors have already been realized by using various methods such as hydrothermal method (J. Qu et al., 2014), Chemical Bath Deposition (C.-P. Lee et al., 2014), Chemical Vapour Deposition (Baxter & Aydil, 2005; H. Chen et al., 2008), Physical Vapour Deposition (Fodjouong et al., 2013; L. E. I. Guo & Kerr, 2011) sol-gel for the fabrication of photoanodes. To improve their performance, ZnO additives or doping have been applied to the working electrode (anode) in these DSSCs. We successfully developed a sol-gel method for the doping of ZnO with tungstic acid in our paper 1 (ZnO-H_2WO_4 properties). We use this electrode to develop the DSSCs in this paper. The results of doping ZnO with tungstic acid showed the presence of W in the ZnO matrix bringing a change of the band gap from 3.3eV to 3.5eV and 3.8 eV depending on the amount of W in the ZnO matrix (see paper 1via sol-gel on ZnO:H_2WO_4). This new metal oxide semiconductor could be an advantageous replacement for TiO_2 and ZnO in the preparation of DSSCs. The efficiency obtained from DSSCs based on ZnO and the dye N719 are around 4 to 5 %. (Gerrit Boschloo et al., 2006; Chauhan et al., 2016; I.-D. Kim et al., 2007; Y.-Z. Zheng et al., 2010).

The isoelectric point (zero charge point) of ZnO is at 8-9 pH (Blok & Bruyn, 1970) which makes it more basic than TiO_2 which has its isoelectric point 5.5 to 6.5 pH (Kosmulski, 2002). Dyes being acidic tend to attack ZnO leading to the formation of agglomerates which slow down the injection of electrons into the conduction band to generate photocurrent (Vittal & Ho, 2017). The modified or H_2WO_4 doped ZnO could facilitate this injection of electrons in the conduction band of the doping element and thus contribute to improve the photocurrent in the solar cell. Indeed the W^{6+} ion with an ionic radius close to the radius of Zn^{2+} is inclined to substitute Zn (Ngom et al., 2009). Photocatalytic properties of W, O and H based additives have been demonstrated in solar cells (Savadogo, 1998; Savadogo & Mandal, 2019a, 2019b) and/or in semiconductor electrodes (J. Li et al., 2013; Sang et al., 2012; Weinstock, 1998).

J. Li et al added some heteropolyacids ($H_3PW_{12}O_{40}$, $H_4SiW_{12}O_{40}$, $H_4GeW_{12}O_{40}$) to ZnO in the fabrication of electrodes for photosensitized cells (J. Li et al., 2013). The results of their work indicate the intact presence of these heteropolyacids at the anode and improve the performance of photosensitized cells. In this work, tungstic acid was a sol-gel dopant of ZnO and used for the fabrication of DSSC photoanodes. The role of tungstic acid in the ZnO semiconductor and in the photosensitized cells was explored in the results and discussions.

In the following paragraph, the fabrication methodology of zinc oxide and tungstic acid doped zinc oxide based on DSSC cells has been described. The anodes of these cells were made by sol-gel route using a single precursor zinc acetate dehydrate. The cathode, sensitizer and electrolyte are identical for the two different DSSC cells. The developed photo-electrochemical cells are constituted at the anode of a dye adsorbed semiconductor (N719) and at the cathode of a metal (platinum) immersed in a redox electrolytic solution (I^-/I_3^-). The substrate used at the anode and cathode is fluorine-doped tin oxide (SnO2:F). The performance results of the 2 cells were presented and discussed in the results and discussion section and a conclusion was made to finish. DSSCs work like a battery when they are under illumination. We can schematize the DSSC as a stack of FTO, semiconductor, dye, electrolyte, platinum, FTO materials schematized on the Figure 6.1.

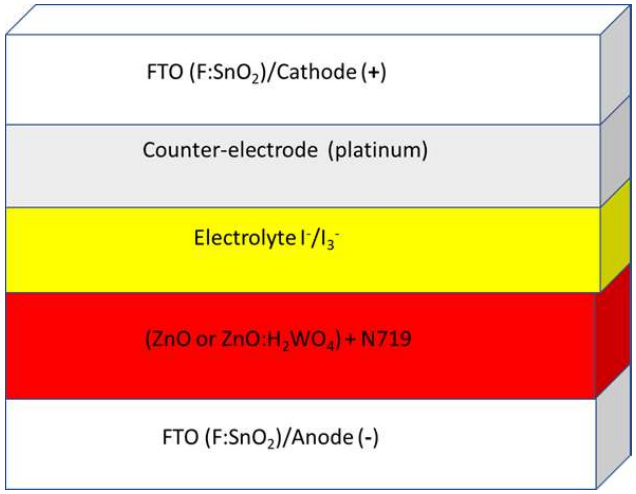

Figure 6.1: Structure of the undoped or doped ZnO-based DSSC

6.3 Materials and methods

6.3.1 Materials

The precursor zinc acetate dihydrate ($Zn(CH_3COO)2\ 2H_2O$, 98.0 to 101.0% Sigma Aldrich), the solvent which is an alcohol: ethanol 95.0%, methanol or isopropanol, catalyst (NaOH >97% Sigma Aldrich, HCl 15% or KOH) and stabilizer (monoethanolamine $HOCH_2CH_2NH_2$ 99.95% Fisher Chemical, diethanolamine, tetramethylammonium hydroxide or ethyldiaminetetraacetate). These chemicals are used without further purification. The substrate used is a glass on which a layer of fluorine-doped tin dioxide FTO ($SnO2$: F, glass) of the brand Sigma Aldrich TEC7 was applied. We used a good FTO substrate for a DSSC fabrication which has the following characteristics: (i) A high transparency to light with a transmittance of 80-82% Visible; (2) low electrical resistance to facilitate electron flow; 7 Ω/m^2; This electrical resistance must be independent of temperature up to a temperature of 500°C, which is the operating temperature of the sol-gel method; (3) Cut surface of the substrate: 2 cm x 2 cm for an active surface of deposit of 1 cm^2.

A kW-4A spin-coater (8500 rpm & 3.9″ max) and Automatic Doctor Blade MSK-AFA-III equipment are also available for the deposition of solutions on the FTO substrate. The solutions deposited at room temperature and under an atmosphere were dried in a Thelco Laboratory OVEN dryer. A VULCAN 3-550 programmable oven was used for annealing ZnO.

The dye used is a synthesized sensitizer N719 from the manufacturer Solaronix. Since it is the dye

that injects the electrons into the cell, we will look for an adsorption of the sensitizer by the doped ZnO semiconductor. This dye is identified or synthesized for a DSSC solar cell because its band edge coupling with the semiconductor meets the following criteria(Katoh, Furube, Barzykin, Arakawa, & Tachiya, 2004; Nelson & Chandler, 2004; J. X. Zhao et al., 2013) :: (i) The Dye regeneration may be faster than the recombination of charge carriers (Katoh, Furube, Barzykin, et al., 2004) ; (ii) its LUMO (lowest unoccupied molecular orbital) level is higher than the conduction band level of the semiconductor (Nelson & Chandler, 2004); (iii) The density of electron acceptor states in the semiconductor might match the electrons injected by the dye; (iv) the HOMO level (highest occupied molecular orbital) of the dye must be higher than the valence band level of the semiconductor; (v) Its structure may allow the dissociation of the exciton charges; (vi) it is Stable in electrolyte, under irradiation; (vii) its absorbs a wide range of solar radiation spectrum: sensitivity ; (viii)The lifetime of the excited state of this dye is long enough to allow charge transfer to the electrodes.

The N719 sensitizer from Solaronix meets these criteria and is the only one used in the manufacture of the 2 DSSCs.

The electrolyte used is iodolyte Z-150 from the manufacturer Solaronix. The electrolyte is a solution containing a redox couple such as I^-/I_3^-. The solvent is methyl3 propionitrite, the additive is alkylbenzimidazole and the redox concentration is 150mM.

The assembly of the DSSCs was carried out using a Dupont Surlyn gasket material (25µm Solaronix) fixed between the two electrodes for the confinement of the electrolyte. The contact of the different components of the cell according to the Figure 6.1 The result is a ZnO-based solar cell sensitized with N719 dye.

6.3.2 Preparation of ZnO/ZnO:H_2WO_4 and DSSC

In fact, tungstic acid (with a W/Zn ratio 0.5 $M10^{-4}$ to 1.5 $M10^{-4}$) is taken as the doping element and added to the mixture of the precursor solution. The mixture is stirred (about 7 minutes) until a homogeneous, colorless solution is obtained.

This section focuses on the description of the manufacturing processes of ZnO samples. Based on the method described by K. L Foo et al. [29] we performed the synthesis as follows: Firstly, 4.4 g of zinc acetate were weighed and introduced into 100 mL of ethanol solution. This solution was

then stirred with a magnetic stirrer at 60°C for 15 minutes which led to a white solution. Tungstic acid was added with three different concentrations: 0.5×10^{-4} M to 1.5 $\times10^{-4}$ M. Then 1.2216 g of monethanolamine (MEA) solution was added dropwise to this mixture which was kept under magnetic stirring at 60°C for 120 minutes. The procedure be justified to reach a pH of 9.5 to 10 for the solution as a neutral to basic medium is appreciated for successfully synthesis of ZnO (Alias & Mohamad, 2014). To ensure the complete dissolution of the tungstic acid, it was necessary to add drop by drop an additional amount of a solution of monoethanolamine until the pH of the solution was between 9.5 and 10. This solution was left for 24 hours at room temperature to give a pH of about 7.5. In a second step, a glass substrate with a conductive FTO (fluorine-doped tin oxide) surface is placed in the solution obtained below for deposition. For this purpose, the FTO conductive glass substrate is first cleaned in an ultrasonic bath with a detergent solution, acetone followed by isopropanol (or ethanol) and then rinsed with deionized water and dried with ozone; In a third step, the edges of the FTO are covered with a Teflon tape and the solution is deposited on the FTO. The FTO-solution assembly is rotated by spin coating at 3000 rpm for 20s allowing a uniform deposition of the solution on the substrate. Then the sample is dried at 150°C for 10 minutes**.** The deposition-drying operation is repeated 3 times. Then, the sample is annealed at 450°C for 120 min using the VULCAN 3-550 programmable oven, followed by cooling in the oven at a speed of 10°C/min from 450°C to 25°C. A thin layer of ZnO or doped ZnO is obtained.

A summary of the synthesis procedures are given in Figure 6.2. a. The sample was immersed in 3.10^{-4} M N719 during 30 min before being removed and dried according to the Figure 6.2. b

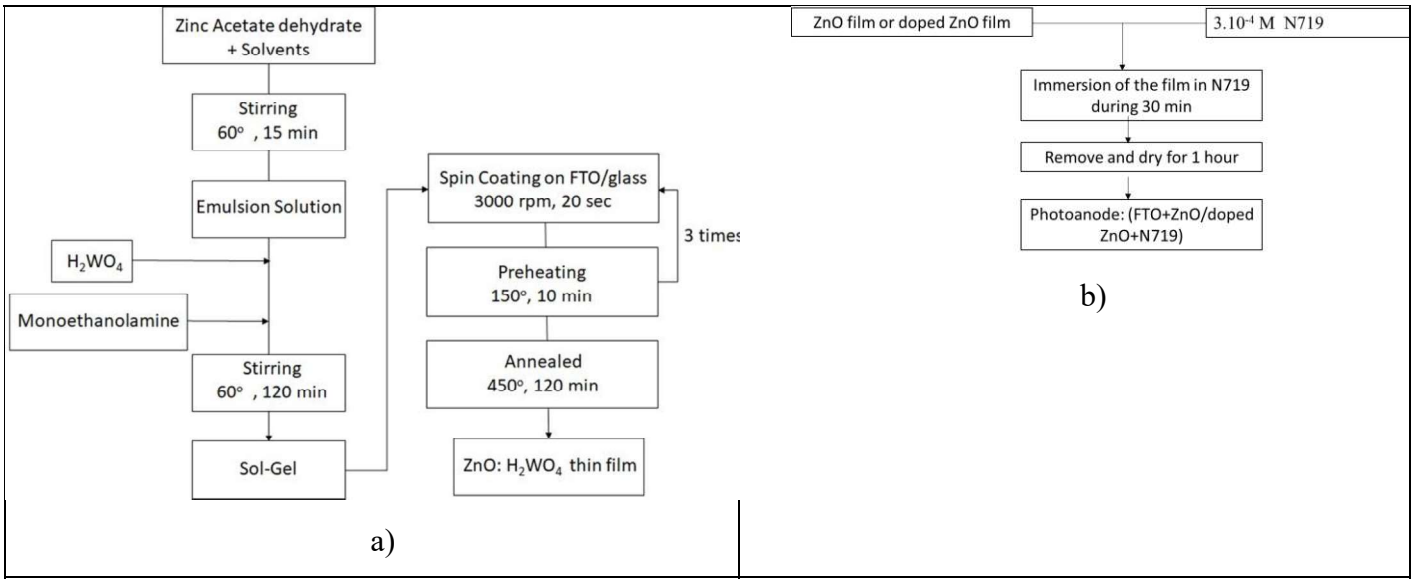

Figure 6.2: a) Summary of the steps of the synthesis method for preparation of tungstic acid-doped ZnO thin film and doping. b) Immersion of the anode in dye: flowchart for the manufacture of the photoanode

The method of elaboration of the cathode consists in depositing a few drops of the Platisol T/SP solution with spreading of a thin layer on the substrate by Doctor Blade (Figure 6.3). The assembly is heated in an oven at a speed of 10°C/min from 25°C to 450°C for 10 minutes. Then the cooling down of at a speed of 10°C/min from 450°C to 25°C follows.

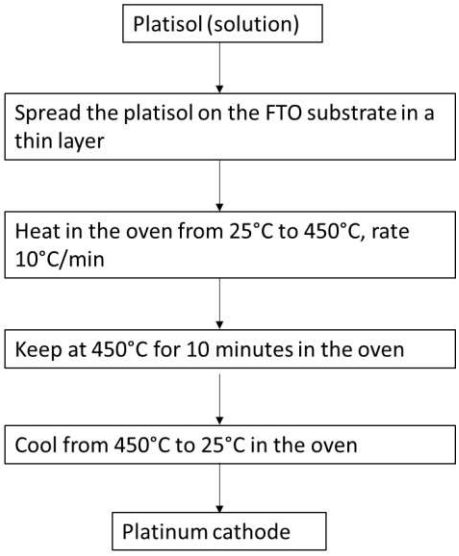

Figure 6.3: Steps of the procedure for manufacturing the cathode from the Platisol solution

To assemble the two electrodes into a DSSC cell, the electrolyte (I^-/I_3^-) is sandwiched between the photoanode and the cathode (Pt) thanks to Dupont Surlyn 25µm of Solaronix. The electrolyte solution was inserted between the 2 electrodes by capillary action. Dupont Surlyn 25µm is a transparent, thermoplastic polymer material used to seal the two electrodes into DSCC.

6.3.3 Characterizations

6.3.3.1 X-ray Diffraction (XRD)

The XRD analysis allowed to identify the crystalline structure of the semiconductor. The diffractometer used in this work was a Buker D8 ADVANCE brand consisting of an X-ray source, a chamber where the ZnO samples are inserted in a slide, and the adhesion is ensured by the vacuum grease. The X-ray source was a tungsten filament at the cathode and copper at the anode. The device emits Kα lines of Cu with a weighted value of 1.5418 angstrom that strike the ZnO-based sample. The imposed voltage was 40 kV and the current was 40 mA. The detector above the sample in the diffractometer detects the diffracted light intensity as a function of the diffraction angle. The incident light arrives on two successive planes (of atoms) which is diffracted. If there is a constructive interference, based on Bragg's law, the following relation will be applied (Le Pevelen, 2010):

$$2d_{hkl}\sin\theta_{hkl} = n\lambda \qquad (76)$$

Where (h,k,l) is Miller index, d is the distance between atomic planes or inter-reticular distance, n is the diffraction order, λ is wavelength, and θ is the angle of incidence.

6.3.3.2 Scanning Electron Microscope (SEM)

The JEOL JSM-7600F SEM was used to observe the surfaces of the ZnO-based samples to interpret their topography and chemical composition. It is a primary electron Field Emission Scanning Electron Microscope (FEG). The electron acceleration voltage was set at 10 kV and the magnifications of the samples were 000 10times and 220 000 times of the particle seeds.

6.3.3.3 Energy dispersive spectroscopy (EDS)

The EDS apparatus used is of the brand OXFORD Instruments coupled to the SEM JEOL JSM-7600F. The same sample analyzed by SEM can be analyzed by EDS.

6.3.3.4 Dektak XT Bruker

It is a high resolution profilometer capable of measuring thin films with thicknesses of less than 10 nm. Dektak XT Bruker is equipped with a diamond-tipped stylus and an optical camera to perform thickness measurement on 3D.

6.3.3.5 Infrared spectroscopy

The samples were subjected to infrared spectroscopic analysis in order to determine the bonding of the molecules of a sample using absorption, emission or transmittance band spectra. The peaks and/or bands of the absorption spectra reflect the vibrational states of the bonds of the molecules in the sample. Also, these peaks and/or absorption bands can be more or less intense, fine or wide depending on the molecules in the sample. This technique allows to determine in a qualitative way the chemical elements of the analyzed sample. The IR spectrometer used in this study is a Perkin Elmer FTIR 65 type ATR (Attenuated Total Reflectance) spectrometer connected to a computer that calculates the Fourier transforms and processes the detected vibrations.

6.3.3.6 Resistance sheets

The resistivity of semiconductors is intermediate 10^{-3} to 10^{3} Ω.m between that of insulators and metals. The instrument for measuring the resistivities of ZnO and doped ZnO thin films is the Delcom Instruments 737 monitor. In contrast to four-point measuring equipment, the measuring technique of this monitor is non-contact and non- destructive. To perform the conductance measurement on two or more layers, the operator must first read the conductance of the first layer and then coat the sample with the new material and perform the second measurement. The conductance of the second layer is obtained from the difference of the two measured values. Delcom guarantees an accuracy of 99.9% in eddy current measurements.

6.3.3.7 Current-voltage measurements

The measurements of the quantities were performed using a Model 273A potentiostat/Galvanostat connected to the terminals of the fabricated DSSC cells submitted under the standard laboratory pressure temperature conditions AM1.5, 25°C P= 1atm. For an illumination of 100 W/cm^2 using a Xenon lamp (XQ-500W, Beijing Changtuo Device, PR), the current-voltage density (Figure 6.11) is acquired.

6.4 Results and discussion

6.4.1 X-ray diffraction (XRD)

For the ZnO deposited by spin-coating, the XRD analysis also allowed to identify the hexagonal crystal structure (ZnO reference pattern 01-071-6424 JCPDS) of the ZnO semiconductor. The diffractometer used is a Buker D8 ADVANCE. The average grain size is 23.82 nanometers. These results confirm that the method used led to a synthesis of ZnO of good purity with a hexagonal crystallographic structure of wurtzite type (a=0.325nm, c=0.521nm)

The XRD spectrum of ZnO deposited on FTO (Figure 6.4) is a superposition of the detected ZnO and FTO spectra.

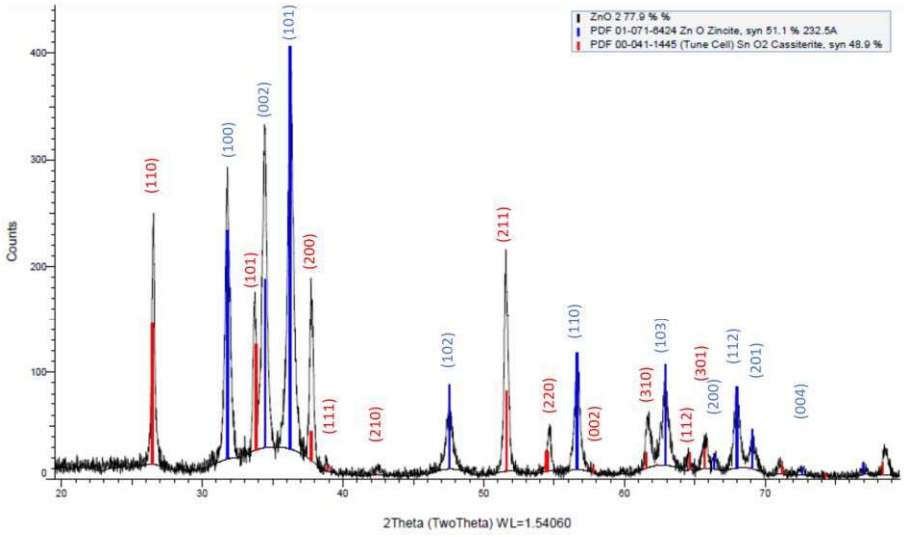

Figure 6.4: XRD spectrum of ZnO (in blue) on FTO (in red): superposition of the 2 spectra. In black the measurement, in red the indexation by the reference of the pure compound of ZnO and in blue the indexation by the reference compound of FTO which allows to identify all the peaks.

XRD analysis of ZnO doping with tungstic acid did not reveal a change in crystal structure but a decrease in crystal size.

Crystal size

The crystal size (denoted by τ) is determined by measuring the broadening of the maximum XRD peak and using the Scherrer formula:

$$\tau = \frac{180}{\pi} \frac{k\lambda}{\cos\theta\sqrt{FWHM^2 + s^2}}$$

With : π=3.142; λ=1.5406: radiation wavelength of CuKα, k=0.89 is the Scherrer constant; s is the instrumental width (corresponds to 0 for Bruker Advanced X-ray solutions D8 instrument); Θ=36°/2 angle corresponding to the (101) plane; FWHM=0.2640 °: is the full width at the (101) half plane. The average grain size is 55.8 nanometers.

These results confirm that the method used led to a synthesis of ZnO of good purity. These values are in accordance with the SEM observation of ZnO seed layer (Figure 6.5 a)).

The tungstic acid additive decreases the size of the ZnO particles during doping. The positions of the diffraction peaks (101), the values of the total width at half maximum (FWHM) and the sizes of the crystallites of the samples calculated are shown in the table 6.1.

Table 6.1: XRD data and crystallites size and sheet resistance of samples

% H_2WO_4 in ZnO	(101) FWHM	Peak Position 2θ(Degree)	Crystallite size τ (nm)	Mean crystallite size (nm)	Sheet resist (Ω/sq)
0	0.339	36.26	27.42	26.88±1	2.29±0.05
0.00005	0.44	36.74	21.11	22.09±0.8	1.81±0.03
0.0001	0.543	36.76	17.14	16.08±0.9	1.45±0.02
0.00015	0.448	36.75	20.4	20.9±0.7	1.95±0.03

6.4.2 Scanning electron microscope (SEM)

The Figure 6.5 a) topographical view gives an observation of ZnO seeds with variable dimensions between 20-40 nm in the form of a sphere. There is a relative uniformity in the distribution of particles on the FTO substrate.

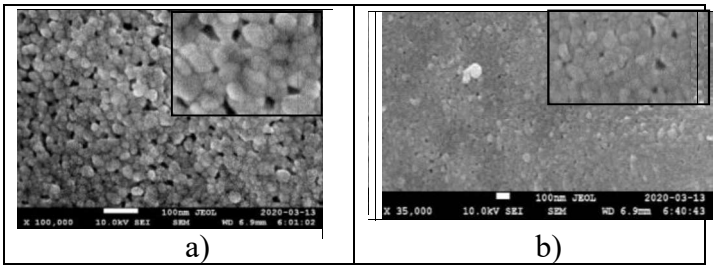

Figure 6.5: (a) SEM micrographs which shows the Morphology of ZnO seed layer deposited on FTO/glass. (b) SEM micrographs of the Morphology of ZnO doped with H_2WO_4 deposited on FTO/glass by spin coating (right).

This topographic view of ZnO at 100,000x magnification (left) and 220,000x magnification (top left) reveal particle seeds. In the Figure 6.5 a), there is a change in the relief of ZnO seed layer into polyhedral seeds, more uniform and smaller in volume for ZnO doped 10^{-4} with H_2WO_4. These morphologies have higher surface-to-volume ratios than the case shown in Figure 6.5 b). The porosities are likely to facilitate the mobility of charge carriers. Also note a better interconnection between particles in the case of ZnO seed layer modification by tungstic acid. The presence of tungsten is observed in the ZnO matrix by a more voluminous and sub-bright phase. These morphological changes are also observed in the synthesis of ZnO doped with Cu (Joshi et al., 2016).

6.4.3 EDS

The analytical spectrum and chemical composition of the sample in mass percentage is given in Figure 6.6. The mass percentages are respectively 20.3% for oxygen and 79.7% for zinc which corresponds to an atomic percentage of 50.86% for oxygen and 49.24% for zinc. (see table 6.2). The measurement was made with a standard deviation of 0.3%.

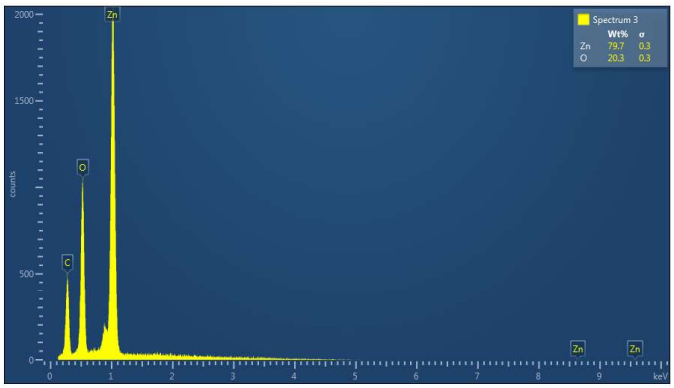

Figure 6.6: EDS semi quantitative analysis of the chemical composition of ZnO: spectrum of the chemical elements and chemical composition in the following Table 6.2.

Table 6.2: Chemical composition of the sample in mass and atomic percentage

Chemical element	Theoretical mass percent (%)	Theoretical atomic percent (%)	Mass EDS percent (%)	Atomic EDS percent (%)
O	19.66	50	20.3	50.86
Zn	80.34	50	79.7	49.14

6.4.4 Profilometer

The profiles of the doped ZnO and ZnO are not uniform but show a rough surface. Over an inspected distance of 7 mm, we have an average thickness of 10 µm. However, a variation in thickness between 0 and 2 mm, swept by the stylus, is noted, with a maximum thickness of 40 nm. Then from 2 to 3.5 mm, we have thickness peaks reaching 0.6 µm, 1.2 µm and 0.27 µm which are at the edges of deposits. Finally, between 3.5 mm and 7.4 mm of stylus reading, the maximum thickness is 14 µm. These thickness variations are explained by the substrate which is a doped compound body does not have a flat surface without roughness and at its edges, we also fixed ribbons to avoid deposits. The edges serve as collection points for the current generated by the cell.

6.4.5 Sheet resistance

The measurement of sheet resistance of doped ZnO/ZnO based electrodes as a function of doping is reported in table 6.1. The resistivity reaches a minimum value for a doping of H_2WO_4 à a concentration of 10^{-4} M when compare to those of ZnO. This result may support the performance of H_2WO_4-doped ZnO-based DSSCs, which might exhibit higher power density than those based on ZnO alone.

6.4.6 FTIR spectroscopy

The FTIR spectroscopy measurements carried out (Figure 6.7 to Figure 6.10) have made possible to highlight the following aspects: Figure 6.7 is the FTIR transmittance spectrum of FTO. The absorption band located between 450 and 700 cm^{-1} correspond to the vibrations of Sn-O and Sn-O-Sn bonds. This result is corroborated by those obtained by Arghya NARAYAN Banerjee and S. Kundoo (Banerjee, Kundoo, Saha, & Chattopadhyay, 2003).

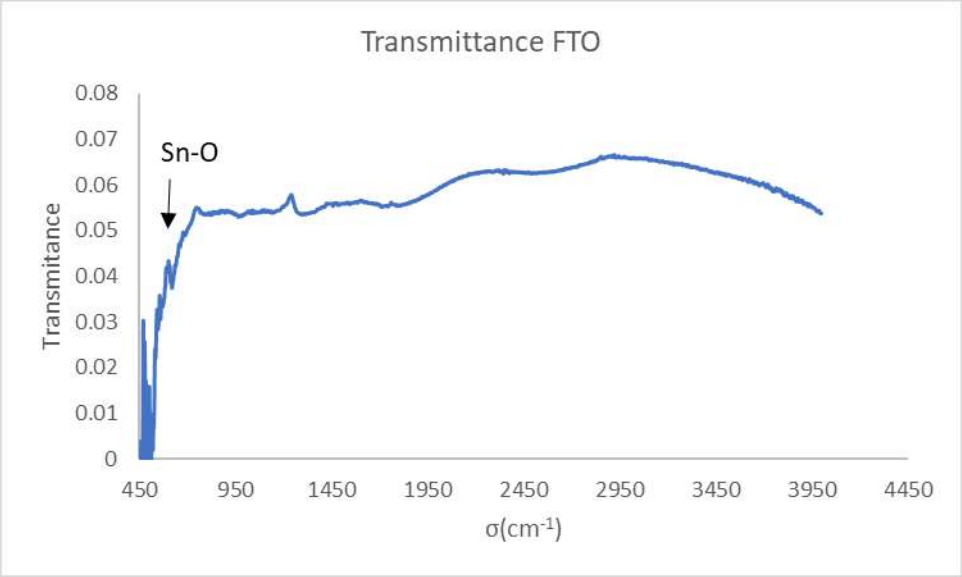

Figure 6.7: FTIR Spectrum of the transmittance energy variation with the wavelength for FTO coated glass.

Figure 6.8 shows the FTIR transmittance spectrum of ZnO seed layer deposited on FTO. Sn-O and Sn-O-Sn peaks between 450 and 700 cm^{-1} in the FTO glass fills Zn-O in the ZnO thin film. The absorption peaks in the region from 425 cm^{-1} to 560 cm^{-1} are due to the elongation vibrations of

the Zn-O (Dhanalakshmi et al., 2016b). M. Kooti and N. Sedeh (Kooti & Naghdi Sedeh, 2013) identified these Zn-O bond vibrations at 436 cm^{-1} while G. Nagaraju et al. (Nagaraju et al., 2017) and H. Kleinwechter et al. (Kleinwechter, Janzen, Knipping, Wiggers, & Roth, 2002) observed vibrations between 425 cm^{-1} to 560 cm^{-1} . According to Dhanalaskshmi (Dhanalakshmi, Natarajan, Ramadas, Palanimurugan, & Thanikaikarasan, 2016a) the observation of a strong peak at 450 cm^{-1} would be attributed to the elongation vibration of ZnO which confirms the Wurzite structure of the synthesized samples. The peaks confirming the presence of Sn-O and Sn-O-Sn (Banerjee et al., 2003) bonds overlap with the vibrations of Zn-O.

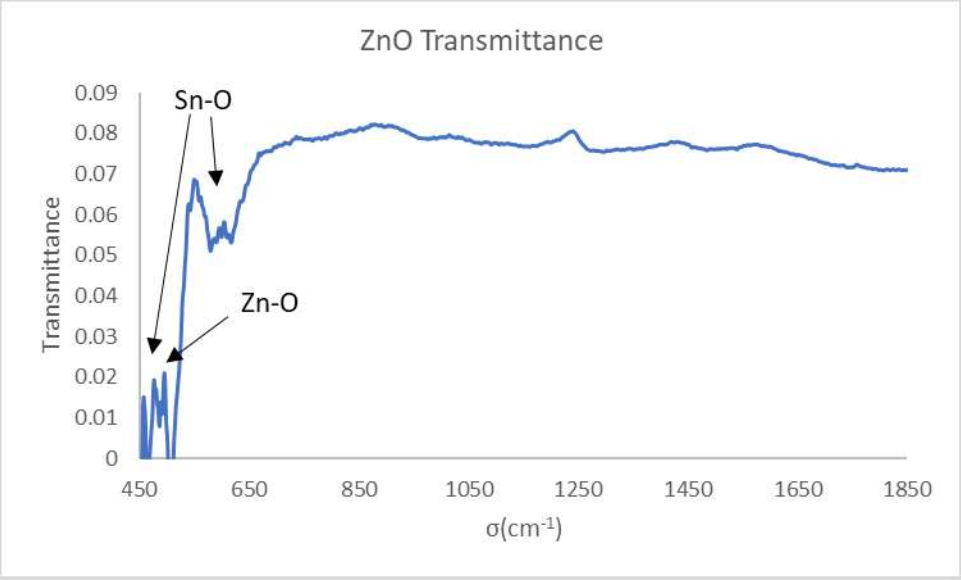

Figure 6.8: FTIR Spectrum of the transmittance energy variation with the wavelength for the ZnO layer deposited on FTO

Figure 6.9 shows the FTIR spectra of the FTO, ZnO alone and an increase of the H_2WO_4 from 0.00005 M to 0.0001 M in the ZnO semiconductor.

We have note experimentally that from 2700 cm^{-1} to 4000 cm^{-1}, there is a strong absorption when we increase the amount of dopant . This is supported by other authors (Dhanalakshmi et al., 2016a). At high wave numbers, we see a transmittance proportional to the amount of dopant. While at low wave numbers, there is a decrease in transmittance from 500 cm^{-1} to 2700 cm^{-1} with the increase in the amount of dopant.

For the FTIR spectra of ZnO with H_2WO_4 additives there are also overlaps of the W-O, Zn-O and

Sn-O absorption peaks between 500 - 900 cm^{-1} (Figure 6.9). It is also worth noting a small shift around the wavelengths of 536 cm^{-1} for the ZnO spectrum and 550 cm^{-1} for those of the ZnO with tungstic acid spectra (0.00005 M and 0.0001 M) . Also, the amplitude of the transmittance spectrum of ZnO without additives is larger than that of the transmittance spectrum of ZnO with $H_2 WO_4$ for strain vibrations between 450- . This is justified by the W-O vibrations which are less important than that of Zn-O because of the size of the W atom which is larger than Zn. Also we can say that the absorbance is more important in the doped samples from 450-2700 cm^{-1}. Consequently, ZnO deposited with tungstic acid might give a nanocomposite material type of $ZnO\text{-}WO_3$ which might have its own bang gap which is different from ZnO and that of WO_3 respectively. We may anticipate that the performance of DSSC based on $ZnO\text{-}WO_3$ will

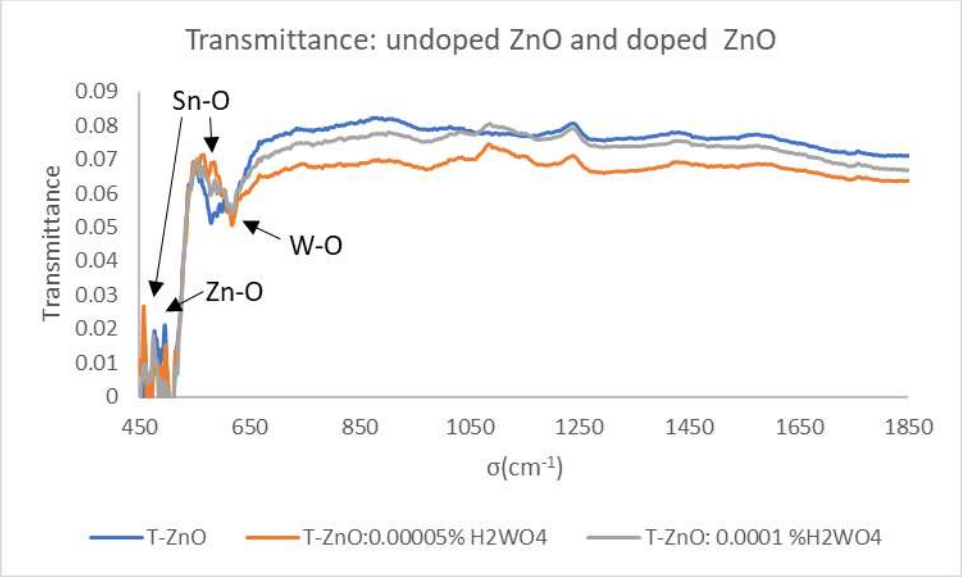

Figure 6.9: FTIR Spectrum of the transmittance energy variation with the wavelength of ZnO thin film (blue), ZnO thin film doped with 5.10^{-4} M H_2WO_4 (brown), ZnO thin film doped with 10^{-4} M H_2WO_4 (grey).

This is supported by the FTIR Spectrum of the transmittance energy variation with the wavelength of H_2WO_4 which is shown in Figure 6.10. We can see in this Figure 6.10 that W-O peaks are observed at 550-950 cm^{-1} and O-H peaks are observed at 1641 cm^{-1} and 3494 cm^{-1} respectively. Accordingly, the broad absorption band located at wave number 3494 cm^{-1} is a feature of the O-H bond elongation vibrations of H_2O contained in $H_2O.WO_3$ (Nogueira, Cavaleiro, Rocha, Trindade, & de Jesus, 2004). The absorption band at 1641 cm^{-1} is also attributed to the O-H bond vibration

(Kleinwechter et al., 2002) .The strong absorption peaks at 550-950 cm^{-1} corresponding to the W-O bonds which is consistent with the results of the work of H.I.S Nogueira et al. (Nogueira et al., 2004), G.N. Kustova et al. (Kustova, Chesalov, Plyasova, Molina, & Nizovskii, 2011).;

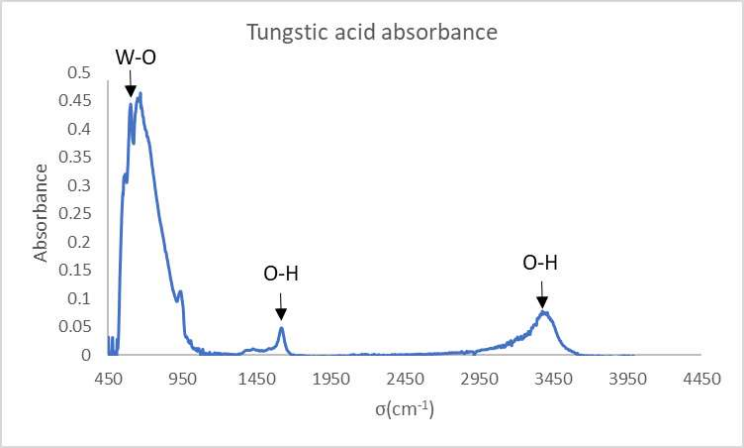

Figure 6.10: FTIR Spectrum of the transmittance energy variation with the wavelength for tungstic acid

6.4.7 Effect of the tungstic acid doping of ZnO photo anode on the DSSC performances

Figure 6.11 shows the curves of the variation of the current vs voltage under illumination of 50 mW/cm^2 and 100 mW/cm^2 of the DSSC based on ZnO fabricated (Cell 1) without tungstic acid and the DSSC based on ZnO fabricated with tungstic acid (Cell 2). Cell 1 is a spin-coated ZnO-based DSSC with a geometric surface area S=1cm x 1 cm= $1cm^2$. Cell 2 is the DSSC based on ZnO doped with H_2WO_4 with a mass ratio of $1:10^{-4}$ and deposited on the FTO conducting glass using spin-coating with the same surface area as the un-doped sample. The curves were obtained using a potentiostat/Galvanostat Model 273A under the normal conditions of laboratory of pressure and temperatures AM1.5, 25°C and p= 1atm.

We do not show the current-voltage curves under dark because in the dark the two DSSC (Cell 1 based on un-doped ZnO and Cell 2 based on tungstic acid doped ZnO) behave like a diode and exhibits the similar curves with a low current density which The Accordingly, in the dark, the tungstic acid doping has no effect on the current voltage characteristics of the cells.

When the two DSSC cells are respectively illuminated there is a significant increase of the current

and the potential. The improvement in the short circuit current (I_{sh}) and the open circuit voltage are more important for DSSC based on cell 2, e,g. ZnO fabricate with tungstic acid than those of cell 1 in comparison to that or ZnO fabricated without tungstic acid (Figure 6.11). The values of the characteristics obtained on the DSCC based on un-doped ZnO are similar to those obtained elsewhere on ZnO-based DSSC (Anta, Guillén, & Tena-Zaera, 2012; Hongsith, Mangkorntong, Mangkorntong, & Choopun, 2008; R. Kumar et al., 2017). This is an indication that the tungstic acid doping of ZnO may change the optoelectronic properties of ZnO or may add another semiconductor (WO_3) to ZnO or induce the formation of new nanocomposite material (ZnO-WO_3) which electronic properties are different from ZnO. The tungstic acid doping may also induce a significant decrease of the trap or carrier recombination centers; enhancing the DSSC performances under illumination.

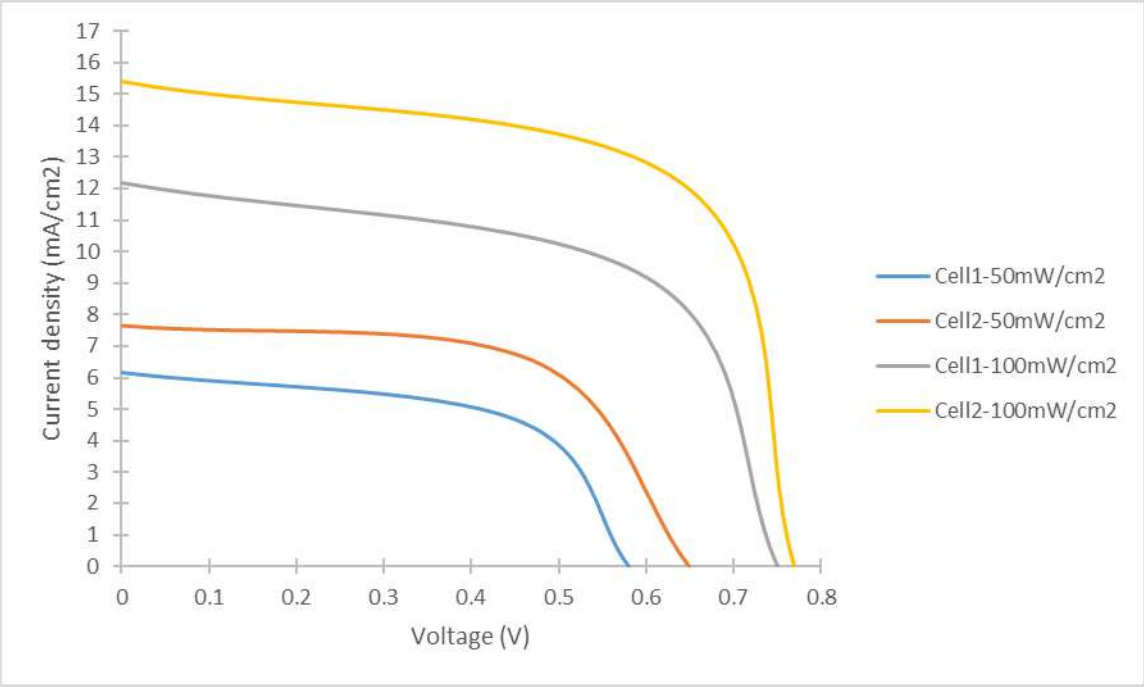

Figure 6.11: Current-voltage curves under dark of DSSCs based on ZnO undoped (Cell 1)and DSSCs based on tungstic doped (Cell 2) for illumination lights of 50 mW/cm^2 and 100 mW/cm^2. The thickness of each ZnO based sample is around 10 µm.

The values of the short circuit current Isc, the open circuit voltage Voc, the optimum or operating current I_M, the optimum or operating potential and the calculated values of the efficiency and the fill factor are summarized in table 6.3 for incident light of 50 mW/cm^2 and 100 mW/cm^2.

Table 6.3: Summary table of the electrical performance of the DSSCs under, respectively, 50 and 100 mW/cm^2

DSSC	Isc (mA/cm^2)	Voc (V)	I_M (mA)	V_M (V)	η (%)	FF(%)
Cell 1	*6.15./**12.2	*0.58/**0.75	*4.67/**9.2	*0.45/**0.60	*4.2/ **5.52	*60./ *60.3
Cell 2	*7.65/**15.4	*0.65/**0.77	*6.55/**12.2	*0.47/**0.64	*6.1./**7.1	*62/**65.8
Increase (%)	*19.6/**20.8.	*10.8/**2.6	*21.6/**24.6	*4.3/**6.25	*31/**22.25	*3.2/**8.4

* Values obtained under 50 *mW/cm^2*; **Values obtained at *100 /mW/cm^2*

The DSSC performances determine in this work are the efficiency, the fill factors and the series and shunt resistances of DSSCs. The parameters involved in the determination of these characteristics are :

V_M : voltage at optimum power (optimal) expressed in V;

J_M : current density at maximum power (optimal) expressed in A/cm^2;

I_M : current at maximum (or optimum) power expressed in A;

V_{oc} circuit voltage in volt (V) measured experimentally;

J_{sc} : short-circuit current density (mA/cm^2).

The electrical conversion efficiency of a DSSC is given by the relation:

$$\eta = \frac{P_M}{P_{inc}} = \frac{V_M \cdot I_M}{P_{inc}} = \frac{V_{oc} \cdot J_{sc} \cdot FF}{P_{inc}}$$

Where

FF is the fill factor;

P_{inc} (W): power of light radiation incident on the DSSC ; $P_{inc} = \emptyset \cdot S$

S : surface of the cell expressed in cm^2

$\emptyset$: irradiation (W/m^2) ; $\emptyset$ = 50, 75 and 100 mW/cm^2.

To verify the following classical relation, we made also measurement under the above 3 incident power light densities. The various parameters are shown in Table 6.4:

$$I_{cc} = kP_{inc}$$

$$\frac{I_{cc1}}{I_{cc2}} = \frac{P_{inc1}}{P_{inc2}}$$

The values in Table 6.3 for DSSC based on ZnO un-doped and ZnO doped with tungstic acid show that there is no significant improvement of the cell open circuit voltage due the tungstic acid doping, in particular under high illumination where the improvement due to doping is almost

2.6% under illumination of 100 mW/cm^2 in comparison to an improvement of 10.8% under illumination of 50 mW/cm^2 (Table 6.3) . This indicates that high voltage can be obtained prior to proper doping of the photoanode. This doping effect might be related to a favorable shift of the band edges upon coupling ZnO to WO_3 nanocomposites and introduce further studies to be done on correlations between band edge shift, recombination rates and tungstic acid doping of ZnO. This interpretation is in agreement with those obtained previously on the improvement of the Voc of TiO_2 – based DSSC doped with ZnO and Au nanoparticles (Borbon et al., 2020). Figure 6.11 and Table 6.3 show also clearly an increase of the short circuit current of cell 2 in comparison to those of cell 1. This improvement is evaluated as $(Isc_2 – Isc_1)/ Isc_2$ which is for example 20.8% for an incident light of 100 mW/cm^2. The most important improvement (24.6% increase) due to the doping of ZnO with tungstic acid is obtained on the operating or optimum current density of the DSSC. The significant increase in the operating current and the short circuit current must be attributed to a lower intrinsic recombination centers or because of the addition of the conduction band edge of WO_3 to that of ZnO for DSSC based on ZnO doped with tungstic acid (Figure 6.11). If the tungstic doping may add WO_3 on ZnO, the injection efficiency may increase because the conduction band of WO_3 is lower than that of ZnO. Accordingly, the carrier injection from the LUMO/dye excited site to the conduction band edge of WO_3 is more favorable than the injection from the LUMO to the ZnO conduction band (Figure 6.12). This simultaneous injection of electrons from the dye excited state (LUMO) to the conduction band of ZnO and WO_3 must be favorable to the enhancement of DSSC performances. Global photoelectrochemical relations are summarized:

i) At the anode

$2S+h\upsilon \rightarrow 2S^*$ (Photon absorption of dye/excitation)

$2S^* \rightarrow 2S^+ + 2e^-$ (two electrons injected to the conduction band of ZnO and WO_3)

$2S^+ + 3I^- \rightarrow 2S + I_3^-$ (dye regeneration)

$3I^- \rightarrow I_3^- + 2e^-$ (oxidation of iodide ions I^-)

ii) At the cathode

$I_3^- + 2\,e^- \rightarrow 3I^-$ (I_3^- reduced by electrons)

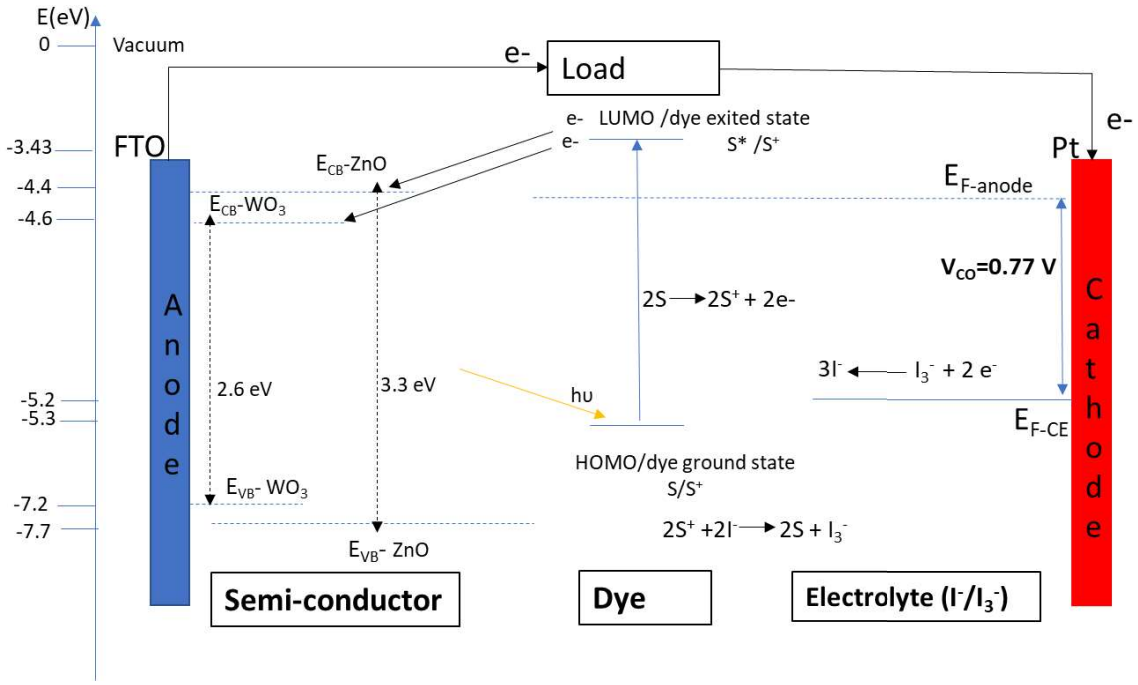

Figure 6.12: Energy diagram of the relative position of the band edges of the HOMO and the LUMO of the dye, the redox energy of I_3^-/I^-, the valence band and the conduction band of ZnO and WO_3 respectively.

This is an indication that more WO_3 in the composite electrode will cause more carrier injection from the dye to both the conduction band of ZnO and WO_3 (Figure 6.12) and consequently the performance of the DSSC characteristics will increase. This can be attributed to a more rapid transport of electrons in DSSC based on the tungstic acid doped ZnO in comparison to the cell based on un-doped ZnO. In other words, this means a higher diffusion coefficient of the electrons in doped ZnO than in un-doped ZnO. This in agreement with studies which have shown that doping levels and illumination intensity may have significant effect on the performances of ZnO-based DSSC (Anta et al., 2012; Tiwana et al., 2011). But if the doping involves two photo anodes electrodes composed of ZnO and a new ZnO-WO_3 nano composite material with its own band gap which might be higher than respectively the individual band gap of WO_3 and ZnO respectively, the injection efficiency could be affected and in this case the role of the relative importance of the intrinsic traps density may more play an important role in the increase of the current density.

The presence of WO_3 is in agreement with other results we obtained previously various

semiconductors doped with silicotungstic acid (Savadogo, 1998; Savadogo & Mandal, 2019a). This interpretation is different to the results and interpretation of J. Li et al (J. Li et al., 2013) who indicated that the doping is achieved without any decomposition of for example the tungstic acid. No WO_3 was identified in their studies. In the present work, the presence of WO_3 contributes to the increase the performance of the characteristics of the DSSC.

Another possibility of this important improvement of the DSSC performances for cell 2 could be an increase in the active surface area when the working electrode of ZnO is doped. Indeed, due to the tungstic acid doping, there is an increase in the interpenetrating dyes in the ZnO lattice which also increased in volume. Accordingly, we would have a better interconnection between the particles for the doped ZnO than pure ZnO (SEM views) which would increase the current. A larger surface area might appear due to the reaction interface between the nanoparticles ZnO and WO_3.

On going investigations are under way to determine which of the above fundamental explanations might be the real raisons of this improvement of the performances of this DSSC characteristics due to tungstic acid doping.

Series resistance R_S and shunt resistance of the cell

The series resistances are due to the ohmic losses in the material and the semiconductor/metal contact. In other words, it depends on the resistivity of each of the components connected in series of the DSSC including those of the electrodes and the semiconductor/metal contact. The series resistance and shunt resistance do not normally affect the solar cell at open-circuit voltage and at short circuit current. But excessively high values of the series resistance can affect the short circuit current. Series resistance contributes in the reduction of the optimum current or/and optimum potential. The fill factor (FF) through the optimum power may also change with the series and the shunt resistances The series resistance is evaluated by determining the inverse of the slope of the current-voltage curve at Voc

The shunt resistance is rather due to the manufacturing defects of the cell than on power losses due to the solar cell design. It has a more drastic effect on the cell characteristics at low light illumination levels. The shunt resistance can be estimated from the slope of the current vs voltage curve near the short circuit current. At low current densities, the effect of the shunt resistance on the celle performance are more important than at high current densities. The shunt resistance of DSSC based on ZnO doped with tungstic acid is higher than those cell fabricate without tungstic

acid.

On the other hand the variation of the optimum or operating power densities of the cell dependence to series resistance is given by: $P_{ms}' = P_m(1-R_s/R_{ch})$ where P_{ms}' is the optimum power with series resistance Rs. Pm is the optimum (operating) power without series resistance and shunt resistance. It is obtained for an ideal cell which does not exist in practice.

$R_{ch}= V_m/I_m$ is the characteristic resistance which may take in account the series and the shunt resistance. V_m is the optimum voltage and I_m is the optimum current. The optimum power dependence of shunt resistance is given by:

$P_{msh}' = P_m(1-R_s/R_{sh})$ where P_{msh}' Is the optimum power with shunt resistance R_{sh}. P_m is the optimum (operating) power without series resistance and R_{ch} is $R_{ch} = V_m/I_m$ is the characteristic resistance of the celle ; V_m is the optimum voltage and I_m is the optimum current. Accordingly, the appropriate way to evaluate the series resistance and the shunt resistance is the determination of the slope of the current vs voltage curve at V_{oc} and at J_{sc}, respectively.

These resistances are determined from curves of Figure 6.11 for Cell 1 based on un-doped ZnO DSSC and for cell 2 based on tungstic acid doped DSSC when they are illuminated under 100 mW/cm^2.We determine the slope($\Delta I/\Delta V$) of the current-voltage curve at Voc of this figure and we calculate the series resistance (R_s) by taking the inverse of this slope ($\Delta V/\Delta I$) of the cell. From the same Figure we use similar approach by taking the slope of the current vs voltage curve ($\Delta I/\Delta V$) at the short circuit current and we calculate the shunt resistance (R_{sh}) by taking the inverse of this slope. The series resistance and the shunt resistance are shown in table 6.4 for DSSC based on un-doped ZnO (Cell 1) and doped ZnO with tungstic acid (Cell 2) under illumination of 100 mW/cm^2. For DSSC based on un-doped ZnO, the values of the series and the shunt resistance obtained in this work are 10 times less than those obtained in reference (Hongsith et al., 2008). This is probably due to the difference of method of fabrication of the ZnO films and the utilization of buffers between ZnO layer and the FTO glass. In reference (Hongsith et al., 2008), radio frequency (rf) sputtering method was used with various buffer whereas in our work the ZnO photo-anode films were fabricated by sol-gel method without any buffer. The differences are supported by, of course, the respective slopes of the curves at the open circuit voltage and at the short circuit current which are high in our study and moderate in the case of reference (Hongsith et al., 2008).

Table 6.4: Summary table of the shunt resistance and series resistance determined from the slope determination of the current voltage curves of Figure 6.11 à V_{oc} and J_{sh} respectively .

	Rsh ($\Omega.cm^2$)	Rs ($\Omega.cm^2$)	Rch $\Omega.cm^2$)	$P_m(mW/cm^2)$
Cell1 (ZnO un-doped with H_2WO_4)	250	8.19	0.065	5.52
Cell2(ZnO doped with H_2WO_4)	310	5.55	0.053	8.81

The shunt resistance of DSSC based on ZnO doped with tungstic acid is higher than that of the cell fabricated without tungstic acid. In contrary the series resistance of DSSC based on ZnO doped with tungstic acid is lower than those of the cell fabricated without doping (Table 6.4). These values agree with the optimum power (Pm) of cell1 which is lower than that of cell2 (Table 6.3)

6.5 Conclusion

Sol-gel method was successfully used for the synthesis of ZnO and ZnO doped with H_2WO_4. Spin-coating based on Doctor Blade method was used to deposit the thin films at the electrodes. The fabricated samples were used to fabricate DSSCs based on ZnO and tungstic acid doped ZnO as photo anode. XRD analysis of these samples confirmed a hexagonal crystallographic structure of wurtzite type (a=0.325 nm, c=0.521nm). SEM micrographs have shown spherical seed layer for un-doped ZnO films and a modification of the relief seed layer into polyhedral seeds for ZnO doped with H_2WO_4.

Voltage-current curves have been acquired for the DSSC based on un-doped ZnO and tungstic acid doped ZnO. The responses under STC illumination, show a significant improvement in short circuit current (19,6%) and the operating current (20,8%) of the DSSC based on ZnO doped with tungstic acid w=in comparison of DSSC based on un-doped ZnO. An improvement of the series resistance and the shunt resistance is also obtained due to the ZnO- tungstic acid doping. Over all, a significant improvement of the DSSC photo-conversion was observed; passing from 5,52% from the DSSC based on un-doped ZnO to 7,1% for DSSC based on H_2WO_4-doped ZnO.

One of the interpretations of the results is based on a mechanism of cell operation based on the presence of two semiconductors (ZnO and WO_3 due to H_2WO_4 doping) has been proposed to explain the effect of the tungstic acid doping on DSSC performance.

CHAPITRE 7 DISCUSSIONS GÉNÉRALES

7.1 Discussion sur les cellules DSSC élaborées

La synthèse des échantillons de ZnO et de ZnO dopé par voie sol-gel s'est opérée à la température ambiante ou proche de celle-ci (25°C à 120°C) exigeant très peu d'énergie (Cf. figure de synthèse et dépôt: Figure 3.1 et Figure 3.2). Seulement, les recuits des électrodes à base de ZnO et de platine ont nécessité une température allant jusqu'à 450°C. Cela démontre que la technologie DSSC est plus respectueuse de l'environnement que celle à silicium.

Le fonctionnement de la cellule DSSC sur les deux faces et sa possible réalisation sur des substrats flexibles sont d'autres avantages de cette technologie qui est en voie d'application sur plusieurs domaines.

Le dopage à 10^{-4} M de l'acide tungstique semble être la meilleure modification de ZnO car elle présente la plus faible résistivité de la couche mince et offre un meilleur rendement de DSSC.

Le dopage de ZnO dans des milieux basiques est une piste pour l'étude d'autres nouveaux matériaux. La fabrication de ces types de cellules solaires sur des substrats flexibles pourraient constituer aussi d'autres pistes de recherches et développement.

7.2 Discussion sur les diffractions XRD

L'acide tungstique n'a pas changé la structure cristalline mais la taille des nanoparticules.

Comparaison entre ZnO recuit et non recuit : effet de la température

L'observation des pics de diffraction de ZnO non recuit et de ZnO recuit montre que les pics de ZnO traité thermiquement sont légèrement supérieurs à ceux non recuits. On a par exemple autour de l'angle de diffraction de $2\theta=36,4°$ l'intensité de pic principal de ZnO recuit est à 1177 alors que celui de ZnO non recuit est de 1036. Les pics de diffraction fort et nets indiquent une bonne cristallinité de l'échantillon même si le traitement thermique semble être sans effet sur la structure cristallographique du ZnO. Nous deduisons de ces résultats que le recuit améliore la cristallinité de l'échantillon de ZnO

Comparaison entre ZnO seul et ZnO dopé à l'acide tungstique : effet du dopage

Les spectres XRD de ZnO et de ZnO dopé par Philipps X'pert montrent que les intensités des pics ne sont pas identiques. Il en est de même pour les mesures effectuées à de l'aide Bruker 8 Advance. Une estimation d'erreur dans les angles de diffraction est estimée $\pm 0{,}01$ °. Le dopage n'a pas changé la structure cristalline du matériau mais a réduit la taille des cristallites. Cette technique n'a pas permis de détecter les dopants qui sont en très faibles quantités.

7.3 Discussion sur les spectres d'absorption, transmission et réflexion UV-visible

Les résultats des mesures des échantillons à base de ZnO obtenus et discutés dans l'article 2 (ZnO :H_2WO_4) sont ceux prévus par Burntein-Moss (Figure 7.1) et certaines littératures citées dans l'article. En effet, la bande interdite de ZnO dopé augmente (jusqu'à 3,57 eV au lieu de rester constante 3,24 eV) avec la concentration des porteurs à cause du décalage de Burstein-Moss (C. C. Singh & Panda, 2018). Le décalage de Burnstein-Moss est observable par une augmentation de la bande interdite lorsque le niveau d'absorption est poussé à des énergies plus élevées à cause de certains états proche de la bande de conduction.

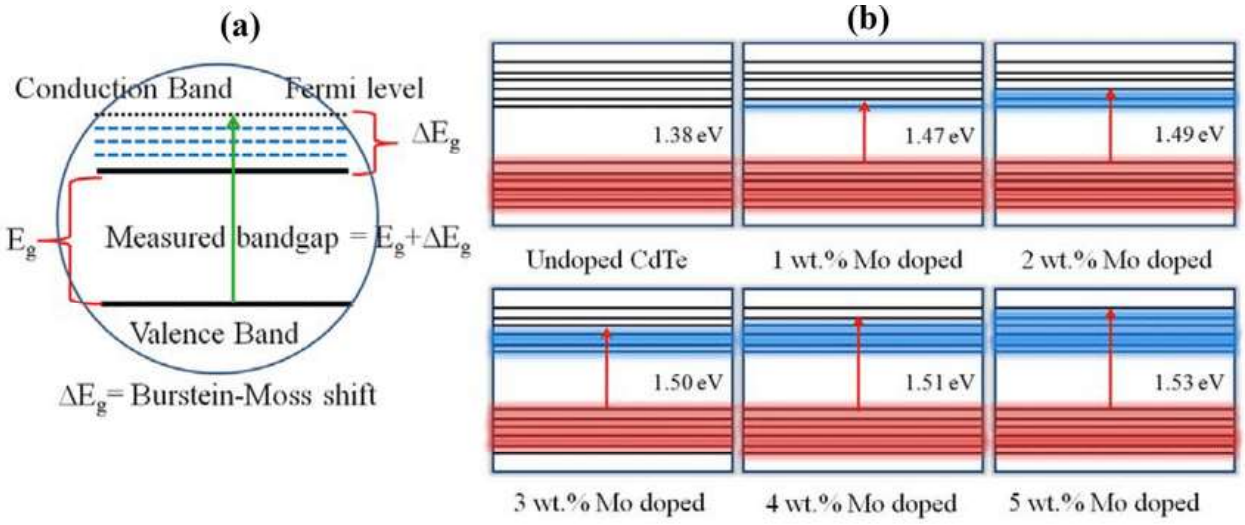

Figure 7.1 : Effet de Burstein-Moss (Manimozhi et al., 2020)

Pour des longueurs d'ondes inférieures à 400 nm, on peut constater que la présence de l'agent dopant acide tungstique tend à faire baisser légèrement l'absorption à la photoanode alors que pour

des longueurs d'ondes compris entre 400 nm à 700 nm, on a une meilleure absorption des rayons lumineux pour l'échantillon ZnO :10^{-4} M H_2WO_4 par rapport aux autres échantillons.

7.4 Discussion sur les pics XPS

Par cette technique d'analyse sous vide, nous avons enregistré des pics correspondant aux liaisons chimiques entre électrons de cœur et atomes ou molécules pour les différents échantillons synthétisés (cf. article 3). Nous avons ensuite procédé à l'identification des éléments présents dans les échantillons analysés ainsi que leur pourcentage atomique (cf. article 3). Nous avons également précisé la structure wurztite des échantillons à base de ZnO et les types de liaisons entre les éléments chimiques de la surface analysée. Pour la synthèse de :

- ZnO, on a selon les pics obtenus les liaisons suivantes : Zn-O, Zn métal.
- ZnO :H_2WO_4, on a selon les pics obtenus, les liaisons suivantes : Zn-O, Zn métal, W-O, W métal.

L'analyse d'une surface d'un matériau est d'une grande importance pour connaitre ses propriétés électroniques, chimiques et physiques ainsi que son interaction avec son environnement. Les réactions aux électrodes d'une cellule électrochimique, la bande interdite d'un semi-conducteur, la résistance de contact d'un matériau, les effets de catalyseur, le phénomène de corrosion ou anti-corrosion, l'adhésion, la transmittance peuvent être élucidés par une analyse XPS.

7.5 Discussion sur la résistivité et la résistance de surfacique

Les conclusions de nos mesures de résistance surfacique ont montré l'effet de l'acide tungstique sur la résistivité de cette couche mince de ZnO. Par exemple, l'effet de l'acide tungstique (pour 10^{-4} M de dopant) a contribué à diminuer la taille des cristallites de 27,42 nm (pour le ZnO intrinsèque) jusqu'à une valeur minimale de 17,14 nm (pour le ZnO dopé). Cette diminution en taille de cristallites s'accompagne d'une amélioration des surfaces spécifiques des nanoparticules, de la diminution des résistances surfaciques (de 2,29 Ω/sq à 1,45 Ω/sq) des couches minces et au final de la diminution des résistances séries (de 8,19 $\Omega.cm^2$ à 5,5 $\Omega.cm^2$) de la cellule DSSC dopée.

Des résultats similaires ont été obtenus dans plusieurs travaux sur le dopage de ZnO avec des éléments comme l'aluminium (Mandal, Mullick, Majumdar, Dhar, & Ray, 2008) ou le cobalt (Habubi, Yousif, & Haider, 2012).

Les propriétés thermoélectriques de ZnO :Al synthétisé par voie hydrothermal ($Zn_{1-x}Al_xO$ où x=0,0; 0,01; 0,02; 0,03 et 0,006) ont été étudiées par expérimentation et par simulation (Jantrasee et al., 2016). S. Jantrasee et al ont effectué des simulations suivies des expérimentations sur les propriétés thermoélectriques de ZnO et ZnO dopés (Jantrasee et al., 2016). La Figure 7.2 montre l'effet de la concentration du dopant et de la température sur l'évolution de la conductivité des échantillons à base de ZnO. La conductivité augmente avec la température de recuit de 400°C atteignant une valeur optimale de 75,48 $(\Omega.m)^{-1}$ pour un dopage de 6% de l'aluminium alors que pour la couche de ZnO non dopé, la conductivité est de 16,01 $(\Omega.m)^{-1}$ à la même température. La conductivité est d'autant plus grande que le dopage augmente de 1 % à 6 % et/ou la température est grande pour des valeurs de 50°C à 400°C.

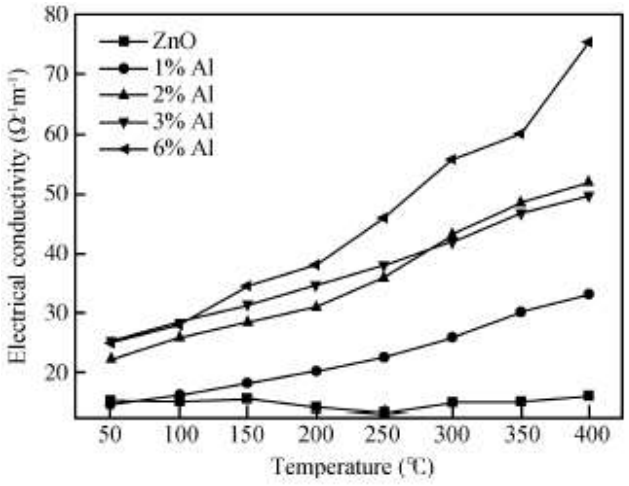

Figure 7.2: Conductivité électrique de ZnO et ZnO dopé à l'aluminium (Jantrasee et al., 2016)

La dépendance de la conductivité électrique de ces échantillons qui augmente sous l'effet de la température est un comportement typique au semi-conducteur (Jantrasee et al., 2016). Les résultats XRD obtenus par Jantrasee et al. ont aussi revelé une diminution de la taille des nanoparticules pour l'oxyde de zinc dopé (Jantrasee et al., 2016). En conclusion, on peut affirmer que la présence de l'élément dopant Al dans le réseau cristallin de ZnO est un facteur influençant les propriétés électriques (amélioration de la conductivité électrique) et la taille des nanocristaux.

S, Mandal et al. (Mandal et al., 2008) ont montré dans leurs travaux que le ZnO dopé présente une réduction de la résistivité de 10^4 **Ω.**cm contre $2{,}2.10^{-3}$ **Ω.**cm lorsque la concentration du dopant augmente de 0 à 5% (Figure 7.3). Une augmentation de la bande interdite de ZnO (3,53 eV) a été mesurée pour les échantillons de ZnO dopés à Al. Ces performances mesurées sont justifiées par

la présence des ions Al^{3+} dans les sites de substitutions des ions Zn^{2+} , des atomes interstitiels d'aluminium et de zinc et des lacunes d'oxygène (Mandal et al., 2008).

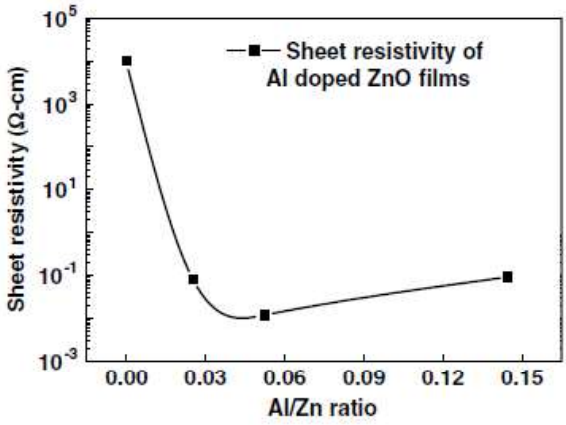

Figure 7.3: Variation de la "sheet resistance" en fonction de la concentration de dopage en aluminium(Mandal et al., 2008)

Plusieurs travaux ont montré l'importance du traitement post-thermique (recuit) des couches minces de ZnO pour améliorer leur conductivité ou diminuer leur résistivité (Jantrasee et al., 2016; Mandal et al., 2008). Quant à l'effet de la température de dépôt sur l'évolution de ces performances électriques des couches minces de ZnO, les conclusions divergent selon la technologie développée. En utilisant la technique de dépôt à arc cathodique filtré sous vide, X.L. Xu et al.(X. L. Xu et al., 2001) ont montré que la résistivité ne varie pas de façon linéraire selon la température du substrat (Figure 7.4). Pour des températures de substrat de 120°C à 230°C, il y a une augmentation de la résistivité de $2{,}38.10^{-4}$ **Ω.**cm à 1,3 **Ω.**cm. Et cette résistivité reste quasiment constante entre 230 °C et 320 °C mais elle décroit à température supérieur à 320°C jusqu'à atteindre une valeur de 6.10^{-3} **Ω.**cm à 440 °C.

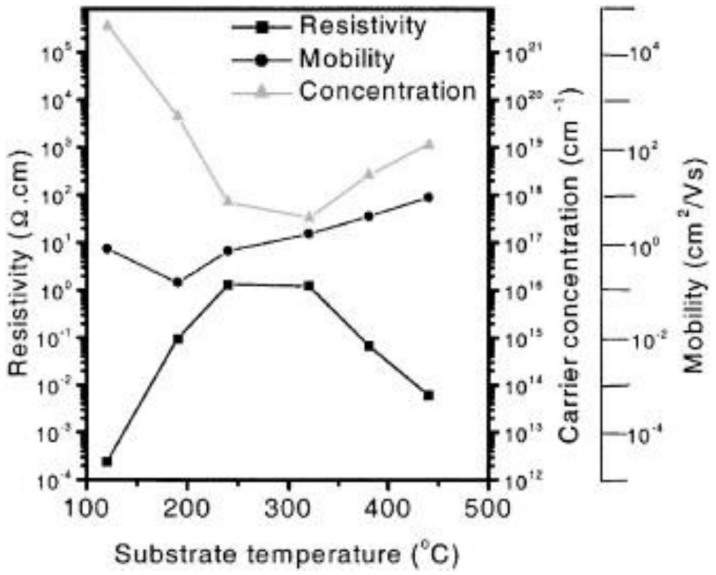

Figure 7.4 : Évolution de la résistivité, de la concentration des porteurs des charges et de la mobilité dans la couche mince de ZnO (X. L. Xu et al., 2001)

En 1999, Subramanyam et al (Subramanyam, Srinivasulu Naidu, & Uthanna, 1999) ont étudié l'effet de la température entre 548 K et 723 K du substrat en verre sur les propriétés physiques des films de ZnO obtenus par pulvérisation magnétron réactive à courant continu. Les auteurs ont trouvé à travers leurs expériences que pour des températures de substrat en verre entre 548 K et 663 K, il y a une amélioration des performances électriques de la couche de ZnO. En effet il y a :

- une décroissance linéaire de la résistivité du film de ZnO de 34 **Ω.**cm (à 548 K) à 6,9 10^{-2} **Ω.**cm (663 K). Cette décroissance a été attribuée à une augmentation, sous l'effet d'une température élevée, des lacunes d'oxygène et des atomes interstitiels de zinc qui agissent tous deux comme des donneurs.
- une croissance linéaire de la mobilité Hall des porteurs de charge de 9,2 $cm^2/V.s$ (à 548 K) à 16,8 $cm^2/V.s$ (à 663 K). L'augmentation de la mobilité des porteurs de charges serait due à l'augmentation des tailles des grains révélés dans les mesures XRD.
- une croissance linéaire des porteurs de charge de 2.10^{16} cm^{-3} (à 548 K) à $5,4.10^{18}$ cm^{-3} (663 K) sous l'effet de l'augmentation de la température du substrat.

Ces performances ont légèrement baissé lorsque la température du substrat continue de croitre jusqu'à 723 K. La diminution de la mobilité (15,8 $cm^2/V.s$ à 723 K) a été attribué à une diminution

des tailles des grains des cristaux. Aussi l'augmentation de la résistivité (9,6 Ω.cm à 723K) a été justifié par une réduction des lacunes d'oxygène et des atomes interstitiels de zinc.

Le Tableau 7.1 dresse un récapitulatif des températures de substrat avec les différentes techniques de dépôts ainsi que les valeurs minimums de résistivité atteinte.

Tableau 7.1 : Résistivités minimums des couches minces de ZnO en fonction des techniques de dépôt et des températures de substrat

Technique de dépôt	Température de substrat (°C)	Résistivité électrique (**Ω.**cm)	Bande interdite (eV)	Référence
DC magnetron sputtering	390	$6{,}9.10^{-2}$ (ZnO)	3,28	(Subramanyam et al., 1999)
DC magnetron sputtering	350	$3{,}8.10^{-2}$ (ZnO : Al)	-	(Sato et al., 1994)
RF magnetron sputtering	380	$4{,}8.10^{-4}$ (ZnO : Al)	3,25 à 3,35	(Martínez, Herrero, & Gutiérrez, 1994)
Ion beam sputtering	350	2.10^{-2} (ZnO)	3,29	(Y. Qu, Gessert, Coutts, & Noufi, 1994)
Evaporation	400	$4{,}3.10^{-3}$ (Zn : Al)	-	(Ma, Ji, Ma, & Li, 1996)
Spray pyrolysis	400	10^{-1} – 10 (ZnO : In)	3,17	(Messaoudi, Sayah, & Abd-lefdil, 1995)
Ultrasonic spray pyrolysis	400	10	3,29	(T. Y. Ma et al., 1996)
Sol-gel	500	0,99 (ZnO)	-	(J.-H. Lee, Ko, & Park, 2003)
Sol-gel	500	9 (ZnO : Al)	3,22-3,44	(M. Sahal, 2006)

7.6 Discussion sur la corrélation entre les propriétés des couches minces et les DSSC

La présence de l'agent dopant H_2WO_4 dans la couche mince de ZnO exerce une influence non négligeable sur la performance globale de la cellule DSSC. En effet, on peut distinguer les avantages (cf.

Tableau 7.2) suivants:

- Une diminution de la taille des cristallites de 27,42 nm à 17,14 nm;
- Une diminution de la résistance surfacique, de la résistance série Rs ;
  Une augmentation de la surface spécifique (polyédriques et fractales) et de la résistance parallèle Rsh (Tableau 7.2);
- Un apport supplémentaire d'une seconde bande interdite du nanocomposite ZnO-WO_3 (Eg_2=3,8±0,02 eV).

Ces propriétés corrélées les uns aux autres justifient l'amélioration des performances des DSSC dopés par rapport à celle non dopé. Par exemple, pour un dopage optimal de 10^{-4} M d'acide tungstique, on obtient un rendement maximal de 7,1 % par rapport 5,52 % pour les cellules non-dopées et une amélioration du facteur de forme atteignant 65,8 % pour les DSSC dopées et 60,3% pour les DSSC non dopées.

Tableau 7.2: Résumé des performances des couches minces et DSSC à base de ZnO et ZnO dopé

% H_2WO_4 dans ZnO	Couche mince (anode)			Cellules solaires (DSSC)			
	τ (nm)	Sheet resistance (Ω/sq)	Eg (eV)	R_{sh} ($\Omega.cm^2$)	R_s ($\Omega.cm^2$)	η (%)	FF (%)
0	27,42	2,29	Eg_1	250	8,19	5,52	60,3
0,00005	21,11	1,81	Eg_1 +Eg_2	281	6,3	6,3	62,5
0,0001	17,14	1,45	Eg_1 +Eg_2	310	5,55	7,1	65,8
0,00015	20,4	1,95	Eg_1 +Eg_2	289	5,8	6,54	63,6

τ (nm) : taille des cristallites;

Eg : bande interdite de l'échantillon;

Eg_1 = 3,25±0,03 eV correspond à la bande interdite de ZnO;

Eg_2 =3,8±0,02 eV correspond à la bande interdite de nanocomposite ZnO-WO_3;

R_{sh} : résistance parallèle; R_s : résistance série; η : rendement de la DSSC; FF : facteur de forme.

Ces performances électriques (tel que le rendement de conversion photovoltaïque de 7,1 %) sont parmi les meilleures performances des DSSC à base de ZnO obtenus de nos jours. Ces DSSC se distinguent par exemple de celles de Memarian et al. (Memarian et al., 2011) qui ont utilisé la technique 'spray pyrolyse' et des nanoparticules 'ZnO hierarchical' qui leur auraient permis d'atteindre un rendement photovoltaïque record de 7,5 %.

CHAPITRE 8 CONCLUSION ET RECOMMANDATIONS

8.1 Conclusions

Des cellules solaires DSSC répondant aux faibles éclairements ont été élaborées à l'aide de ZnO et ZnO dopé à l'acide tungstique. L'oxyde de zinc a été dopé à différents pourcentages de H_2WO_4 à l'anode de la cellule. Le dopage à 10^{-4} M de l'acide tungstique a donné un effet d'amélioration sur les performances électriques courant-tension par rapport aux autres pourcentages de dopage ou des DSSC élaborées sans dopage de ZnO dans les mêmes conditions.

La méthode sol-gel a été adoptée à cause de son mode opératoire peu énergivore et peu onéreux pour fabriquer le ZnO/ZnO dopé à partir du précurseur acétate de zinc dihydraté. Une dissolution et dissociation de l'acide tungstique ont été observées lorsque la synthèse a été effectuée en milieu basique (pour un pH avoisinant 10). En milieu neutre ou pour des pH inférieurs à 9 l'acide tungstique reste intact dans le processus de synthèse.

Les techniques de dépôts des couches minces sur le substrat FTO utilisées sont : spin-coating, doctor blade et le dip-coating. La synthèse de l'oxyde de zinc, sa modification avec l'acide tungstique et leurs dépôts sur le FTO, une dizaine d'analyses ont été effectuées :

- la caractérisation XRD des échantillons pour prouver la cristallinité hexagonale de l'oxyde de zinc et le calcul des tailles des cristallites ;
- la caractérisation au MEB pour l'observation de la morphologie des grains. Les observations au microscope électronique à balayage (ou MEB) ont révélé des changements morphologiques et des meilleures interconnexions pour les échantillons dopés à 10^{-4} M.
- L'analyse à la spectroscopie UV-visible a permis de déterminer différentes bandes gap des échantillons dopés allant de 3,24 à 3,57 eV. La spectroscopie photoélectronique à rayons X ou XPS et la spectroscopie par la transformée de Fourier ont confirmé les liaisons chimiques tel que Zn-O, W-O dans les échantillons.
- Les mesures de sheet resistance par la méthode de courant de Foucault ont été effectuées. Les performances électriques sont la caractérisation courant-tension, les résistances série, shunt et surfacique ont été mesurées pour les différentes DSSC.

Le dopage a apporté une seconde bande interdite supplémentaire (Eg_1 et Eg_2) et a diminué la taille des cristallites ; cependant on assite à une augmentation de la surface spécifique des nanoparticules dopés polyédriques et fractales par rapport au nanoparticule sphérique pour le ZnO pur. Ces améliorations de propriétés anodiques ont contribué au développement des nouvelles DSSC avec ZnO: H_2WO_4 présentant un meilleur rendement de 7,1 % par rapport 5,52 % pour les cellules non-dopé soit un accroissement de 22,24 % de performance.

L'originalité de ce projet est l'étude des DSSC à base de ZnO dopé avec H_2WO_4 dans un milieu que nous avons déterminé basique. Contribution au développement des connaissances scientifiques et technologiques : l'effet de l'acide tungstique sur ZnO (modification de la bande interdite) et la cellule DSSC. Le milieu basique joue un rôle déterminant dans la décomposition de l'acide tungstique. En perspectives post-doctorat, L'étude pourrait s'étendre sur le dopage de ZnO avec les additifs HPAs en milieu basique dans le but de rechercher des nouveaux matériaux comme électrodes photocatalyseurs.

8.2 Recommandations

En guise de recommandations d'autres mesures complémentaires pourraient être effectuées :

- l'élaboration de ces DSSC en intégrant les pérovskites pour augmenter leurs rendements et les rendre compétitifs avec les cellules solaires à base de silicium;
- l'élaboration de ces DSSC sur des substrats flexibles;
- sur la stabilité des cellules à base de ZnO dopé et non dopé;
- l'étude du composite ZnO+WO_3 pour comparer les résultats;
- la fabrication de ZnO avec un autre semi-conducteur qui aura un niveau de la bande de conduction plus haut que celui du niveau de l'état excité (LUMO) du dye.

Les applications de ces travaux sont le développement des procédés de fabrications économiques et respectueuses de l'environnement en photovoltaïque. Soulignons également l'adaptation de ces cellules photovoltaïques flexibles à couche mince comme source d'alimentation autonome ou d'appoint en énergie sur des objets portables ou tout récepteur électrique (sur les vitres, à l'intérieur pour capter l'éclairement des ampoules, …), intégration sur les ordinateurs portables, les sacs portables, les habits, etc. car les cellules DSCC fonctionnent même aux faibles éclairements.

REFERENCES

Agarwal, Reema, Vyas, Yogeshwari, Chundawat, Priyanka, Dharmendra, & Ameta, Chetna. (2021). Outdoor Performance and Stability Assessment of Dye-Sensitized Solar Cells (DSSCs). *IntechOpen*. doi:10.5772/intechopen.98621

Agarwal, Sonalika, Jangir, Lokesh K., Rathore, Kuldeep S., Kumar, Manoj, & Awasthi, Kamlendra. (2019). Morphology-dependent structural and optical properties of ZnO nanostructures. *Applied Physics A, 125*(8). doi:10.1007/s00339-019-2852-x

Ahn, Sung Hoon, Kim, Dong Jun, Chi, Won Seok, & Kim, Jong Hak. (2014). Hierarchical Double-Shell Nanostructures of TiO2Nanosheets on SnO2Hollow Spheres for High-Efficiency, Solid-State, Dye-Sensitized Solar Cells. *Advanced Functional Materials, 24*(32), 5037-5044. doi:10.1002/adfm.201400774

Ajay Jena, Shyama Prasad Mohanty , Pragyensh Kumar , Johns Naduvath , Vivekanand Gondane , P. Lekha , . . . Bhargava, P. (2012). Dye Sensitized Solar Cells: A Review. *Transactions of the Indian Ceramic Society*.

Alias, Siti Salwa, & Mohamad, Ahmad Azmin. (2014). *Synthesis of Zinc Oxide by Sol–Gel Method for Photoelectrochemical Cells (SpringerBriefs in Materials)*. In S.K. Bhatia, Diebold, A., Hu, J., Krishnan, K.M., Narducci, D., Sinha Ray, S., Wilde, G. (Ed.), (pp. X, 52 p. 31 illus., 16 illus. in color.).

Amogne, Negese Yazie, Ayele, Delele Worku, & Tsigie, Yeshitila Asteraye. (2020). Recent advances in anthocyanin dyes extracted from plants for dye sensitized solar cell. *Materials for Renewable and Sustainable Energy, 9*(4). doi:10.1007/s40243-020-00183-5

Aneesiya, K. Rajan, & Louis, Cindrella. (2020). Localized surface plasmon resonance of Cu-doped ZnO nanostructures and the material's integration in dye sensitized solar cells (DSSCs) enabling high open-circuit potentials. *Journal of Alloys and Compounds, 829*. doi:10.1016/j.jallcom.2020.154497

Anta, Juan A., Guillén, Elena, & Tena-Zaera, Ramón. (2012). ZnO-Based Dye-Sensitized Solar Cells. *The Journal of Physical Chemistry C, 116*(21), 11413-11425. doi:10.1021/jp3010025

Anwar, Hafeez, George, Andrew E., & Hill, Ian G. (2013). Vertically-aligned carbon nanotube counter electrodes for dye-sensitized solar cells. *Solar Energy, 88*, 129-136. doi:10.1016/j.solener.2012.11.013

Archana, P. S., Jose, R., Vijila, C., & Ramakrishna, S. (2009). Improved Electron Diffusion Coefficient in Electrospun TiO2 Nanowires. *The Journal of Physical Chemistry C, 113*(52), 21538-21542. doi:10.1021/jp908238q

Arya, Sandeep, Mahajan, Prerna, Mahajan, Sarika, Khosla, Ajit, Datt, Ram, Gupta, Vinay, . . . Oruganti, Sai Kiran. (2021). Review—Influence of Processing Parameters to Control Morphology and Optical Properties of Sol-Gel Synthesized ZnO Nanoparticles. *Ecs Journal of Solid State Science and Technology, 10*(2). doi:10.1149/2162-8777/abe095

Babar, Falak, Mehmood, Umer, Asghar, Hafza, Mehdi, M. Hassan, Khan, Anwar Ul Haq, Khalid, Hamza, . . . Fatima, Zaira. (2020). Nanostructured photoanode materials and their deposition methods for efficient and economical third generation dye-sensitized solar cells: A comprehensive review. *Renewable and Sustainable Energy Reviews, 129*. doi:10.1016/j.rser.2020.109919

Banerjee, A. N., Kundoo, S., Saha, P., & Chattopadhyay, K. K. (2003). Synthesis and characterization of nano-crystalline fluorine-doped tin oxide thin films by sol-gel method. *Journal of Sol-Gel Science and Technology, 28*(1), 105-110. doi:Doi 10.1023/A:1025697322395

Bard, Allen J., & Faulkner, Larry R. (2001). *Electrochemical Methods Fundamentals and Applications* (second ed.). 605 Third Avenue, New York, United States of America: John Wiley & Sons, Inc.

Barnes, J. S., Nguyen, H. P., Shen, S., & Schug, K. A. (2009). General method for extraction of blueberry anthocyanins and identification using high performance liquid chromatography-electrospray ionization-ion trap-time of flight-mass spectrometry. *J Chromatogr A, 1216*(23), 4728-4735. doi:10.1016/j.chroma.2009.04.032

Baxter, Jason B., & Aydil, Eray S. (2005). Nanowire-based dye-sensitized solar cells. *Applied Physics Letters, 86*(5). doi:10.1063/1.1861510

Belaid, H., Nouiri, M., Sayari, A., Ben Ayadi, Z., Djessas, K., & El Mir, L. (2015). Modifications in electrical properties of ZnO:In/PS/Si (100) heterojunction by ZnO intermediate layer. *Canadian Journal of Physics, 93*(11), 1240-1245. doi:10.1139/cjp-2014-0736

Benabdallh, Taouti Mohamed. (2008). *Synthèses et caractérisations structurales d'iodates métalliques, matériaux lasers convertisseurs de fréquences.* UNIVERSITÉ JOSEPH FOURIER-GRENOBLE 1-France. UNIVERSITÉ HADJ LAKHDAR-BATNA-ALGÉRIE, Retrieved from https://www.researchgate.net/publication/30514935_Syntheses_et_caracterisations_structurales_d'iodates_metalliques_materiaux_lasers_convertisseurs_de_frequences/link/5730724a08ae7441519120ac/download

Bhandari, Khagendra P., Collier, Jennifer M., Ellingson, Randy J., & Apul, Defne S. (2015). Energy payback time (EPBT) and energy return on energy invested (EROI) of solar photovoltaic systems: A systematic review and meta-analysis. *Renewable and Sustainable Energy Reviews, 47*, 133-141. doi:10.1016/j.rser.2015.02.057

Biswas, Rajat, & Chatterjee, Suman. (2020). Effect of surface modification via sol-gel spin coating of ZnO nanoparticles on the performance of WO3 photoanode based dye sensitized solar cells. *Optik, 212*, 164142.

Blok, L., & Bruyn, P. L. De. (1970). The ionic double layer at the interface. *Journal of Colloid and Interface Science, 32*(3), 518-526. doi:10.1016/0021-9797(70)90141-4

Borbon, S., Lugo, S., Pourjafari, D., Pineda Aguilar, N., Oskam, G., & Lopez, I. (2020). Open-Circuit Voltage (V OC) Enhancement in TiO2-Based DSSCs: Incorporation of ZnO Nanoflowers and Au Nanoparticles. *ACS Omega, 5*(19), 10977-10986. doi:10.1021/acsomega.0c00794

Borniol, Mervyn de. (2006). *Photosensibilisation d'oxydes semi-conducteurs par des dérivés organostanniques du pérylène -3,4-dicarboximideApplication à la conversion photovoltaïque.* Bordeaux1,

Boro, B., Rajbongshi, B. M., & Samdarshi, S. K. (2016). Synthesis and fabrication of TiO2–ZnO nanocomposite based solid state dye sensitized solar cell. *Journal of Materials Science: Materials in Electronics, 27*(9), 9929-9940. doi:10.1007/s10854-016-5062-8

Boro, Bibha, Gogoi, B., Rajbongshi, B. M., & Ramchiary, A. (2018). Nano-structured TiO2/ZnO nanocomposite for dye-sensitized solar cells application: A review. *Renewable and Sustainable Energy Reviews, 81*, 2264-2270. doi:10.1016/j.rser.2017.06.035

Boschloo, G., & Hagfeldt, A. (2009). Characteristics of the iodide/triiodide redox mediator in dye-sensitized solar cells. *Acc Chem Res, 42*(11), 1819-1826. doi:10.1021/ar900138m

Boschloo, Gerrit, Edvinsson, Tomas, & Hagfeldt, Anders. (2006). Chapter 8 - Dye-Sensitized Nanostructured ZnO Electrodes for Solar Cell Applications. *Nanostructured Materials for Solar Energy Conversion*, 227-254.

Boumaiza, A., Boudine, B., & Sebais, M. (2021). Fabrication and Characterization of Pure and Pb-doped ZnO Thin Films Prepared by Sol–Gel and Dip-coeting Method. *Journal of Inorganic and Organometallic Polymers and Materials, 31*(8), 3350-3355. doi:10.1007/s10904-021-01990-7

BRISSET, FRANÇOIS. (15 Janvier 2009). *MICROSCOPE ÉLECTRONIQUE À BALAYAGE*: EDPSCI.

BROURI, Tayeb. (2011). *Élaboration et étude des propriétés électriques de couches minces et de nanofils de ZnO.* Thèse de doctorat d'Université Paris-Est, Retrieved from https://www.researchgate.net/publication/278637171

Burdett, J. K., Hughbanks, T., Miller, G. J., Richardson, J. W., & Smith, J. V. (1987). Structural Electronic Relationships in Inorganic Solids - Powder Neutron-Diffraction Studies of the Rutile and Anatase Polymorphs of Titanium-Dioxide at 15 and 295-K. *Journal of the American Chemical Society, 109*(12), 3639-3646. doi:DOI 10.1021/ja00246a021

Burschka, J., Pellet, N., Moon, S. J., Humphry-Baker, R., Gao, P., Nazeeruddin, M. K., & Gratzel, M. (2013). Sequential deposition as a route to high-performance perovskite-sensitized solar cells. *Nature, 499*(7458), 316-319. doi:10.1038/nature12340

Burschka, Julian, Brault, Vincent, Ahmad, Shahzada, Breau, Livain, Nazeeruddin, Mohammad K., Marsan, Benoît, . . . Grätzel, Michael. (2012). Influence of the counter electrode on the photovoltaic performance of dye-sensitized solar cells using a disulfide/thiolate redox electrolyte. *Energy & Environmental Science, 5*(3). doi:10.1039/c2ee03005e

Center, Los Angeles Chinese Learning. (Consulté le 28 Novembre 2021). General Information of Zinc.

Chakrabarti, S., & Dutta, B. K. (2004). Photocatalytic degradation of model textile dyes in wastewater using ZnO as semiconductor catalyst. *Journal of Hazardous Materials, 112*(3), 269-278. doi:10.1016/j.jhazmat.2004.05.013

Chalkias, D. A., Verykokkos, N. E., Kollia, E., Petala, A., Kostopoulos, V., & Papanicolaou, G. C. (2021). High-efficiency quasi-solid state dye-sensitized solar cells using a polymer blend electrolyte with "polymer-in-salt" conduction characteristics. *Solar Energy, 222*, 35-47. doi:10.1016/j.solener.2021.04.051

Chang, Ling-Yu, Lee, Chuan-Pei, Li, Chun-Ting, Yeh, Min-Hsin, Ho, Kuo-Chuan, & Lin, Jiang-Jen. (2014). Synthesis of a novel amphiphilic polymeric ionic liquid and its application in quasi-solid-state dye-sensitized solar cells. *J. Mater. Chem. A, 2*(48), 20814-20822. doi:10.1039/c4ta05436a

Chauhan, Ratna, Shinde, Manish, Kumar, Abhinav, Gosavi, Suresh, & Amalnerkar, Dinesh P. (2016). Hierarchical zinc oxide pomegranate and hollow sphere structures as efficient photoanodes for dye-sensitized solar cells. *Microporous and Mesoporous Materials, 226*, 201-208. doi:10.1016/j.micromeso.2015.11.054

Chen, C. Y., Wang, M., Li, J. Y., Pootrakulchote, N., Alibabaei, L., Ngoc-le, C. H., . . . Gratzel, M. (2009). Highly efficient light-harvesting ruthenium sensitizer for thin-film dye-sensitized solar cells. *ACS Nano, 3*(10), 3103-3109. doi:10.1021/nn900756s

Chen, Chia-Yuan, Wu, Shi-Jhang, Wu, Chun-Guey, Chen, Jian-Ging, & Ho, Kuo-Chuan. (2006). A Ruthenium Complex with Superhigh Light-Harvesting Capacity for Dye-Sensitized Solar Cells. *Angewandte Chemie, 118*(35), 5954-5957. doi:10.1002/ange.200601463

Chen, Chien-Chih, & Ting, Chen-Ching. (2013). Photoelectrode Fabrication of Dye-Sensitized Nanosolar Cells Using Multiple Spray Coating Technique. *International Journal of Photoenergy, 2013*, 1-8. doi:10.1155/2013/629059

Chen, Hanhong, Du Pasquier, Aurelien, Saraf, Gaurav, Zhong, Jian, & Lu, Yicheng. (2008). Dye-sensitized solar cells using ZnO nanotips and Ga-doped ZnO films. *Semiconductor Science and Technology, 23*(4). doi:10.1088/0268-1242/23/4/045004

Chen, Hsin-Wei, Lin, Chia-Yu, Lai, Yi-Hsuan, Chen, Jian-Ging, Wang, Chun-Chieh, Hu, Chih-Wei, . . . Ho, Kuo-Chuan. (2011). Electrophoretic deposition of ZnO film and its compression for a plastic based flexible dye-sensitized solar cell. *Journal of Power Sources, 196*(10), 4859-4864. doi:10.1016/j.jpowsour.2011.01.057

Chen, Kuan-Ru, Yeh, Hsiu-Feng, Chen, Hung-Chih, Liu, Ta-Jo, Huang, Shu-Jiuan, Wu, Ping-Yao, & Tiu, Carlos. (2013). Optical-Electronic Properties of Carbon-Nanotubes Based Transparent Conducting Films. *Advances in Chemical Engineering and Science, 03*(01), 105-111. doi:10.4236/aces.2013.31013

Cheng, Hsin-Ming, Chiu, Wei-Hao, Lee, Chia-Hua, Tsai, Song-Yeu, & Hsieh, Wen-Feng. (2008). Formation of Branched ZnO Nanowires from Solvothermal Method and Dye-Sensitized Solar Cells Applications. *The Journal of Physical Chemistry C, 112*(42), 16359-16364. doi:10.1021/jp805239k

Chiba, Yasuo, Islam, Ashraful, Watanabe, Yuki, Komiya, Ryoichi, Koide, Naoki, & Han, Liyuan. (2006). Dye-Sensitized Solar Cells with Conversion Efficiency of 11.1%. *Japanese Journal of Applied Physics, 45*(No. 25), L638-L640. doi:10.1143/jjap.45.L638

Chou, Chuen-Shii, Chou, Feng-Cheng, & Kang, Jhe-Yuan. (2012). Preparation of ZnO-coated TiO2 electrodes using dip coating and their applications in dye-sensitized solar cells. *Powder Technology, 215*, 38-45.

Choudhury, Mohammad Shamimul Haque, Kishi, Naoki, & Soga, Tetsuo. (2016). Compression of ZnO nanoparticle films at elevated temperature for flexible dye-sensitized solar cells. *Journal of Alloys and Compounds, 656*, 476-480. doi:10.1016/j.jallcom.2015.09.138

Clifford, John N., Palomares, Emilio, Nazeeruddin, Md K., Grätzel, M., & Durrant, James R. (2007). Dye Dependent Regeneration Dynamics in Dye Sensitized Nanocrystalline Solar Cells: Evidence for the Formation of a Ruthenium Bipyridyl Cation/Iodide Intermediate. *The Journal of Physical Chemistry C, 111*(17), 6561-6567. doi:10.1021/jp067458t

Coleman, V. A., & Jagadish, C. (2006). Basic properties and applications of ZnO. Zinc oxide bulk, thin films and nanostructures. Processing, properties and applications. *Elsevier*, 1-20. doi:10.1016/B978-008044722-3/50001-4

Colodrero, Silvia, Mihi, Agustín, Häggman, Leif, Ocaña, Manuel, Boschloo, Gerrit, Hagfeldt, Anders, & Míguez, Hernán. (2009). Porous One-Dimensional Photonic Crystals Improve the Power-Conversion Efficiency of Dye-Sensitized Solar Cells. *Advanced materials, 21*(7), 764-770. doi:10.1002/adma.200703115

Corporation, MTI, & group, KJ. (1994-2022). A super store for material Reseachers & Engineers. A world leader in advanced material & laboartory equipment. Retrieved from https://www.mtixtl.com/EQ-HDS-150.aspx

Craddock, P. T., & Museum, British. (1998). *2000 years of zinc and brass*. In London : British Museum (Ed.), (pp. 258).

Cromer, Don T., & Herrington, K. (2002). The Structures of Anatase and Rutile. *Journal of the American Chemical Society, 77*(18), 4708-4709. doi:10.1021/ja01623a004

D.C.Look, D.C.Reynolds, J.R.Sizelove, R.L.Jones, C.W.Litton, G.Cantwell, & W.C.Harsch. (1998). Electrical properties of bulk ZnO. *Solid State Communications, 105*(6), 399-401. doi:10.1016/S0038-1098(97)10145-4

Dai, Xiaojuan, Jiao, Zeqing, Ma, Zehan, Liu, Kunhui, Wang, Chen, & Su, Hongmei. (2019). Capturing the Long-Lived Photogenerated Electrons in Au/TiO2 upon UV or Visible Irradiation by Time-Resolved Infrared Spectroscopy. *The Journal of Physical Chemistry C, 123*(33), 20325-20332. doi:10.1021/acs.jpcc.9b05096

Das, Abinash, Wary, Riu Riu, & Nair, Ranjith G. (2020). Cu modified ZnO nanoflakes: An efficient visible light-driven photocatalyst and a promising photoanode for dye sensitized solar cell (DSSC). *Solid State Sciences, 104*. doi:10.1016/j.solidstatesciences.2020.106290

de Jongh, P. E., & Vanmaekelbergh, D. (1997). Investigation of the Electronic Transport Properties of Nanocrystalline Particulate TiO2Electrodes by Intensity-Modulated Photocurrent Spectroscopy. *The Journal of Physical Chemistry B, 101*(14), 2716-2722. doi:10.1021/jp962226n

Dhanalakshmi, A., Natarajan, B., Ramadas, V., Palanimurugan, A., & Thanikaikarasan, S. (2016a). Structural, morphological, optical and antibacterial activity of rod-shaped zinc

oxide and manganese-doped zinc oxide nanoparticles. *Pramana, 87*(4). doi:10.1007/s12043-016-1248-0

Dhanalakshmi, A., Natarajan, B., Ramadas, V., Palanimurugan, A., & Thanikaikarasan, S. (2016b). Structural, morphological, optical and antibacterial activity of rod-shaped zinc oxide and manganese-doped zinc oxide nanoparticles. *Pramana-Journal of Physics, 87*(4). doi:ARTN 57

10.1007/s12043-016-1248-0

Dong, Rui-Xuan, Shen, Sheng-Yen, Chen, Hsin-Wei, Wang, Chun-Chieh, Shih, Po-Ta, Liu, Chung-Te, . . . Ho, Kuo-Chuan. (2013). A novel polymer gel electrolyte for highly efficient dye-sensitized solar cells. *Journal of Materials Chemistry A, 1*(29). doi:10.1039/c3ta11331k

Du, Pingfan, Song, Lixin, Xiong, Jie, Li, Ni, Xi, Zhenqiang, Wang, Longcheng, . . . Yuan, Yongfeng. (2012). Coaxial electrospun TiO2/ZnO core–sheath nanofibers film: Novel structure for photoanode of dye-sensitized solar cells. *Electrochimica Acta, 78*, 392-397.

Dürkop, T., Getty, S. A., Cobas, Enrique, & Fuhrer, M. S. (2004). Extraordinary Mobility in Semiconducting Carbon Nanotubes. *Nano Letters, 4*(1), 35-39. doi:10.1021/nl034841q

El-Agez, Taher M., Tayyan, Ahmed A. El, Al-Kahlout, Amal, Taya, Sofyan A., & l-Latif, Monzir S. Abde. (2012). Dye-Sensitized Solar Cells Based on ZnO Films and Natural Dyes. *International Journal of M aterials and Chemistry*. doi:10.5923/j.ijm c.20120203.04

El Hamidi, A., El Mahboub, E., Meziane, K., El Hichou, A., & Almaggoussi, A. (2021). The effect of electronegativity on optical properties of Mg doped ZnO. *Optik, 241*. doi:10.1016/j.ijleo.2021.167070

Ellmer, Klaus, & Klein, Andreas. (2008). *Transparent Conductive Zinc Oxide. Basics and applications in thin film solar cells* (Klaus Ellmer, Andreas Klein, & Bernd Rech Eds.): Springer Science & Business Media.

Emanetoglu, N. W., Gorla, C., Liu, Y., Liang, S., & Lu, Y. (1999). Epitaxial ZnO piezoelectric thin films for saw filters. *Materials Science in Semiconductor Processing, 2*(3), 247-252. doi:10.1016/s1369-8001(99)00022-0

Esgin, Halil, Caglar, Yasemin, & Caglar, Mujdat. (2022). Photovoltaic performance and physical characterization of Cu doped ZnO nanopowders as photoanode for DSSC. *Journal of Alloys and Compounds, 890*. doi:10.1016/j.jallcom.2021.161848

Fan, Pu, Zhang, Dayong, Wu, Yao, Yu, Junsheng, & Russell, Thomas P. (2020). Polymer-Modified ZnO Nanoparticles as Electron Transport Layer for Polymer-Based Solar Cells. *Advanced Functional Materials, 30*(32). doi:10.1002/adfm.202002932

Faraji, Ghader, Kim, Hyoung Seop, & Kash, Hessam Torabzadeh. (2018). *Severe Plastic Deformation: Methods, Processing and Properties* (Elsevier Ed.): Matthew Deans.

Fay, Sylvie. (2003). *L'oxyde de zinc par dépôt chimique en phase vapeur comme contact électrique transparent et diffuseur de lumière pour les cellules solaires.* École Polytechnique Fédérale de Lausanne,

Fodjouong, Ghislain Joel, Feng, Yamin, Sangare, Moussa, & Huang, Xintang. (2013). Synthesis of ZnO nanostructure films by thermal evaporation approach and their application in dye-sensitized solar cells. *Materials Science in Semiconductor Processing, 16*(3), 652-658. doi:10.1016/j.mssp.2012.12.005

Foo, K. L., Hashim, U., Muhammad, K., & Voon, C. H. (2014). Sol-gel synthesized zinc oxide nanorods and their structural and optical investigation for optoelectronic application. *Nanoscale Res Lett, 9*(1), 429. doi:10.1186/1556-276X-9-429

Frederichi, D., Scaliante, Mhno, & Bergamasco, R. (2021). Structured photocatalytic systems: photocatalytic coatings on low-cost structures for treatment of water contaminated with micropollutants-a short review. *Environ Sci Pollut Res Int, 28*(19), 23610-23633. doi:10.1007/s11356-020-10022-9

Fu, Qiaoming, Zhao, Chungui, Yang, Suping, & Wu, Jihuai. (2014). The photoelectric performance of dye-sensitized solar cells fabricated by assembling pigment–protein complexes of purple bacteria on nanocrystalline photoelectrode. *Materials Letters, 129*, 195-197. doi:10.1016/j.matlet.2014.05.054

Gardeniers, J. G. E., Rittersma, Z. M., & Burger , G. J. (1998). Preferred orientation and piezoelectricity in sputtered ZnO films. *Journal of Applied Physics, 83*(12), 7844-7854. doi:10.1063/1.367959

Georgieva, J., Armyanov, S., Valova, E., Poulios, I., & Sotiropoulos, S. (2007). Enhanced photocatalytic activity of electrosynthesised tungsten trioxide–titanium dioxide bi-layer coatings under ultraviolet and visible light illumination. *Electrochemistry Communications, 9*(3), 365-370. doi:10.1016/j.elecom.2006.09.028

Ghosh, Surajit, Sartape, Rohan, & Chakraborty, Jayanta. (2020). Role of dye-induced corrosion in determining the efficiency of ZnO-based DSSC: the case of ZnO nanoforest in N719. *Journal of Materials Science: Materials in Electronics, 31*(3), 2202-2220. doi:10.1007/s10854-019-02752-5

Giannouli, Myrsini. (2013). Nanostructured ZnO, TiO2, and composite ZnO/TiO2 films for application in dye-sensitized solar cells. *International Journal of Photoenergy, 2013*.

Gillet, M., Aguir, K., Lemire, C., Gillet, E., & Schierbaum, K. (2004). The structure and electrical conductivity of vacuum-annealed WO3 thin films. *Thin Solid Films, 467*(1-2), 239-246. doi:10.1016/j.tsf.2004.04.018

Grätzel, Michael. (1999). Mesoporous oxide junctions and nanostructured solar cells. *Current Opinion in Colloid & Interface Science, 4*(4), 314-321. doi:10.1016/s1359-0294(99)90013-4

Green, Martin A., Dunlop, Ewan D., Hohl-Ebinger, Jochen, Yoshita, Masahiro, Kopidakis, Nikos, & Hao, Xiaojing. (2021). Solar cell efficiency tables (Version 58). *Progress in Photovoltaics: Research and Applications, 29*(7), 657-667. doi:10.1002/pip.3444

Guillén, E., Peter, L. M., & Anta, J. A. (2011). Electron Transport and Recombination in ZnO-Based Dye-Sensitized Solar Cells. *The Journal of Physical Chemistry C, 115*(45), 22622-22632. doi:10.1021/jp206698t

Guilln-Santiago, A., de la L. Olvera, M., Maldonado, A., Asomoza, R., & Acosta, D. R. (2004). Electrical, structural and morphological properties of chemically sprayed F-doped ZnO films: effect of the ageing-time of the starting solution, solvent and substrate temperature. *Physica Status Solidi (a), 201*(5), 952-959. doi:10.1002/pssa.200306727

Guo, L. E. I., & Kerr, Lei L. (2011). GROWTH OF ANTIMONY DOPED ZnO FIBER AND ITS APPLICATION IN DYE SENSITIZED SOLAR CELLS. *Functional Materials Letters, 03*(04), 279-283. doi:10.1142/s179360471000141x

Guo, P., & Aegerter, M. A. (1999). RU(II) sensitized Nb 2 O 5 solar cell made by the sol-gel process. *Thin Solid Films, 351*(1-2), 290-294. doi:10.1016/s0040-6090(99)00215-1

Guo, Tengchao, Xu, Guoyue, Tan, Shujuan, Yang, Zhihong, Bu, Honghan, Fang, Gang, . . . Pan, Lingyu. (2019). Controllable synthesis of ZnO with different morphologies and their morphology-dependent infrared emissivity in high temperature conditions. *Journal of Alloys and Compounds, 804*, 503-510. doi:10.1016/j.jallcom.2019.07.011

Habubi, Nadir Fadhil, Yousif, Ali Ahmed, & Haider, Adawiya. (2012). Nanostructure Zinc Oxide with Cobalt Dopant by PLD for Gas Sensor Applications. *JOURNAL OF NANO-AND ELECTRONICPHYSICS*.

Haque, S. A., Palomares, E., Cho, B. M., Green, A. N., Hirata, N., Klug, D. R., & Durrant, J. R. (2005). Charge separation versus recombination in dye-sensitized nanocrystalline solar cells: the minimization of kinetic redundancy. *J Am Chem Soc, 127*(10), 3456-3462. doi:10.1021/ja0460357

Hara, K., Zhao, Z. G., Cui, Y., Miyauchi, M., Miyashita, M., & Mori, S. (2011). Nanocrystalline electrodes based on nanoporous-walled WO3 nanotubes for organic-dye-sensitized solar cells. *Langmuir, 27*(20), 12730-12736. doi:10.1021/la201639f

Hasnidawani, J. N., Azlina, H. N., Norita, H., Bonnia, N. N., Ratim, S., & Ali, E. S. (2016). Synthesis of ZnO Nanostructures Using Sol-Gel Method. *Procedia Chemistry, 19*, 211-216. doi:https://doi.org/10.1016/j.proche.2016.03.095

Hongsith, Niyom, Mangkorntong, Chaiyuth Sae-kang2 Pongsri, Mangkorntong, Nikorn, & Choopun, Supab. (2008). JV Characteristics of Dye-sensitized Solar Cell Based on ZnO Nanobelts with Different Buffer Layer.

Hu, Q., Wu, J., Jiang, C., Liu, T., Que, X., Zhu, R., & Gong, Q. (2014). Engineering of electron-selective contact for perovskite solar cells with efficiency exceeding 15%. *ACS Nano, 8*(10), 10161-10167. doi:10.1021/nn5029828

Ikhioya, Imosobomeh L., Akpu, Nwamaka I., & Nkele, Agnes C. (2021). Influence of ytterbium (Yb) dopant on the optical properties of electrochemically deposited zinc oxide (ZnO) films. *Materials Research Express, 8*(1). doi:10.1088/2053-1591/abd5d6

Ito, S., Ha, N. L., Rothenberger, G., Liska, P., Comte, P., Zakeeruddin, S. M., . . . Gratzel, M. (2006). High-efficiency (7.2%) flexible dye-sensitized solar cells with Ti-metal substrate for nanocrystalline-TiO2 photoanode. *Chem Commun (Camb)*(38), 4004-4006. doi:10.1039/b608279c

Ito, Seigo, Chen, Peter, Comte, Pascal, Nazeeruddin, Mohammad Khaja, Liska, Paul, Péchy, Péter, & Grätzel, Michael. (2007). Fabrication of screen-printing pastes from TiO2 powders for dye-sensitised solar cells. *Progress in Photovoltaics: Research and Applications, 15*(7), 603-612. doi:10.1002/pip.768

Jäger-Waldau, Arnulf. (2019). Snapshot of Photovoltaics—February 2019. *Energies, 12*(5). doi:10.3390/en12050769

Jantrasee, S., Moontragoon, P., & Pinitsoontorn, S. (2016). Thermoelectric properties of Al-doped ZnO: experiment and simulation. *Journal of Semiconductors, 37*(9). doi:10.1088/1674-4926/37/9/092002

Jeaidi, Hana El Khal. (2017). *Relations frittage – microstructure -propriétés électriques des céramiques de type LAMOX.* COMMUNAUTÉ UNIVERSITÉ GRENOBLE ALPES, Retrieved from https://www.researchgate.net/figure/Schema-de-principe-dun-microscope-electronique-a-balayage_fig51_324103820

Ji, R., Zheng, D., Zhou, C., Cheng, J., Yu, J., & Li, L. (2017). Low-Temperature Preparation of Tungsten Oxide Anode Buffer Layer via Ultrasonic Spray Pyrolysis Method for Large-Area Organic Solar Cells. *Materials (Basel), 10*(7). doi:10.3390/ma10070820

Jiang, C. Y., Sun, X. W., Tan, K. W., Lo, G. Q., Kyaw, A. K. K., & Kwong, D. L. (2008). High-bendability flexible dye-sensitized solar cell with a nanoparticle-modified ZnO-nanowire electrode. *Applied Physics Letters, 92*(14). doi:10.1063/1.2905271

Jie, J., Wang, G., Wang, Q., Chen, Y., Han, X., Wang, X., & Hou, J. G. (2004). Synthesis and Characterization of Aligned ZnO Nanorods on Porous Aluminum Oxide Template. *J Phys Chem B, 108*(32), 11976-11980. doi:10.1021/jp048974r

Johansson, Patrik Gosta. (2013). *Photoinduced charge transfer processes: Charge separation and recombination at sensitized titanium dioxide interfaces with phenylenethynylene bridged ruthenium(II)-sensitizers.* (Doctor of Philosophy), Johns Hopkins University, ProQuest LLC 789 East Eisenhower Parkway P.O. Box 1346 Ann Arbor, Ml 48106-1346.

Joshi, Kanchan, Rawat, Mukesh, Gautam, Subodh K., Singh, R. G., Ramola, R. C., & Singh, Fouran. (2016). Band gap widening and narrowing in Cu-doped ZnO thin films. *Journal of Alloys and Compounds, 680*, 252-258. doi:10.1016/j.jallcom.2016.04.093

Jun, Yongseok, Kim, Jongdae, & Kang, Man Gu. (2007). A study of stainless steel-based dye-sensitized solar cells and modules. *Solar Energy Materials and Solar Cells, 91*(9), 779-784. doi:10.1016/j.solmat.2007.01.007

Kaidashev, E. M., Lorenz, M., Wenckstern, H. von, Rahm, A., Semmelhack, H.-C., Han, K.-H., . . . Grundmann, M. (2003). High electron mobility of epitaxial ZnO thin films on *Applied Physics Letters*. doi:10.1063/1.1578694

Kakiage, K., Aoyama, Y., Yano, T., Oya, K., Fujisawa, J., & Hanaya, M. (2015). Highly-efficient dye-sensitized solar cells with collaborative sensitization by silyl-anchor and carboxy-anchor dyes. *Chem Commun (Camb), 51*(88), 15894-15897. doi:10.1039/c5cc06759f

Kalowekamo, Joseph, & Baker, Erin. (2009). Estimating the manufacturing cost of purely organic solar cells. *Solar Energy, 83*(8), 1224-1231. doi:10.1016/j.solener.2009.02.003

Kamaruddin, Sharul Ashikin, Chan, Kah-Yoong, Yow, Ho-Kwang, Zainizan Sahdan, Mohd, Saim, Hashim, & Knipp, Dietmar. (2010). Zinc oxide films prepared by sol–gel spin coating technique. *Applied Physics A, 104*(1), 263-268. doi:10.1007/s00339-010-6121-2

Kang, Man Gu, Park, Nam-Gyu, Ryu, Kwang Sun, Chang, Soon Ho, & Kim, Kang-Jin. (2006). A 4.2% efficient flexible dye-sensitized TiO2 solar cells using stainless steel substrate. *Solar Energy Materials and Solar Cells, 90*(5), 574-581. doi:10.1016/j.solmat.2005.04.025

Kang, Youn-Seon, Kim, Hae-Yeol, & Lee, Jai-Young. (2000). Effects of Hydrogen on the Structural and Electro-optical Properties of Zinc Oxide Thin Films. *Journal of The Electrochemical Society, 147*(12). doi:10.1149/1.1394113

Karuppuchamy, S. (2002). Cathodic electrodeposition of oxide semiconductor thin films and their application to dye-sensitized solar cells. *Solid State Ionics, 151*(1-4), 19-27. doi:10.1016/s0167-2738(02)00599-4

Kato, Hiroyuki, Sano, Michihiro, Miyamoto, Kazuhiro, & Yao, Takafumi. (2003). Effect of O/Zn Flux Ratio on Crystalline Quality of ZnO Films Grown by Plasma-Assisted Molecular Beam Epitaxy. *Japanese Journal of Applied Physics*. doi:10.1143/JJAP.42.2241

Katoh, Ryuzi, Furube, Akihiro, Barzykin, Alexander V., Arakawa, Hironori, & Tachiya, M. (2004). Kinetics and mechanism of electron injection and charge recombination in dye-sensitized nanocrystalline semiconductors. *Coordination Chemistry Reviews, 248*(13-14), 1195-1213. doi:10.1016/j.ccr.2004.03.017

Katoh, Ryuzi, Furube, Akihiro, Yoshihara, Toshitada, Hara, Kohjiro, Fujihashi, Gaku, Takano, Shingo, . . . Tachiya, M. (2004). Efficiencies of Electron Injection from Excited N3 Dye into Nanocrystalline Semiconductor (ZrO2, TiO2, ZnO, Nb2O5, SnO2, In2O3) Films. *The Journal of Physical Chemistry B, 108*(15), 4818-4822. doi:10.1021/jp031260g

Kay, Andreas, & Grätzel, Michael. (1996). Low cost photovoltaic modules based on dye sensitized nanocrystalline titanium dioxide and carbon powder. *Solar Energy Materials and Solar Cells, 44*(1), 99-117. doi:10.1016/0927-0248(96)00063-3

Kay, Andreas, & Grätzel, Michael. (2002). Dye-Sensitized Core−Shell Nanocrystals: Improved Efficiency of Mesoporous Tin Oxide Electrodes Coated with a Thin Layer of an Insulating Oxide. *Chemistry of Materials, 14*(7), 2930-2935. doi:10.1021/cm0115968

Kayanuma, Y. (1988). Quantum-size effects of interacting electrons and holes in semiconductor microcrystals with spherical shape. *Phys Rev B Condens Matter, 38*(14), 9797-9805. doi:10.1103/physrevb.38.9797

Keis, K., Bauer, C., Boschloo, G., Hagfeldt, A., Westermark, K., Rensmo, H., & Siegbahn, H. (2002). Nanostructured ZnO electrodes for dye-sensitized solar cell applications. *Journal of Photochemistry and Photobiology A: Chemistry, 148*(1-3), 57-64. doi:10.1016/s1010-6030(02)00039-4

Keis, Karin, Lindgren, Jan, Lindquist, Sten-Eric, & Hagfeldt, Anders. (2000). Studies of the Adsorption Process of Ru Complexes in Nanoporous ZnO Electrodes. *Langmuir, 16*(10), 4688-4694. doi:10.1021/la9912702

Khranovskyy, V., Lazorenko, V., Lashkarev, G., & Yakimova, R. (2012). Luminescence anisotropy of ZnO microrods. *Journal of Luminescence, 132*(10), 2643-2647. doi:10.1016/j.jlumin.2012.04.048

Kim, Il-Doo, Hong, Jae-Min, Lee, Byong Hong, Kim, Dong Young, Jeon, Eun-Kyung, Choi, Duck-Kyun, & Yang, Dae-Jin. (2007). Dye-sensitized solar cells using network structure of electrospun ZnO nanofiber mats. *Applied Physics Letters, 91*(16). doi:10.1063/1.2799581

Kim, Kyoung-Kook, Niki, Shigeru, Oh, Jin-Yong, Song, June- O., Seong, Tae-Yeon, Park, Seong-Ju, . . . Kim, Sang-Woo. (2005). High electron concentration and mobility in Al-doped n-ZnO epilayer achieved via dopant activation using rapid-thermal annealing. *Journal of Applied Physics, 97*(6). doi:10.1063/1.1863416

Kleinwechter, H., Janzen, C., Knipping, J., Wiggers, H., & Roth, P. (2002). Formation and properties of ZnO nano-particles from gas phase synthesis processes. *Journal of Materials Science, 37*(20), 4349-4360. doi:10.1023/a:1020656620050

Ko, S. H., Lee, D., Kang, H. W., Nam, K. H., Yeo, J. Y., Hong, S. J., . . . Sung, H. J. (2011). Nanoforest of hydrothermally grown hierarchical ZnO nanowires for a high efficiency dye-sensitized solar cell. *Nano Lett, 11*(2), 666-671. doi:10.1021/nl1037962

Kokkonen, M., Talebi, P., Zhou, J., Asgari, S., Soomro, S. A., Elsehrawy, F., . . . Hashmi, S. G. (2021). Advanced research trends in dye-sensitized solar cells. *J Mater Chem A Mater, 9*(17), 10527-10545. doi:10.1039/d1ta00690h

Kolodziejczak-Radzimska, A., & Jesionowski, T. (2014). Zinc Oxide-From Synthesis to Application: A Review. *Materials (Basel), 7*(4), 2833-2881. doi:10.3390/ma7042833

Kooti, M., & Naghdi Sedeh, A. (2013). Microwave-Assisted Combustion Synthesis of ZnO Nanoparticles. *Journal of Chemistry, 2013*, 1-4. doi:10.1155/2013/562028

Kosmulski, Marek. (2002). The significance of the difference in the point of zero charge between rutile and anatase. *Advances in Colloid and Interface Science, 99*(3), 255-264. doi:10.1016/s0001-8686(02)00080-5

Krüger, Jessica, Plass, Robert, Grätzel, Michael, & Matthieu, Hans-Jörg. (2002). Improvement of the photovoltaic performance of solid-state dye-sensitized device by silver complexation of the sensitizer cis-bis(4,4′-dicarboxy-2,2′bipyridine)-bis(isothiocyanato) ruthenium(II). *Applied Physics Letters, 81*(2), 367-369. doi:10.1063/1.1490394

Kumar, Aditya, & Nanda, Debasis. (2019). Superhydrophobic Polymer Coatings. In.

Kumar, Rajesh, Umar, Ahmad, Kumar, Girish, Nalwa, Hari Singh, Kumar, Anil, & Akhtar, M. S. (2017). Zinc oxide nanostructure-based dye-sensitized solar cells. *Journal of Materials Science, 52*(9), 4743-4795. doi:10.1007/s10853-016-0668-z

Kustova, G. N., Chesalov, Yu A., Plyasova, L. M., Molina, I. Yu, & Nizovskii, A. I. (2011). Vibrational spectra of WO3·nH2O and WO3 polymorphs. *Vibrational Spectroscopy, 55*(2), 235-240. doi:10.1016/j.vibspec.2010.12.004

LAHMANI, Marcel, BRÉCHIGNAC, Catherine, & HOUDY, Philippe. (2012). *Les nanosciences 2- Nanomatériaux et nanochimie* (BELIN Ed. Échelles ed.).

LAHMANI, Marcel, DUPAS, Claire, & HOUDY, Philippe. (2009). *Les nanosciences 1- Nanotechnologies et nanophysique* (BELIN Ed. Échelles ed.).

Lambertz, Andreas, Finger, Friedhelm, Schropp, Ruud EI, Rau, Uwe, & Smirnov, Vladimir. (2015). Preparation and measurement of highly efficient a-Si: H single junction solar cells and the advantages of μc-SiOx: H n-layers. *Progress in Photovoltaics: Research and Applications, 23*(8), 939-948.

Laurent, K., Yu, D. P., Tusseau-Nenez, S., & Leprince-Wang, Y. (2008). Thermal annealing effect on optical properties of electrodeposited ZnO thin films. *Journal of Physics D: Applied Physics, 41*(19). doi:10.1088/0022-3727/41/19/195410

Law, M., Greene, L. E., Johnson, J. C., Saykally, R., & Yang, P. (2005). Nanowire dye-sensitized solar cells. *Nat Mater, 4*(6), 455-459. doi:10.1038/nmat1387

Le Pevelen, Delphine D. (2010). Small Molecule X-Ray Crystallography, Theory and Workflow. In John C. Lindon (Ed.), *Encyclopedia of Spectroscopy and Spectrometry (Second Edition)* (pp. 2559-2576). Oxford: Academic Press.

Lee, Chuan-Pei, Chou, Chen-Yu, Chen, Chia-Yuan, Yeh, Min-Hsin, Lin, Lu-Yin, Vittal, R., . . . Ho, Kuo-Chuan. (2014). Zinc oxide-based dye-sensitized solar cells with a ruthenium dye containing an alkyl bithiophene group. *Journal of Power Sources, 246*, 1-9. doi:http://dx.doi.org/10.1016/j.jpowsour.2013.05.101

Lee, Jin-Hong, Ko, Kyung-Hee, & Park, Byung-Ok. (2003). Electrical and optical properties of ZnO transparent conducting films by the sol–gel method. *Journal of Crystal Growth, 247*(1-2), 119-125. doi:10.1016/s0022-0248(02)01907-3

Lee, Kang Min, Lee, Eung Seok, Yoo, Bongyoung, & Shin, Dong Hyuk. (2013). Synthesis of ZnO-decorated TiO2 nanotubes for dye-sensitized solar cells. *Electrochimica Acta, 109*, 181-186.

Lee, Kun-Mu, Chiu, Wei-Hao, Wei, Hung-Yu, Hu, Chih-Wei, Suryanarayanan, Vembu, Hsieh, Weng-Feng, & Ho, Kuo-Chuan. (2010). Effects of mesoscopic poly(3,4-ethylenedioxythiophene) films as counter electrodes for dye-sensitized solar cells. *Thin Solid Films, 518*(6), 1716-1721. doi:10.1016/j.tsf.2009.11.058

Li, Fengrong, Jiao, Yu, Xie, Shuhong, & Li, Jiangyu. (2015). Sponge-like porous TiO2/ZnO nanodonuts for high efficiency dye-sensitized solar cells. *Journal of Power Sources, 280*, 373-378.

Li, Jiansheng, Sang, Xiaojing, Chen, Weilin, Qin, Chao, Wang, Shiming, Su, Zhongmin, & Wang, Enbo. (2013). The Application of ZnO Nanoparticles Containing Polyoxometalates in Dye-Sensitized Solar Cells. *European Journal of Inorganic Chemistry, 2013*(10-11), 1951-1959. doi:10.1002/ejic.201201120

Li, Q. Y., Kang, Z. H., Mao, B. D., Wang, E. B., Wang, C. L., Tian, C. G., & Li, S. H. (2008). One-step polyoxometalate-assisted solvothermal synthesis of ZnO microspheres and their

photoluminescence properties. *Materials Letters, 62*(15), 2531-2534. doi:10.1016/j.matlet.2007.12.041

Li, Zuopeng, Ye, Baoxi, Hu, Xiaodong, Ma, Xiangyuan, Zhang, Xiaoping, & Deng, Youquan. (2009). Facile electropolymerized-PANI as counter electrode for low cost dye-sensitized solar cell. *Electrochemistry Communications, 11*(9), 1768-1771. doi:10.1016/j.elecom.2009.07.018

Lin, Hsuan Ching, Su, Chaochin, & Li, Wen-Ren. (2013). *The effect of ZnO coatings om the performance of WO3 dye-sensitized solar cells*. Paper presented at the The 2013 World Congress on Advances in Nano, Biomechanics, Robotics, and Energy Research (ANBRE13).

Lin, Jeng-Yu, & Liao, Jen-Hung. (2011). Mesoporous Electrodeposited-CoS Film as a Counter Electrode Catalyst in Dye-Sensitized Solar Cells. *Journal of The Electrochemical Society, 159*(2), D65-D71. doi:10.1149/2.036202jes

Liu, Huiyong, Avrutin, V., Izyumskaya, N., Özgür, Ü, & Morkoç, H. (2010). Transparent conducting oxides for electrode applications in light emitting and absorbing devices. *Superlattices and Microstructures, 48*(5), 458-484. doi:10.1016/j.spmi.2010.08.011

Liu, Rui, Yang, Wein-Duo, Qiang, Liang-Sheng, & Liu, Hsin-Yi. (2012). Conveniently fabricated heterojunction ZnO/TiO2 electrodes using TiO2 nanotube arrays for dye-sensitized solar cells. *Journal of Power Sources, 220*, 153-159.

Liu, X., Luo, Y., Li, H., Fan, Y., Yu, Z., Lin, Y., . . . Meng, Q. (2007). Room temperature fabrication of porous ZnO photoelectrodes for flexible dye-sensitized solar cells. *Chem Commun (Camb)*(27), 2847-2849. doi:10.1039/b700472a

Liu, Xueyang, Fang, Jian, Liu, Yong, & Lin, Tong. (2016). Progress in nanostructured photoanodes for dye-sensitized solar cells. *Frontiers of Materials Science, 10*(3), 225-237. doi:10.1007/s11706-016-0341-0

Look, D. C. (2001). Recent advances in ZnO materials and devices. *Materials Science and Engineering: B, 80*(1-3), 383-387. doi:10.1016/s0921-5107(00)00604-8

Look, D. C., Claflin, B., Alivov, Ya I., & Park, S. J. (2004). The future of ZnO light emitters. *Physica Status Solidi (a), 201*(10), 2203-2212. doi:10.1002/pssa.200404803

Look, D. C., Reynolds, D. C., Hemsky, J. W., Jones, R. L., & Sizelove, J. R. (1999). Production and annealing of electron irradiation damage in ZnO. *Applied Physics Letters, 75*(6), 811-813. doi:10.1063/1.124521

Lu, Yicheng, Emanetoglu, Nuri W., & Chen, Ying. (2006). Chapter 13 - ZnO Piezoelectric Devices. *Elsevier*. doi:10.1016/B978-008044722-3/50013-0

M. Sahal, B. Hartiti, B. Mari, A. Ridah, M. Mollar2. (2006). Etude des propriétés physiques des couches minces de ZnO dopées Al, préparées par la méthode de « sol-gel » associée au « spin coating » *Afrique SCIENCE 02(3) (2006) 245 - 254*.

Ma, Jin, Ji, Feng, Ma, Hong-lei, & Li, Shu-ying. (1996). Electrical and optical properties of ZnO: Al films prepared by an evaporation method. *Thin Solid Films, 279*(1-2), 213-215. doi:10.1016/0040-6090(95)08173-9

Ma, Tae Young, Kim, Sang Hyun, Moon, Hyun Yul, Park, Gi Cheol, Kim, Young Jin, & Kim, Ki Wan. (1996). Substrate Temperature Dependence of ZnO Films Prepared by Ultrasonic Spray Pyrolysis. *Japanese Journal of Applied Physics, 35*.

Maeda, Katsumi, Sato, Mitsuru, Niikura, Ikuo, & Fukuda, Tsuguo. (2005). Growth of 2 inch ZnO bulk single crystal by the hydrothermal method. *Semiconductor Science and Technology*. doi:10.1088/0268-1242/20/4/006

Mahajan, Prerna, Ahmed, Aamir, Datt, Ram, Gupta, Vinay, & Arya, Sandeep. (2022). Chemically Synthesized ZnO-WO3 Nanoparticles as Electron and Hole Transport Layer in Organic Solar Cells. *ECS Transactions, 107*(1), 9199-9209. doi:10.1149/10701.9199ecst

Mandal, S., Mullick, H., Majumdar, S., Dhar, A., & Ray, S. K. (2008). Effect of Al concentration in grain and grain boundary region of Al-doped ZnO films: a dielectric approach. *Journal of Physics D: Applied Physics, 41*(2). doi:10.1088/0022-3727/41/2/025307

Manimozhi, T., Logu, T., Archana, J., Navaneethan, M., Sethuraman, K., & Ramamurthi, K. (2020). Enhanced photo-response of CdTe Thin film via Mo doping prepared using electron beam evaporation technique. *Journal of Materials Science: Materials in Electronics, 31*(23), 21059-21072. doi:10.1007/s10854-020-04618-7

Manseki, K., Jarernboon, W., Youhai, Y., Jiang, K. J., Suzuki, K., Masaki, N., . . . Yanagida, S. (2011). Solid-state dye-sensitized solar cells fabricated by coupling photoelectrochemically deposited poly(3,4-ethylenedioxythiophene) (PEDOT) with silver-paint on cathode. *Chem Commun (Camb), 47*(11), 3120-3122. doi:10.1039/c0cc04841k

Markets, Future, & Inc. (2015). *The Global Market for Zinc Oxide Nanoparticles*. Retrieved from Rockville, MD, USA:

Marschall, Roland. (2014). Semiconductor Composites: Strategies for Enhancing Charge Carrier Separation to Improve Photocatalytic Activity. *Advanced Functional Materials, 24*(17), 2421-2440. doi:10.1002/adfm.201303214

Martínez, M. A., Herrero, J., & Gutiérrez, M. T. (1994). Properties of RF sputtered zinc oxide based thin films made from different targets. *Solar Energy Materials and Solar Cells, 31*(4), 489-498. doi:10.1016/0927-0248(94)90191-0

Mathew, S., Yella, A., Gao, P., Humphry-Baker, R., Curchod, B. F., Ashari-Astani, N., . . . Gratzel, M. (2014). Dye-sensitized solar cells with 13% efficiency achieved through the molecular engineering of porphyrin sensitizers. *Nat Chem, 6*(3), 242-247. doi:10.1038/nchem.1861

Matsubara, K., Fons, P., Iwata, K., Yamada, A., Sakurai, K., Tampo, H., & Niki, S. (2003). ZnO transparent conducting films deposited by pulsed laser deposition for solar cell applications. *Thin Solid Films, 431*, 369-372. doi:10.1016/S0040-6090(03)00243-8

Matsumura, Michio, Matsudaira, Shigeyuki, Tsubomura, Hiroshi, Takata, Masasuke, & Yanagida, Hiroaki. (1980). Dye Sensitization and Surface Structures of Semiconductor Electrodes.

Industrial & Engineering Chemistry Product Research and Development, 19(3), 415-421. doi:10.1021/i360075a025

Mehdi, Hussein. (2019). *Etude delapassivationduGaAs(100)parnitruration par plasmaN2sousultra-vide.* UNIVERSITÉ DE CLERMONT AUVERGNE,

Memarian, Nafiseh, Concina, Isabella, Braga, Antonio, Rozati, Seyed Mohammad, Vomiero, Alberto, & Sberveglieri, Giorgio. (2011). Hierarchically Assembled ZnO Nanocrystallites for High-Efficiency Dye-Sensitized Solar Cells. *Angewandte Chemie, 123*(51), 12529-12533. doi:10.1002/ange.201104605

Messaoudi, C., Sayah, D., & Abd-lefdil, M. (1995). Transparent conducting undoped and indium-doped zinc oxide films prepared by spray pyrolysis. *Physica Status Solidi (a), 151*(1), 93-97. doi:10.1002/pssa.2211510110

Metivier, R. P., Francis, F. J., & Clydesdale, F. M. (1980). Solvent Extraction of Anthocyanins from Wine Pomace. *Journal of Food Science, 45*(4), 1099-1100. doi:10.1111/j.1365-2621.1980.tb07534.x

Minami, Tadatsugu. (2005). Transparent conducting oxide semiconductors for transparent electrodes. *Semiconductor Science and Technology, 20*(4), S35-S44. doi:10.1088/0268-1242/20/4/004

Miyamoto, Kazuhiro, Sano, Michihiro, Kato, Hiroyuki, & Yao, Takafumi. (2004). High-electron-mobility ZnO epilayers grown by plasma-assisted molecular beam epitaxy. *Journal of Crystal Growth, Volume 265*(1-2), 34-40. doi:10.1016/j.jcrysgro.2004.01.035

Moulder, John F., Stickle, William F., Sobol, Peter E., & Bomben, Kenneth D. (1995). *Handbookof X-ray Photoelectron Spectroscopy* (Jill Chastain Ed.).

Murakami, Takurou N., & Grätzel, Michael. (2008). Counter electrodes for DSC: Application of functional materials as catalysts. *Inorganica Chimica Acta, 361*(3), 572-580. doi:10.1016/j.ica.2007.09.025

Murakami, Takurou N., Ito, Seigo, Wang, Qing, Nazeeruddin, Md Khaja, Bessho, Takeru, Cesar, Ilkay, . . . Grätzel, Michael. (2006). Highly Efficient Dye-Sensitized Solar Cells Based on Carbon Black Counter Electrodes. *Journal of The Electrochemical Society, 153*(12). doi:10.1149/1.2358087

Nagaraju, G., Udayabhanu, Shivaraj, Prashanth, S. A., Shastri, M., Yathish, K. V., . . . Rangappa, D. (2017). Electrochemical heavy metal detection, photocatalytic, photoluminescence, biodiesel production and antibacterial activities of Ag–ZnO nanomaterial. *Materials Research Bulletin, 94*, 54-63. doi:10.1016/j.materresbull.2017.05.043

Nakade, S., Matsuda, M., Kambe, S., Saito, Y., Kitamura, T., Sakata, T., . . . Yanagida, S. (2002). Dependence of TiO2Nanoparticle Preparation Methods and Annealing Temperature on the Efficiency of Dye-Sensitized Solar Cells. *The Journal of Physical Chemistry B, 106*(39), 10004-10010. doi:10.1021/jp020051d

Nause, J, & Nemeth, B. (2005). Pressurized melt growth of ZnO boules. *Semiconductor Science and Technology*. doi:10.1088/0268-1242/20/4/005

Nazeeruddin, M. K., De Angelis, F., Fantacci, S., Selloni, A., Viscardi, G., Liska, P., . . . Gratzel, M. (2005). Combined experimental and DFT-TDDFT computational study of photoelectrochemical cell ruthenium sensitizers. *J Am Chem Soc, 127*(48), 16835-16847. doi:10.1021/ja0524671

Nelson, Jenny, & Chandler, Rosemary E. (2004). Random walk models of charge transfer and transport in dye sensitized systems. *Coordination Chemistry Reviews, 248*(13-14), 1181-1194. doi:10.1016/j.ccr.2004.04.001

Ngamsinlapasathian, Supachai, Sreethawong, Thammanoon, & Yoshikawa, Susumu. (2008). Enhanced efficiency of dye-sensitized solar cell using double-layered conducting glass. *Thin Solid Films, 516*(21), 7802-7806. doi:10.1016/j.tsf.2008.03.037

Ngom, B. D., Mpahane, T., Manyala, N., Nemraoui, O., Buttner, U., Kana, J. B., . . . Beye, A. C. (2009). Structural and optical properties of nano-structured tungsten-doped ZnO thin films grown by pulsed laser deposition. *Applied Surface Science, 255*(7), 4153-4158. doi:10.1016/j.apsusc.2008.10.122

Nogueira, Helena I. S., Cavaleiro, Ana M. V., Rocha, João, Trindade, Tito, & de Jesus, Júlio D. Pedrosa. (2004). Synthesis and characterization of tungsten trioxide powders prepared from tungstic acids. *Materials Research Bulletin, 39*(4-5), 683-693. doi:10.1016/j.materresbull.2003.11.004

Norton, D. P., Heo, Y. W., Ivill, M. P., Ip, K., Pearton, S. J., Chisholm, M. F., & Steiner, T. (2004). ZnO: growth, doping & processing. *Materials Today, 7*(6), 34-40. doi:10.1016/s1369-7021(04)00287-1

O'Regan, Brian, & Grätzel, Michael. (1991). A low-cost, high-efficiency solar cell based on dye-sensitized colloidal TiO2 films. *Nature, 353*(6346), 737-740. doi:10.1038/353737a0

Olsen, Espen, Hagen, Georg, & Eric Lindquist, Sten. (2000). Dissolution of platinum in methoxy propionitrile containing LiI/I2. *Solar Energy Materials and Solar Cells, 63*(3), 267-273. doi:10.1016/s0927-0248(00)00033-7

Omar, Azimah, & Abdullah, Huda. (2014). Electron transport analysis in zinc oxide-based dye-sensitized solar cells: A review. *Renewable and Sustainable Energy Reviews, 31*, 149-157. doi:10.1016/j.rser.2013.11.031

Onwona-Agyeman, Boateng, Kaneko, Shoji, Kumara, Asoka, Okuya, Masayuki, Murakami, Kenji, Konno, Akinori, & Tennakone, Kirthi. (2005). Sensitization of Nanocrystalline SnO2Films with Indoline Dyes. *Japanese Journal of Applied Physics, 44*(No. 23), L731-L733. doi:10.1143/jjap.44.L731

Özgür, Ümit, & Morkoç, Hadis. (2018). Zinc Oxide Materials and Devices Grown by Molecular Beam Epitaxy. *Science direct*.

Palomares, Emilio, Clifford, John N, Haque, Saif A, Lutz, Thierry, & Durrant, James R. (2002). Slow charge recombination in dye-sensitised solar cells (DSSC) using Al 2 O 3 coated nanoporous TiO 2 films. *Chemical Communications*(14), 1464-1465.

Pan, Hanqing, Risley, Victoria A., Martindale, Kristian R., & Heagy, Michael D. (2018). Photocatalytic Reduction of Bicarbonate to Formic Acid Using Hierarchical ZnO

Nanostructures. *ACS Sustainable Chemistry & Engineering, 7*(1), 1210-1219. doi:10.1021/acssuschemeng.8b04861

Pang, Shan, Xie, Tengfeng, Zhang, Yu, Wei, Xiao, Yang, Min, Wang, Dejun, & Du, Zuliang. (2007). Research on the Effect of Different Sizes of ZnO Nanorods on the Efficiency of TiO2-Based Dye-Sensitized Solar Cells. *The Journal of Physical Chemistry C, 111*(49), 18417-18422. doi:10.1021/jp0763073

Paradiso, J. A., & Starner, T. (2005). Energy Scavenging for Mobile and Wireless Electronics. *IEEE Pervasive Computing, 4*(1), 18-27. doi:10.1109/mprv.2005.9

Park, N. G., Kang, M. G., Kim, K. M., Ryu, K. S., Chang, S. H., Kim, D. K., . . . Frank, A. J. (2004). Morphological and photoelectrochemical characterization of core-shell nanoparticle films for dye-sensitized solar cells: Zn-O type shell on SnO2 and TiO2 cores. *Langmuir, 20*(10), 4246-4253. doi:10.1021/la036122x

Pearton, Stephen J., Norton, David P., Ivill, Matt P., Hebard, Art F., Zavada, John M., Chen, Weimin M., & Buyanova, Irina A. (2007). ZnO Doped With Transition Metal Ions. *IEEE Transactions on Electron Devices, 54*(5), 1040-1048. doi:10.1109/ted.2007.894371

Pelet, Serge, Moser, Jacques- E., & Grätzel, Michael. (2000). Cooperative Effect of Adsorbed Cations and Iodide on the Interception of Back Electron Transfer in the Dye Sensitization of Nanocrystalline TiO2. *The Journal of Physical Chemistry B, 104*(8), 1791-1795. doi:10.1021/jp9934477

Pham, Duy Phong, Nguyen, Huu Truong, Phan, Bach Thang, Hoang, Van Dung, Maenosono, Shinya, & Tran, Cao Vinh. (2015). Influence of addition of indium and of post-annealing on structural, electrical and optical properties of gallium-doped zinc oxide thin films deposited by direct-current magnetron sputtering. *Thin Solid Films, 583*, 201-204. doi:10.1016/j.tsf.2015.03.068

Photovoltaics report. (2021). Retrieved from www.ise.fraunhofer.de: https://www.ise.fraunhofer.de/content/dam/ise/de/documents/publications/studies/Photovoltaics-Report.pdf

Picollo, Marcello, Aceto, Maurizio, & Vitorino, Tatiana. (2019). UV-Vis spectroscopy. *Physical Sciences Reviews, 4*(4). doi:doi:10.1515/psr-2018-0008

Pradhan, Basudev, Batabyal, Sudip K., & Pal, Amlan J. (2007). Vertically aligned ZnO nanowire arrays in Rose Bengal-based dye-sensitized solar cells. *Solar Energy Materials and Solar Cells, 91*(9), 769-773. doi:10.1016/j.solmat.2007.01.006

Qin, Y., Wang, X., & Wang, Z. L. (2008). Microfibre-nanowire hybrid structure for energy scavenging. *Nature, 451*(7180), 809-813. doi:10.1038/nature06601

Qiu, J., Guo, M., & Wang, X. (2011). Electrodeposition of hierarchical ZnO nanorod-nanosheet structures and their applications in dye-sensitized solar cells. *ACS Appl Mater Interfaces, 3*(7), 2358-2367. doi:10.1021/am2002789

Qu, Jie, Yang, Yongan, Wu, Qingduan, Coxon, Paul R., Liu, Yingjun, He, Xiong, . . . Ding, Jianning. (2014). Hedgehog-like hierarchical ZnO needle-clusters with superior electron

transfer kinetics for dye-sensitized solar cells. *RSC Adv., 4*(22), 11430-11437. doi:10.1039/c3ra45929b

Qu, Y., Gessert, T. A., Coutts, T. J., & Noufi, R. (1994). Study of ion-beam-sputtered ZnO films as a function of deposition temperature. *Journal of Vacuum Science & Technology A: Vacuum, Surfaces, and Films, 12*(4), 1507-1512. doi:10.1116/1.579346

Ramos, F. J., Lopez-Santos, M. C., Guillen, E., Nazeeruddin, M. K., Gratzel, M., Gonzalez-Elipe, A. R., & Ahmad, S. (2014). Perovskite solar cells based on nanocolumnar plasma-deposited ZnO thin films. *Chemphyschem, 15*(6), 1148-1153. doi:10.1002/cphc.201301215

Richhariya, Geetam, Kumar, Anil, Tekasakul, Perapong, & Gupta, Bhupendra. (2017). Natural dyes for dye sensitized solar cell: A review. *Renewable and Sustainable Energy Reviews, 69*, 705-718. doi:10.1016/j.rser.2016.11.198

Roy-Mayhew, J. D., Bozym, D. J., Punckt, C., & Aksay, I. A. (2010). Functionalized graphene as a catalytic counter electrode in dye-sensitized solar cells. *ACS Nano, 4*(10), 6203-6211. doi:10.1021/nn1016428

Saito, Yasuteru, Kubo, Wataru, Kitamura, Takayuki, Wada, Yuji, & Yanagida, Shozo. (2004). I−/I3− redox reaction behavior on poly(3,4-ethylenedioxythiophene) counter electrode in dye-sensitized solar cells. *Journal of Photochemistry and Photobiology A: Chemistry, 164*(1-3), 153-157. doi:10.1016/j.jphotochem.2003.11.017

Sajjad, Ahmed Khan Leghari, Sajjad, Shamaila, Iqbal, Anum, & Ryma, Najam-ul-Athar. (2018). ZnO/WO3 nanostructure as an efficient visible light catalyst. *Ceramics International, 44*(8), 9364-9371. doi:10.1016/j.ceramint.2018.02.150

Saleem, M. (2012). Effect of zinc acetate concentration on the structural and optical properties of ZnO thin films deposited by Sol-Gel method. *International Journal of the Physical Sciences, 7*(23). doi:10.5897/ijps12.219

Sang, Xiaojing, Li, Jiansheng, Chen, Weilin, & Wang, Enbo. (2012). Polyoxometalate-assisted synthesis of the ZnO polyhedra in an alkali solution and their photoelectrical properties. *Materials Letters, 87*, 39-42. doi:10.1016/j.matlet.2012.07.100

Saranya, K., Rameez, Md, & Subramania, A. (2015). Developments in conducting polymer based counter electrodes for dye-sensitized solar cells – An overview. *European Polymer Journal, 66*, 207-227. doi:10.1016/j.eurpolymj.2015.01.049

Satapathi, Soumitra, Gill, Hardeep Singh, Das, Sriya, Li, Lian, Samuelson, Lynne, Green, Micah J., & Kumar, Jayant. (2014). Performance enhancement of dye-sensitized solar cells by incorporating graphene sheets of various sizes. *Applied Surface Science, 314*, 638-641. doi:10.1016/j.apsusc.2014.07.003

Sato, H., Minami, T., Tamura, Y., Takata, S., Mouri, T., & Ogawa, N. (1994). Aluminium content dependence of milky transparent conducting ZnO:Al films with textured surface prepared by d.c. magnetron sputtering. *Thin Solid Films, 246*(1-2), 86-91. doi:10.1016/0040-6090(94)90736-6

Sauvage, F., Chen, D., Comte, P., Huang, F., Heiniger, L. P., Cheng, Y. B., . . . Graetzel, M. (2010). Dye-sensitized solar cells employing a single film of mesoporous TiO2 beads achieve power conversion efficiencies over 10%. *ACS Nano, 4*(8), 4420-4425. doi:10.1021/nn1010396

Savadogo, O. (1998). Chemically and electrochemically deposited thin films for solar energy materials. *Solar Energy Materials and Solar Cells, 52*(3-4), 361-388. doi:10.1016/s0927-0248(97)00247-x

Savadogo, O., & Mandal, K. C. (2019a). Characterizations of Antimony Tri-Sulfide Chemically Deposited with Silicotungstic Acid. *Journal of The Electrochemical Society, 139*(1), L16-L18. doi:10.1149/1.2069211

Savadogo, O., & Mandal, K. C. (2019b). Low Cost Schottky Barrier Solar Cells Fabricated on CdSe and Sb2 S 3 Films Chemically Deposited with Silicotungstic Acid. *Journal of The Electrochemical Society, 141*(10), 2871-2877. doi:10.1149/1.2059248

Segets, D., Gradl, J., Taylor, R. K., Vassilev, V., & Peukert, W. (2009). Analysis of optical absorbance spectra for the determination of ZnO nanoparticle size distribution, solubility, and surface energy. *ACS Nano, 3*(7), 1703-1710. doi:10.1021/nn900223b

Senadeera, R., Fukuri, N., Saito, Y., Kitamura, T., Wada, Y., & Yanagida, S. (2005). Volatile solvent-free solid-state polymer-sensitized TiO2 solar cells with poly(3,4-ethylenedioxythiophene) as a hole-transporting medium. *Chem Commun (Camb)*(17), 2259-2261. doi:10.1039/b500546a

Sengupta, J., Sahoo, R. K., Bardhan, K. K., & Mukherjee, C. D. (2011). Influence of annealing temperature on the structural, topographical and optical properties of sol-gel derived ZnO thin films. *Materials Letters, 65*(17-18), 2572-2574. doi:10.1016/j.matlet.2011.06.021

Shah, A. V., Schade, H., Vanecek, M., Meier, J., Vallat-Sauvain, E., Wyrsch, N., . . . Bailat, J. (2004). Thin-film silicon solar cell technology. *Progress in Photovoltaics: Research and Applications, 12*(23), 113-142. doi:10.1002/pip.533

Shalini, S., Balasundaraprabhu, R., Kumar, T. Satish, Prabavathy, N., Senthilarasu, S., & Prasanna, S. (2016). Status and outlook of sensitizers/dyes used in dye sensitized solar cells (DSSC): a review. *International Journal of Energy Research, 40*(10), 1303-1320. doi:10.1002/er.3538

Sharma, Dhirendra Kumar, Shukla, Sweta, Sharma, Kapil Kumar, & Kumar, Vipin. (2020). A review on ZnO: Fundamental properties and applications. *Materials Today: Proceedings*. doi:10.1016/j.matpr.2020.10.238

Shuai, X., Shen, W., Hou, Z., Ke, S., Xu, C., & Jiang, C. (2014). A versatile chemical conversion synthesis of Cu2S nanotubes and the photovoltaic activities for dye-sensitized solar cell. *Nanoscale Res Lett, 9*(1), 513. doi:10.1186/1556-276X-9-513

Silva, Camila, Santos, Andrés, Salazar, Rodrigo, Lamilla, Claudio, Pavez, Boris, Meza, Pablo, . . . Barrientos, Leticia. (2019). Evaluation of dye sensitized solar cells based on a pigment obtained from Antarctic Streptomyces fildesensis. *Solar Energy, 181*, 379-385. doi:10.1016/j.solener.2019.01.035

Singh, Chetan C., & Panda, Emila. (2018). Zinc interstitial threshold in Al-doped ZnO film: Effect on microstructure and optoelectronic properties. *Journal of Applied Physics, 123*(16). doi:10.1063/1.5021736

Singh, Manorama, Sahu, Anjumala, Mahata, Suhasini, Shukla, Prashant, Rai, Ankita, & Rai, Vijai K. (2019). Efficient electrocatalytic oxidation of p-phenylenediamine using a novel PANI/ZnO anchored bio-reduced graphene oxide nanocomposite. *New Journal of Chemistry, 43*(17), 6500-6506. doi:10.1039/c9nj00837c

Sivakumar, A., Victor, C., Nayak, M. Muralidhr, & Dhas, S. A. Martin Britto. (2019). Structural, optical, and morphological stability of ZnO nano rods under shock wave loading conditions. *Materials Research Express, 6*(4). doi:10.1088/2053-1591/aafae6

Song, Dengyuan, Aberle, Armin G., & Xia, James. (2002). Optimisation of ZnO:Al films by change of sputter gas pressure for solar cell application. *Applied Surface Science, 195*(1-4), 291-296. doi:10.1016/s0169-4332(02)00611-6

Srikant, V., & Clarke, D. R. (1998). On the optical band gap of zinc oxide. *Journal of Applied Physics, 83*(10), 5447-5451. doi:10.1063/1.367375

Stuckelberger, Michael, Biron, Rémi, Wyrsch, Nicolas, Haug, Franz-Josef, & Ballif, Christophe. (2017). Review: Progress in solar cells from hydrogenated amorphous silicon. *Renewable and Sustainable Energy Reviews, 76*, 1497-1523. doi:10.1016/j.rser.2016.11.190

Studenikin, S. A., Golego, N., & Cocivera, M. (1998). Fabrication of green and orange photoluminescent, undoped ZnO films using spray pyrolysis. *Journal of Applied Physics, 84*(4), 2287-2294. doi:Doi 10.1063/1.368295

Su'ait, M. S., Rahman, M. Y. A., & Ahmad, A. (2015). Review on polymer electrolyte in dye-sensitized solar cells (DSSCs). *Solar Energy, 115*, 452-470. doi:10.1016/j.solener.2015.02.043

Subramanyam, T. K., Srinivasulu Naidu, B., & Uthanna, S. (1999). Effect of substrate temperature on the physical properties of DC reactive magnetron sputtered ZnO films. *Optical Materials, 13*(2), 239-247. doi:10.1016/s0925-3467(99)00070-1

Sun, Huicheng, Qin, Da, Huang, Shuqing, Guo, Xiaozhi, Li, Dongmei, Luo, Yanhong, & Meng, Qingbo. (2011). Dye-sensitized solar cells with NiS counter electrodes electrodeposited by a potential reversal technique. *Energy & Environmental Science, 4*(8). doi:10.1039/c0ee00791a

Suzuki, Kazuharu, Yamaguchi, Makoto, Kumagai, Mikio, & Yanagida, Shozo. (2003). Application of Carbon Nanotubes to Counter Electrodes of Dye-sensitized Solar Cells. *Chemistry Letters, 32*(1), 28-29. doi:10.1246/cl.2003.28

Svensson, J. S. E. M., & Granqvist, C. G. (1984). Electrochromic tungsten oxide films for energy efficient windows. *Solar Energy Materials, 11*(1-2), 29-34. doi:10.1016/0165-1633(84)90025-x

Taguchi, Taketo, Zhang, Xin-tong, Sutanto, Irwan, Tokuhiro, Ken-ichi, Rao, Tata N, Watanabe, Hiroko, . . . Fujishima, Akira. (2003). Improving the performance of solid-state dye-

sensitized solar cell using MgO-coated TiO 2 nanoporous film. *Chemical Communications*(19), 2480-2481.

Tan, S. T., Chen, B. J., Sun, X. W., Fan, W. J., Kwok, H. S., Zhang, X. H., & Chua, S. J. (2005). Blueshift of optical band gap in ZnO thin films grown by metal-organic chemical-vapor deposition. *Journal of Applied Physics, 98*(1). doi:10.1063/1.1940137

Tan, Wai Kian, Lockman, Zainovia, Abdul Razak, Khairunisak, Kawamura, Go, Muto, Hiroyuki, & Matsuda, Atsunori. (2013). Enhanced dye-sensitized solar cells performance of ZnO nanorod arrays grown by low-temperature hydrothermal reaction. *International Journal of Energy Research*, n/a-n/a. doi:10.1002/er.3026

Tang, H., Prasad, K., Sanjinès, R., Schmid, P. E., & Lévy, F. (1994). Electrical and optical properties of TiO2anatase thin films. *Journal of Applied Physics, 75*(4), 2042-2047. doi:10.1063/1.356306

Taya, Sofyan A. (2013). Dye-Sensitized Solar Cells Using Fresh and Dried Natural Dyes. *International Journal of Materials Science and Applications, 2*(2). doi:10.11648/j.ijmsa.20130202.11

Thomas, D. G. (1960). The exciton spectrum of zinc oxide. *Journal of Physics and Chemistry of Solids, 15*(1-2), 86-96. doi:10.1016/0022-3697(60)90104-9

Tiwana, P., Docampo, P., Johnston, M. B., Snaith, H. J., & Herz, L. M. (2011). Electron mobility and injection dynamics in mesoporous ZnO, SnO(2), and TiO(2) films used in dye-sensitized solar cells. *ACS Nano, 5*(6), 5158-5166. doi:10.1021/nn201243y

Trancik, J. E., Barton, S. C., & Hone, J. (2008). Transparent and catalytic carbon nanotube films. *Nano Lett, 8*(4), 982-987. doi:10.1021/nl071945i

Trémillon, Bernard. (1993). *Électrochimie analytique et réactions en solution. Tome 2. Réactions et méthodes électrochimiques* (Masson Paris Ed.). Paris Cedex 06.

Tributsch, H., & Calvin, M. (1971). Electrochemistry of Excited Molecules: Photo-Electrochemical Reactions of Chlorophylls. *Photochemistry and Photobiology, 14*(2), 95-112. doi:10.1111/j.1751-1097.1971.tb06156.x

Tsoukleris, D. S., Arabatzis, I. M., Chatzivasilogiou, E., Kontos, A. I., Belessi, V., Bernard, M. C., & Falaras, P. (2005). 2-Ethyl-1-hexanol based screen-printed titania thin films for dye-sensitized solar cells. *Solar Energy, 79*(4), 422-430. doi:10.1016/j.solener.2005.02.017

Ueno, Shintaro, Utsunomiya, Hirokazu, & Fujihara, Shinobu. (2013). Low-Temperature Fabrication of Dye-Sensitized ZnO Electrodes via Zinc Hydroxide Acetate by Utilizing Liquid Phase. *Key Engineering Materials, 582*, 202-205. doi:10.4028/www.scientific.net/KEM.582.202

Uk Lee, Sung, Seok Choi, Won, & Hong, Byungyou. (2010). A comparative study of dye-sensitized solar cells added carbon nanotubes to electrolyte and counter electrodes. *Solar Energy Materials and Solar Cells, 94*(4), 680-685. doi:10.1016/j.solmat.2009.11.030

Umar, A. (2009). Growth of Comb-like ZnO Nanostructures for Dye-sensitized Solar Cells Applications. *Nanoscale Res Lett, 4*(9), 1004-1008. doi:10.1007/s11671-009-9353-3

Utsunomiya, Hirokazu, Ueno, Shintaro, & Fujihara, Shinobu. (2013). Fabrication of Nanostructured Zinc Oxide Films on Plastic Substrates by Pyrolysis Method and their Application to Dye-Sensitized Solar Cells. *Key Engineering Materials, 582*, 206-209. doi:10.4028/www.scientific.net/KEM.582.206

Van de Walle, C. G. (2000). Hydrogen as a cause of doping in zinc oxide. *Physical Review Letters, 85*(5), 1012-1015. doi:DOI 10.1103/PhysRevLett.85.1012

Vankar, Padma S. (2000). Chemistry of natural dyes. *Resonance, 5*(10), 73-80. doi:10.1007/bf02836844

Vega-Poot, A. G., Macias-Montero, M., Idigoras, J., Borras, A., Barranco, A., Gonzalez-Elipe, A. R., . . . Anta, J. A. (2014). Mechanisms of electron transport and recombination in ZnO nanostructures for dye-sensitized solar cells. *Chemphyschem, 15*(6), 1088-1097. doi:10.1002/cphc.201301068

Vijayaprasath, G., Murugan, R., Ravi, G., Mahalingam, T., & Hayakawa, Y. (2014). Characterization of dilute magnetic semiconducting transition metal doped ZnO thin films by sol–gel spin coating method. *Applied Surface Science, 313*, 870-876. doi:10.1016/j.apsusc.2014.06.093

Villanueva-Cab, J., Oskam, G., & Anta, J. A. (2010). A simple numerical model for the charge transport and recombination properties of dye-sensitized solar cells: A comparison of transport-limited and transfer-limited recombination. *Solar Energy Materials and Solar Cells, 94*(1), 45-50. doi:10.1016/j.solmat.2009.06.004

Visimberga, G., Faulkner, C. C., Boese, M., & O'Dwyer, C. (2012). Core-Shell ZnO Nanorod Lasers. *ECS Transactions, 45*(7), 51-59. doi:10.1149/1.3701525

Vittal, R., & Ho, Kuo-Chuan. (2017). Zinc oxide based dye-sensitized solar cells: A review. *Renewable and Sustainable Energy Reviews, 70*, 920-935. doi:10.1016/j.rser.2016.11.273

Vyas, Sumit. (2020). A Short Review on Properties and Applications of Zinc Oxide Based Thin Films and Devices : ZnO as a promising material for applications in electronics, optoelectronics, biomedical and sensors. *Johnson Matthey Technology Review, 64*(2), 202-218. doi:10.1595/205651320x15694993568524

Wang, Feifei, Liu, Ruibin, Pan, Anlian, Xie, Sishen, & Zou, Bingsuo. (2007). A simple and cheap way to produce porous ZnO ribbons and their photovoltaic response. *Materials Letters, 61*(23-24), 4459-4462. doi:10.1016/j.matlet.2007.02.021

Wang, Lisheng, Zhang, Xiaozhong, Zhao, Songqing, Zhou, Guoyuan, Zhou, Yueliang, & Qi, Junjie. (2005). Synthesis of well-aligned ZnO nanowires by simple physical vapor deposition on c-oriented ZnO thin films without catalysts or additives. *Applied Physics Letters, 86*(2). doi:10.1063/1.1851607

Wang, M., Anghel, A. M., Marsan, B., Cevey Ha, N. L., Pootrakulchote, N., Zakeeruddin, S. M., & Gratzel, M. (2009). CoS supersedes Pt as efficient electrocatalyst for triiodide reduction in dye-sensitized solar cells. *J Am Chem Soc, 131*(44), 15976-15977. doi:10.1021/ja905970y

Wang, P., Zakeeruddin, S. M., Exnar, I., & Gratzel, M. (2002). High efficiency dye-sensitized nanocrystalline solar cells based on ionic liquid polymer gel electrolyte. *Chem Commun (Camb)*(24), 2972-2973. doi:10.1039/b209322g

Wang, Y., Zhou, C. L., Elquist, A. M., Ghods, A., Saravade, V. G., Lu, N., & Ferguson, I. (2018). A review of earth abundant ZnO-based materials for thermoelectric and photovoltaic applications. *Oxide-Based Materials and Devices Ix, 10533*. doi:10.1117/12.2302467

Wei, Junfeng, Zhang, Chujun, Ji, Guoqi, Han, Yunfei, Ismail, Irfan, Li, Hengyue, . . . Ma, Chang-Qi. (2019). Roll-to-roll printed stable and thickness-independent ZnO:PEI composite electron transport layer for inverted organic solar cells. *Solar Energy, 193*, 102-110. doi:10.1016/j.solener.2019.09.037

Weinstock, I. A. (1998). Homogeneous-Phase Electron-Transfer Reactions of Polyoxometalates†. *Chemical Reviews, 98*(1), 113-170. doi:10.1021/cr9703414

Williams, Richard. (1960). Becquerel Photovoltaic Effect in Binary Compounds. *The Journal of Chemical Physics, 32*(5), 1505-1514. doi:10.1063/1.1730950

Wu, J., Lan, Z., Lin, J., Huang, M., Huang, Y., Fan, L., . . . Wei, Y. (2017). Counter electrodes in dye-sensitized solar cells. *Chem Soc Rev, 46*(19), 5975-6023. doi:10.1039/c6cs00752j

Wu, J., Xie, C. S., Bai, Z. K., Zhu, B. L., Huang, K. J., & Wu, R. (2002). Preparation of ZnO-glass varistor from tetrapod ZnO nanopowders. *Materials Science and Engineering B-Solid State Materials for Advanced Technology, 95*(2), 157-161.

Wu, Jihuai, Li, Qinghua, Fan, Leqing, Lan, Zhang, Li, Pinjiang, Lin, Jianming, & Hao, Sanchun. (2008). High-performance polypyrrole nanoparticles counter electrode for dye-sensitized solar cells. *Journal of Power Sources, 181*(1), 172-176. doi:10.1016/j.jpowsour.2008.03.029

Xia, Jiangbin, Chen, Ling, & Yanagida, Shozo. (2011). Application of polypyrrole as a counter electrode for a dye-sensitized solar cell. *Journal of Materials Chemistry, 21*(12). doi:10.1039/c0jm04116e

Xiang, J. H., Zhu, P. X., Masuda, Y., Okuya, M., Kaneko, S., & Koumoto, K. (2006). Flexible solar-cell from zinc oxide nanocrystalline sheets self-assembled by an in-situ electrodeposition process. *J Nanosci Nanotechnol, 6*(6), 1797-1801. doi:10.1166/jnn.2006.244

Xie, Yu-Long, Li, Zi-Xia, Xu, Zhu-Guo, & Zhang, Hao-Li. (2011). Preparation of coaxial TiO2/ZnO nanotube arrays for high-efficiency photo-energy conversion applications. *Electrochemistry Communications, 13*(8), 788-791.

Xu, Chengkun, Wu, Jiamin, Desai, Umang V, & Gao, Di. (2012). High-efficiency solid-state dye-sensitized solar cells based on TiO2-coated ZnO nanowire arrays. *Nano letters, 12*(5), 2420-2424.

Xu, X. L., Lau, S. P., Chen, J. S., Sun, Z., Tay, B. K., & Chai, J. W. (2001). Dependence of electrical and optical properties of ZnO films on substrate temperature. *Materials Science in Semiconductor Processing, 4*(6), 617-620. doi:10.1016/s1369-8001(02)00029-x

Yang, Dong, Zhou, Xin, Yang, Ruixia, Yang, Zhou, Yu, Wei, Wang, Xiuli, . . . Chang, Robert P. H. (2016). Surface optimization to eliminate hysteresis for record efficiency planar perovskite solar cells. *Energy & Environmental Science, 9*(10), 3071-3078. doi:10.1039/c6ee02139e

Yella, A., Lee, H. W., Tsao, H. N., Yi, C., Chandiran, A. K., Nazeeruddin, M. K., . . . Gratzel, M. (2011). Porphyrin-sensitized solar cells with cobalt (II/III)-based redox electrolyte exceed 12 percent efficiency. *Science, 334*(6056), 629-634. doi:10.1126/science.1209688

Yilbas, Bekir Sami, Al-Sharafi, Abdullah, & Ali, Haider. (2019). Surfaces for Self-Cleaning. In *Self-Cleaning of Surfaces and Water Droplet Mobility* (1st Edition ed., pp. 45-98).

Yin, Xiong, Liu, Xizhe, Wang, Long, & Liu, Bin. (2010). Electrophoretic deposition of ZnO photoanode for plastic dye-sensitized solar cells. *Electrochemistry Communications, 12*(9), 1241-1244. doi:10.1016/j.elecom.2010.06.029

Yoo, Y. Z., Jin, Zheng-Wu, Chikyow, T., Fukumura, T., Kawasaki, M., & Koinuma, H. (2002). S doping in ZnO film by supplying ZnS species with pulsed-laser-deposition method. *Applied Physics Letters, 81*(20), 3798-3800. doi:10.1063/1.1521577

Yoshikawa, Hisashi, & Adachi, Sadao. (1997). Optical Constants of ZnO. *Japanese Journal of Applied Physics, 36*(Part 1, No. 10), 6237-6243. doi:10.1143/jjap.36.6237

Yoshikawa, Kunta, Yoshida, Wataru, Irie, Toru, Kawasaki, Hayato, Konishi, Katsunori, Ishibashi, Hirotaka, . . . Yamamoto, Kenji. (2017). Exceeding conversion efficiency of 26% by heterojunction interdigitated back contact solar cell with thin film Si technology. *Solar Energy Materials and Solar Cells, 173*, 37-42. doi:10.1016/j.solmat.2017.06.024

Zhang, Y., & Xu, X. (2020). Machine Learning Band Gaps of Doped-TiO2 Photocatalysts from Structural and Morphological Parameters. *ACS Omega, 5*(25), 15344-15352. doi:10.1021/acsomega.0c01438

Zhao, D., Li, J., Sathasivam, S., & Carmalt, C. J. (2020). n-Type conducting P doped ZnO thin films via chemical vapor deposition. *RSC Adv, 10*(57), 34527-34533. doi:10.1039/d0ra05667g

Zhao, J. X., Zheng, Y. Z., Lu, X. H., Chen, J. F., Tao, X., & Zhou, W. (2013). Characterizing the role of iodine doping in improving photovoltaic performance of dye-sensitized hierarchically structured ZnO solar cells. *Chemphyschem, 14*(9), 1977-1984. doi:10.1002/cphc.201300066

Zhao, Jianhua, Wang, Aihua, Green, Martin A., & Ferrazza, Francesca. (1998). 19.8% efficient "honeycomb" textured multicrystalline and 24.4% monocrystalline silicon solar cells. *Applied Physics Letters, 73*(14), 1991-1993. doi:10.1063/1.122345

Zheng, H., Tachibana, Y., & Kalantar-Zadeh, K. (2010). Dye-sensitized solar cells based on WO3. *Langmuir, 26*(24), 19148-19152. doi:10.1021/la103692y

Zheng, Haidong, Ou, Jian Zhen, Strano, Michael S., Kaner, Richard B., Mitchell, Arnan, & Kalantar-zadeh, Kourosh. (2011). Nanostructured Tungsten Oxide - Properties, Synthesis, and Applications. *Advanced Functional Materials, 21*(12), 2175-2196. doi:10.1002/adfm.201002477

Zheng, Jin You, Haider, Zeeshan, Van, Thanh Khue, Pawar, Amol Uttam, Kang, Myung Jong, Kim, Chang Woo, & Kang, Young Soo. (2015). Tuning of the crystal engineering and photoelectrochemical properties of crystalline tungsten oxide for optoelectronic device applications. *CrystEngComm, 17*(32), 6070-6093. doi:10.1039/c5ce00900f

Zheng, Jin You, Song, Guang, Hong, Jisang, Van, Thanh Khue, Pawar, Amol Uttam, Kim, Do Yoon, . . . Kang, Young Soo. (2014). Facile Fabrication of WO3 Nanoplates Thin Films with Dominant Crystal Facet of (002) for Water Splitting. *Crystal Growth & Design, 14*(11), 6057-6066. doi:10.1021/cg5012154

Zheng, Yan-Zhen, Tao, Xia, Wang, Li-Xin, Xu, Hui, Hou, Qian, Zhou, Wei-Lie, & Chen, Jian-Feng. (2010). Novel ZnO-Based Film with Double Light-Scattering Layers as Photoelectrodes for Enhanced Efficiency in Dye-Sensitized Solar Cells†. *Chemistry of Materials, 22*(3), 928-934. doi:10.1021/cm901780z

Zhuang, Shuxin, Lu, Mi, Zhou, Nan, Zhou, Litao, Lin, Daqin, Peng, Zhengyu, & Wu, Qihui. (2019). Cu modified ZnO nanoflowers as photoanode material for highly efficient dye sensitized solar cells. *Electrochimica Acta, 294*, 28-37. doi:10.1016/j.electacta.2018.10.045

Znaidi, Lamia. (2010). Sol–gel-deposited ZnO thin films: A review. *Materials Science and Engineering: B, 174*(1-3), 18-30. doi:10.1016/j.mseb.2010.07.001

Zou, F., Hu, X., Li, Z., Qie, L., Hu, C., Zeng, R., . . . Huang, Y. (2014). MOF-derived porous ZnO/ZnFe(2)O(4)/C octahedra with hollow interiors for high-rate lithium-ion batteries. *Adv Mater, 26*(38), 6622-6628. doi:10.1002/adma.201402322